



HAL
open science

Compréhension des mécanismes de formation des gouttes en émulsification membranaire assistée par vibrations transversales

Aude Bertrandias

► **To cite this version:**

Aude Bertrandias. Compréhension des mécanismes de formation des gouttes en émulsification membranaire assistée par vibrations transversales. Autre. Université Paris Saclay (COmUE), 2016. Français. NNT : 2016SACLC094 . tel-01532723

HAL Id: tel-01532723

<https://theses.hal.science/tel-01532723>

Submitted on 3 Jun 2017

HAL is a multi-disciplinary open access archive for the deposit and dissemination of scientific research documents, whether they are published or not. The documents may come from teaching and research institutions in France or abroad, or from public or private research centers.

L'archive ouverte pluridisciplinaire **HAL**, est destinée au dépôt et à la diffusion de documents scientifiques de niveau recherche, publiés ou non, émanant des établissements d'enseignement et de recherche français ou étrangers, des laboratoires publics ou privés.

NNT : 2016SACLC094

THÈSE DE DOCTORAT
DE
L'UNIVERSITÉ PARIS-SACLAY
PRÉPARÉE À
"CENTRALESUPÉLEC"

ÉCOLE DOCTORALE N° 579
Sciences mécaniques et énergétiques, matériaux et
géosciences - SMEMAG

Spécialité de doctorat : Génie des Procédés

Par

Mme Aude Bertrandias

Understanding drop generation mechanisms in transversally
vibrating membrane emulsification

Thèse présentée et soutenue à Châtenay-Malabry, le 2 décembre 2016

Composition du Jury :

M. C. Clanet	Directeur de recherches, Ecole Polytechnique	Président
M. H.-Z. Li	Professeur, ENSIC	Rapporteur
M. D. Legendre	Professeur, Institut de Mécanique des Fluides de Toulouse	Rapporteur
M. H. Duval	Maître de Conférences HDR, CentraleSupélec	Directeur de thèse
Mme M.-L. Giorgi	Professeur, CentraleSupélec	Co-encadrant de thèse
M. C. Arnaud	Fondateur et gérant d'Emulsar	Invité

Abstract (English and French)

Title: Understanding drop generation mechanisms in transversally vibrating membrane emulsification.

Keywords: emulsion, drop, jet, vibration, resonance, hydrodynamics.

Abstract: In transversally vibrating membrane emulsification, significantly smaller drops are generated in certain conditions. We aim to explain the mechanisms involved. To do so, two experimental setups were developed. A single drop is formed from a nozzle into an outer phase, which is either stationary or cross-flowing. The nozzle can be submitted to axial vibrations.

For a drop formed into a stationary phase, a transition in drop generation occurs above a critical forcing amplitude. Below the threshold, a large drop forms by dripping. Above the threshold, a drop detaches when its first eigenfrequency and the forcing frequency coincide. The drop then resonates and detaches once a critical elongation ratio is reached. We model a drop as a linearly forced

harmonic oscillator and add an extra damping term to account for the viscous dissipation between the drop and nozzle surface. We well reproduce the threshold amplitudes and drop diameters.

We also study drops generated into cross-flow. In dripping mode, drop diameters are described by a torque balance. At a critical inner Weber number function of the outer capillary and Ohnesorge numbers, a transition to jetting occurs. Jet widening or narrowing takes place depending on the phase velocity ratio. We propose a model to account for the transition to jetting based on the drop equation of motion. Overall, we adequately account for the jetting velocity and drop diameters, with discrepancies which were explained.

Titre : Compréhension des mécanismes de formation des gouttes en émulsification membranaire assistée par vibrations transversales.

Mots clés : émulsion, goutte, jet, vibration, résonance, hydrodynamique.

Résumé : Dans certaines conditions, une baisse significative de la taille des gouttes se produit en émulsification membranaire avec vibrations transversales. Pour comprendre les mécanismes impliqués, nous avons développé deux dispositifs expérimentaux, dans lesquels une goutte unique est formée à travers un capillaire dans une phase externe, qui est soit stationnaire, soit en écoulement. Le capillaire peut être mis en vibration parallèlement à son axe.

Lorsque la phase externe est stationnaire, au-delà d'une amplitude seuil de forçage, la taille des gouttes formées diminue significativement. La goutte entre en résonance quand sa fréquence propre coïncide avec la fréquence de forçage et elle se détache si elle atteint une élongation critique. La goutte est modélisée comme un oscillateur harmonique linéaire forcé. Un terme

d'amortissement additionnel décrit la dissipation visqueuse entre la goutte et la surface du capillaire. Ce modèle prédit bien les amplitudes seuils et les diamètres de gouttes.

Lorsque la phase externe s'écoule, nous avons étudié deux régimes de formation de gouttes, en goutte à goutte (dripping) ou à partir d'un jet (jetting). Expérimentalement, la transition du dripping au jetting se produit à un nombre de Weber interne seuil, dont la valeur dépend des nombres capillaire et d'Ohnesorge externes. Le jet se rétrécit (narrowing) ou s'élargit (widening) selon le rapport de vitesses des phases choisi. En dripping, les diamètres de gouttes sont bien prédits par un bilan des moments. En jetting, un modèle basé sur l'équation du mouvement permet d'estimer la vitesse critique permettant la transition au jetting et les diamètres de gouttes résultants.

Acknowledgements

Quand je dis « 2 décembre », beaucoup me répondent « bataille d'Austerlitz ». Pour moi, cette date représente autre chose : ma soutenance de thèse. Mais, je n'en suis pas arrivée là seule et je souhaite remercier les personnes qui m'ont accompagnée durant ces trois années.

Je souhaite d'abord remercier de tout cœur Hervé, mon directeur de thèse, pour son encadrement. Je le remercie spécialement pour son implication, ses idées toujours foisonnantes et son humour. Ça a été un vrai plaisir de travailler avec lui. Il m'a appris beaucoup de choses et j'ai apprécié nos discussions régulières. Je remercie également Marie-Laurence qui a co-encadré ma thèse, pour ses conseils à chaque fois pertinents, son honnêteté, son optimisme et pour les financements, notamment pour les montages expérimentaux et la fin de la thèse. J'ai eu de la chance d'avoir deux encadrants impliqués, compétents et avec des qualités humaines indéniables.

Je tiens aussi à remercier Patrick Perré, directeur du LGPM, d'avoir soutenu ma candidature pour effectuer ma thèse au LGPM et d'avoir créé au sein du laboratoire un environnement de travail agréable, permettant un vrai échange entre collègues.

Je remercie également Benoît et Catherine de l'Ecole Doctorale, pour leur soutien, leur accueil chaleureux et leur aide avec l'association des doctorants, l'UJ2CP.

Je tiens à remercier particulièrement Joel, qui m'a permis de mener à bien mes expériences. Il m'a aidé à prendre en main le premier dispositif et je n'aurais pas pu développer le deuxième montage sans son aide et son expertise. Il a toujours été impliqué, disponible et très compétent. J'ai aussi apprécié nos discussions lors des fameuses pauses goûter !

Merci aussi à Thierry et Jean, pour leur aide sur le développement des montages et d'avoir participé pleinement à la réflexion dessus. J'ai apprécié de travailler avec eux grâce à leur compétence, leur bonne humeur et leur patience lorsqu'ils me voyaient arriver dans l'atelier, ce qui signifiait en général : problème sur le montage !

Je souhaite remercier Cyril pour les mesures au microscope, Jamila pour son aide sur le tensiomètre et le viscosimètre, Frédéric Douit pour le prêt du pot vibrant du laboratoire MSSMat, Thomas Reiss de m'avoir permis d'utiliser le rhéomètre du laboratoire MSSMat, Nicolas Roubier pour le prêt de l'objectif Questar du laboratoire EM2C, Didier Coudray et Pierre Lecoy pour le prêt d'un outil de découpage de fibre optique du laboratoire LISA puis Erika Jean-Bart pour les découpes de caoutchouc au laser au laboratoire EM2C.

Je remercie sincèrement les membres du jury, d'avoir accepté de faire partie du jury et de l'intérêt qu'ils ont porté à mon travail. Merci à Christophe Clanet, d'avoir bien voulu présider le jury. Merci à Dominique Legendre et Huai-Zhi Li, d'avoir lu et commenté mon manuscrit puis d'avoir assisté à la soutenance en tant que rapporteurs. Merci enfin à Christophe Arnaud, de ses quelques visites pour échanger sur les expériences et d'avoir été présent à ma soutenance en tant qu'invité.

Merci aussi à tous ceux qui ont rendu l'ambiance durant ces trois années agréable au laboratoire, en particulier Marie, Pascal, Huan, Mathilde, Joel, Cyril, Thierry, Jean, Jamila, Coco, Imène et Benham. Merci aussi aux doctorants des autres labos que j'ai pu rencontrer et avec qui j'ai sympathisé, notamment Emmanuel et nos nombreux retours en RER.

Enfin, merci à ma famille, spécialement mes parents, mes proches et mes amis qui m'ont soutenue et encouragée durant ces trois années.

General preamble

The work described in this thesis manuscript was carried out at the laboratory LGPM (Laboratoire de Génie des Procédés et Matériaux), belonging to CentraleSupélec (Université Paris-Saclay).

The manuscript is based on three publications, which make up chapters 3, 4 and 5, with some additional unpublished information also included. The contents of the publications were unchanged except for the section, figure, table and equation numbers and the corresponding references to these in the text (the numbering was adapted to follow the manuscript format). The publication references are the following:

- A. Bertrandias, H. Duval, J. Casalinho and M. L. Giorgi, « Good vibrations — Transition in drop generation from an immersed capillary tube », *EPL*, 111, 44004, 2015. (doi: 10.1209/0295-5075/111/44004).
- A. Bertrandias, H. Duval, J. Casalinho and M. L. Giorgi, « Drop generation from a vibrating nozzle in an immiscible liquid-liquid system », *Phys. Fluids*, 28, 102103, 2016. (doi: 10.1063/1.4964378).
- A. Bertrandias, H. Duval, J. Casalinho and M. L. Giorgi, « Dripping to jetting transition for cross-flowing liquids », which will be submitted.

This work was also presented during oral presentations at three international conferences, which are the following:

- 15th Conference of the International Association of Colloid and Interface Scientists: IACIS 2015, 24th to 29th May 2015, Mainz, Germany.
A. Bertrandias, H. Duval and M. L. Giorgi, « Mechanisms of Droplet Breakup During High-amplitude Forced Oscillations: Understanding Membrane Emulsification Coupled with Transversal Vibrations ».
- 10th European Congress of Chemical Engineering: ECCE 10, 27th September to 1st October 2015, Nice, France.
A. Bertrandias, H. Duval, J. Casalinho and M. L. Giorgi, « Droplet generation assisted by axial vibrations: a sensitivity study ».
- 9th International Conference on Multiphase Flow: ICMF 2016, 22nd to 27th May, 2016, Firenze, Italy.
A. Bertrandias, H. Duval, J. Casalinho and M. L. Giorgi, « Drop in drop diameter from a vibrating capillary tube ».

Contents

Abstract (English and French)	i
Acknowledgements	iii
General preamble	v
Contents	vii
List of abbreviations and acronyms	1
List of symbols	3
List of Greek letters	7
Introduction	9
Chapter 1: Literature review	11
1. Emulsions and emulsification	12
1.1. Emulsions.....	12
1.2. Emulsification	19
1.3. Membrane emulsification	21
1.4. Conclusions.....	32
2. Drop generation mechanisms	34
2.1. Hydrodynamic instabilities	34
2.2. Jet breakup	40
2.3. Drop breakup.....	45
2.4. Models for drop generation in membrane emulsification.....	49
2.5. Conclusions.....	52
3. Single drop behavior under forced oscillations	54
3.1. Free drop	54
3.2. Partially bound drop under small-amplitude forcing.....	59
3.3. Partially bound drop under high-amplitude forcing	63
3.4. Conclusions.....	68
4. Conclusions and aims of the work	70
Chapter 2: Materials and methods	73

1.	Single drop formation setup without continuous phase flow	74
1.1.	Experimental setup	74
1.2.	Parameters investigated	79
1.3.	Experimental methods	83
1.4.	Summary of the trials performed.....	84
2.	Setup with continuous phase flow	85
2.1.	Experimental setup	85
2.2.	Parameters investigated	91
2.3.	Experimental methods	91
2.4.	Summary of the trials performed.....	94
3.	General methods	95
3.1.	System characterisation	95
3.2.	Process characterisation	97
3.3.	Cleaning protocol	98
3.4.	Image analysis	100
3.5.	Data analysis.....	104
4.	Conclusions.....	106
Chapter 3: Impact of axial vibrations on drop generation in dripping mode		107
1.	Preamble	108
2.	Good vibrations - Transition in drop generation from an immersed capillary tube	109
2.1.	Abstract	109
2.2.	Introduction.....	109
2.3.	Experimental setup	110
2.4.	Drop detachment mode without vibration.....	111
2.5.	Detachment modes with vibration	112
2.6.	Threshold.....	113
2.7.	Resonance	114
2.8.	Force-based analysis	116
2.9.	Elongation-based analysis	118
2.10.	Conclusion	119
2.11.	Acknowledgements	119
3.	Additional information.....	120
3.1.	Harkins-Brown correction factor.....	120
3.2.	Factor ϕ	120
3.3.	Tate-like model.....	120
4.	References.....	122

Chapter 4: Model for drop generation in dripping mode with axial vibrations	123
1. Preamble	124
2. Drop generation from a vibrating nozzle in an immiscible liquid-liquid system.....	125
2.1. Abstract	125
2.2. Introduction.....	125
2.3. Experimental setup	128
2.4. Transition from dripping to stretching mode.....	131
2.5. Impact of process parameters and system properties	133
2.6. Further analysis	136
2.7. Conclusion	142
2.8. Appendix: additional friction term β film	142
2.9. Supplementary material.....	144
2.10. Acknowledgements	149
3. Additional information.....	150
3.1. Initial conditions for the model	150
4. References.....	151
Chapter 5: Transition from dripping to jetting	153
1. Preamble	154
2. Dripping to jetting transition for cross-flowing liquids	155
2.1. Abstract	155
2.2. Introduction.....	155
2.3. Experimental	157
2.4. Drop generation by dripping with cross-flow	160
2.5. Dripping to jetting transition (DJT).....	162
2.6. Conclusions.....	169
2.7. Appendix.....	170
2.8. Supplementary material.....	170
2.9. Acknowledgements	175
3. Additional information.....	175
3.1. Influence of the dispersed phase viscosity.....	175
4. References.....	177
Conclusion.....	179
Appendix 1: Surfactant molecules formulae	183

Appendix 2: CAD of the experimental setups	187
1. Setup 1: single drop formation into a stationary outer phase	188
2. Setup 2: single drop formation into cross-flow	189
Appendix 3: Complementary results on drop generation in stretching mode with a stationary outer phase	191
1. Complementary experimental results	192
1.1. Impact of dispersed phase flow rate	192
1.2. Impact of the pore diameter	195
1.3. Impact of the continuous phase viscosity	195
2. Brief analysis of the results	196
2.1. Dimensionless frequency	196
2.2. Predictions from the full model	197
2.3. Conclusions.....	198
Appendix 4: Drops simultaneously submitted to vibration and cross-flow	199
1. Experimental methods: choice of the investigation range.....	200
1.1. Choice of the continuous phase flow rate	200
1.2. Choice of the vibration parameters	201
2. Results and analysis	201
3. Conclusions.....	203
Appendix 5: Jets simultaneously submitted to vibration and cross-flow	205
1. Experimental observations: different transitions.....	206
1.1. First transition: from jetting to dripping	206
1.2. Second transition: from dripping to stretching.....	206
2. Experimental results: observations	207
2.1. System 4: high dispersed phase viscosity.....	207
2.2. Reference system	208
3. Discussion.....	209
3.1. Different transitions	209
3.2. Drop size.....	209
3.3. Absolute and convective instabilities.....	210
4. Conclusions.....	210

Appendix 6: Understanding previous results in industrial transversally vibrating membrane emulsification	211
1. Results of C. Arnaud	212
1.1. Calculations	212
1.2. Drop generation mechanisms	212
2. Results of E. Lepercq-Bost	213
1.1. Drop generation without vibration	213
1.2. Drop generation with vibration.....	215
3. Conclusions.....	216
References	217
List of figures	227
List of tables	237
French summary (résumé français)	239

List of abbreviations and acronyms

2D	Two-dimensional
3D	Three-dimensional
A	Absolute instability
Brij 58	Polyethylene glycol hexadecyl ether
C	Convective instability
CAD	Computer-aided design
CCLD	Constant current supply
CFD	Computational Fluid Dynamics
CMC	Critical Micellar Concentration
CTAB	Cetyl trimethylammonium bromide
DJT	Dripping to jetting transition
EDR	Extreme dynamic range
FB	Force balance
fps	Frames per second
HLB	Hydrophilic Lipophilic Balance
HLD	Hydrophilic Lipophilic Deviation
HPH	High Pressure Homogeniser
HPLC	High-performance liquid chromatography
LCD	Liquid-crystal display
LED	Light-emitting diode
LFHO	Linearly forced harmonic oscillator
ME	Direct membrane emulsification
O	Oil
PACS	Physics and Astronomy Classification Scheme
PDMS	Polydimethylsiloxane
PEEK	Polyether ether ketone
pH	Potential hydrogen
PIT	Phase Inversion Temperature
PIV	Particle image velocimetry

PSP	Polyamid Seeding Particles
PTFE	Polytetrafluoroethylene
PVC	Poly(vinyl chloride)
RZ	Resonance zone
S	Solid
SDS	Sodium dodecyl sulphate
SLR	Simple Linear Regression
Span 80	Sorbitan monoleate
SPG	Shirasu Porous Glass
TB	Torque balance
Tween 20	Polysorbate 20
Tween 80	Polysorbate 80
UT	Ultra Turrax (rotor stator device)
VOF	Volume of fluid
W	Water

List of symbols

a	Acceleration (m.s^{-2})
a_{cap}	Nozzle/capillary acceleration (m.s^{-2})
a_{eff}	Effective nozzle/capillary acceleration (m.s^{-2})
$a_n P_n$	Legendre polynomials with coefficients (m)
A	Amplitude of vibration (m)
A_d	Amplitude of displacement of the drop centre of mass (m)
A_{pp}	Peak-to-peak amplitude of vibration (m)
A_{th}	Threshold amplitude for the onset of the stretching mode (m)
\bar{A}	Area (m^2)
b	Channel height (m)
Bo, Bo_o	Bond number and outer Bond number (-)
C	Surfactant bulk concentration (mol.L^{-1})
C_0	Free coefficient for estimating the fit on the drag coefficient (-)
C	Multiplier constant for β_{film} (-)
Ca, Ca_{out}	Capillary number and outer capillary number (-)
c_d	Drag coefficient (-)
d	Layer thickness (m)
\mathcal{D}	Bulk diffusion coefficient ($\text{m}^2.\text{s}^{-1}$)
D_d	Drop diameter (m)
D_j	Thread diameter (m)
D_m	Mass diameter at the end of the receding thread (kg)
D_p	Pore diameter (m)
D_t	Tube diameter (m)
\mathcal{D}_s	Surface diffusivity ($\text{m}^2.\text{s}^{-1}$)
D_r, D_{mb}, D_h	Rod, membrane and hydraulic diameters (m)
e	Error (%)

f	Forcing frequency (Hz)
f_c	Characteristic frequency (Hz)
f_n	Mode n eigenfrequency (Hz)
f_r	Resonance frequency (Hz)
F	Helmholtz free energy (J)
F_b	Buoyancy force (N)
F_d	Drag force (N)
F_{exc}	Excitation force (N)
F_{film}	Friction force in the film (N)
F_γ	Retaining capillary force (N)
F_{HB}	Harkins Brown correction factor (-)
g	Standard gravity (9.81 m.s ⁻²)
G	Shear rate (s ⁻¹)
HC	Kinetic energy correction (s)
J_d	Dispersed phase flux (L.h ⁻¹ .m ⁻²)
k, k'	Constant (- unless stated otherwise), logarithm of k constant (-)
k_B	Boltzmann constant (J.K ⁻¹)
K	Membrane permeability (m ²)
\bar{kS}	Time averaged transfer coefficient-area product (m ³ .s ⁻¹)
L, L_{max}	Drop length and maximum drop length (m)
\bar{L}	Characteristic length (m)
l_c	Capillary length (m)
l_d	Detachment distance during pinch off (m)
L_n	Thread length (m)
m	Azimuthal wavenumber (-)
M, M_a	Drop mass at the end of a receding jet and added mass (kg)
n	Polar wavenumber (mode number) (-)
n_p, n_{act}, n_{tot}	Number of pores, number of active pores, total number of pores (-)
n_{cp}	Continuous phase refractive index (-)

n_{dp}	Dispersed phase refractive index (-)
O	Circularity (-)
Oh, Oh_{dp}, Oh_{cp}	Ohnesorge number, inner and outer Ohnesorge number (-)
P	Perimeter (m)
P_c	Critical permeation pressure (Pa)
$P_{cp,in}, P_{cp,out}$	Continuous phase pressure at the membrane inlet and outlet (Pa)
P_{dp}	Dispersed phase pressure (Pa)
Pe	Péclet number (-)
P_{tm}	Transmembrane pressure (Pa)
Q	Quality factor (-)
q	Dispersed phase volumetric flow rate ($m^3.s^{-1}$)
q_{cp}	Continuous phase volumetric flow rate ($m^3.s^{-1}$)
r	Drop shape (m)
r_d	Distance from the drop axis to the half drop centre of mass (m)
R	Radius (m)
\bar{R}	Gas constant ($J.mol^{-1}.K^{-1}$)
r_d	Distance between the axis and half drop centre of mass (m)
$Re, Re_{cap}, Re_{in}, Re_p$	Reynolds number, Reynolds number in the capillary tube, inner Reynolds number, particle Reynolds number (-)
Ri	Richardson number (-)
S	Jet cross-section (m^2)
S_d	Surface area of the volume-equivalent sphere (m^2)
S_j	Surface area of the thread cross-section (m^2)
S_m	Membrane surface area (m^2)
Sh_{cp}	Continuous phase Sherwood number (-)
SP	Spreading parameter ($N.m^{-1}$)
t	Time (s)
t_c	Capillary time (s)
t_{max}	Time taken for the receding mass to travel from 0 to x_{max} (s)

T	Temperature (K)
U	Characteristic velocity ($\text{m}\cdot\text{s}^{-1}$)
U_o, U_A, U_B	Overall, type A and type B uncertainties (same unit as the quantity)
V, V_d, V_p, V_n	Volume, detached drop volume, pendant drop volume, volume fed to the drop during necking (m^3)
v_{cp}	Continuous phase flow velocity ($\text{m}\cdot\text{s}^{-1}$)
v_{dp} or v_d	Dispersed phase flow velocity ($\text{m}\cdot\text{s}^{-1}$)
$v_{s/c}$	Sedimentation or creaming velocity ($\text{m}\cdot\text{s}^{-1}$)
v_j	Velocity of the dispersed phase in the thread ($\text{m}\cdot\text{s}^{-1}$)
v_{xd}	Velocity of the drop centre of mass ($\text{m}\cdot\text{s}^{-1}$)
W	Work (J)
w_x, w_y	Weighting coefficient for the x and y variable (-)
We, We_c	Weber number and critical Weber number (-)
We_{in}, We_{out}	Inner Weber number and outer Weber number (-)
x or x_{cap}	Capillary position with respect to its rest position (m) or mass position with respect to its initial position for chapter 5 (m)
X_d	Position of the drop centre of mass with respect to the capillary/nozzle surface (m)
x_d	Position of the drop centre of mass with respect to its rest position (m)
\dot{x}_d	Velocity of the drop centre of mass ($\text{m}\cdot\text{s}^{-1}$)
x_{max}	Maximum drop recession distance before the start of pinch off (m)
$x_{1/2}$	Position of the centre of mass of the half drop with respect to the drop axis (m)

List of Greek letters

α	Exponent for drop size scaling (-)
β	Damping constant (s^{-1})
β_{film}	Damping coefficient for the additional friction in the film (s^{-1})
Γ	Surface excess concentration ($mol.m^{-2}$)
Γ_1	Surface concentration at the intermediate plateau ($mol.m^{-2}$)
Γ_∞	Limiting surfactant concentration ($mol.m^{-2}$)
γ	Interfacial tension ($N.m^{-1}$)
δ	Phase shift (rad)
δ_0	Free coefficient for estimating the fit on the drag coefficient (-)
ΔP	Laplace pressure (Pa)
$\Delta\rho$	Difference in fluid densities ($kg.m^{-3}$)
ΔU	Difference in fluid velocities ($m.s^{-1}$)
ε	Membrane porosity (-)
ζ	Viscosity ratio (dispersed to continuous phase) (-)
η	Fluid dynamic viscosity (Pa.s)
η_{cp} or η_c	Continuous phase dynamic viscosity (Pa.s)
η_{dp} or η_d	Dispersed phase dynamic viscosity (Pa.s)
θ	Contact angle ($^\circ$)
$\theta(t)$	Wedge angle variation in time, between the drop and nozzle surface ($^\circ$)
θ_a	Attachment angle ($^\circ$)
Θ	Wedge angle between the drop at rest and nozzle surface ($^\circ$)
λ	Wavelength (m)
λ^*	Optimal wavelength (m)
λ_1	Mode 1 eigenvalue (-)
λ_n	Mode n eigenvalue (-)
ν	Kinematic viscosity ($m^2.s^{-1}$)
ξ	Exponent for power law (-)

Π	Surface pressure (N.m ⁻¹)
ρ	Fluid density (kg.m ⁻³)
ρ_{cp} or ρ_c	Continuous phase dynamic density (kg.m ⁻³)
ρ_{dp} or ρ_d	Dispersed phase dynamic density (kg.m ⁻³)
$\sigma_x, \sigma_y, \sigma_{k'}, \sigma_\xi$	Uncertainty for the x, y, k' and ξ variable (same unit as the quantity)
τ	Characteristic time (s)
τ_{diff}	Characteristic time to reach the intermediate plateau (diffusion) (s)
τ_{dc}	Characteristic time to reach the intermediate plateau (diffusion coupled to convection) (s)
τ_n	Necking time (s)
τ_w	Shear stress at the membrane surface (Pa)
ϕ	Factor to obtain the effective capillary displacement (-)
ψ	Pore tortuosity (-)
ω	Forcing pulsation (Hz)
ω^*	Dimensionless drop eigenpulsation (Hz)
ω_n	Mode n eigenpulsation (Hz)
ω_r	Resonance pulsation (Hz)

Introduction

Context

An emulsion is a liquid-liquid system, where one fluid is in the form of drops in the second, outer, immiscible fluid. A typical example is salad dressing (vinaigrette). Emulsions are widespread in the food industry but also in the cosmetics, pharmaceutical or chemical industries. Various industrial-scale emulsification processes have thus been developed to produce the emulsions. These have been widely studied in order to better control the resulting product, notably drop size and drop size distribution. Indeed, drop size and drop size distribution affect the product properties, in particular its stability.

We focus on a specific process named cross-flow membrane emulsification (ME), developed in the 90s. In this process, a liquid is forced through a porous, inorganic membrane. The drops are formed on the other side of the membrane, into the continuous cross-flowing phase. For the moment, the low throughput does not make ME interesting for large-scale production. However, this process is of interest as it has other advantages compared to existing processes, including a lower energy density as well as lower shear and temperatures induced. Also, small drop sizes can be obtained, with a narrow size distribution (monodispersed emulsions) which is often industrially sought after.

ME has been recently coupled with vibration for an enhanced control on the generated drops. A patent was deposited by C. Arnaud (2006) on the process with transversal vibrations (perpendicular to the membrane surface) [1]. A decrease in the peak of the volume-weighted drop size distribution (from 30 μm to 10 μm) was obtained at a forcing frequency between 15 and 20 kHz compared to without vibration (forcing amplitude not reported). On the same membrane, E. Lepercq-Bost (2008) applied frequencies of 7740 Hz to 12710 Hz, with a forcing amplitude of 1.1 μm [2]. With PDMS of molecular weight 770 $\text{g}\cdot\text{mol}^{-1}$ as the oil phase, the mean drop diameter shifted from 6.14 μm without vibration to 1.57 μm with vibration. A population of drops of 0.2 μm appeared with vibration, which is smaller than the pore size. With soy oil as the oil phase, no significant change in drop size was found for the same operating conditions [2]. Consequently, transversal vibrations may significantly reduce mean drop sizes, in specific conditions.

Questions raised

For the above observations on drop size reduction in transversally vibrating ME, no mechanisms were advanced to explain drop detachment and resulting drop sizes. In order to better control the process, understanding the mechanisms is key. This is the initial purpose of the present work. The questions raised are therefore:

- Why are smaller drops produced in certain vibration conditions?
- How do other parameters affect drop sizes in combination with vibration?
- Can we predict drop generation knowing the input parameters?

Organisation of the work

First, an in depth literature review was performed and summarised in chapter 1. The first, general part of this chapter concerns emulsions and emulsification processes. The second part considers drop generation mechanisms identified in various configurations, including ME. The final part concerns drop behaviour submitted to vibration, in diverse configurations. Formulae of surfactant molecules reported in this first chapter are given in Appendix 1.

To answer the questions raised above and gain insight into transversally vibrating ME, drop generation is investigated in two simplified configurations, each with a dedicated experimental setup developed. Both setups are described in detail in chapter 2, together with the general experimental methods. The CAD representations of the setups are given in Appendix 2.

The first configuration concerns single drop formation from a capillary tube submitted to high-amplitude oscillations. The drops are generated into a stationary outer phase. This enables to observe only the impact of vibration on drop generation. We investigate the impact of the inner pore diameter, interfacial tension, dispersed phase velocity, dispersed and continuous phase viscosities combined with the impact of the forcing parameters (frequency and amplitude). From our experiments, we put to light a transition in drop generation, with a reduction in drop size above a threshold forcing amplitude. A few results and the mechanisms are presented in chapter 3. We then expose further experimental results and propose a model to account for the transition in chapter 4. Supplementary experimental results to those in chapter 4 and comparisons with the model are described in Appendix 3.

The second configuration concerns single drop formation from a capillary tube, this time into a cross-flowing outer phase. Drop generation is first investigated without vibration (which mimics cross-flow ME). Then, the combined effect of cross-flow and vibration is considered (which mimics transversally vibrating ME). In addition, the transition from dripping to jetting is investigated, both without and with vibration. This is important as this transition may occur in ME depending on the operating conditions. Previous mechanisms reported in chapters 3 and 4 only hold for drops generated in dripping mode. Results for drops generated in cross-flow without vibration are presented in chapter 5. Results for drops formed in cross-flow coupled with vibration are described in Appendices 4 and 5 for dripping and jetting, respectively.

Finally, in Appendix 6, the results of C. Arnaud (2006) and E. Lepercq-Bost (2008) which constituted the starting point of the work are analysed with the knowledge gained.

Chapter 1: Literature review

1. Emulsions and emulsification

This work intends to bring insight into the mechanisms of drop generation in transversally vibrating membrane emulsification. The aim of this section is therefore firstly to present the basic principles of emulsions. Then, the main emulsification processes which exist will be briefly described. Finally, membrane emulsification will be specifically detailed at the end of this section, including the different parameters which affect its functioning. The impact of vibration, although less investigated, will equally be described.

1.1. Emulsions

1.1.1. Definitions

An emulsion is a system made up of two immiscible liquid phases. A dispersed, inner phase exists in the form of drops inside the bulk, outer phase (continuous phase). The main types of simple emulsions are oil-in-water emulsions (O/W, fig. 1.1(a)), where the dispersed phase is the organic, oil phase and water-in-oil emulsions (W/O, fig. 1.1(b)), where the dispersed phase is the aqueous phase. Double emulsions are also common. These are emulsions of a simple emulsion (W/O/W or O/W/O) (fig. 1.1(c) and (d)). The last letter represents the bulk phase [3,4].

Other emulsions also exist, for example other simple emulsions such as water-in-water emulsions (W/W) or oil-in-oil emulsions (O/O). There are also concentrated emulsions (high volume fraction of dispersed phase), microemulsions (thermodynamically stable monophasic systems) or nanoemulsions (mean drop diameter below 100 nm). These will not be discussed further as we focus in this work on O/W macroemulsions, which we will refer to henceforth simply as “emulsions”.

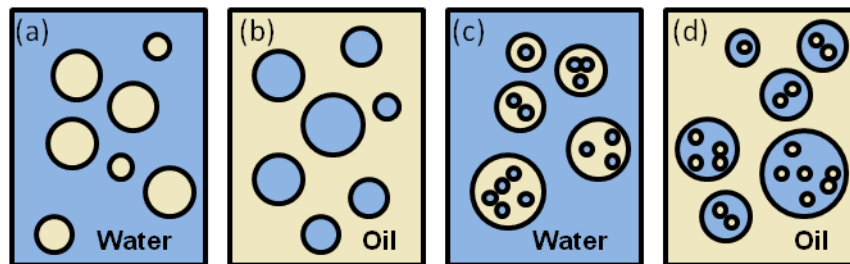


Figure 1.1: Main types of emulsions: (a) oil-in-water (O/W); (b) water-in-oil (W/O); (c) water-in-oil-in-water (W/O/W); (d) oil-in-water-in-oil (O/W/O).

If drops in a system have the same size, *i.e.*, a drop distribution with a relative standard deviation below 10%, the emulsion is said to be monodispersed. Otherwise, it is considered to be polydispersed. Monodispersion is sought after industrially, in particular for emulsion stability (see 1.1.3). In order to generate emulsions, various processes may be employed, detailed in 1.2.

Emulsions are produced in many industries, for example:

- food industry (mayonnaise, butter, vinaigrette)
- cosmetics industry (creams, shampoos, make-up removers)
- pharmaceutical industry (vaccines)
- petrochemical industry (drilling fluids, bitumen).

Emulsions can also be undesirable, such as when petrol is emulsified during extraction. In some cases, they are found naturally, *e.g.* milk or latex [4].

1.1.2. Physical aspects

1.1.2.1. Interfacial tension

At the liquid-liquid interface, hydrogen bonds cannot be formed between the water (polar) and oil (non-polar) molecules. To increase the interfacial area, energy input is necessary to break the hydrogen bonds between the water molecules surrounding the interface [3].

The surface energy (J.m^{-2}), or interfacial tension (N.m^{-1}), corresponds to the work W needed to increase the interfacial area by one surface unit:

$$\delta W = \gamma d\bar{A} \quad (1.1)$$

with γ the interfacial tension and \bar{A} the surface area [4–6]. Interfacial tensions in the order of $50.10^{-3} \text{ N.m}^{-1}$ are reported for clean alkane-water interfaces [7]. For example, for a clean dodecane-water interface, a value of $51.2.10^{-3} \text{ N.m}^{-1}$ was measured by Deshiikan *et al.* (1998). This value is lowered in the presence of surfactants (mechanisms described in 1.1.4) [8].

1.1.2.2. Helmholtz free energy

The surface energy (J.m^{-2}), or interfacial tension (N.m^{-1}), also corresponds to the variation in Helmholtz free energy F when increasing the interfacial area by one surface unit. The Helmholtz free energy F is a thermodynamic variable, expressed for a constant temperature, volume and composition by:

$$dF = \gamma d\bar{A} \quad (1.2)$$

with γ the interfacial tension and \bar{A} the surface area [4–6].

A system always behaves in order to minimize the total free energy [6]. Thus, emulsions are thermodynamically unstable, as they contain a high total interfacial area. The system will tend to demulsify to reduce overall interfacial area.

Although emulsions are thermodynamically unstable, they can be kinetically stable. Various means of kinetic stabilisation are used industrially to enhance product stability and are described in 1.1.4.

1.1.2.3. Laplace pressure

The interfacial tension induces a pressure difference between the inside and outside of the drop, called the Laplace pressure. This pressure ΔP is given by:

$$\Delta P = \gamma \left(\frac{1}{R} + \frac{1}{R'} \right) \quad (1.3)$$

with γ the interfacial tension and R and R' the radii of curvature [4,5].

For spherical drops, the two radii of curvature correspond to the drop radius, therefore the Laplace pressure ΔP reads:

$$\Delta P = \frac{4\gamma}{D_d} \quad (1.4)$$

with γ the interfacial tension and D_d the drop diameter [3–5]. This pressure difference has an impact on emulsion stability and on emulsion generation, as it affects drop rupturing.

1.1.2.4. Wetting

An oil drop deposited on a solid surface will spread more or less depending on surface wettability. The spreading parameter SP in the configuration of fig. 1.2 (liquid drop in the surrounding liquid phase) is given by:

$$SP = \gamma_{sw} - (\gamma_{so} + \gamma) \quad (1.5)$$

with γ_{sw} , γ_{so} and γ the interfacial tensions between the solid/water, solid/oil and oil/water, respectively. If $SP > 0$, spontaneous spreading occurs and a film is formed (perfect wetting) whereas if $SP < 0$, spreading will not occur spontaneously. The drop will tend to an equilibrium, hemispherical shape, described by a contact angle θ (fig. 1.2) [5,6,9].

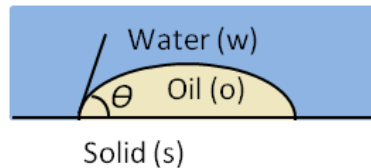


Figure 1.2: Contact angle θ of an oil drop in water on a solid substrate.

The extent of spreading is measured by the contact angle made by the drop on the substrate. Young's equation relates the interfacial tensions to the contact angle:

$$\gamma \cos \theta = \gamma_{sw} - \gamma_{so} \quad (1.6)$$

A contact angle of $\theta = 0^\circ$ corresponds to perfect wetting. A contact angle of $\theta = 180^\circ$ corresponds to perfect non-wetting (a spherical drop lies above the surface). Partial wetting occurs between these values. For contact angles of $0^\circ < \theta \leq 90^\circ$, the wettability is high and low wettability occurs for contact angles of $90^\circ < \theta < 180^\circ$ [5,6,9].

1.1.3. Emulsion destabilisation

As seen in 1.1.2, emulsions are thermodynamically unstable systems. The four main emulsion destabilisation mechanisms are presented in this section and are summarized in fig. 1.3.

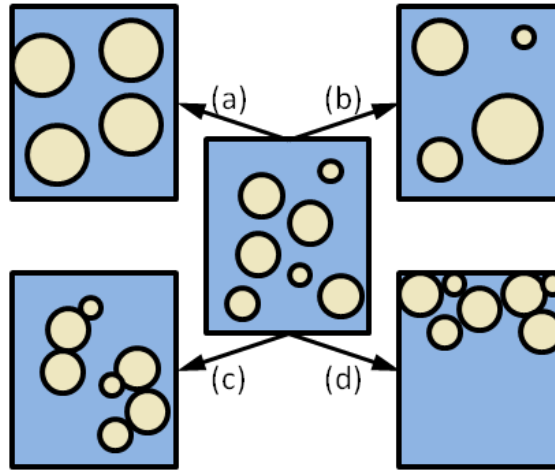


Figure 1.3: Emulsion destabilisation mechanisms: (a) Ostwald ripening; (b) coalescence; (c) flocculation; (d) creaming.

1.1.3.1. Ostwald ripening

As seen in 1.1.2.3, the Laplace pressure for spherical drops is inversely proportional to drop size. As a result, the pressure inside small drops is higher than that in larger drops. In order to return to a thermodynamic equilibrium, diffusion of matter occurs from the small drops to the large ones. This leads to drop size standardization, with the large drops maintained. This irreversible phenomenon is named Ostwald ripening and is represented in fig. 1.3(a). To reduce the occurrence of this type of destabilisation, it is therefore important to produce monodispersed emulsions [3,4].

1.1.3.2. Coalescence

Micron-sized drops (or smaller) are subjected to Brownian movement, leading to impacts between them. If the interfacial film ruptures upon impact, they merge into a single, larger drop. This corresponds to coalescence, shown in fig. 1.3(b), which is an irreversible phenomenon. This leads to a decrease in interfacial area, thus a decrease in overall free energy, which stabilises the system. If coalescence is repeated a sufficient amount of times, the system eventually demixes or demulsifies, which is the most thermodynamically stable state: the two phases become separate and the emulsion is lost [3,4].

1.1.3.3. Flocculation

As mentioned above, small drops undergo impacts due to Brownian movement. If sufficient van der Waals interactions exist between the drops upon impact, they remain associated to each other (in the case where the onset of coalescence does not occur). This corresponds to Lifshitz-

van der Waals flocculation, represented in fig. 1.3(c). The drops do not coalesce, however this can become possible if drops remain associated for too long. The phenomenon therefore becomes irreversible whereas flocculation itself is reversible [3,4]. Other types of flocculation can occur if micelles or polymers are present in the system and these types are described by P. Brochette (1999) [3].

1.1.3.4. Creaming

If the dispersed phase is denser than the continuous phase, drops migrate downwards leading to sedimentation. If the dispersed phase is less dense, drops migrate upwards leading to creaming, shown in fig. 1.3(d). These phenomena occur due to gravity forces exerted on the drops. They are reversible but again, if drops remain in contact too long, irreversible coalescence may occur.

The sedimentation or creaming rate $v_{s/c}$ is obtained from balancing gravity forces with the drag forces exerted on the drops (the drag forces being established by Stoke's law):

$$v_{s/c} = \frac{2 \Delta\rho g D_d^2}{9 \cdot 4\eta_{cp}} \quad (1.7)$$

with $\Delta\rho$ the difference in phase densities, η_{cp} the continuous phase viscosity and D_d the drop diameter [3,4]. As can be deduced from eq. (1.7), increased emulsion stability can be obtained by generating smaller drops in the emulsion (by adjusting the process and/or formulation). Enhanced stability can also be obtained by adapting the formulation to reduce the difference in phase densities or by increasing the continuous phase viscosity.

1.1.4. Emulsion stabilisation by surfactants

As was seen in 1.1.3.4, emulsion stability can be increased by various means including reducing drop size and adapting the emulsion formulation (phase densities and viscosities). In 1.1.3.1, it was seen that emulsions were more stable if they were monodispersed, therefore process parameters must be optimized. In addition, emulsions can be stabilised kinetically by adding various molecules including ionic substances, colloidal particles, polymers or surfactants, the latter on which we focus here [6].

1.1.4.1. Surfactant molecules

Surfactants, often employed in mixtures, are the most widely used molecules to stabilize emulsions in the industry. They are globally made up of two parts, schematically represented in fig. 1.4, which are [3,5,9,10]:

- a hydrophilic “head”, turned towards the aqueous phase. The “head” can be made up of any polar molecule. This polar molecule can be non ionic, cationic, anionic or zwitterionic.
- a hydrophobic “tail”, with an affinity to the organic phase. It is either an aliphatic or aromatic compound.

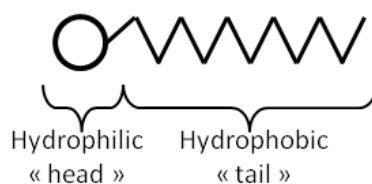


Figure 1.4: Schematic representation of a surfactant molecule.

The HLB (Hydrophilic-Lipophilic Balance) system describes the extent of surfactant solubility in a given phase. It is calculated depending on the chemical structure of the molecule. Values of 0 to 20 are calculated for non-ionic surfactants and 0 to 40 for ionic surfactants. For high HLB values (> 8), surfactants are hydrophilic and stabilise O/W emulsions. For low values (< 7), they are hydrophobic and are used in W/O emulsions. In mixtures, HLB values are weighted [6,9,10]. The HLB values of a few common surfactants are 16.7 for Tween 20, 15 for Tween 80, 4.2 for Span 80 and 18.1 for Brij 58 (formulae in Appendix 1) [10].

Other common methods employed to choose an adequate surfactant for emulsion formulation are the Phase Inversion Temperature method (PIT) or the Hydrophilic Lipophilic Deviation method (HLD) and are described by P. Brochette (1999) or Rosen and Kunjappu (2012) [3,9].

1.1.4.2. *Stabilisation mechanism*

The amphiphilic nature of surfactants means that they adsorb at the liquid-liquid interface, with the hydrophilic “head” turned towards the aqueous phase and the hydrophobic “tail” turned towards the organic phase.

The Gibbs adsorption isotherm gives the surface excess concentration Γ of the surfactant in the case of non-ionic surfactants in dilute solutions [6,9]:

$$\Gamma = -\frac{1}{\bar{R}T} \left(\frac{d\gamma}{d\ln C} \right)_T \quad (1.8)$$

with \bar{R} the universal gas constant, T the temperature, γ the interfacial tension and C the surfactant concentration in the bulk, continuous phase. According to eq. (1.8), for a given surfactant concentration, surfactant adsorption at the interface leads to a decrease in interfacial tension, which stabilises the emulsion [10]. Indeed, a lower interfacial tension leads to the system having a lower overall free energy (as seen in 1.1.2.2).

It must be noted that the extent of the decrease in interfacial tension depends on various parameters, *e.g.* surfactant concentration, presence of salts and temperature [8].

Also, in addition to lowering the interfacial tension, surfactants can induce electrostatic repulsions between drops if they are ionic. They can also induce steric hindering between drops if the surfactants have a large functional group. Both of these mechanisms favour emulsion stabilisation as they limit contacts between drops, reducing the likelihood of flocculation or coalescence, which destabilise the emulsion, as detailed in 1.1.3 [10].

1.1.4.3. Critical Micelle Concentration (CMC)

Above a certain concentration of surfactant called the Critical Micelle Concentration (CMC), the liquid-liquid interface is saturated in surfactant. Therefore, the excess surfactant cannot be adsorbed at the interface. It is spontaneously associated into micelles. These micelles do not intervene in further reduction of the interfacial tension. Therefore, below the CMC, adding surfactant to the system results in a decrease in interfacial tension whereas above the CMC, the interfacial tension remains constant, even with additional surfactant (fig. 1.5) [5,9,10].

The CMC of a few common surfactants are of $6.91 \cdot 10^{-3} \text{ mol.L}^{-1}$ for SDS, $2.5 \cdot 10^{-6} \text{ mol.L}^{-1}$ for Brij 58 and $9.12 \cdot 10^{-4} \text{ mol.L}^{-1}$ for CTAB (formulae in Appendix 1) [8].

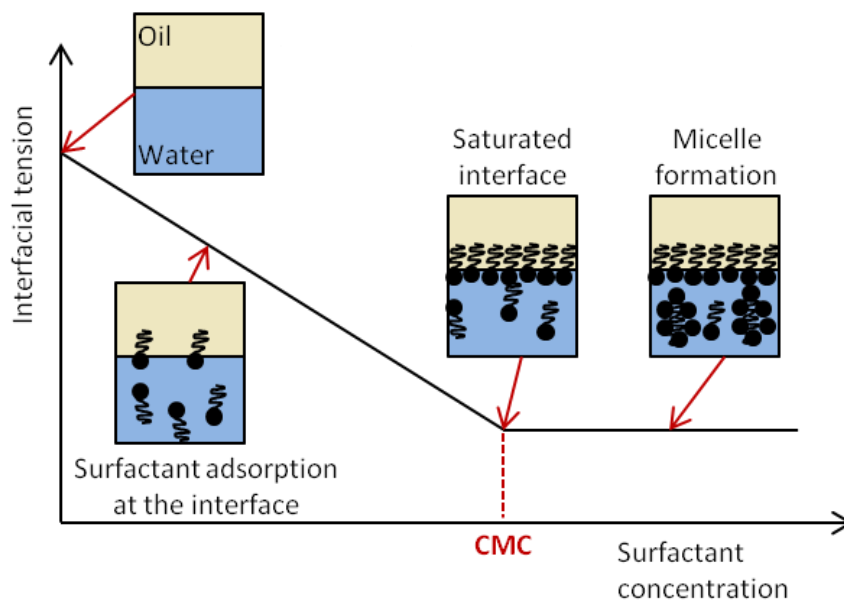


Figure 1.5: Surfactant concentration impact on interfacial tension of an O/W emulsion.

We note that the Krafft point is the temperature at which the surfactant solubility is equal to the CMC. For ionic surfactants, below the Krafft point, the reduction in interfacial tension is therefore limited by the concentration of surfactant at saturation rather than by the CMC. The Krafft points of two common ionic surfactants, SDS and CTAB, are reported at 24.2°C and 25°C, respectively [9].

1.2. Emulsification

Various processes have been developed to emulsify the initially two separate phases. Some of these processes are exposed in this section. In this work, we focus on a novel process (membrane emulsification), which will be detailed specifically in section 1.3.

1.2.1. High pressure homogenisation

The most common type of high pressure homogenisers are radial diffusers. For these homogenisers, the dispersion unit is made up of a valve, valve seat and impact ring (fig. 1.6). The two individual phases or a coarse pre-emulsion are sent through the dispersion unit at high pressures (between 30 and 2500 bar). The phases are projected through the slit between the valve and valve seat onto the impact ring at high speeds (between 100 and 400 m.s⁻¹). As a result, the emulsion is generated [11,12].

Other less common types of homogenisers are counter-jet-dispergators and axial flow nozzle systems. These are described by Schultz *et al.* (2004) [12].

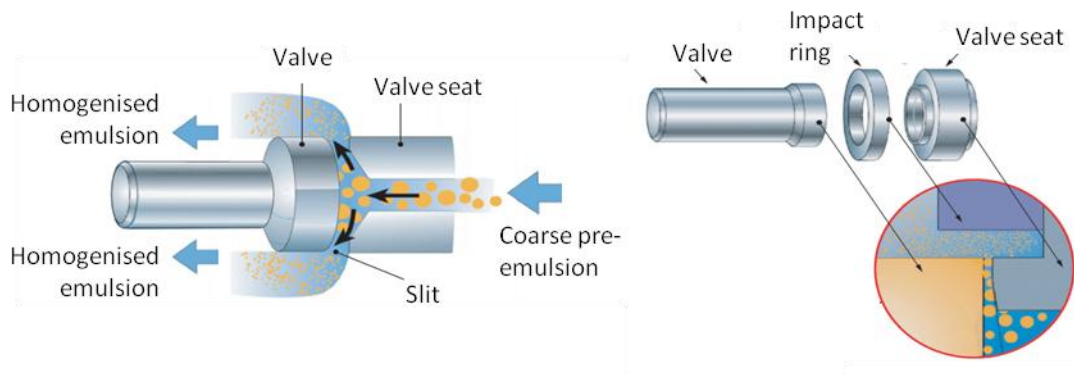


Figure 1.6: Radial diffuser dispersion unit (from [11], modified).

Different mechanisms have been advanced to explain the reduction in drop size in high pressure homogenisation. These are the shear resulting from the product passing through the slit, the micro-turbulences and cavitation induced by the process as well as the contact of the phases with the impact ring at high speeds. The predominant mechanism explaining drop generation depends on various parameters including phase viscosities, interfacial tension, temperature and pressure [11,12].

High pressure homogenisation is a continuous process, which is often employed industrially. Fine emulsions of 0.1 to 5 μm can be generated. However, this process is energy-consuming due to the significant increase in temperature which occurs (around 1°C increase per 40 bar). As a result of the temperature increase, the final product can be affected if it contains heat-sensitive ingredients such as proteins or vitamins [11,12].

1.2.2. Ultrasounds

Ultrasonic emulsification occurs when an ultrasound (20 to 40 kHz) is applied to two separate phases or to a coarse pre-emulsion. In some examples, the frequency exerted on the phases can reach up to a few MHz [13]. The most likely drop breakup mechanism which has been advanced is cavitation. Cavitation is most efficient when the eigenfrequency of the bubble matches the set ultrasonic frequency [13,14].

Ultrasonic emulsification is most often operated by batch, thus it is seldom used industrially. Fine emulsions of below 1 μm can be achieved, with drop size depending on the process duration, process power, temperature, phase viscosities, phase volume ratios and interfacial tension [13,14].

1.2.3. Rotor stator devices

Rotor stator devices are either colloidal mills or gear-rim dispersion machines. The moving part (rotor) rotates inside the immobile part (stator) (fig. 1.7). This creates a vacuum which induces fluid circulation through the device. As a result, the fluid is projected against the device and turbulent eddies are generated.

Shear stress due to the fluid passing through the gap between the rotor and stator induce drop breakup. The projection against the device can also enhance drop rupturing. Inertia and shear which result from the motion of the turbulent eddies have also been advanced as mechanisms which explain drop breakup [12,15].

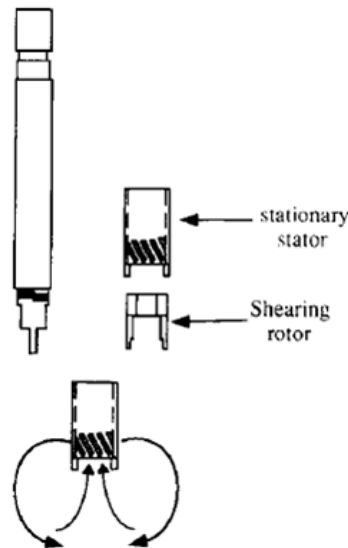


Figure 1.7: Rotor-stator device (from [15]).

These processes can be operated either by batch or continuously. Drops produced are generally larger than with the previous processes described (above 1 μm). Drop size is controlled by adapting either the process parameters (rotational speed, processing time, device dimensions or shape) or the formulation (phase viscosities, volume ratios of both phases and the interfacial tension) [12,15].

1.2.4. Static mixers

Static mixers are motionless mixers. They are made up of different elements, which are inserted into a pipe or column (fig. 1.8). These elements divert the two fluids from the main flow transversally, which results in mixing. The shear induced elongates the drops, leading to breakup by different instabilities.

The geometry, flow rates and flow type (laminar or turbulent), number of elements and dimensions of the static mixers determine their mixing properties. The emulsion generated also depends on the viscosities, densities and interfacial tension of the two phases.

Static mixers consume little energy, are cheap, small and require little maintenance due to their motionless nature. However, drops generated are generally large, above 1 μm . This type of mixer is therefore often used to produce the primary, coarse pre-emulsion which is then put through other processes such as high pressure homogenisation to obtain finer emulsions [16].

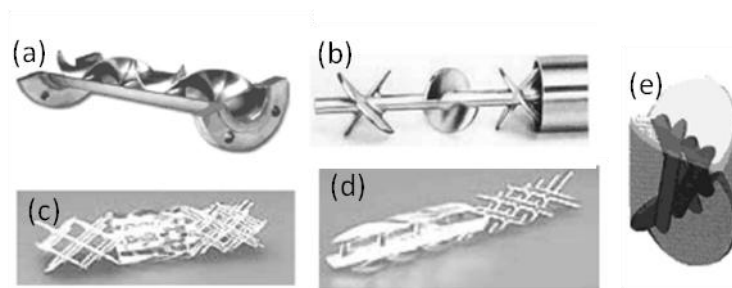


Figure 1.8: Static mixers: (a) open design with helices; (b) with blades; (c) corrugated plates; (d) multi-layer; (e) closed design with channels or holes (from [16], modified).

1.3. Membrane emulsification

The initial goal of this work is to understand drop detachment mechanisms in transversally vibrating membrane emulsification. The different parameters which have been found to affect classic membrane emulsification will first be detailed. Concerning the impact of vibration, few studies exist, especially in the transversal case. These few studies will be exposed here. However, literature concerning drops subjected to vibrations in general rather than in ME is more abundant. This literature will be reviewed in section 3.

1.3.1. Different types of membrane emulsification

1.3.1.1. Direct membrane emulsification

Direct membrane emulsification (ME) was first presented in Japan by Nakashima *et al.* in 1988. A dispersed phase is forced through an inorganic, porous membrane by a transmembrane pressure. The drops are formed on the other side of the membrane and detach into the continuous, circulating phase. This forms the emulsion (fig. 1.9). The emulsion is carried away by the circulating phase and the fluid is recirculated until the desired volume fraction of dispersed phase is reached [17–20].

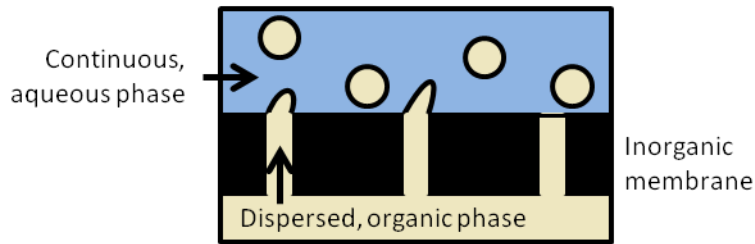


Figure 1.9: Direct membrane emulsification.

Direct ME can be operated continuously or by batch. Membranes are often made of Shirasu porous glass (SPG) or ceramics, with pore sizes of 0.1 to 20 μm . Other materials such as PTFE, silicon, silicon nitride and α -alumina or zirconia coatings have been reported [19,20].

Due to a low throughput, direct ME is often used at laboratory scale. However, it has been used industrially to produce a low fat spread (Morinaga Milk Industry), polydivinylbenzene microspheres for LCDs, monodispersed silica powder for HPLC and cosmetics (Miyazaki Industrial Technology Center and Suzuki Yushi Industries) and drug delivery systems for liver cancer treatment (Miyazaki Medical College) [18].

Parameters which affect direct ME are detailed in 1.3.3 and drop detachment mechanisms are described in 2.4. In this work, we focus on direct ME, so will hereafter refer to it as « membrane emulsification » or simply as « ME ».

1.3.1.2. Premix membrane emulsification

In premix membrane emulsification, a coarse pre-emulsion rather than a dispersed phase is forced through a membrane by a transmembrane pressure (fig. 1.10). This process functions continuously or by batch. The membranes used are mainly of glass (SPG) or PTFE [20,21].

Drops break up due to the shear induced and to the interfacial tension effects that occur with drop deformation as they pass through the pores. Parameters which affect premix membrane emulsification are the coarse emulsion properties, membrane material, pore size, transmembrane pressure and the number of cycles applied [20,21]. Emulsions with high volume fractions of dispersed phase can be produced, however the emulsions are more polydispersed than in direct ME [21].

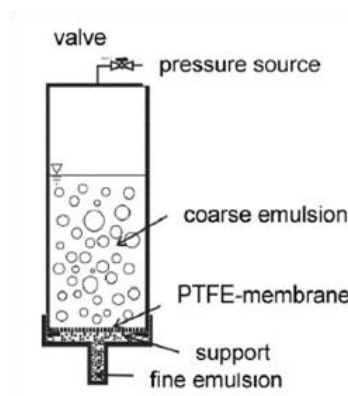


Figure 1.10: Premix membrane emulsification (from [20]).

1.3.1.3. Microchannel membrane emulsification

In microchannel membrane emulsification, the dispersed phase is forced through microchannels, which end in a non cylindrical shape. The drop is formed partly on the terrace and partly in the well (fig. 1.11), which leads to pressure differences due to differences in curvature (see 1.1.2.3). Once the drop reaches a given size, the Laplace pressure in the part of the drop in the well is higher than in the part on the terrace. This leads to an increase in dispersed phase flow into the drop, so it grows, the pressure difference increases more leading to a yet higher dispersed phase flow. This repeats itself until a neck is formed. The neck is subjected to Laplace instabilities, inducing drop detachment. Above a critical dispersed phase velocity, a neck cannot be formed and this mechanism is no longer possible [20].

This process is affected by the plate geometry and material, dispersed phase velocity and interfacial tension. Monodispersed drops are produced, but resulting emulsions are larger than for ME or premix membrane emulsification [20].

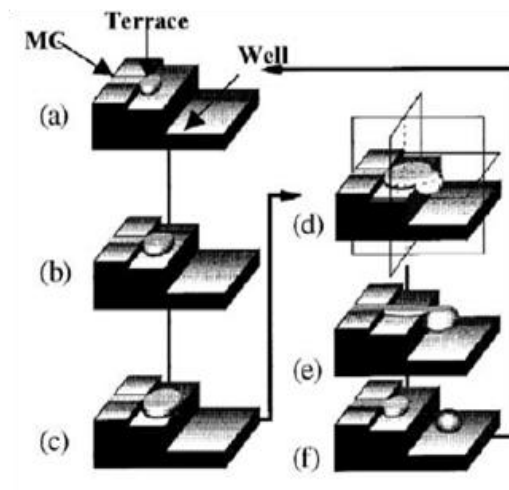


Figure 1.11: Microchannel membrane emulsification (from [20]).

1.3.2. Advantages and drawbacks of direct membrane emulsification

1.3.2.1. Advantages

The main advantage of ME is that it has a lower energy density compared to other common emulsification processes (fig. 1.12). Indeed, most of the energy input for high pressure homogenisation or rotor stator devices is converted and lost as heat.

Figure 1.12 also illustrates that ME enables to form a wide range of drop sizes. It is possible to generate fine emulsions, with drop sizes comparable to other common processes. In some cases, nanoemulsions were even reported to be formed, with drop sizes in the order of 100 nm [22,23]. Additionally, narrow size distributions can be obtained in ME, producing monodispersed emulsions [19,24]. We note that the Sauter diameter reported in fig. 1.12 corresponds to the diameter of a sphere with the same volume to surface area ratio for the

considered particle. For a spherical drop, the Sauter diameter coincides with the drop diameter [13].

As mentioned above, the temperature increase in ME is lower compared to other processes, which explained the lower energy density. As a result, heat-sensitive ingredients can be included in the emulsions, such as proteins and vitamins [25]. Also, ME is a process where little shear is exerted. This implies that shear-sensitive ingredients can also be included [19,24,25]. These points are particularly interesting if the emulsion is used as vectors for sensitive molecules, in particular in the pharmaceutical industry.

Less emulsifier is needed in the emulsion formulation in ME compared to high-shear processes. In the latter, excess emulsifier reduces coalescence, which is frequent due to the many collisions induced by the high-shear environment. The gradual formation of drops in ME (slow increase in interfacial area) explains the lower need for surfactant. This is advantageous regarding cost, environmental impact and consumer image [19,25].

Finally, ME is easily scaled up and controlled [19].

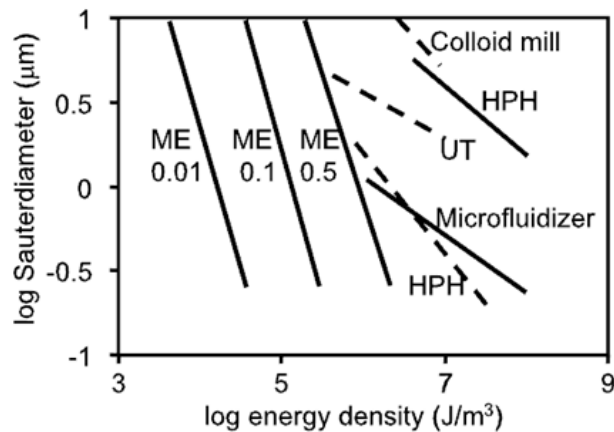


Figure 1.12: Drop diameter depending on the energy density for a colloid mill; rotor stator (UT); microfluidizer; high pressure homogeniser (HPH) with flat valve (solid line) and orifice valve (dashed line); ME (with dispersed phase fraction below) (from [24]).

1.3.2.2. Drawbacks

The main drawbacks of ME are that, as in any membrane process, membrane fouling occurs. This can be at the surface of the membrane or inside the pores. At the surface, membrane properties such as wetting will be modified which affects the process (see 1.3.3.2). Inside the pores, clogging occurs which obstructs the throughput of dispersed phase, which slows or stops the process [19].

Another drawback is that the productivity of the process is low due to the low throughput of dispersed phase. This means ME is not industrially viable as a low yield is obtained, apart from the production high added value products [19,20,24].

Finally, the membrane must be replaced often, which is costly [19].

1.3.3. Impact of various parameters on membrane emulsification

The impact of different parameters on ME including process, membrane and formulation parameters are described here, with a table summarizing the information at the end of the section. The impact of vibration specifically will be detailed in 1.3.4.

1.3.3.1. Process parameters

Pore activation

A minimum, critical pressure must be applied for the dispersed phase to overcome the capillary pressure, thus flow through the pores. This is the permeation pressure P_c given by Jurin's law:

$$P_c = \frac{4\gamma \cos \theta}{D_p} \quad (1.9)$$

with γ the interfacial tension, D_p the pore diameter and θ the contact angle between the membrane surface and the drop. P_c may vary with pore configuration and porosity [18,19,26]. Although eq. (1.9) suggests that pores are active (*i.e.*, dispersed phase flows through them) above P_c , only a fraction of the pores are actually found to be active [24,26,27]. Abrahamse *et al.* (2002) measured 16% of active pores at $3P_c$ [24] and Vladislavljević and Schubert (2003) found 1.3%, 1.4% and 8.5% of active pores at $1.1P_c$, $1.9P_c$ and $5.7P_c$, respectively [26]. A pressure drop under the membrane after the dispersed phase flows through the first pores explains this. A further increase in pressure is thus needed to activate a higher fraction of pores [24].

The number of active pores was found to increase either linearly [24] or exponentially [26,28] with transmembrane pressure.

Transmembrane pressure and flux

The transmembrane pressure P_{tm} is defined by:

$$P_{tm} = P_{dp} - \left(\frac{P_{cp,in} + P_{cp,out}}{2} \right) \quad (1.10)$$

with P_{dp} the dispersed phase pressure and $P_{c,in}$ and $P_{c,out}$ the pressures of the continuous phase at the membrane inlet and outlet, respectively [25,27]. P_{tm} must be larger than P_c for ME to begin to function, as described above.

Darcy's law gives the linear relationship between P_{tm} and dispersed phase flux v_{dp} :

$$v_{dp} = \frac{K P_{tm}}{\eta_{dp} d} \quad (1.11)$$

with η_{dp} the dispersed phase viscosity, d and K the membrane thickness and permeability, respectively. The membrane permeability is calculated by $K = n_p D_p^2 / 32\pi$ (Hagen-Poiseuille law), with n_p the number of uniform cylindrical pores and D_p the pore diameter [19].

Schröder *et al.* (1998) demonstrated that Darcy's law was followed for a 0.8 μm aluminium oxide membrane but an exponential increase in dispersed phase flux with transmembrane pressure occurred for the 0.2 μm membrane [27]. This exponential increase was also obtained by Vladislavljević and Schubert (2003) for 0.2 μm , 0.5 μm and 0.8 μm SPG membranes [26] and by Lepercq-Bost *et al.* (2010) for a 4.8 μm alumina membrane [28]. Additionally, Lepercq-Bost *et al.* (2010) demonstrated that the response was hysteretic: a linear decrease in flux was obtained when decreasing transmembrane pressure whereas the increase in flux was exponential with transmembrane pressure [28].

The impact of the transmembrane pressure P_{tm} on drop sizes generated in ME is the following [25,29]:

- For low P_{tm} , the dominant mechanism for drop detachment is cross-flow shear. Therefore, the transmembrane pressure does not significantly affect drop size in this zone (fig. 1.13(a)).
- For intermediate P_{tm} , the dispersed phase flux is increased and drops detach according to the balance between inertial and interfacial tension forces. An increase in transmembrane pressure leads to an increase in drop size (fig. 1.13(b)). Indeed, the drops are filled more quickly, so the interface is formed faster, resulting in a higher interfacial tension. As a result, the retaining force at the pore is higher, so the drop detaches at larger sizes [30,31]. This was confirmed experimentally by other authors [27,32]. Also, drop detachment time was found to be similar when increasing transmembrane pressure. As the flux is higher, more dispersed phase is fed to the drop in the given time leading to larger drops [33].
- Above a critical P_{tm} , the dispersed phase flows out of the pores in a jetting mode (see 2.2.1). In this configuration, drops break up due to Plateau-Rayleigh instabilities (see 2.2.1), so transmembrane pressure no longer significantly affects drop size in this zone (fig. 1.13(c)) [34].

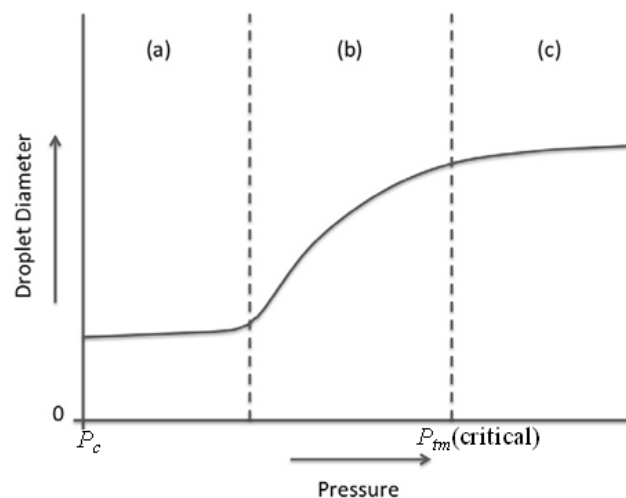


Figure 1.13: Drop detachment regime depending on P_{tm} : (a) cross-flow shear; (b) transmembrane pressure; (c) Plateau-Rayleigh instability (from [29], modified).

Oppositely, Abrahamse *et al.* (2002) reported a decrease in drop size with a transmembrane pressure increase. The number of active pores increased with increasing transmembrane pressure, so drops were more likely formed at adjacent pores. In this case, steric hindrance occurred rather than coalescence, promoting drop detachment and thus leading to smaller drop sizes [24]. This push-off force was also observed and modelled by Kosvintsev *et al.* (2008) in ME without shear [35], in simulations of Tingren *et al.* (2009) for drops detaching at low dispersed phase velocities [36] and by Zhu and Barrow (2005) in ME with a silicon nitride membrane [30].

Another result was that drop size remained constant when transmembrane pressure was decreased after having been increased until a maximum [32].

Shear

Many different authors showed that increasing the cross-flow velocity of the continuous phase leads to an increase in the shear exerted by the continuous phase on the drops being formed. This results in the generation of smaller drops [25,26,29,30,32,33].

This is of course true for low transmembrane pressures, where cross-flow velocity determines drop detachment, as detailed above. A narrow size distribution can be maintained if other process parameters are well adapted [26].

Temperature

Temperature has not been investigated in depth for ME. Oh *et al.* (2011) found that increasing the temperature of the continuous phase decreased drop size [23]. Oppositely, Laouini *et al.* (2012) found that increasing temperature increased drop size [22]. In both studies, a broader size distribution was obtained when increasing the temperature, explained by increased coalescence or Ostwald ripening.

Overall, the impact of temperature on ME depends on the phases and emulsifier used (emulsion formulation). Indeed, temperature affects parameters such as phase viscosities and emulsifier solubility.

1.3.3.2. Membrane parameters

Pore diameter

The impact of pore diameter on drop size has been widely investigated, as it was one of the first parameters of ME to be studied [18,24,37,38]. A linear relationship exists between the drop diameter D_d and pore diameter D_p : $D_d = kD_p$. This is verified for both O/W and W/O emulsions [18]. Coefficients k of 2 to 10 are reported for SPG membranes and of 3 to 50 for other types of membranes [19]. For example, higher values of k from 7 to 36 were found by Abrahamse *et al.* (2002) when a silicon nitride membrane was used, with low cross-flow velocities [24].

Pore spacing

Pore spacing corresponds to the distance between two adjacent pores, in the direction of the continuous phase flow. Membrane coalescence was described by Christov *et al.* (2002) and Lepercq-Bost *et al.* (2010). The three phase contact line of a pore moves and can coincide with the contact line of an adjacent pore, depending on the surfactant or membrane properties, notably the contact angle. Hence, a drop forms from two pores rather than one, resulting in larger drops generated (fig. 1.14) [28,39]. To limit this phenomenon, the number of active pores at a distance $D_d/2$ of a given pore must be lower than 2 [28].

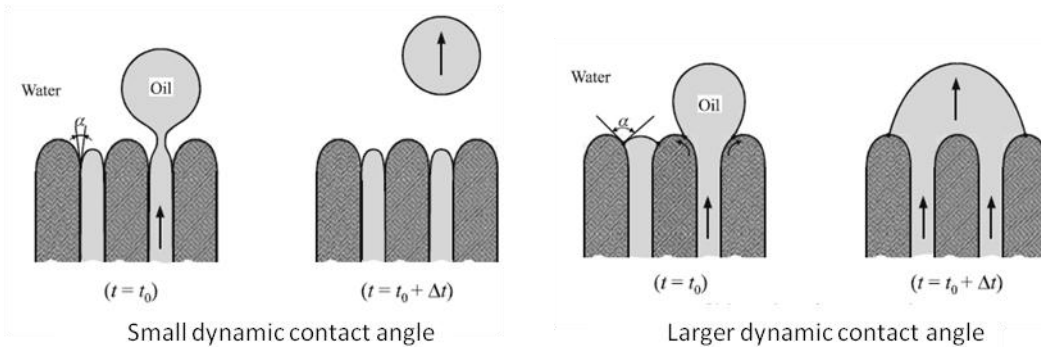


Figure 1.14: Membrane coalescence depending on the contact angle (from [39], modified).

In a numerical study of Timgren *et al.* (2009), at a spacing of 15 and 20 times the pore diameter, drops were monodispersed. At a spacing of 10 times the pore diameter, smaller drops were produced (push-off force) but with a larger size distribution. Coalescence occurred between drops inside the continuous phase (after their formation). By reducing the continuous phase velocity, fewer collisions occurred however this is not industrially optimal [36]. Other examples where push-off occurred are described in 1.3.3.1 [24,30,35,36].

Abrahamse *et al.* (2001) modelled a single pore of ME and found that a spacing of 10 times the pore diameter limits interactions between growing drops. For a uniform grid pore arrangement, a maximum porosity of 1.2% was estimated to avoid interactions. For a staggered pore arrangement, this value was of 1.5% [40].

The onset of coalescence or push-off depends on the interfacial tension. If drops are small and the interfacial tension has not had time to lower enough, drops will more likely coalesce. For high enough surfactant concentrations, drops should undergo push-off mechanisms rather than coalescence. An optimal pore spacing exists to promote push-off mechanisms without inducing coalescence [30].

Wetting

To prepare an O/W emulsion, the membrane must be hydrophilic so that the oil forms a drop rather than spreading on the membrane surface and in order to be able to control drop size. Similarly, to prepare a W/O emulsion, the membrane surface must be hydrophobic [37,38]. Membrane surface treatments, for example with silanes, can be applied to modify the wettability of the surface. However, for the specific example of silanes, they are banned in the

food industry [41]. A hydrophilic membrane can also be pre-soaked in the oil phase to make it hydrophobic, as did Katoh *et al.* (1996) [38].

During ME operation, the membrane may lose its hydrophilic character with time due to the adsorption of various molecules at the membrane surface. As a result, larger drops are produced in time [30].

The wettability of the surface affects the surfactant which must be chosen. For a hydrophilic SPG membrane, monodisperse O/W emulsions are obtained except when a cationic surfactant is used, *e.g.* CTAB. The glass membrane is negatively charged due to the dissociation of silanol groups (below pH 8). CTAB, which is cationic, is adsorbed to the negatively charged surface, rendering it hydrophobic. It therefore becomes wetted by oil, leading to emulsion polydispersion [18,34].

1.3.3.3. Formulation parameters

Emulsifiers

A higher surfactant concentration leads to a faster decrease in the interfacial tension, hence smaller drops are formed. Indeed, a lower interfacial tension means that the capillary force retaining the drop at the pore is lower. Consequently, the drop detaches earlier, for smaller sizes [29,32].

Faster adsorbing surfactants lead to smaller drops. As above, a lower interfacial tension means that the capillary force retaining the drop at the pore is lower. Also, coalescence is less likely, so drops remain small [27,29,34,42], with a narrow drop size distribution [34]. Hancocks *et al.* (2013) showed that slow adsorbing protein (whey, sodium caseinate) produce larger drops than fast adsorbing molecules (SDS, Tween 20, Tween 80) [29]. Spyropoulos *et al.* (2011) found that for O/W emulsions, surfactants with a higher HLB induced a faster decrease in drop size with increasing surfactant concentration. Above a limit concentration, drop size was the same for all surfactants tested (SDS, Tween 20, Tween 80) [25].

Hancocks *et al.* (2013) also considered surfactant charge. A negatively charged surfactant (SDS) leads to smaller drops than a non ionic surfactant (Tween 20). SDS is adsorbed faster, but it also limits coalescence by inducing electrostatic repulsions between drops [29].

Electrostatic repulsions can also occur between the drops and the membrane surface, leading to drops detaching earlier, thus for smaller sizes. As mentioned above, a glass membrane has a negatively charged surface. Mine *et al.* (1996) found that lysophosphatidylcholine (an egg phospholipid) was an adequate surfactant to form O/W emulsions with a glass membrane due to its anionic nature [37]. Kukizaki (2009) also found that electrostatic repulsions occur between drops and the membrane surface with the anionic surfactant SDS [34].

Lecithin exhibits different behaviour to other surfactants. Larger drops are produced and the decrease in drop size with increasing surfactant concentration is slow. The interface is elastic, so drops grow larger before detaching [25]. Also, lecithin forms vesicles, so a longer time is necessary for the lecithin to adsorb, as the vesicles must first be dissociated [29].

Phase viscosities

The impact of phase viscosities has not been widely investigated in the context of ME. The few studies which have been performed to our knowledge are reported here, however the difference in experimental conditions (especially the presence or not of continuous phase flow) make the results difficult to compare.

Hancocks *et al.* (2013) demonstrated that as the continuous phase viscosity increases, drop diameter decreases. This is because a higher shear is exerted by the continuous phase which flows on the drops when its viscosity is increased. This leads to earlier drop detachment hence smaller drop sizes [29]. Without shear, Kukizaki (2009) found the opposite result: an increase in continuous phase viscosity leads to an increase in drop diameter. The viscous continuous phase delays drop detachment, so it is filled with more dispersed phase before detaching. Also, a broader size distribution is obtained when increasing the continuous phase viscosity, as surfactant diffusion is slowed, leading to increased coalescence [34].

Concerning dispersed phase viscosity, Timgren *et al.* (2009) numerically found a decrease in drop size with an increase in dispersed phase viscosity for a drop formed from a capillary, with cross-flow which was applied. This is expected as the drag coefficient increases with an increased drop viscosity, so the exerted drag force leading to detachment increases [43]. Without shear, Kukizaki (2009) showed that an increase in dispersed phase viscosity also leads to a decrease in drop size. This is explained as the dispersed phase flux is decreased according to Darcy's law (eq. (1.11)) [34].

When both continuous phase and dispersed phase viscosities were varied but keeping a constant viscosity ratio of 1.1, drop size was unchanged [34].

1.3.4. Impact of vibration on membrane emulsification

1.3.4.1. Longitudinal vibration

In longitudinally vibrating ME with a silicon nitride membrane, Zhu and Barrow (2005) found a decrease in drop size compared to standard ME. A threshold amplitude of vibration was necessary to observe drop size reduction, which was obtained at 125 V (around 10-12 μm) at 10 Hz. At this value of 125 V, the minimum drop diameter was obtained at 5 Hz. For higher frequencies, drop diameter increased until a threshold. The increase was explained due to mechanical damping of the system [30].

A decrease in drop size was also observed with an increase in oscillation intensity (frequency or amplitude) for a steel micro screen by Gomaa *et al.* (2014). The increase in the drag force which results from an increase in frequency or amplitude explains the earlier detachment of the drop from the pore, hence the smaller drop size [31,42]. Also, a higher oscillation intensity increases the surfactant transfer rate from the continuous phase to the interface. Therefore, the interfacial tension is lower, which is another reason for a premature detachment of the drop (as mentioned before), thus smaller drop sizes [31].

Kelder, Janssen and Boom (2007) numerically determined that smaller drops were generated only if the vibrating membrane was well designed, *e.g.* by adapting cross-flow velocity or dispersed phase velocity [44].

Lloyd *et al.* (2014) performed rotating ME with an SPG membrane. Tangential shear is exerted on the drops being formed, which is similar to a longitudinally vibrating ME configuration. The higher the rotational speed, the higher the shear and the smaller the drops generated, until a limit value of shear. A limit drop size is reached, where it no longer depends on shear but on other operating parameters [45].

In this last study, an increase in the continuous phase viscosity led to an increase in drop size, which is opposite to what is expected as the drag force is increased. Drops cannot move away from the membrane due to the viscosity (which hinders drop movement and limits Taylor vortices) and density effects. They therefore remain close to the membrane surface and coalesce, producing larger drops [45].

1.3.4.2. Transversal vibration

Few studies have considered ME with transversal vibrations. An international patent was deposited by C. Arnaud (2006) concerning this process. In this patent, an example is given where an O/W emulsion with 4.8% Tween 20 is formulated with a membrane of 0.8 μm . A significant decrease in the peak of the volume-weighted drop size distribution from 30 μm to 10 μm occurs at a forcing frequency between $f = 15$ and 20 kHz compared to without vibration (power of 50 W vs. 0 W). However, the mechanisms for drop detachment were not explained [1].

On the same membrane, E. Lepercq-Bost (2008) applied frequencies of 7740 Hz to 12710 Hz, with an amplitude of 1.1 μm . For a soy oil/water emulsion with 2% SDS, no difference in drop diameter was observed with or without vibration. The viscosity of the soy oil was too high to obtain a shift in drop diameter. With a less viscous oil, the mean diameter shifted from 6.14 μm to 1.57 μm with vibration compared to without vibration. The shift is notably explained by a population of drops of 0.2 μm appear, which is smaller than the pore size. Although vibration was found to impact drop size, again no mechanisms were advanced to explain this observation [2].

1.4. Conclusions

Summary

Emulsions are two-phase systems, both phases being liquids, which are of interest in a great number of industries including the food, cosmetics and pharmaceutical industries. In order to produce controlled and stable systems, the emulsion formulation and process must be adapted. Various processes have been designed to form the drops of one phase inside the other, that is, to emulsify the system. The main industrial processes used currently are high-pressure homogenisation as well as rotor-stator systems.

The process of interest in this work is membrane emulsification, which has been designed and studied since the 1990s. It consists in a porous, inorganic membrane through which the dispersed phase is forced, to form the drops on the other side inside the continuous, flowing phase. Although this process has many advantages, notably the low energy density, low shear environment and easiness to control, its use is yet limited industrially due to the low throughput in dispersed phase.

The impact of many different parameters on drop generation in ME have been investigated since the 1990s. These include process parameters (transmembrane pressure, dispersed phase flux, temperature, cross-flow velocity), membrane parameters (material, pore size and spacing) and formulation parameters (emulsifier type and concentration, dispersed phase viscosity, continuous phase viscosity).

An additional parameter has only been studied in the last 15 years, which is the impact of vibration coupled with the process. Experimental work has been performed in the case of longitudinal vibrations, and some models have been proposed, though they are not fully satisfactory. For transversal vibrations, very few studies exist and no models have been proposed. A summary of the impact of all the parameters is presented in table 1.1.

Aims

The initial aim of this work is to gain insight on transversally vibrating ME, in particular to explain the mechanisms for drop generation which are still unknown. Experimental work will therefore be carried out on a simplified setup to better understand the industrial process. This includes investigating the impact of the frequency and amplitude of vibration, in combination with other parameters including the inner pore diameter, dispersed phase flow rate, continuous and dispersed phase viscosities, interfacial tension as well as the continuous phase flow rate. A model will be proposed based on the experimental results obtained. The simplified setup consists in a single pore, as did for example Peng and Williams (1998) or E. Lepercq-Bost (2008) [2,33].

Table 1.1: Effects of various parameters on ME.

Parameter group	Parameter	Effect	Reference
Formulation	Emulsifier	Adsorption kinetics $\uparrow \Rightarrow D_d \downarrow$ and monodispersion \uparrow	[27,29,34,42]
		[Emulsifier] $\uparrow \Rightarrow D_d \downarrow$ and monodispersion \uparrow	[29,32]
		Emulsifier charged negatively with a negatively charged membrane $\Rightarrow D_d \downarrow$ and monodispersion \uparrow	[34,37]
	Viscosities	Different results depending on different conditions	[29,34,43]
Membrane	Pores	Pore size $\downarrow \Rightarrow D_d \downarrow$	[18,19,24,37,38]
		Pore spacing $\uparrow \Rightarrow D_d \downarrow$ due to the reduction of coalescence Pore spacing $\downarrow \Rightarrow D_d \downarrow$ if push-off mechanisms occur	[28,30,35,36,39,40]
	Wettability	Wettability between dispersed phase and membrane surface $\downarrow \Rightarrow$ monodispersion \uparrow	[18,30,37,38,41]
Process	Transmembrane pressure	For intermediate P_{tm} , $P_{tm} \uparrow \Rightarrow D_d \uparrow$ unless push-off mechanisms occur For high or low P_{tm} , no effect on D_d	[24,25,27,29–36]
	Continuous phase flow rate or shear	Continuous phase flow rate $\uparrow \Rightarrow$ shear $\uparrow \Rightarrow D_d \downarrow$	[25,26,29,30,32,33]
	Temperature	Different results depending on different conditions	[22,23]
Vibration	Longitudinal	Amplitude or frequency $\uparrow \Rightarrow D_d \downarrow$	[28,29,40,42,43]
	Transversal	Amplitude $\uparrow \Rightarrow D_d \downarrow$	[1,2]

2. Drop generation mechanisms

The breakup of liquid jets, fluid threads or liquid drops into smaller drops has been widely investigated. From this, some now well-known hydrodynamic instabilities have been put to light. Otherwise, if these instabilities do not directly apply, various mechanisms or models have been proposed to explain drop generation in different experimental situations. These will be reviewed here, with section 2.4 dedicated to drop generation mechanisms and models proposed specifically in ME, including vibrating ME.

2.1. Hydrodynamic instabilities

Some well-documented instabilities which could apply in the context of this work are described below. Indeed, the instabilities detailed are due to jet breakup (Plateau-Rayleigh instabilities), to the vibration of an interface (Faraday waves) and to viscosity, density or velocity discontinuities (Saffman-Taylor, Rayleigh-Taylor or Kelvin-Helmholtz instabilities, respectively). Other common instabilities, for example those induced by temperature discontinuities such as Rayleigh-Bénard or Bénard-Marangoni instabilities, are detailed by Guyon, Hulin and Petit (1991) [46].

2.1.1. Dimensionless numbers

Dimensionless numbers often used in fluid mechanics and involved in describing hydrodynamic instabilities are detailed here. They are constructed by comparing two competing forces which affect a phenomenon. Often, a dimensionless number threshold delimits different behavior of a system, regardless of the experimental conditions set. This allows scaling-up between laboratory, pilot and industrial scales. It also enables to compare experiments carried out in different operating conditions.

2.1.1.1. Reynolds number

The Reynolds number (Re) represents the ratio between inertial and viscous forces:

$$\text{Re} = \frac{U\bar{L}}{\nu} \quad (1.12)$$

with U a characteristic velocity of the flow, \bar{L} a characteristic length and ν the kinematic viscosity of the fluid [46].

The Reynolds number is particularly employed to determine whether a flow is laminar or turbulent. For a flow inside a cylindrical pipe, values of approximately $\text{Re} < 2000$ induce laminar flow and values of $\text{Re} > 4000$ roughly induce turbulent flow. In between, a transient regime occurs. The values determining the transition must of course be adapted, for example to pipe geometry and surface properties.

2.1.1.2. Weber number

The Weber number (We) compares inertial and capillary forces:

$$\text{We} = \frac{\rho U^2 \bar{L}}{\gamma} \quad (1.13)$$

with ρ the fluid density, U a characteristic velocity of the flow, \bar{L} a characteristic length and γ the interfacial tension [5].

2.1.1.3. Ohnesorge number

The Ohnesorge number (Oh) is a ratio of a viscocapillary time scale to an inertial-capillary time scale:

$$\text{Oh} = \frac{\eta}{\sqrt{\rho\gamma\bar{L}}} = \frac{\sqrt{\text{We}}}{\text{Re}} \quad (1.14)$$

with ρ the fluid density, η its viscosity, γ the interfacial tension and \bar{L} a characteristic length [47]. As can be seen from eq. (1.14), the Ohnesorge number is also constructed from the Weber and Reynolds numbers described above.

2.1.1.4. Capillary number

The capillary number (Ca) compares viscous and capillary forces:

$$\text{Ca} = \frac{\eta U}{\gamma} \quad (1.15)$$

with η the viscosity, U a characteristic velocity of the flow and γ the interfacial tension [5].

2.1.1.5. Bond number

The Bond number (Bo) denotes the importance of capillary forces compared to gravity forces:

$$\text{Bo} = \frac{\Delta\rho g \bar{L}^2}{\gamma} = \frac{\bar{L}^2}{l_c^2} \quad (1.16)$$

with $\Delta\rho$ the difference in fluid densities, \bar{L} a characteristic length for instance the drop radius, γ the interfacial tension and l_c a characteristic length, called the capillary length.

The capillary length is calculated by:

$$l_c = \sqrt{\frac{\gamma}{\Delta\rho g}} \quad (1.17)$$

This length is compared to characteristic dimensions of a system to determine the importance of interfacial tension effects [5,46].

2.1.2. Plateau-Rayleigh instabilities

Plateau-Rayleigh instabilities are driven by surface tension and induce the breakup of a fluid cylinder into drops. This instability can be observed for example at the end of a dripping faucet or during the breakup of a jet in inkjet printing.

The pioneering experiments leading to the discovery of this instability are attributed to Savart (1833), who studied a liquid jet projected through an orifice [48]. Plateau (1873) later observed and characterised the instability, showing that it occurred if the wavelength was greater than a value between 3.13 and 3.18 times the cylinder diameter [49]. Lord Rayleigh (1878) then analytically explained the instabilities. An optimal wavelength of 4.51 was found for the instabilities to occur, close to the value of 4.38 given by Plateau (1873) based on the results of Savart (1833) [50].

A fluid cylinder undergoes sinusoidal perturbations at its surface. It breaks up into drops if the overall surface area, hence surface energy, is reduced for the multiple drops compared to the original cylinder (fig. 1.15). This occurs if the wavelength of the surface perturbation λ_{PR} is larger than the perimeter of the jet, *i.e.*, if $\lambda_{PR} > 2\pi R$, with R the jet radius. We note that this gives a minimum wavelength of 3.14 times the cylinder diameter, in accordance with the values of 3.13 to 3.18 reported by Plateau (1873).

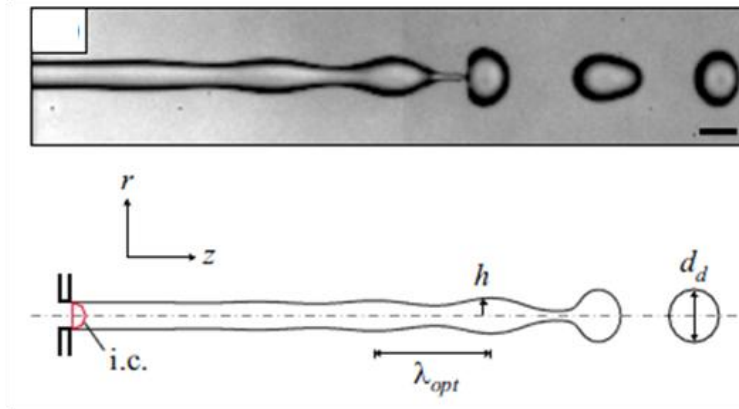


Figure 1.15: Plateau-Rayleigh instability for a 40 wt% glycerol solution in a 0.9 wt% saline solution and schematic representation, with scale bar representing 50 μm (from [51]).

The wavelength λ_{PR}^* with the fastest growth rate occurs:

$$\lambda_{PR}^* = 2\pi\sqrt{2}R \quad (1.18)$$

This yields an optimum wavelength of 4.44 times the cylinder diameter, in accordance with the optimal values of 4.51 calculated by Lord Rayleigh (1878) or of 4.38 deduced by Plateau (1873) based on the results of Savart (1833). We note that Weber (1931) further analysed this work and gave an expression for the optimal wavelength by taking into account the fluid properties (viscosity, density and surface tension) [52].

Consequently, from eq. (1.18), we deduce that the cylinder spontaneously breaks up into drops, with the drops all having the same size [5,47,51]. In some cases, small satellite drops can be formed, which depends on the Weber and Ohnesorge numbers. The satellite drops result

from the thin thread formed between two main drops detaching, which forms a small drop rather than separating into the two main drops [51].

The characteristic time of the Plateau-Rayleigh instability τ_{PR} corresponds to the equilibrium between inertial forces and capillary forces:

$$\tau_{PR} \sim \left(\frac{\rho R^3}{\gamma} \right)^{1/2} \quad (1.19)$$

with ρ the cylinder density and γ the interfacial tension [5,47,51,53].

For a jet confined in a tube, Hagedorn, Martys and Douglas (2004) and Duclaux, Clanet and Quéré (2006) found that the onset and behavior of the Plateau-Rayleigh instabilities depends on the ratio between the jet and tube diameters [54,55].

Lindner and Wagner (2009) experimentally observed Plateau-Rayleigh instabilities for non-Newtonian fluids (the previous descriptions were only valid for Newtonian fluids). In these experiments, a polymer was added to a low viscosity, Newtonian solvent. The viscoelastic nature of the mixed fluid led to the formation of apparent beads linked between them by long filaments. For high enough concentrations of polymer, the fluid thread never broke up, thus drops were no longer formed [53].

2.1.3. Rayleigh-Taylor instabilities

Rayleigh-Taylor instabilities induce the breakup of a liquid film into drops, with the driving force being gravity. An example of this instability is when paint dries on a ceiling and forms pendant drops.

This instability can take place if a fluid of higher density is above a fluid of lighter density (density discontinuity). The instability occurs if the latter, lighter density fluid is accelerated perpendicularly to the interface towards the former, higher density fluid. The instability is a competition between gravity and interfacial tension, therefore it is characterised by the Bond number.

The optimal wavelength λ_{RT}^* for the instabilities to occur for a liquid film in air is selected kinetically and is:

$$\lambda_{RT}^* = 2\pi\sqrt{2} \sqrt{\frac{\gamma}{\rho g}} \quad (1.20)$$

The characteristic time of the instability τ_{RT} is calculated by:

$$\tau_{RT} = 12 \frac{\gamma\eta}{\rho^2 g^2 d^3} \quad (1.21)$$

with η , ρ , d the film viscosity, density and thickness, respectively and γ the interfacial tension between the film and surrounding air [4,5,46].

2.1.4. Faraday waves

When a fluid is vibrated vertically, *i.e.*, perpendicularly to the interface, wave patterns appear at the surface, with a frequency at half of the forcing frequency (subharmonic response). Although previous work had been performed on vibrated powders, these waves were first qualitatively detailed for different fluids and for different fluid depths by Faraday (1831) in the appendix of his work.

The wave patterns which appear are capillary waves if $Bo \ll 1$ and gravity waves if $Bo \gg 1$. Above a threshold acceleration of vibration, a parametric instability occurs, with the onset of Faraday waves (fig. 1.16).

In the capillary wave limit, the threshold acceleration a_{FW} for the instability is calculated by:

$$a_{FW} \sim \nu \left(\frac{\rho}{\gamma} \right)^{1/3} (2\pi f)^{5/3} \quad (1.22)$$

with ν the kinematic viscosity, ρ the fluid density, γ the interfacial tension and f the forcing frequency.

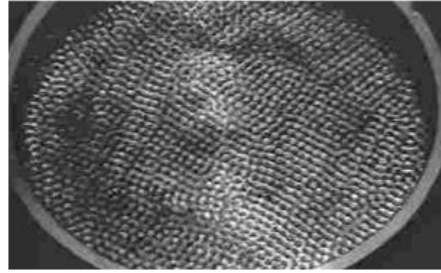


Figure 1.16: Faraday waves for a 2 mm deep water tray vibrated at 300 Hz (from [56]).

If the acceleration is increased above a second critical acceleration $a_{FW,ej}$, drops are ejected from the end of the waves. This critical acceleration is given by:

$$a_{FW,ej} \sim \left(\frac{\gamma}{\rho} \right)^{1/3} f^{4/3} \quad (1.23)$$

The diameters D_{FW} of the drops produced are proportional to the Faraday wavelength λ_{FW} :

$$D_{FW} \sim k_{FW} \lambda_{FW} \sim k_{FW} \left(\frac{\gamma}{\rho} \right)^{1/3} f^{-2/3} \quad (1.24)$$

with k_{FW} reported between 0.2 and 0.34 [56,57].

Lindner and Wagner (2009) investigated the impact of non-Newtonian, concentrated polymer solutions on the Faraday instability. Subharmonic and harmonic responses could occur simultaneously if the inverse of the relaxation time of the fluid was comparable to the forcing frequency. In this case, superlattices (new patterns) could be observed [53].

2.1.5. Kelvin-Helmholtz instabilities

Kelvin-Helmholtz instabilities occur if two fluids, one above the other, have different velocities (velocity discontinuity), where the flow directions are parallel to the interface (fig. 1.17). These can be observed for example in clouds or on the sea surface.

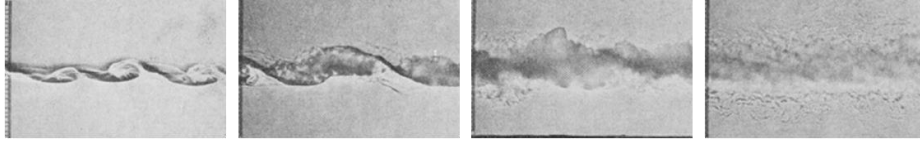


Figure 1.17: Kelvin-Helmholtz instability for fresh water on top (flow from right to left) and brine below (flow from left to right), from instability to turbulence (from [58], modified).

The instability occurs (in a linear approximation) if the following equation is verified:

$$4\rho_1\rho_2\left(\frac{\Delta U}{2(\rho_1+\rho_2)}\right)^2 > \frac{g\rho_1-\rho_2}{k\rho_1+\rho_2} + \frac{\gamma k}{\rho_1+\rho_2} \quad (1.25)$$

with ρ_1, ρ_2 the two fluid densities, ΔU the difference in fluid velocities, γ the interfacial tension and k the wave vector. If eq. (1.25) is not verified, the waves decay exponentially in time once the perturbation stops because of the fluid viscosity which damps the movements [46,58].

The instability is characterised by the formation of waves, which overturn to form billows (fig. 1.17). The billows appear when there is a transition to turbulence, which is reported to take place when the billow height reaches around 1/3 of its wavelength. The onset of the instability is obtained for Richardson numbers below 0.25. The Richardson number is a dimensionless number which describes the ratio between buoyancy forces and the flow gradient, defined by $Ri = g\Delta\rho d/2\rho_1 U^2$, with d the layer thickness and U a characteristic velocity [58].

2.1.6. Saffman-Taylor instabilities

Saffman-Taylor instabilities, also commonly called “viscous fingering”, occur when a less viscous fluid pushes a more viscous fluid inside a narrow channel or pore (fig. 1.18) (viscosity discontinuity). The amplified perturbations of the interface are induced by viscous effects whereas surface tension tends to stabilize the interface. Therefore, the capillary number Ca is key to determine the instability.

Indeed, the maximum growth rate occurs for the optimum wavelength λ_{ST}^* :

$$\lambda_{ST}^* = \frac{\pi b}{\sqrt{Ca}} \quad (1.26)$$

with b the channel height and Ca the capillary number. The perturbations induced lead to the appearance of so-called fingers, with eventually only one finger which is selected and which remains. The width of this finger is determined by the ratio between the channel width and the wavelength λ_{ST} . The finger cannot have a diameter of less than half of the channel width for Newtonian fluids [53].

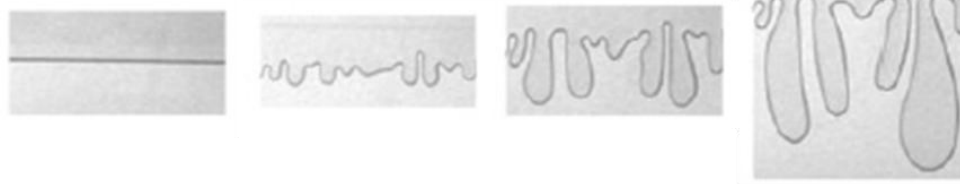


Figure 1.18: Saffman-Taylor instability for an air-silicon oil system, from the interface to fingers (from [53], modified).

Lindner and Wagner (2009) experimentally observed the Saffman-Taylor instabilities for non-Newtonian, shear-thickening fluids. In this case, the remaining, selected finger width was increased compared to in a classic, Newtonian fluid. Oppositely, for shear-thinning solutions, the finger width was decreased [53].

2.2. Jet breakup

2.2.1. Transition between dripping and jetting

When a liquid flows out through an open nozzle, it can either exit the pore drop by drop, *i.e.*, in dripping mode (fig. 1.19(a)), or as a continuous jet, *i.e.*, in jetting mode (fig. 1.19(c)).

In jetting mode, the jet was found to break up into drops by Plateau-Rayleigh instabilities [59,60]. The jetting regime is detailed further on (see 2.2.2). At a critical, low velocity, drops are formed in dripping mode, following a force balance between gravity and retaining interfacial tension forces, which will be described in 2.3.1. We note that the pinch off point is the point where the jet ruptures, resulting in the formation of a drop.

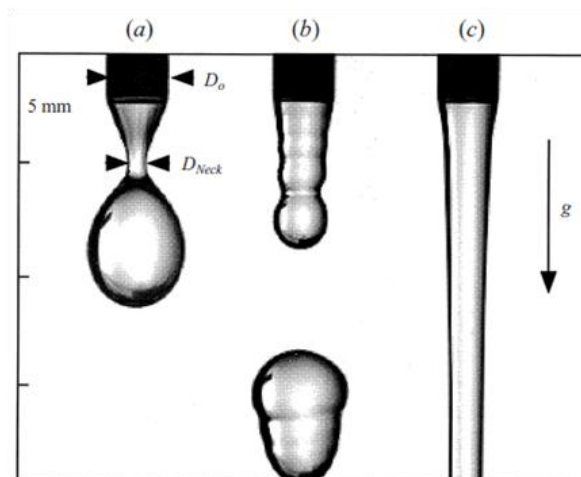


Figure 1.19: Flow modes from a 2.769 mm diameter nozzle: (a) dripping ($We = 0.063$); (b) intermediate chaotic regime ($We = 1.73$); (c) jetting ($We = 2.3$) (from [59]).

It must be added that the transition is not so simple. An intermediate regime can also exist, with drops formed in a chaotic manner (fig. 1.19(b)). Indeed, Clanet and Lasheras (1999) reported an intermediate regime with drops formed in either a quasi periodic manner or a

chaotic manner [59]. Ambravaneswaran *et al.* (2004) also studied the dripping to jetting transition from a faucet and reported two gross transitions (with the limit when the Ohnesorge number was at a critical value of 0.5). The first is between dripping and complex dripping (fig. 1.19(a) to (b)) and the second between complex dripping to jetting (fig. 1.19(b) to (c)) [61].

2.2.2. Investigation of jetting mode

2.2.2.1. Breakup into air

The transition between dripping and jetting occurs at a critical inner Weber number, that is, when the inertial forces are sufficient to overcome the restoring capillary forces. Consequently, for a given fluid and nozzle, *i.e.*, fixed density, interfacial tension and characteristic dimensions of the nozzle, the transition occurs above a critical fluid velocity.

This was illustrated by Webster and Longmire (2001): the pinch off point due to Plateau-Rayleigh instabilities gradually moved upwards towards the nozzle exit as the fluid jet velocity was decreased. At a critical low velocity, Plateau-Rayleigh instabilities no longer occurred and drops were formed close to the nozzle exit in dripping mode [62].

Clanet and Lasheras (1999) investigated water drops formed from a nozzle into air under gravity. The critical inner Weber number for the transition from dripping to jetting depended on Bond numbers, as dripping is gravity controlled in this configuration. A function was established to estimate the critical Weber number We_c for jetting to occur, given in the following equation:

$$We_c = 4 \frac{Bo_o}{Bo} \left[1 + kBoBo_o - ((1 + kBoBo_o)^2 - 1)^{1/2} \right]^2 \quad (1.27)$$

with Bo and Bo_o the Bond numbers based on the inner and outer diameter of the nozzle, respectively ($Bo = (\rho g D^2 / (2\gamma))^{1/2}$). k is a constant worth 0.37 for water injected into air. This function is obtained by considering the equation of motion of the drop and calculating the point at which the maximum length reachable by the drop becomes smaller than the detachment distance by pinch off [59]. In the case where the drop does not wet the nozzle tip, only Bo would be relevant.

Ambravaneswaran *et al.* (2004) also investigated drops formed from a nozzle into air and considered the impact of fluid viscosity. High viscosity liquids, *i.e.*, with Ohnesorge numbers above 0.5, directly transitioned from dripping to jetting above a critical Weber number, without undergoing complex dripping (intermediate regime). As the viscosity increased, the critical Weber number for jetting to occur decreased, which accords with the theory based on the competition between the time scales of the flow and the capillary breakup [61].

2.2.2.2. Breakup into an immiscible liquid

Webster and Longmire (2001) considered a fluid injected into an immiscible stationary liquid phase. The pinch-off point in jetting mode was closer to the nozzle with an increased

outer phase viscosity as this delayed the flow of the jet. The resulting drops formed were larger. For high injection velocities, thin filaments joined the drops between them. For even higher velocities, no stable jet could be formed at the nozzle exit [62].

Scheele and Meister (1968) predicted the jetting velocity in this configuration (liquid injected into a stationary, outer liquid). The transition occurs when the upward force (kinetic and excess pressure forces) overcomes the retaining capillary force. Thus a jet forms rather than drop enlargement. A mean error of 6.6% was found for a wide range of results. A second model was proposed where a jet forms if the drop rises less than one drop diameter during the time of formation of the next drop (thus the drops merge into a jet), similarly to the model of Clanet and Lasheras (1999). This model was less accurate than the former model [63].

Richards, Beris and Lenhoff (1995) performed numerical simulations with a VOF method and a continuous surface force method (CSF) to explain the results of Scheele and Meister. They well predicted drop sizes for both dripping and jetting by taking into account many factors including surface-tension induced deformation of the interface or gravity, for example. We note that predictions were less accurate for the smallest nozzle [64].

2.2.2.3. Breakup into an immiscible liquid with co-flow

In ME, the outer liquid phase is not stationary but flows. For a liquid injected into a co-flowing liquid, Utada *et al.* (2007) showed that the dripping to jetting transition depends on the inner Weber number $We_{in} = \rho_{dp} D_p v_{dp}^2 / \gamma$ and the outer capillary number $Ca_{out} = \eta_{cp} v_{cp} / \gamma$, which they mapped (black points for dripping and white points for jetting, fig. 1.20).

Overall, jetting occurs when the surface tension forces are overcome, either by the inertial or viscous forces. The inertial-induced jetting or viscous-induced jetting were determined by the criteria $We_{in} > O(1)$ or $Ca_{out} > O(1)$, respectively, represented by the horizontal and vertical grey lines in fig. 1.20, respectively. Two jetting regimes occurred, depending on the velocities of the inner and outer phases. These were a regime with jet widening (for high inner velocities) and a regime with jet narrowing (for high outer velocities) [60].

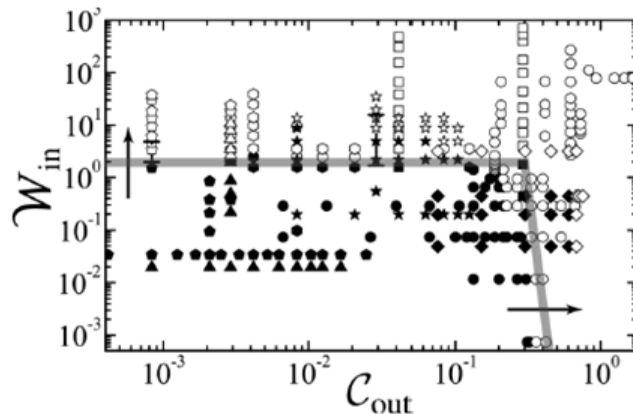


Figure 1.20: Dripping to jetting transition depending on the inner Weber number W_{in} and outer capillary number C_{out} , for various surface tensions and viscosity ratios. Black: dripping; white: jetting (from [60]).

Castro-Hernández *et al.* (2009) experimentally studied both the widening and narrowing regimes. The inertial force drove the dripping to jetting transition if the inner Reynolds number $Re_{in} > 1$, otherwise, viscous forces drove the transition. They wrote a unified equation to predict drop sizes for both regimes, with relative errors of 30% [65].

Chen, Wu and Zhang (2013) performed CFD simulations with a VOF method to explain the results of Utada *et al.* (2007). Differences in growth rates between the front and rear end of the neck explained the narrowing regime. Viscous drag dominated breakup, thus the transition from dripping to this regime is governed by the capillary number. Jet widening occurred when the inertial force was such that the drop was formed downstream. The outer phase slowed the drop, leading to a wider zone along the jet. A thin neck is formed compared to the drop size, inducing large pressures inside the neck, leading to pinch off [66].

In the same configuration and when investigating the impact of various parameters, Cramer, Fischer and Windhab (2004) found a sudden decrease in drop size in jetting mode compared to dripping mode. An increase in the dispersed phase viscosity lowered the continuous phase velocity necessary for the transition. This was also true for a lowered interfacial tension [67].

We note that Guillot *et al.* (2007) considered the dripping to jetting transition inside a confined microfluidic channel for co-flowing liquids. The external flow was parabolic due to wall effects. They mapped dripping regions (drop or plug-like drop regions), and different jetting regions, depending on both phase velocities. They performed a linear analysis to predict the regime depending on the operating conditions (interfacial tension, phase viscosities and capillary dimensions) [68].

2.2.2.4. Breakup into an immiscible liquid with cross-flow

In the previous studies, the co-flowing streams were parallel. However in ME, the dispersed phase arrives at 90° to the continuous phase (cross-flow) before being in a near co-flow situation depending on the continuous phase velocity. This was mimicked by injecting a liquid through a single pore into a continuous, flowing phase, either experimentally by Meyer and Crocker (2009) [69] or numerically by M. Pathak (2011) [70].

The dripping to jetting transition occurs above a critical inner Weber number for the inertial force controlled transition (vertical arrow, fig. 1.20). However, it is a function of the outer capillary number Ca_{out} instead of the Bond number, as dripping is shear controlled rather than gravity controlled. Thus, in analogy to the work of Clanet and Lasheras (1999), Bo and Bo_o were replaced in eq. (1.27) by the capillary number to obtain the critical Weber number, with adjusted coefficients. The authors mapped the dripping and jetting zones as a function of We_{in} and Ca_{out} [69,70].

A surface tension force controlled transition was also described by M. Pathak (2011), where breakup occurs due to viscous drag. This transition occurs at a fixed Weber number and by increasing the capillary number above a critical value (horizontal arrow, fig. 1.20) [70].

In addition, Meyer and Crocker (2009) found a dependence of the transition with the inner Ohnesorge number [69]. Overall, Meyer and Crocker (2009) summed up that jetting occurs

when the force leading to surface extension exceeds that leading to surface contraction (interfacial tension force). The extension force can be either due to the kinetic energy of the dispersed phase (related to the dispersed phase flow rate), the drag of the flowing phase (related to the continuous phase flow rate) or gravity in the case of a liquid jet in air [69].

2.2.3. Impact of vibration on jetting mode

2.2.3.1. Breakup in air with applied vibrations

Crane, Birch and McCormack (1964) and Wissema and Davies (1969) studied the impact of vibration on the breakup of a liquid jet injected into air, with vibration perpendicular to the jet flow. The results of Crane, Birch and McCormack (1964) were in agreement with the studies of Lord Rayleigh (1878) and Weber (1931). An increase in the vibration amplitude or frequency (the other being held fixed) led to a decrease in the jet breakup length. A bunching effect of the jet was observed for high amplitudes due to nonlinearity [71].

Wissema and Davies (1969) found no impact on drop breakup for low frequencies. For high frequencies, the jet broke up closer to the nozzle exit. A threshold frequency was needed to produce uniform-sized drops. An increase in amplitude resulted in breakup closer to the nozzle exit and above a critical amplitude, two streams of drops were generated in different directions (each stream on a different side of the nozzle axis) [72].

Other studies exist for liquid-air systems and are not described further here because in the scope of our work, we consider liquid-liquid systems.

2.2.3.2. Breakup in a second liquid with applied vibrations

Webster and Longmire (2001) considered a liquid jet injected into a liquid phase with a vibrating nozzle, vibrating parallel to its axis, *i.e.*, parallel to the jet. In jetting mode, the pinch-off point was shifted towards the nozzle as a forcing frequency was applied. The position of the point depended on the forcing amplitude. The size and size distribution of the drops depended on the forcing frequency. An increase in the surrounding phase viscosity led to a decrease in the vibration frequency necessary to obtain the fundamental pinch off mode, *i.e.*, a drop formed at each cycle [62].

Sauret, Spandagos and Shum (2012) studied co-flowing streams with ultralow interfacial tensions ($\sim 10 \mu\text{N}\cdot\text{m}^{-1}$). Vibrations were induced by pressure fluctuations of the dispersed phase by vibrating the tube for the dispersed phase influx perpendicularly to the dispersed phase flow. Without vibration, no perturbations occurred. For low frequencies, the jet interface oscillated without breakup. Then, in a range of frequencies, the jet broke up into monodispersed drops. Above a critical frequency, corrugations appeared. The optimum frequencies to form monodispersed drops deviated from Rayleigh's predictions due to the fact that the bulk phase is a liquid rather than air [73].

Zhu, Tang and Wang (2016) and Cordero, Gallaire and Baroud (2011) investigated the impact of pressure-induced fluctuations (by vibrating the dispersed phase influx tubing

perpendicularly to the dispersed phase flow) and flow fluctuations induced by laser heating, respectively. Both studied co-flowing streams, with an aqueous phase injected into silicon oil in a microfluidic channel. In jetting mode, applying vibration decreased jet length. For a range of frequencies, drop generation became synchronized with the vibration frequency, producing monodispersed drops. This occurred above a threshold amplitude. For optimized frequencies, drops were formed in dripping mode, which illustrates a delay in the dripping-jetting transition induced by vibrations. The higher the forcing amplitude, the more the transition to jetting is delayed. Increasing the forcing frequency led to a decrease in drop size [74,75].

2.3. Drop breakup

2.3.1. Breakup in dripping mode from a nozzle

2.3.1.1. Tate's law

In dripping mode, drops are formed individually from the nozzle. They detach when the gravity or buoyancy forces overcome the retaining capillary force, as stated by Tate's law (1864) [76]. Harkins and Brown (1919) later introduced a correction factor \mathcal{F}_{HB} ($\mathcal{F}_{HB} < 1$), which accounts for the fraction of liquid volume which stays attached to the nozzle tip after drop detachment [77]. Tate's law corrected by the Harkins Brown factor reads:

$$(\rho_{cp} - \rho_{dp}) \frac{\pi}{6} D_d^3 g = \mathcal{F}_{HB} \pi D_p \gamma \quad (1.28)$$

with ρ_{cp} and ρ_{dp} the continuous and dispersed phase densities, respectively, D_d the drop diameter, D_p the pore diameter and γ the interfacial tension. Various correlations have been proposed since 1919 to calculate the Harkins Brown factor, which is a function of the pore diameter and the drop volume. These correlations were summarized and a new one proposed in the work of Mori (1990) [78].

Tate's law is valid for static conditions. In dynamic conditions, Scheele and Meister (1968) wrote a force balance for drop detachment which included a drag and kinetic force. They also added a term to account for the dispersed phase fed to the drop during necking, which can contribute significantly to final drop size depending on the injection velocity. Their model estimated drop volume with a mean percentage deviation of 11% for a broad range of parameters tested, in a liquid-liquid system (the second being stationary) [79].

2.3.1.2. Experimental results

Liquid drop generation into air in dripping mode has been widely investigated, notably by Zhang and Basaran (1995), who considered the impact of fluid viscosity, tube radius, surface tension and fluid injection velocity. They applied Scheele and Meister's equation to their results and found a maximum relative deviation of 25% for the volume of the drops obtained. As drop viscosity increased, a longer and thinner thread linked the drop to the capillary before break off,

explained by pressure variations in the drop and neck during the different stages of drop formation. A critical length for breakup was characterised depending on the different parameters. The appearance of satellite drops was also investigated [80]. Henderson *et al.* (1997) studied a similar configuration with a focus on the thread between the drop and orifice [81]. Other studies will not be discussed here as we focus on liquid-liquid systems.

Cramer, Fischer and Windhab (2004) experimentally investigated dripping with two immiscible co-flowing fluids. As the outer phase velocity increases, the drag force increases resulting in a shorter detachment time, thus smaller drops. As the inner phase velocity increases, the detachment time decreases, until a limit velocity where necking time determines drop breakup. In reality, the difference in phase velocities is the relevant parameter. Drop size was not affected by dispersed phase viscosity (as predicted by Tate's law) however the increased viscous pressure led to the formation of satellite drops. Smaller drops were formed for lower interfacial tensions, as expected as the retaining force is lower [67].

2.3.2. Breakup of a free drop submitted to shear

A four roll mill was first developed by Taylor in 1934 to investigate drop behavior and breakup under extensional flow. Drop deformation was found to be equal to a ratio between viscous and interfacial tension forces, in the limit of small deformations. Deformation until drop burst was affected by the viscosity ratio and by the flow type (simple shear or extensional flows were considered). The four roll mill was thereafter used in many experiments to extend Taylor's pioneering work, a few of which are described below [82].

Grace (1982) used the four roll mill as well as a Couette device and illustrated the critical ratio between viscous and interfacial tension forces needed for drop burst as a function of the viscosity ratio. This constitutes the famous Grace curve (fig. 1.21). We note that drop burst is most favorable when the two phases have the same viscosity [83].

The critical force ratio is assimilated to a critical capillary number and was determined by Bentley and Leal (1986) for various types of flow in between the rotational and irrotational cases as well as for simple shear flow. They adequately calculated drop deformation and burst for most viscosity ratios, capillary numbers and flow types tested, particularly for small deformations [84].

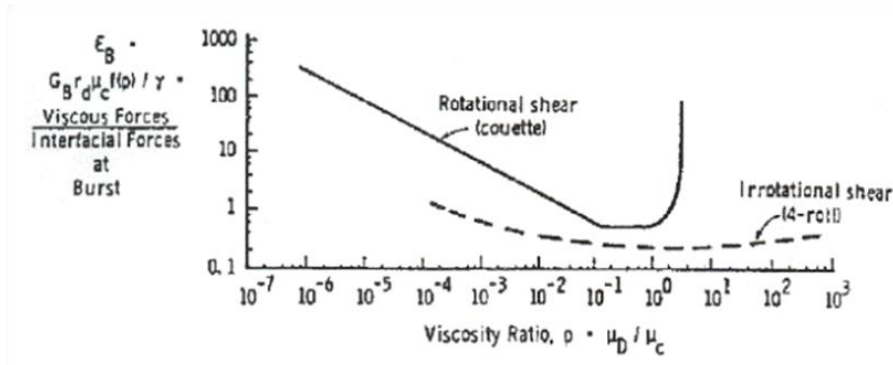


Figure 1.21: Grace curve: force ratio (viscous to interfacial forces) for burst E_B depending on the viscosity ratio $p = \eta_{dp}/\eta_{cp}$ (from [83]).

Stone, Bentley and Leal (1986) also investigated the four roll mill. Drops were elongated when shear was applied and could break up into two distinct drops once the flow was stopped. The interfacial tension-driven mechanism for breakup was end pinching. It is due to pressure variations at the bulbous ends of the fluid thread, *i.e.*, the elongated drop. It occurred on a shorter time scale than Plateau-Rayleigh instabilities, which were only observed for the most elongated threads. Drops broke up above a critical elongation ratio (drop half length to the undeformed drop radius), which depended on the viscosity ratio between the drop and the outer phase. Otherwise, the drop relaxed back to a sphere (fig. 1.22). Again, breakup is most favorable for drops having the same viscosity as the outer phase [85].

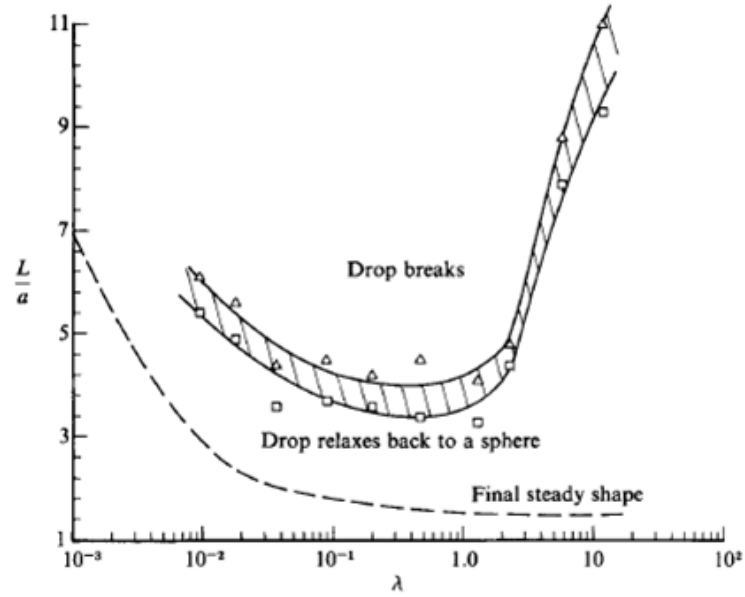


Figure 1.22: Critical elongation ratio L/a (drop half length to the undeformed drop radius) for breakup as a function of the viscosity ratio $\lambda = \eta_{dp}/\eta_{cp}$ (from [85]).

Stone and Leal (1990) pursued the work by studying the impact of surfactants on drop breakup. In the presence of surfactants, depending on the Péclet number, deformation can be increased leading to a shift in the critical capillary number for breakup. The Péclet number is a dimensionless number which compares convective and diffusive effects, given by $Pe = GD_a^2/4\mathfrak{D}_s$, with G the shear rate and \mathfrak{D}_s the surface diffusivity. For Péclet numbers in the order of 100, convective effects dominate, leading to gradients in surfactant on the drop which induce the increased deformation [86].

2.3.3. Individual fluid thread breakup

Further work similar to that on drop breakup was performed on individual fluid thread breakup into an inactive, ambient fluid, *e.g.* air. Indeed, the fluid threads were elongated and their behaviour (onset or not of breakup) was analysed.

Schulkes (1996) first numerically determined that fluid thread breakup depended on the Ohnesorge number. For $Oh > 1$, the thread contracted into a sphere, regardless of its length.

For sufficiently small Oh (in the order of 10^{-3}), bulbous ends formed on the thread, which broke up into drops [87].

Similarly, Notz and Basaran (2004) numerically determined that breakup depended on the Ohnesorge number but also on the initial thread aspect ratio (initial thread half length to the initial thread radius). In analogy, we saw that the dependence of breakup on drop length was demonstrated for drops submitted to shear.

Notz and Basaran (2004) found that for $Oh > 0.1$, the thread always relaxes into a sphere, whatever the initial aspect ratio set (between 5 and 30). This was also shown by Schulkes (1996) for high Oh (in their case for $Oh > 1$). For low values of Oh (< 0.01), thread behaviour depends on the initial aspect of the thread, as shown in fig. 1.23. For example, for $Oh = 10^{-3}$, initially long threads ($L_0 = 15$) undergo end pinching, with break up at both ends forming separate drops. Short threads ($L_0 = 5$) relax into a sphere after oscillating, at long times. Complicated dynamics exist for intermediate L_0 ($L_0 = 10$). Results for different Oh and L_0 are summarized in fig. 1.23 [88].

Castrejon-Pita *et al.* (2012) experimentally studied fluid thread behaviour. They verified that for $Oh > 1$, fluid thread breakup never occurred, nor did it occur for threads below a critical length (initial aspect), irrespectively of Oh . They compared their results to the simulations of Notz and Basaran (2004), which were relatively in accordance. Differences were observed for intermediate Oh . This was attributed to surface effects which may occur in experiments or to the meshing established in simulations [89].

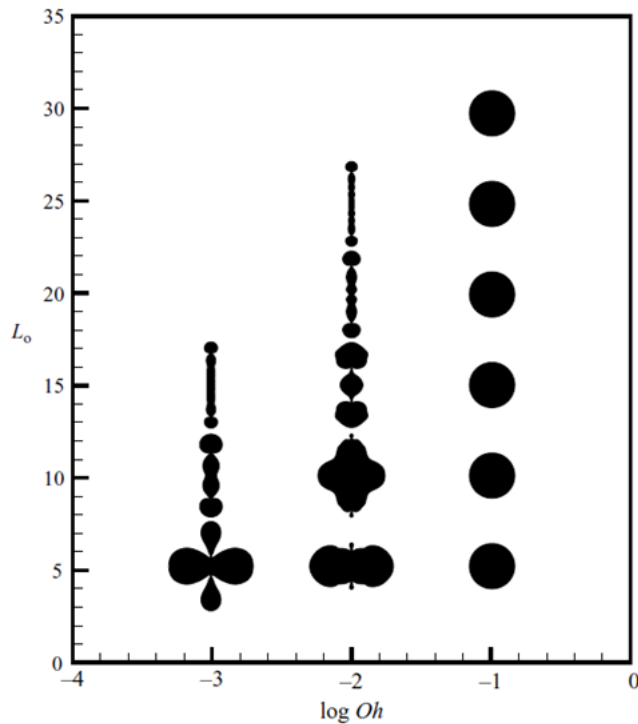


Figure 1.23: Fluid thread final shapes depending on the initial aspect ratio L_0 (initial thread half length to the initial thread radius) and Oh (from [88]).

2.4. Models for drop generation in membrane emulsification

Some models or mechanisms for drop breakup have been specifically proposed in the case of ME or ME with vibration. Indeed, it is of interest to understand drop generation be able to control drop size and size distribution resulting from the process to control the emulsion produced. As the original aim of our work is to understand drop detachment mechanisms in transversally vibrating ME, these targeted studies are presented in this section.

2.4.1. Macroscopic models

Force or torque balance models have been developed to describe drop detachment in ME: these are macroscopic models. In these models, the different forces exerted on the drop are considered. In the example shown in fig. 1.24, the forces involved are drag, the retaining capillary force, buoyancy, dynamic lift and the Young-Laplace force. Depending on the studies, more or less forces may be considered than in this example, *e.g.* an inertial force may also intervene. Indeed, some forces can be neglected compared to others depending on the experimental conditions. The forces which are always included in ME (main forces) are the retaining capillary force and detaching drag force induced by the continuous phase flow [27,33,69,90].

2.4.1.1. Comparison between models

In the torque model, the drop is considered rigid and the interfacial tension is considered uniform. When the torques from a set point on the pore circumference in clockwise and anticlockwise directions are balanced, the drop detaches. In the force model, the drop is considered deformable. The drop detaches when the capillary force can no longer counterbalance the other forces. In real conditions, it is expected that drop size predictions should be in between those predicted by the force and torque models, which are the extreme cases of a completely deformable or rigid drop, respectively [33,90].

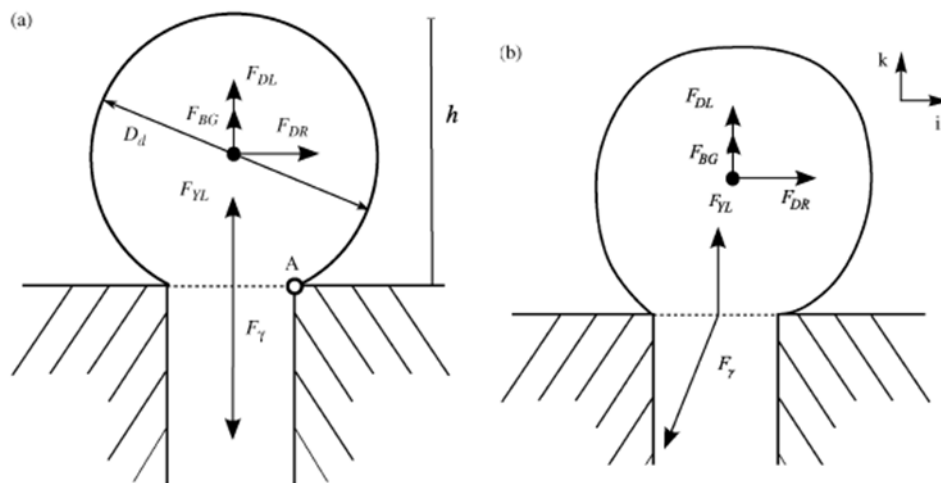


Figure 1.24: Forces exerted on a drop in ME for (a) torque balance; (b) force balance. Forces: Young-Laplace F_{YL} , buoyancy F_{BG} , dynamic lift F_{DL} , drag F_{DR} , capillary F_{γ} (from [90]).

De Luca *et al.* (2008) compared both the force and torque models to various sets of experimental results, including those of Katoh *et al.* (1996) [38] and Vladislavljević and Schubert (2003) [26]. The force model gave a better trend in drop size with cross-flow velocity and better estimations for drop diameters at high shear stresses (> 7 Pa) and small pore diameters (< 1.5 μm). The torque model gave more adequate results for large pore diameters [90]. Peng and Williams (1998) also applied both models and found a good correlation between drop size as a function of cross-flow velocity for a force model [33].

Meyer and Crocker (2009) experimentally formed drops from a single pore under cross-flow to model ME. They obtained a reasonable agreement between a force model and experiments by considering only the capillary and drag forces, however better agreement would be expected by including other forces or by including neck and hydrodynamic effects [69]. Xu *et al.* (2005) modelled ME by studying drop formation from a single square hole. They obtained good results from a torque balance compared to experimental results for three systems, with slight differences being due to the impact of the dispersed phase flow rate [91]. Timgren *et al.* (2010) obtained an improved force balance model by taking into account the rotation of the drop due to the continuous phase flow [92].

2.4.1.2. Extensions of the macroscopic models

In order to better predict drop sizes with a force balance, the extra dispersed phase fed to the drop during necking time can be taken into account. Scheele and Meister (1968) considered neck effects for drops formed from a nozzle into air [63]. Peng and Williams (1998) later applied this method to ME, in a liquid-liquid system [33]. Xu *et al.* (2005) also applied it for drops formed from a single pore with cross-flow to model ME [91].

Kelder, Janssen and Boom (2007) extended the force balance model for longitudinally vibrating ME, which has additional inertial and drag force components due to the vibration induced. Without vibration, agreement with experimental drop sizes were good for high cross-flow velocities and less for low velocities, where push-off mechanisms occurred experimentally giving smaller drop sizes than predicted. However, with vibration, this simplified force balance model was not accurate [44].

2.4.2. Microscopic and mesoscopic models

2.4.2.1. Spontaneous transformation

A spontaneous transformation based mechanism for drop formation was applied to cross-flow ME by Yasuno *et al.* (2002). Drop formation is driven by interfacial tension, with the model considering the overall interfacial free energy of the system. If the energy of the detached drop plus the energy of the interface at the pore is lower than the energy of the attached drop, then it detaches. This mechanism better explains drop detachment in ME than force based models for low continuous and dispersed phase flow rates. Depending on the values

of these two parameters, drop detachment can be attributed more or less to spontaneous transformation or to shear force [93].

Rayner *et al.* (2004) considered the Gibbs free energy as the drop generation mechanisms and obtained an average error compared to experimental results of 8% when the correct pore geometry was applied [94].

2.4.2.2. Computational Fluid Dynamics (CFD)

Computational fluid dynamics (CFD) are relatively less used than macroscopic force or torque balance models as these methods usually take longer to implement. This is especially true if many parameters are varied or if a fine mesh is used.

Abrahamse *et al.* (2001) applied a finite-volume method to a single pore in order to model drop generation in ME. This study enabled to gain insight on drop shape and detachment and led to propositions for membrane design to limit coalescence [40]. Similarly, Pathak (2011) applied a finite-volume method to a single pore, in this case to model the transition between dripping and jetting as detailed in 2.2.1 [70].

Timgren *et al.* (2009) used the volume of fluid (VOF) method to model drop formation from a capillary with cross-flow conditions, similarly to what would occur in ME. Drop volume and drop formation time were well estimated compared to experimentally with a maximum error of 10% [43].

Kelder, Janssen and Boom (2007) developed a 3D CFD model for longitudinally vibrating ME, as the extended force balance model was not satisfactory. Without vibration, the 3D CFD model gave satisfactory results. With vibration, this model is expected to yield better results than the force balance model, however further experimental validation is said to be necessary to validate the model [44].

Lattice-Boltzmann methods have also been considered to model drop generation, for example by van der Zwan *et al.* (2009). However, this method was applied to microchannel ME rather than to cross-flow ME [95].

2.5. Conclusions

Summary

Drop generation mechanisms have been investigated in various experimental or numerical conditions. For example, drop generation from a nozzle has been widely investigated, in two different regimes that are dripping and jetting. The transition between these regimes has received particular attention and has been determined as a function of adequate dimensionless numbers. Free drops or fluid threads have also received a fair amount of attention, when they break up into multiple drops after having been submitted to different types of shear. For the different types of configurations considered, the criteria for the onset of breakup have been summarized in table 1.2.

In some cases, well documented hydrodynamic instabilities can be applied directly to the results to explain drop formation. In other cases, models have been proposed as a result of these studies, mostly based on force balances and characterised by threshold dimensionless numbers.

In the example of ME, the most widely applied models to describe drop generation are macroscopic models, including force balance or torque balance models. Results are more or less satisfactory for each model depending on the operating conditions applied. These models are easy and fast to implement compared to CFD modeling, which have also been occasionally used to describe drop generation in ME. CFD modeling may however be expected to yield more precise results. Other models based on spontaneous transformation have also been described in a few cases.

Aims

For vibrating ME, very few experiments and even fewer models exist. Attempts have been made to adapt a force balance for longitudinally vibrating ME however results were not satisfactory and CFD simulations were performed however not validated. For transversally vibrating ME, few experiments have been performed and no models have been proposed to our knowledge. We therefore aim to propose mechanisms and a model to describe drop generation in this process. In order to better understand potential drop behavior submitted to axial vibrations as would be the case in transversally vibrating ME, the following section 3 describes the existing literature on drops submitted to vibrations.

Table 1.2: Criteria for the onset of liquid breakup.

Configuration	Type	Criteria for onset	Reference
Well-known instabilities	Plateau-Rayleigh	Driven by surface tension Occurs for a wavelength $\lambda_{pR}^* = 2\pi\sqrt{2}R$	[48–51]
	Rayleigh-Taylor	Driven by gravity (density discontinuity) Occurs for a wavelength $\lambda_{RT}^* = 2\pi\sqrt{2} \sqrt{\frac{\gamma}{\rho g}}$	[4,5,46]
	Faraday waves	Driven by the vertical vibration of a fluid interface Occurs for an acceleration $a_{FW} \sim v \left(\frac{\rho}{\gamma}\right)^{1/3} (2\pi f)^{5/3}$ (in the capillary wave limit)	[56,57]
	Kelvin-Helmholtz	Driven by a velocity discontinuity Occurs for $Ri < 0.25$	[46,58]
	Saffman-Taylor	Driven by a viscosity discontinuity Occurs for a wavelength $\lambda_{ST}^* = \frac{\pi b}{\sqrt{Ca}}$	[53]
Jet	Liquid in air	Function of critical values of Bo and We_{in} For a set nozzle and fluid, occurs above a critical v_{cp}	[59,61–63]
	Liquid in liquid (co- or cross-flow)	Function of critical values of Ca_{out} and We_{in} Also dependent on Oh_{dp} Widening or narrowing regime function of v_{dp}/v_{cp}	[60,65–67,69,70]
	Vibrating jet	Vibration $\Rightarrow \downarrow$ jet length (even more so when \uparrow amplitude) Forcing frequency $\uparrow \Rightarrow \downarrow D_d$ Optimum frequency range for uniform drop sizes	[62,71–75]
Drop or individual thread	Without flow	Breakup when gravity forces exceed capillary forces	[76,77]
	With flow	Breakup when drag forces exceed capillary forces Torque balance for rigid drops, force balance for deformable drops	[27,33,67,69,90–92]
	With shear	Breakup for low Oh ($\sim O(0.01)$) for high initial aspect ratio Elongation ratio for breakup dependent on η_{dp}/η_{cp}	[85,87–89]

3. Single drop behavior under forced oscillations

As was seen in the previous sections, the mechanisms and behavior of drops in transversally vibrating ME have not been observed in detail nor understood. Therefore, the behavior of individual drops submitted to oscillations is exposed in this section. First, the behavior of an oscillating free drop will be developed, as this has been widely investigated since 1879 and is thus now well understood. Then, the behavior of a partially bound drop as can be found in ME will be reviewed. Finally, the impact of large-amplitude vibrations will be described, as in the studies performed on transversally vibrating ME, the amplitudes of vibration were large (in the order of the drop diameter).

3.1. Free drop

3.1.1. The Rayleigh theory

In the second appendix of his work, Lord Rayleigh (1879) considered a free, inviscid and incompressible drop in a vacuum, without gravity. The drop, which had an originally spherical shape, was subjected to small-amplitude oscillations about its initial shape, that is, the amplitude of oscillations were small compared to the initial drop radius. The vibrations considered were symmetrical about an axis. The calculation of the drop shape during oscillations was performed, in spherical coordinates (r, θ, Φ) :

$$r = R + \sum a_n P_n(\cos\theta) \quad (1.29)$$

with R the radius of the original, undeformed sphere, a_n coefficients, P_n the n^{th} order Legendre polynomial and θ the polar angle.

A drop has an infinite number of fundamental oscillation modes. The eigenmodes are characterized by two integers: a polar wavenumber $n \geq 2$ and an azimuthal wavenumber $m \in [-n; n]$. For axisymmetric modes, $m = 0$. Each axisymmetric mode is defined in terms of the Legendre polynomials, P_n and has a characteristic shape. The first four oscillation modes ($n = 2$ to $n = 5$) with their characteristic shapes are illustrated in fig. 1.25.

Using this equation as a starting point, Lord Rayleigh defined the drop eigenfrequency for any mode n (the first being $n = 2$) by:

$$f_{\text{Rayleigh}} = \frac{1}{2\pi} \sqrt{\frac{8n(n-1)(n+2)\gamma}{\rho D_d^3}} \quad (1.30)$$

with ρ the liquid density, D_d the drop diameter and γ the interfacial tension. A major result is that the eigenfrequency of the drop scales as $D_d^{-3/2}$ [96].

We note that similarly to Lord Rayleigh, Minnaert (1933) first calculated the natural resonance frequency of an air bubble undergoing small-amplitude oscillations in a liquid: the frequency has a similar form to eq. (1.30) but depends on the surrounding pressure and

polytropic index rather than the interfacial tension and is a function of D_a^{-1} rather than $D_a^{-3/2}$. This was named the Minnaert frequency and is valid by assuming adiabatic conditions and neglecting surface tension [97].

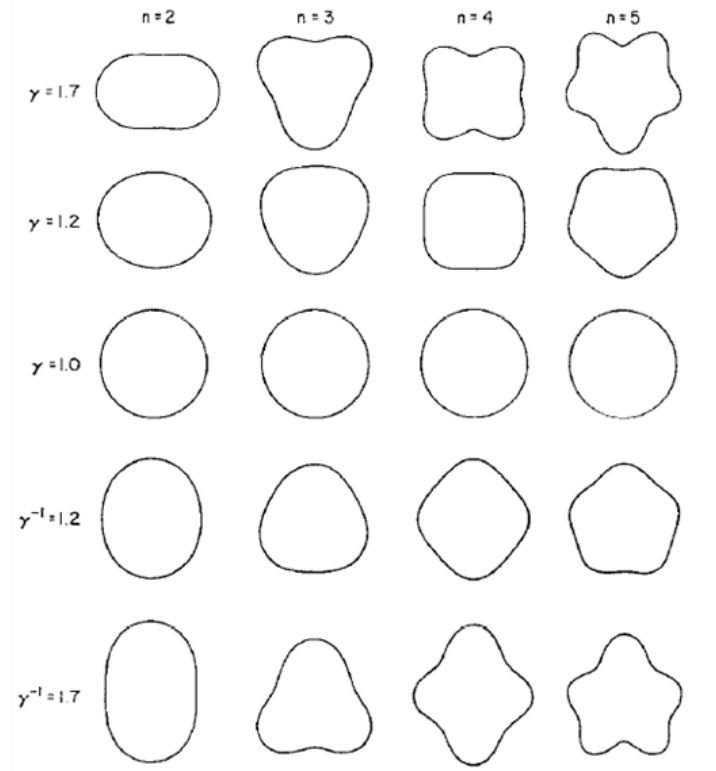


Figure 1.25: Drop shapes from the Rayleigh theory for modes $n=2$ to 5 , depending on the axial ratio γ (horizontal to vertical axis length) (from [98]).

3.1.2. Extension of the Rayleigh theory

The Rayleigh theory has since 1879 been extended in various ways. Moderate- or large-amplitude oscillations have been considered, for example in the works of G. B. Foote (1973), Tsamopoulos and Brown (1983) and Patzek *et al.* (1991). Patzek *et al.* (1991) resumed the magnitude of the oscillations considered in various work by reporting the ratio of the deformation of the interface A to a length scale proportional to the drop radius L (fig. 1.26). The impact of drop viscosity has also been considered as well as the impact of gravity.

Foote (1973) numerically investigated free viscous drops undergoing large-amplitude oscillations using the Marker-and-Cell method, in 2D. Amplitudes were such that the axial drop deformation ratio reached 1.9. He focused on the oblate-prolate oscillation mode ($n = 2$). For small amplitudes, the numerical results agreed with the Rayleigh theory. For large amplitudes, drop oscillations were not symmetric as in the Rayleigh theory but were asymmetric, with a longer time spent in the prolate shape than oblate shape. This was in accordance with experimental observations [98].

Tsamopoulos and Brown (1983) also numerically investigated moderate-amplitude oscillations for an inviscid, free drop in a vacuum. They set the forcing amplitudes such that the

axial drop deformation ratio was of 1.81. Results were in accordance with those of G. B. Foote (1973). Additionally, as the oscillation amplitude increased, the resonance frequency decreased. This is characteristic of nonlinear effects. These results agreed with experimental results of Trinh and Wang (1982) [99] for large drops [100].

The simulation results of Patzek *et al.* (1991) on free, inviscid drops were in accordance with both the results of Foote (1973) and Tsamopoulos and Brown (1983). In addition, they described the effect of the viscosity of the drop. Varying the viscosity induces changes in the time spent in prolate or oblate form, depending on drop release [101].

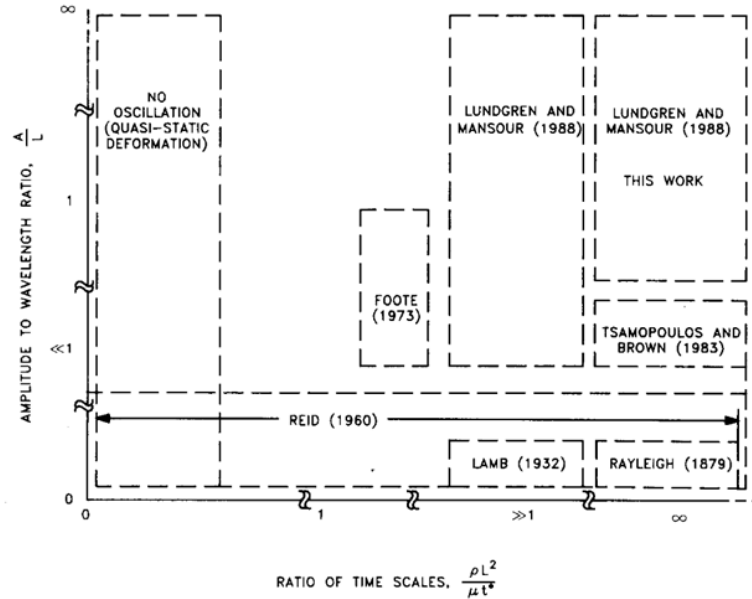


Figure 1.26: Summary of work on free, vibrated drops depending on the ratio of the interface deformation A to a length scale proportional to the drop radius L and the ratio of time scales: small-amplitude oscillations $A/L \rightarrow 0$; moderate-amplitude oscillations $A/L \ll 1$; large-amplitude oscillations $A/L \approx O(1)$ (from [101]).

Prosperetti (1980) also considered the impact of viscosity for a liquid drop submitted to small-amplitude oscillations in a vacuum. For small viscosities, damping constants were well estimated. However, they were overpredicted for large viscosities. Above a critical viscosity of the drop, no oscillations were found to occur. The drop relaxed to an equilibrium shape (overdamped system) [102].

Finally, Rayleigh's work on free drops was also extended to free, levitated drops undergoing small-amplitude oscillations but where gravity cannot be neglected. In this configuration, the resonance frequency cannot be calculated by eq. (1.30) as the change in drop shape due to gravitational effects must be accounted for. Perez *et al.* (2000) well predicted the lower resonance frequencies obtained under gravity by considering real drop shape. Perez *et al.* (2000) modelled the drop as a harmonic oscillator, with nonlinear behavior. Hysteresis was observed above a critical forcing amplitude. This critical amplitude was increased for higher drop viscosities [103]. As mentioned above, nonlinear effects had already been observed for drops submitted to moderate or large amplitudes.

3.1.3. Extension to liquid-liquid systems

3.1.3.1. *The Lamb theory*

Lamb (1932) generalised the Rayleigh theory by calculating the eigenpulsation of an inviscid drop oscillating with small amplitudes in a surrounding inviscid fluid rather than in a vacuum. Lamb found the same scaling law between the eigenfrequency f_{Lamb} and drop diameter D_d :

$$f_{Lamb} = \frac{1}{2\pi} \sqrt{\frac{8(n-1)n(n+1)(n+2)\gamma}{(\rho_{dp}(n+1) + \rho_{cp}n)D_d^3}} \quad (1.31)$$

with n the mode number, ρ_{dp} , ρ_{cp} the densities of the dispersed and continuous phases, respectively and γ the interfacial tension.

An increase in the drop viscosity reduces the oscillation amplitude in time (damping is modified) but hardly affects the value of the resonance frequency. Lamb also extended the Rayleigh theory to include viscous effects for a drop in air or for a bubble in an outer viscous liquid [104].

Valentine, Sather and Heideger (1965) performed experimental work to compare to Lamb's theory. Errors were of 35% for the resonance frequency and the decay factor was 5 to 7 times higher in predictions compared to experiments. Errors were attributed to the fact that various hypotheses were made for the calculations which were inaccurate in the real experimental conditions. These included neglecting viscosity, the assumption of irrotational flow and the consideration of small-amplitude oscillations [105].

3.1.3.2. *Extensions of the Lamb theory*

Miller and Scriven (1968) extended Lamb's work to consider viscous effects of both phases (not only one phase). They gave expressions to be solved numerically to obtain oscillation frequencies and decay factors, for both free and inextensible interfaces. For low viscosities or for inviscid fluids, their results agreed with those of Lamb [106]. We note that Prosperetti (1980) obtained an order of magnitude difference in decay factors compared to those of Miller and Scriven (1968), due to an error in the equations of Miller and Scriven, which other authors have equally reported [102].

Lu and Apfel (1991) also investigated interfacial properties (interfacial tension, Gibbs elasticity, dilatational and shear viscosities) for a liquid-liquid system with low viscosities and with gravity being neglected. Damping constants and oscillation frequencies were well predicted. They responses are complex depending on the different combined properties [107]. Miller and Scriven (1968) showed that the damping rate was not significantly affected for an inextensible interface compared to a free interface if both fluids had low viscosities. However if one of the two phases was a gas, damping rates increased for an inextensible interface compared to a free interface [106].

Basaran, Scott and Byers (1989) confirmed that the low viscosity approximation given by Miller and Scriven (1968) was accurate for low fluid viscosities (both having the same order of magnitude). The high viscosity approximation was accurate for high viscosities (both having the same order of magnitude). However, for a significantly larger continuous phase viscosity compared to the drop viscosity and for large drops, significant errors occurred. The relative flow between the phases must be taken into account in the latter case. The authors numerically solved the dispersion equation rather than using approximations to improve the agreement between theory and experiments. They concluded that errors observed in previous studies were induced by finite-amplitude oscillations, surface tension gradients and variation of physico-chemical properties (densities, viscosities) [108].

Prosperetti (1980) numerically investigated the damping rates and resonance frequencies of liquid drops in an immiscible liquid phase depending on both phase densities and viscosities. The damping rate and resonance frequency decreased as the outer phase density increased in comparison with the inner phase density. The effect of phase viscosities on the damping rate was a complex response depending on the density ratio of the two phases. The resonance frequency decreased as the drop viscosity increased or as the surrounding phase viscosity increased. The extent depended on the density ratio of the two phases. For example, the effect of the viscosity of the inner phase was hardly significant if the outer phase had a density an order of magnitude higher than the inner phase. Results were in accordance with experimental data for initial oscillations but not final oscillations. Decay rates were well estimated in certain conditions but were twice lower in other conditions, which was not satisfactory [102].

Lamb's theory was also extended to large-amplitude oscillations. Trinh and Wang (1982) experimentally investigated a liquid drop inside an immiscible liquid phase. The resonance frequency decreased as the forcing amplitude increased, which demonstrates soft nonlinear behavior, as was previously found for a free drop undergoing moderate or high amplitude oscillations [99]. Internal circulations in the drop were observed with dye (fig. 1.27). For high amplitudes, new patterns appeared, with the appearance of rotational movements (fig. 1.27(b)). These instabilities were either due to an extra running wave mode or to experimental difficulties. Finally, if the amplitude was sufficiently high, drop splitting could occur (for an acoustic wavelength in the order of the drop diameter). It is noted that Lamb's theory was confirmed for small-amplitude oscillations [109].

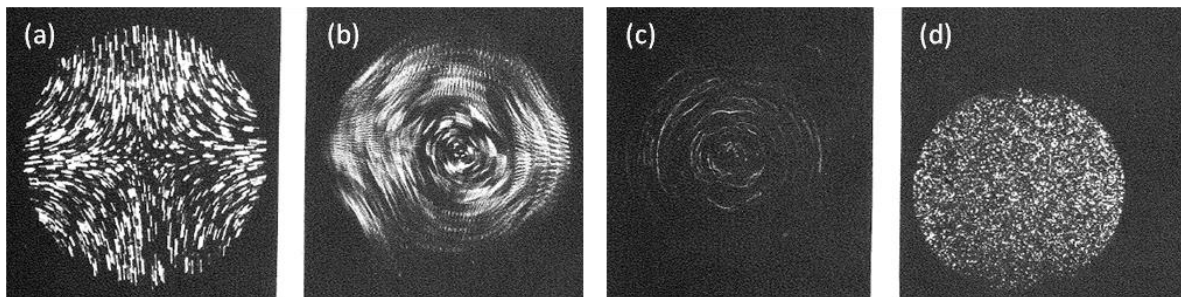


Figure 1.27: Internal flow patterns: (a) oscillating drop in mode $n = 2$; (b) rotating-oscillating drop; (c) rotating drop after drive is stopped; (d) still drop (from [109], modified).

Trinh, Thiessen and Holt (1998) also experimentally considered the impact of large-amplitude oscillations. They observed mode coupling. Subharmonic excitation was more efficient than the high mode oscillation due to the higher viscous damping of the latter [110].

3.2. Partially bound drop under small-amplitude forcing

As seen in 3.1, the free drop has been extensively studied, with the initial work of Lord Rayleigh (1879) having been extended in many ways, *e.g.* to account for the impact of viscosity, density, gravity, moderate- or large-amplitude oscillations. However, in transversally vibrating ME, the vibrating drop is not free but is partially bound to the pore at the membrane surface before detachment. Therefore, this section focuses on the behavior of bound drops submitted to vibration.

3.2.1. Impact of the surface on drop resonance

Without vibration, a partially bound liquid drop in an immiscible outer liquid already presents differences with a free drop. It is not spherical as is the free drop, but has a distorted, elongated shape due to the effects of buoyancy combined with the effects of the asymmetrical binding of the drop. The larger the drop, the larger the drop deformation at rest [111].

With vibration, similarly to the free drop, when the forcing frequency applied to the bound drop coincides with a resonance frequency in a given mode, the drop vibrates in that mode. Abi Chebel, Risso and Masbernat (2011) studied a rising heptane drop through a capillary tube into water, submitted to small-amplitude oscillations. For modes $n = 2$ to $n = 5$, for large drops, drop dynamics at resonance were similar to those of a free drop, especially if a neck was formed. Drop deformation, thus the observed shape, was slightly different compared to the free drop to adapt to the constraint imposed by the capillary tube which supports the drop. Drop dynamics for small drops were on the other hand very different from those of the free drop [111].

Strani and Sabetta (1984) mathematically investigated bound drop linear oscillations inside an outer immiscible fluid, with the drop attached to a support being a spherical bowl, under inviscid and zero-gravity assumptions. The presence of the support increased the resonance frequencies at a set wavenumber for modes $n \geq 2$, depending on the bowl dimensions [112]. Abi Chebel, Risso and Masbernat (2011) found no impact of the presence of the support (capillary tube) on resonance frequencies [111], which was in accordance with the results of Strani and Sabetta (1984) given the capillary tube dimensions [112], but not with those of Bostwick and Steen (2009) [113].

Indeed, the type of drop binding (spherical bowl in the case of Strani and Sabetta (1984) or ring in the work of Bostwick and Steen (2009)) can affect the shape mode resonances [111]. Vejrazka *et al.* (2013, 2014) experimentally studied pendant water drops in air from a ring or capillary tube and compared their results to those of Strani and Sabetta and Bostwick and Steen. For small support to drop diameter ratios, the frequency response and damping rate of an

oscillating drop is independent of the constraint (bowl or ring). Differences in the frequency response or damping rate are observed between the models of Strani and Sabetta and Bostwick and Steen for high attachment angles (above 25 to 30°) or for high resonance modes ($n \geq 3$) at moderate attachment angles (above 15 to 20°) (fig. 1.28) [114,115].

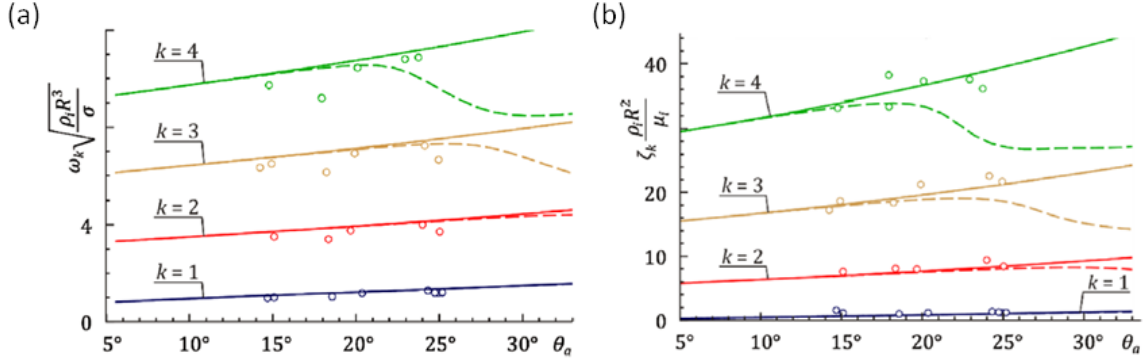


Figure 1.28: Experimental points for (a) eigenfrequency in mode k ; (b) damping rate, for different attachment angles θ_a on a tube compared to the models of Strani and Sabetta (1984) (solid lines) and Bostwick and Steen (2009) (dashed lines) (from [115], modified).

3.2.2. An additional resonance mode: mode 1

For drops which are not free but partially bound to a surface, Rodot *et al.* (1979) and Bisch *et al.* (1982) performed pioneering experimental work. A drop was submitted to small-amplitude vibrations in a surrounding fluid of the same density, to simulate microgravity. The drop was partially bound to a solid support, with its contact line pinned to the rod edge. The support diameter was smaller than the drop diameter (ratios of drop to support diameter above 1.3 were investigated) [116,117]. The first four vibration modes obtained with their characteristic shapes are represented in fig. 1.29.

Strani and Sabetta's (1984) mathematical calculations were applied to the experimental work described above, with the support being a spherical bowl. This enabled them to test various support angles (equivalent to a ratio between the support and drop diameter). An additional low-frequency mode appears compared to the classical modes exposed for the free drop. This is the $n = 1$ mode, which occurs with a displacement of the bound drop centre of mass [112].

This first mode resonance was observed by Bisch *et al.* (1982), as can be seen in the first image on the left in fig. 1.29. At the uppermost and lowermost position of the support, the drop resonating in mode 1 takes on shapes of an ellipsoid of revolution, alternating between oblate and prolate forms, respectively.

This additional, translation resonance mode was also observed by Abi Chebel, Risso and Masbernat (2011) when the support was not a solid surface nor spherical bowl but a capillary tube (open support) [111] as well as by Vejrazka *et al.* for a pendant water drop from a ring or capillary tube [114,115].

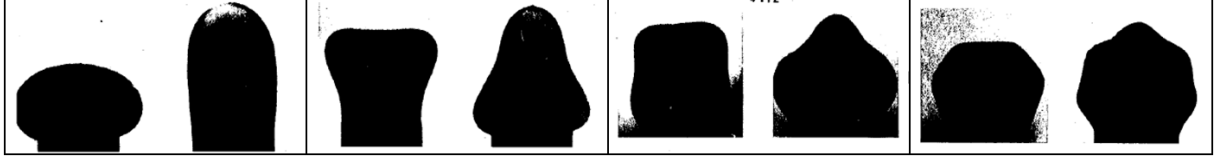


Figure 1.29: First four resonance modes for a partially bound drop. From left to right: mode 1 (1 Hz), mode 2 (2.5 Hz), mode 3 (4 Hz), mode 4 (5.9 Hz) (from [117], modified).

3.2.3. Models for mode 1

Bisch *et al.* (1982) studied mode 1 resonance for a large range of liquid couples and proposed an empirical formula to estimate the first mode resonance frequency:

$$f_{Bisch} = \frac{1}{2\pi} \sqrt{\frac{6k\gamma}{\pi\rho_{dp}} \frac{\sqrt{D_p}}{D_d^2}} \quad (1.32)$$

with ρ_{dp} the dispersed phase density, γ the interfacial tension, D_p the support diameter, D_d the drop diameter and k a “constant” equal to 9 for fluids of equal densities. The constant should vary depending on the fluid density ratio.

From eq. (1.32), we see that the first mode resonance frequency scales as D_d^{-2} and not as $D_d^{-3/2}$ such as was established for the free drop, by Lord Rayleigh (1879) or Lamb (1932). However, for high drop to support diameter ratios, the drop behaves similarly to a free drop and the previous scaling law is obtained [117].

Strani and Sabetta approximated the mode 1 eigenfrequency over intervals by D_d^α with α between -2.9 and -1.75 for drop to support diameter ratios of 1.3 to 7, respectively. This is in accordance with $\alpha = 2$ of Bisch *et al.* illustrated in eq. (1.32) [112].

The eigenfrequency f_{Strani} calculated by Strani and Sabetta (1984) is given by:

$$f_{Strani} = \frac{1}{2\pi} \sqrt{\frac{8\gamma}{D_d^3 \rho_{dp} \lambda_1}} \quad (1.33)$$

with ρ_{dp} the dispersed phase density, γ the interfacial tension, D_d the drop diameter and λ_1 the eigenvalue corresponding to mode 1, which is function of the support angle and density ratio. Smithwick and Boulet (1989) described the method to calculate the eigenvalue in the appendix of their work. Their calculations and experiments were in accordance with Strani and Sabetta’s work for support angles up to 130° . For vibrated mercury drops (pinned contact line) on a solid surface, a maximum error of 3.3% was obtained compared to experimental results [118].

We note that for the $n = 1$ mode, eigenfrequencies and damping rates are unchanged for a model of a drop attached either to a spherical bowl (Strani and Sabetta (1984)) or to a ring (Bostwick and Steen (2009)). In addition, the models established for both types of binding well predict the experimental eigenfrequencies and damping rates of pendant drops attached to a capillary tube or ring (with a small correction to account for viscosity in the calculation of eigenfrequencies) (fig. 1.28) [114,115].

Returning to Strani and Sabetta's model, it was in good agreement with the results of Bisch *et al.*, but resonance frequencies were overpredicted by 20%. By taking into account viscous effects, the differences were reduced to 10% [119]. However, both the inviscid and viscous models largely overpredicted resonance frequencies for large support angles (support to drop diameter ratio), due to nonlinear effects [112,119].

Bisch *et al.* (1982) also estimated the damping rate as a function of the kinematic viscosities of both phases, however to a limited range of liquid couples [117]. Strani and Sabetta (1988) mathematically calculated damping constants and compared them to available experimental results, which were performed among others for different viscosity ratios or different support angles. Calculations were satisfactory, at least for low support angles [119].

3.2.4. Extent of the centre-of-mass motion

As was described above, mode 1 resonance corresponds to a centre-of-mass motion mode. The extent of displacement of the drop centre of mass depends on the excitation parameters, fluid viscosity and contact line pinning.

An oscillating drop has sometimes been assimilated to a harmonic oscillator. Thus, the drop centre-of-mass motion can be described by a second order differential equation. It will therefore essentially depend on drop viscosity, drop eigenfrequency, *i.e.*, drop size, but also on the forcing frequency and forcing amplitude [103,111,113].

Strani and Sabetta (1984) found that when the drop to pore diameter ratio is large, the drop undergoes a zero-frequency rigid motion (no more movement of the centre of mass relatively to the support surface). A large drop to pore diameter ratio is equivalent to a contact line reducing to a single point [112].

Bostwick and Steen (2009) numerically showed that a zero- or nonzero-frequency motion depends on the position of the circle of contact. In the two limit cases where the contact line reduces to a single point (circle of contact positioned at the poles), a zero-frequency motion occurs. This is nearly the case in the first image on the left of fig. 1.30 [113].

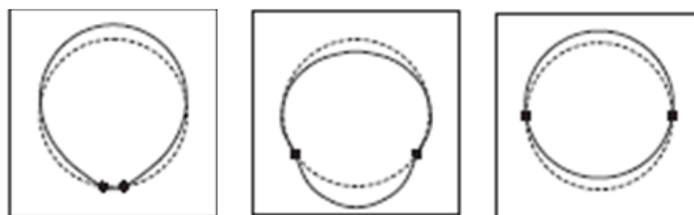


Figure 1.30: Drop shape for mode 1 resonance depending on the position of the circle of contact (points) (from [113], modified).

3.3. Partially bound drop under high-amplitude forcing

In 3.2, bound drops were submitted to small-amplitude oscillations, *i.e.*, oscillation amplitudes were small compared to the initial drop radius. In transversally vibrating ME, oscillation amplitudes may become large, for example E. Lepercq-Bost applied amplitudes in the order of the drop diameter [2]. Basaran (1992) first developed a CFD model based on the Galerkin/finite-element technique to study the behaviour of pendant viscous drops in air submitted to moderate or large-amplitude oscillations [120]. This model was used and developed in much future work, described in detail in this final section [121–124].

3.3.1. Impact on the resonance frequency

Basaran and DePaoli (1994) used Basaran's model (1992) [120] to investigate pendant drops from a rod with a pinned contact line to the rod edges. The drop was submitted to large-amplitude oscillations, in air. The oscillation frequency of the drops decreased with increasing initial deformation amplitude, as initially observed by Basaran (1992). This is also expected in comparison with a free drop model. However, for initially skinny drops, the opposite was observed. Therefore, the oscillation frequency depends on drop shape [124].

Wilkes and Basaran (1997) further investigated this work with a focus on drop resonance. They used the same model to study large-amplitude axisymmetric oscillations of a viscous bound drop on a rod, with its contact line pinned to the rod edge. They showed that the dominant mode of vibration was the $n = 1$ mode, which is the additional vibration mode for partially bound drops, as described in 3.2.2. When the forcing frequency was set at the first mode eigenfrequency, drops resonated, resulting in an increase in drop length. The maximum drop deformation observed increased with forcing amplitude and Bond number and decreased with the Ohnesorge number and mode number n . The drop resonance frequency varied slightly with amplitude at high Ohnesorge numbers but decreased significantly with amplitude at low Ohnesorge numbers. A downwards shift in the resonance frequency was also obtained as the Bond number or drop size increased [121]. Concerning the Bond number, this was only the case for hemispherical or fat drops. For skinny drops, the Bond number had an insignificant effect on the resonance frequency [124]. The downwards shift in the resonance frequency with increasing amplitude is expected with nonlinear effects.

If a drop hangs from a tube (open support) rather than a rod (solid support), drop deformation at resonance increases and the hysteresis range (range of frequencies over which the drop has two stable oscillatory states) is shifted to higher values of forcing frequency. The solid surface of the rod adds a restraining constraint. The resonance frequency is also affected by whether the support is an open tube or solid rod. The rod surface slows drop movement due to increased damping. Therefore, the oscillation frequency is reduced. However, resonance frequencies were only slightly affected [122].

Noblin *et al.* (2004) studied a sessile drop on a surface submitted to vertical vibrations. A transition from a pinned to a mobile contact line occurred above a critical forcing amplitude,

due to the contact angle variation being above the contact angle hysteresis. When the contact line was mobile (for high forcing), a decrease in resonance frequency was found [125].

3.3.2. Nonlinear drop behavior

DePaoli *et al.* (1995) experimentally investigated the behaviour of pendant drops in air submitted to high-amplitude forcing. They found that the pendant drop behaved as a soft nonlinear oscillator, as did Wilkes and Basaran (1997) later in their numerical calculations on a similar configuration. The downwards shift in resonance frequency with increasing forcing amplitude previously described in 3.3.1 illustrates this nonlinear behavior [121,126]. A drop can therefore be assimilated to a Duffing oscillator, as described by Nayfeh and Mook (1995). It corresponds to a driven oscillator whose displacement is given by a second order differential equation which includes a damping term and a cubic nonlinear term, to account for the nonlinear response of the restoring force [127].

Hysteresis in drop response was found above a critical forcing amplitude. For a set forcing frequency, the maximum drop deformation $(a/b)_m$ was higher when a downwards forcing amplitude sweep was performed (curves on the right, fig. 1.31) compared to an upwards amplitude sweep (curves on the left, fig. 1.31), the amplitude being represented on the x -axis [122]. We note that a/b corresponds to the drop length divided by the rod diameter (on which the drop is pinned). Also, the oscillation amplitude was lower when a frequency sweep was performed upwards compared to downwards, for a set forcing amplitude [122,126].

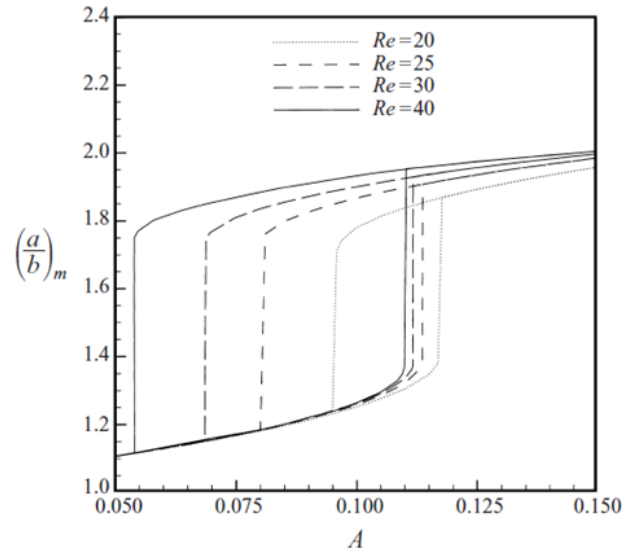


Figure 1.31: Hysteresis in drop response depending on the dimensionless amplitude A (rod oscillation amplitude divided by the rod radius R), for a dimensionless frequency (rod oscillation frequency multiplied by the capillary time $t_c = \sqrt{\rho_{dp}R^3/\gamma}$) of 3.4, for different $Re = \rho/\eta \sqrt{\gamma R/\rho} = 1/Oh$ (from [122]).

Wilkes and Basaran (1999) numerically confirmed that drops showed hysteretic responses. They delimited the region where this was the case, establishing the critical forcing amplitude necessary for the onset of hysteresis for different Ohnesorge numbers and forcing frequencies.

The critical amplitude could be as low as 3% of the support radius (with the drop and rod radii of the same order). Below a critical drop viscosity, hysteresis is no longer observed [122].

3.3.3. Drop detachment

3.3.3.1. Partially bound drop detachment from a vibrating support

Bound drops submitted to sufficiently high-amplitude oscillations can detach from their support. Wilkes and Basaran (2001) used CFD to describe pendant drop ejection from an oscillating rod, the drops having a pinned contact line to the rod edge. As the forcing amplitude increased, drop deformation increased, which accords with intuition. Above a critical forcing amplitude, the drop ruptured and a primary drop was ejected, which was a fraction of the volume of the initial drop. A critical drop length enabled drop ejection. The variations of the critical amplitude as a function of the forcing pulsation had a V-shape (the minimum corresponds to drop resonance). Furthermore, for a set rod diameter, the critical amplitude increases when Oh decreases or when the bound drop volume increases. Critical amplitudes for ejection range between 25% and 80% of the rod radius [123].

Pressure and velocity gradients inside the drop induced pinch off, corresponding to an end pinching mechanism. A diagram showing the combination of frequencies and amplitudes where ejection was permitted was established by Wilkes and Basaran (2001) (fig. 1.32) [123].

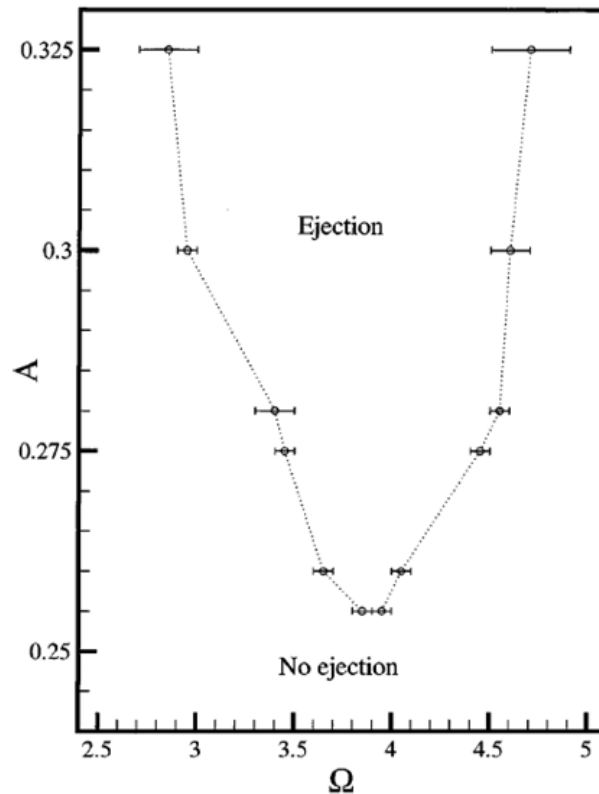


Figure 1.32: Drop ejection from an oscillating rod: dimensionless amplitude A (rod oscillation amplitude over the rod radius R) function of the dimensionless frequency Ω (rod oscillation frequency multiplied by the capillary time $t_c = \sqrt{\rho_{dp} R^3 / \gamma}$) for $1/Oh = 20$ (from [123]).

When drop viscosity was increased, a higher amplitude was needed to observe drop ejection. Also, the initial position of the rod changed the drop response. Drop ejection could or could not occur for the same vibration conditions and physico-chemical properties with simply the initial rod position which changed in the laboratory inertial frame of reference (start position either at $z = 0$ or $z = \pm A$). Indeed, this affects the dynamics of the transient response as it is equivalent to inducing a change in the oscillation phase [123].

Kim (2004) experimentally studied a pendant drop having a mobile contact line and detaching from a smooth vibrating surface (ceiling). The amplitude of vibration which led to drop detachment was minimal when the forcing frequency and resonance frequency of the drop coincided, that is when the drop resonated. Indeed, the variations of the critical amplitude (inducing drop detachment) as a function of the forcing frequency have a W-shape. The minima concord well with the $n = 1$ and $n = 2$ modes of the bound drop as calculated by Strani and Sabetta, thus they correspond to drop resonance with the support motion. The agreement between experiments and calculations of Strani and Sabetta is remarkable as the contact line mobility is different and experimental oscillation amplitudes are beyond the linear regime. In this example, the entire drop detached and not a fraction of it [128].

3.3.3.2. *Partially bound drop detachment from a liquid jet*

James, Smith and Glezer (2003) qualitatively found similar behaviour for drop ejection, though not from a solid surface but from the end of a liquid jet (broader context of atomization). They performed similar numerical work to Wilkes and Basaran (2001), which was confirmed experimentally by Vukasinovic, Smith and Glezer (2007). It was found that a single drop could be formed by pinch off of the jet, itself having been formed from a free-surface wave of a larger drop. A critical amplitude was necessary for the jet to have sufficient inertia for drop ejection. The critical amplitude increased with increasing forcing frequency [129,130], contrary to our expectations. The effect of the forcing amplitude, frequency and phase were investigated as well as the effect of gravity (Bond number) and viscosity (Reynolds number) [130].

3.3.3.3. *Drops formed from a vibrating nozzle in dripping mode*

Li *et al.* (2015) considered drops formed in dripping mode inside a microfluidic channel with co-flowing streams. A critical amplitude of vibration (function of the interfacial tension) was necessary to obtain synchronization between drop generation and the applied frequency. An increase in frequency led to a decrease in drop size, which was in accordance with equations of mass conservation [131].

Zhu, Tang and Wang (2016) studied a similar setup. Without vibration, drops formed at a natural rate of 25 Hz. With frequencies applied (pressure-induced fluctuations) below 25 Hz, drops were polydispersed. From 25 Hz to 86 Hz, monodispersed drops were formed, with the drop generation rate synchronized with the applied frequency. In this range, an increase in frequency led to a decrease in drop size, as for Li *et al.* (2015). Above 86 Hz, no further impact

on drop generation occurred. An optimum range of forcing amplitudes exists where drops are monodispersed (below, synchronization is lost and above, satellite drops appear) [75].

E. Lepercq-Bost (2008) performed experimental work on a model setup consisting in a single, axially vibrating nozzle to gain insight on transversally vibrating ME. The second liquid was stationary. Above a threshold amplitude of vibration, drops were formed in tenths of a second, resulting in significantly smaller drops (this was called the “accelerated detachment” regime). The threshold amplitude depended on the forcing frequency and drop viscosity. Higher drop viscosities implied higher threshold amplitudes necessary for accelerated detachment. Above a limit viscosity, accelerated detachment was no longer observed. The mechanisms to explain the premature detachment were however not understood [2].

3.4. Conclusions

Summary

Drop vibration has extensively been studied for a free drop since the original work of Lord Rayleigh in 1879 [96]. Since then, the work has been pursued and extended in various ways, including the impact of large-amplitude oscillations, gravity, viscous effects but also changing the system to a drop in a surrounding fluid rather than in a vacuum. These liquid-liquid system models have also been extended in various ways to consider interfacial properties, large-amplitude oscillations or viscous effects.

For all these studies, drops were free. Partially bound drops attached to a vibrating substrate have equally received attention since the 1980s. In particular, the presence of a support induces an additional low-frequency resonance mode called mode 1. This mode can be described as a centre-of-mass motion mode, the drop alternating between a prolate and oblate ellipsoid of revolution. The extent of displacement of the centre of mass depends on various parameters including the vibration parameters (frequency and amplitude), drop pinning and drop size as well as drop viscosity.

For large amplitudes of vibration, bound drops submitted to forced vibration exhibit different behavior than in the small-amplitude limit. For example, a shift in resonance frequency is observed due to nonlinear effects which intervene. For sufficiently high amplitudes, drops may even detach from the vibrating surface.

A summary of the impact of the different parameters on both the free and partially bound drops is given in table 1.3.

Aims

In transversally vibrating ME, drops may be assimilated to some extent to drops partially bound to a vibrating surface, with high amplitudes (in the order of drop size). Our experiments are based on this assumption: we study the impact of large-amplitude oscillations on a single drop formed through a nozzle. We will therefore consider and compare our results to the previous work found in this last section.

Table 1.3: Effects of various parameters on drop vibration.

Drop type	Parameter	Effect	Reference
Free drop: eigenfrequency $f_n \sim D_d^{-3/2}$ ([96,104])	Forcing amplitude	$A \uparrow \Rightarrow$ nonlinear effects $\Rightarrow f_n \downarrow$ and hysteresis	[99–101,103]
		$A \uparrow \Rightarrow$ longer time in prolate than oblate shape for mode $n = 2$	[98,100,101,103]
	Drop viscosity	$\eta_{dp} \uparrow \Rightarrow$ damping $\uparrow \Rightarrow$ drop oscillation amplitude $A_d \downarrow$ Above a critical η_{dp} , $A_d = 0$ (overdamped system)	[102,104]
		$\eta_{dp} \uparrow \Rightarrow f_n \downarrow$ (depending on ρ_{dp}/ρ_{cp})	[102]
	Gravity effects	Gravity effects $\Rightarrow f_n \downarrow$	[103]
	Surface properties	Inextensible interface \Rightarrow damping \uparrow (if one of the fluids is a gas) Variation of combined surface dilatational viscosity and elasticity \Rightarrow complex response of f_n and damping	[106,107]
Bound drop: eigenfrequency $f_n \sim D_d^{-2}$ ([112,117])	Constraint (support)	Support \Rightarrow appearance of the $n = 1$ centre-of-mass motion mode	[111,112,114–117,119]
		No impact of support type (bowl, ring) on f_n or damping for $n \leq 2$ or for attachment angles below 15° for $n \geq 3$ Otherwise, $f_n \downarrow$ and damping \downarrow for a ring instead of a bowl For tube instead of a rod, $f_n \downarrow$, hysteresis range shifted to higher frequencies and drop deformation \uparrow	[112–115,122]
		Support angle $\uparrow \Rightarrow$ drop centre-of-mass motion \downarrow When contact line \sim single point, zero-frequency rigid motion	[112,113]
	Forcing amplitude	$A \uparrow \Rightarrow$ nonlinear effects $\Rightarrow f_n \downarrow$ and hysteresis	[120–122,124,126]
		$A \uparrow \Rightarrow$ drop deformation \uparrow and drop detachment above a critical A	[2,121,123,128]
		$A \uparrow \Rightarrow$ transition from pinned to mobile contact line above a threshold	[125]
	Gravity effects	$Bo \uparrow \Rightarrow$ drop deformation \uparrow and $f_n \downarrow$	[121,124]
	Drop viscosity	$\eta_{dp} \uparrow \Rightarrow$ drop deformation \downarrow and $f_n \uparrow$	[121,123]

4. Conclusions and aims of the work

Literature review summary

Emulsions are liquid-liquid systems, with a dispersed phase present in the form of drops inside a continuous, outer phase. They are generally formed by high-pressure homogenisation or rotor-stator devices. However, a novel process was developed to form emulsions in the 1990s, called membrane emulsification (ME). In this process, a dispersed phase is forced through a porous inorganic membrane, forming the drops inside a continuous, flowing phase. Various parameters affecting ME have been extensively studied, however ME has only recently been coupled with vibrations. Vibrations were found to promote drop detachment, leading to smaller drop sizes. When ME was coupled with transversal vibrations, *i.e.*, perpendicular to the membrane surface, significantly smaller drops were produced and a patent was deposited by C. Arnaud (2006) on this process [1]. Although observations on drop size decrease were made, no physical explanations or models were advanced. Also, the observations were made on one system, thus the impact of various parameters on the process were not investigated.

Much work has been performed on the breakup of liquid drops, fluid threads or jets since the pioneering work of Taylor in 1934 [82]. Various hydrodynamic instabilities are now well understood which explain fluid breakup in certain specific conditions. The rupturing of drops or fluid threads undergoing shear which deform and eventually break up have also been widely investigated. Breakup mechanisms were often attributed to simple force balance models. In ME, force or torque balance models were equally employed to model drop detachment from the membrane. Additional microscopic models such as CFD modeling or spontaneous transformation models were employed, though less frequently. For drops undergoing vibrations in ME, no satisfactory models exist to our knowledge, especially in the transversal case where no models at all have been proposed.

Extensive research has been carried out on the behavior of free drops submitted to vibrations since the original work of Lord Rayleigh in 1879 [96]. Rayleigh's work has since then been extended to account for many other effects including gravity, viscosity, large amplitudes or an outside liquid phase. Partially bound drops undergoing vibrations only received attention a century later, in the 1980s, with the original experimental work of Rodot, Bisch and Lasek [116]. The main impact of drop binding is that a new resonance mode appears, called mode 1, which is a centric-of-mass motion mode. Drop resonance in this mode was qualitatively found to assist drop detachment under high-amplitude forcing but in-depth studies have not been performed. Additionally, the principal studies on the matter are mainly numerical. We also note that studies of bound drop vibration under high-amplitude forcing often limit themselves to

vibration without detachment, to investigate nonlinear effects and hysteresis. In the case of detachment, no models were developed to our knowledge to predict drop generation.

Goals of the work

The starting point of our work is to understand the mechanisms for drop generation in transversally vibrating ME. In this process, we consider each drop being formed as a partially bound drop on a transversally vibrating surface, submitted to high-amplitude oscillations. We therefore designed two experimental setups, described in the following chapter (chapter 2), with the CAD representations of the setups shown in Appendix 2. These setups enable the formation of a single drop (with or without cross-flow) which can be submitted to high-amplitude axial vibrations. The drops are in the order of the millimeter to be able to observe and analyze drop formation. From these experiments, mechanisms for drop detachment and a model will be proposed, both which are currently lacking in the literature. In addition to focusing on ME, this work generally brings further understanding to the behavior of bound drops submitted to high-amplitude axial oscillations.

The work was therefore separated into different parts, each enabling to deepen understanding on the subject:

- The first part, described in chapter 3, aims at understanding the physical mechanisms involved in drop detachment when drops are submitted to large-amplitude, axial oscillations. Although in the literature resonance was said to assist drop detachment, no in-depth experimental studies exist and no satisfactory models have been developed. We will study this experimentally in a simple configuration, without cross-flow. We will concentrate on why smaller, monodispersed drops are produced in certain operating conditions (which we called the stretching mode). A simple model will be proposed to account for this stretching mode.
- The second part, detailed in chapter 4 with supplementary results in Appendix 3, concerns the impact of various parameters on drop formation in the stretching mode, which was characterized in the first part. The parameters considered are the pore diameter, interfacial tension, dispersed and continuous phase velocities and both phase viscosities. We will especially focus on the impact of vibration (forcing frequency and amplitude), which is most lacking in the literature. Again, the configuration is simplified with the absence of cross-flow. From this parametric study, a more precise model will be proposed to be able to predict drop detachment depending on the various parameters set. Both drop size and threshold amplitudes for the stretching mode will be accounted for.

- The last part concerns a more complex setup, where cross-flow is applied in addition to vibration. Drop generation will firstly be observed without vibration (in analogy to simple cross-flow ME), reported in chapter 5 and compared to results found in the literature. Then, drop generation will be observed with vibration, the objective being a better understanding of the impact of cross-flow coupled with axial vibration as is the case in transversally vibrating ME (described in Appendix 4). To extend this work, the transition from dripping to jetting will be investigated, exposed in chapter 5. The impact of vibration on jetting will also be analysed, which, in this configuration, has not been described before in the literature to our knowledge. As this study is not complete, it is described in Appendix 5
- We note that in Appendix 6, we describe our interpretation of the initial results of C. Arnaud and E. Lepercq-Bost on an industrial transversally vibrating membrane, taking into account all the knowledge gained from this work.

Chapter 2: Materials and methods

1. Single drop formation setup without continuous phase flow

First, a single-pore vibrating setup was designed to observe single drop formation in a liquid-liquid system, with a stationary outer phase (fig. 2.1). We note that the CAD representation of this setup is shown in Appendix 2. This setup is used for obtaining the results of chapters 3 and 4 and Appendix 3, however it is described and characterized here in more detail. The single drop, formed through a capillary tube, undergoes forced, axial vibrations, without cross-flow. This allows us to see the impact of axial vibrations on drop formation to gain understanding and model what occurs in a single pore of transversally vibrating ME, keeping in mind the simplified configuration.

1.1. Experimental setup

1.1.1. Setup description

The setup is made up of a PVC tank in which 70 mL of stationary aqueous phase is poured (fig. 2.1(a)). Inside the tank, a single, glass capillary tube is placed (fig. 2.1(b)), with an inner pore diameter D_p , measured by the method of 3.2.1. The capillary is moulded onto a resin disc, which itself is screwed firmly onto the central part of the setup with two emerging screws (fig. 2.1(c)). During moulding, care is taken to avoid resin from entering the pore.



Figure 2.1: Photograph of the single drop formation setup: (a) continuous phase; (b) capillary tube; (c) screw; (d) syringe; (e) syringe pump; (f) vibrating exciter; (g) laser sensor; (h) anti-vibration table (i) light source; (j) macro lens mounted on high speed camera.

The dispersed phase is forced through the capillary at a constant flow rate q , achieved with a 12 mL plastic syringe (fig. 2.1(d)) filled with the dispersed phase and fixed on a syringe pump

(R-99, Razel Instruments or PHD ULTRA, Harvard Apparatus, depending on the trials (see 3.2.2)) (fig. 2.1(e)). The dispersed phase flows from the syringe through a flexible, plastic tube into the capillary, forming single drops sequentially into the continuous phase.

We compared the data obtained from the flexible plastic tube to that obtained from a rigid metal tube. The absolute relative differences were calculated on the data fit as results were only performed once for the rigid tube. We obtain differences of 2 to 6 % for drop size and 1 to 9 % for the threshold values (amplitudes). This is in the order of experimental uncertainty (1 to 7% for drop size and 2 to 10% for threshold amplitudes). Experimental results obtained with a rigid metal tube were thus not significantly different from those obtained with flexible plastic tubing. Therefore, the flexible tube was maintained for practical purposes.

The capillary on the resin disc is fixed on the central part of the setup, which itself is fixed onto a vibrating exciter (type 4810, Brüel & Kjaer) (fig. 2.1 (f)). The central part, thus the capillary, is driven with a sinusoidal motion x_{cap} function of time t : $x_{cap} = A \sin(2\pi ft)$. A is the amplitude of vibration, measured with a laser sensor (M5L/2, Bullier Automation) (fig. 2.1(g)) with a precision in the order of 10 μm (see 1.1.2). The light spot of the laser sensor is focused on the painted screw (fig. 2.1(c)) which emerges from the setup, as a white mat surface is needed for measurement. The screw is fixed firmly on the central part on which the capillary is attached, hence the signal measured from the screw movement corresponds to the capillary movement. The signal is retrieved from the laser sensor using an oscilloscope (FI 3104, Française d'Instrumentation). f is the forcing frequency, set on the signal generator (33512B Arbitrary Waveform Generator, Agilent), which creates the signal sent to the vibrating exciter. In addition to the frequency set, a tension is set, which is related to the amplitude of vibration (see 1.1.3). The signal is amplified with a power amplifier (type 2706, Brüel & Kjaer). The vibrations induced are parallel to the nozzle axis. Consequently, drops oscillate axially. We observe that the continuous phase at the top of the tank is accelerated by the exciter, as shown by Faraday waves at the free surface.

The resulting excitation force is:

$$F_{exc} = (\rho_{cp} - \rho_{dp}) \frac{\pi}{6} D_d^3 a_{cap} \quad (2.1)$$

with $a_{cap} = A \omega^2 \sin(\omega t + \pi)$ the nozzle acceleration in the laboratory inertial frame and $\omega = 2\pi f$ the forcing pulsation, f being the forcing frequency. ρ_{cp} and ρ_{dp} are the continuous and dispersed phase densities, respectively and D_d is the drop diameter. The vibrating exciter is placed on an anti-vibration table (fig. 2.1(h)), in order to maximally isolate the setup from any external vibrations.

In between upper part of the setup (tank) and the bottom part of the setup, a flexible, rubber seal is placed in order to make the setup water-tight. The seal is flexible so that the movement of the central part of the setup, on which the capillary is fixed, can freely undergo the vibrating motion induced by the vibrating exciter. This enables us to make the most of the vibrating exciter vibration range, to a certain extent (see 1.1.3.2).

A halogen cold light source (KL 2500 LCD, Schott) lights up the system (fig. 2.1(i)), with a negligible temperature increase. This is important as temperature variations affect phase viscosities, which can affect drop formation as seen previously in the literature review in 1.3.3.3. Images are then captured using a high-speed camera (Phantom v310) mounted with a macro lens (AF Zoom-Micro Nikkor 70-180mm f/4.5-5.6D ED, Nikon) (fig. 2.1(j)). A resolution of 800×600 px² is employed. The observation and image acquisition is made possible by the two transparent windows on either side of the tank. An acquisition frequency of ten times the forcing frequency is used for drops generated when undergoing forced vibrations or 100 fps for drops formed without vibration. The camera, which is fixed on a tripod, is linked to a computer and images are recorded using the Phantom 675.2 software. The images are then analysed by the method described in 3.4 to obtain various data, notably drop size.

1.1.2. Parasite vibrations

For the setup described above, the laser sensor (M5L/2, Bullier Automation) was used to obtain the setup vibration amplitudes. The sensor was fixed on a clamp stand, with the light spot focusing on the painted screw surface and was adjusted to the middle of its measurement range for each experiment. From this method, we found an uncertainty in the order of 10 μm , by using the sensor to measure the vibration amplitudes of a calibration exciter, whose vibrating parameters are well controlled. We explain the uncertainty due to parasite vibrations: the clamp stand is on the same table as the vibrating exciter, so the sensor undergoes part of these vibrations. The resulting signal is therefore a superimposition of the real signal plus the parasite vibrations.

However, this measurement method remains more accurate than by measuring the setup vibration amplitude with the images obtained from the high speed camera, for which the uncertainty is in the order of 30 μm due to image resolution. We compared amplitudes measured by both methods at 10 Hz for various tensions fixed on the signal generator and find relative errors between both methods for the vibration amplitudes of maximum 9%.

1.1.3. Setup behaviour under vibrations

1.1.3.1. Setup vibrations

As described previously, a vibrating exciter type 4810 induces forced sinusoidal oscillations to the capillary. Before using the experimental setup, we first characterised the response (vibration amplitudes) of the setup, without continuous phase, for different signal generator tensions set (fig. 2.2) and for different forcing frequencies applied (fig. 2.3). To do so, we used the M5L/2 laser sensor (Bullier Automation) and measured the resulting displacement amplitude in triplicate each time.

The response in amplitude depending on the signal generator tension is linear for all the forcing frequencies investigated (10 Hz to 200 Hz with steps of 10 Hz). Six of the frequencies

tested are reported in fig. 2.2. For a set forcing frequency, we could thus control the vibration amplitude by varying the tension on the signal generator, by calibrating the system beforehand.

On the other hand, the setup response depending on the forcing frequency is not linear, for the different tensions investigated (0.5V to 4V, for a set amplifier gain, shown in fig. 2.3). For a set tension, as the frequency increases, the displacement amplitude increases. A maximum is reached at 50 Hz, after which the amplitude decreases with increasing frequency. The decrease is expected from the performance curves of the vibrating exciter. However the increase and peak at 50 Hz is not expected. We attribute the peak at 50 Hz to the setup resonance.

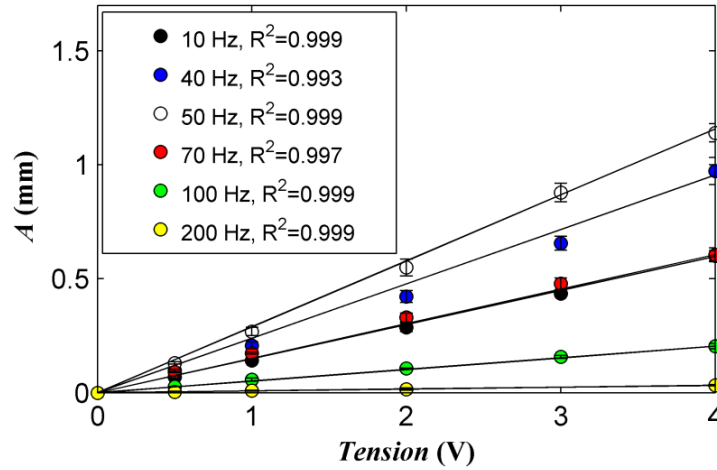


Figure 2.2: Vibration amplitude of the empty setup, depending on the signal generator tension, for different frequencies.

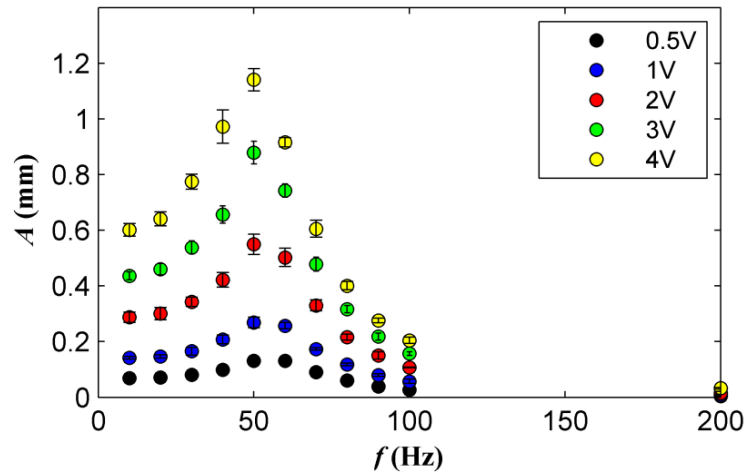


Figure 2.3: Vibration amplitude of the empty setup depending on the forcing frequency, for different tensions.

Results were reproducible, with a maximum relative standard deviation of less than 8.3% for more than 90% of the data (fig. 2.3). Standard deviations were highest for high tensions and for frequencies close to the resonance peak. For high tensions, higher amplitudes of vibration occur. A larger dispersion in measured amplitudes therefore occurs due to increased parasite

vibrations, described in 1.1.2. At resonance, vibration is not as controlled, so larger dispersion also occur. This is also visible in fig. 2.2, where standard deviations are highest for the data represented at 50 Hz, around the resonance peak.

With 70 mL water in the setup as would be the case during trials, amplitudes were not significantly changed at 10 Hz and 100 Hz compared to with an empty setup. A maximum 15% difference in amplitude was obtained.

1.1.3.2. Impact of the rubber, flexible seal

Results were significantly impacted when the upper part of the setup was removed, that is, when the seal rigidity no longer intervened (represented by the squares in fig. 2.4). We call this configuration without the upper part the “central part” configuration, in opposition to the entire setup (represented by the circles in fig. 2.4).

At 10 Hz, amplitudes were higher with the central part compared to the entire setup by 74% and 82% for a tension of 1V and 2V, respectively. Setup vibration is thus hindered by the seal. This difference is reduced for higher forcing frequencies, for example at 100 Hz, the amplitudes were higher with the central part by 10% and 14% for a tension of 1V and 2V, respectively (fig. 2.4). The seal hinders the setup motion significantly only for low forcing frequencies.

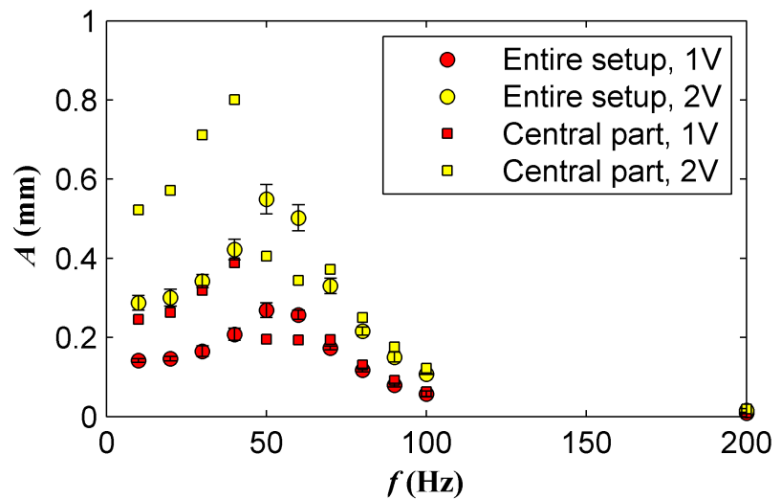


Figure 2.4: Vibration amplitude depending on the forcing frequency, for different setup configurations and tensions.

At 50 Hz and 60 Hz, vibration amplitudes were higher for the entire setup than for the central part. It seems there is a sudden drop in response amplitude at these frequencies for the central part motion, which could be explained by an anti-resonance peak.

It must be underlined that specific behaviour, *i.e.*, resonance or anti-resonance peaks, should be shifted depending on the vibrating exciter type, setup weight and design. The setup could be modified to avoid having the resonance zone in the investigation range.

1.1.3.3. Conclusions

The experimental setup response is complicated, due to the setup resonance frequency being in the trial range. Instead of attempting to calibrate or modify the setup design to control the vibration amplitudes, trials are performed with the amplitudes being unknown. The real displacement amplitudes are measured directly for each trial using the laser sensor (M5L/2, Bullier Automation). This enables to overcome the complicated setup response and to have the real amplitudes for each experimental point, bearing in mind the uncertainty.

The seal between the upper and lower part of the setup could also be adapted, for example by modifying the material type and thickness. This would reduce vibration hindering, especially for low forcing frequencies. For the purpose of our tests, sufficient amplitudes were reached to observe the phenomena we investigated. Thus the rubber seal was maintained as such.

1.1.4. Setup limitations to describe ME

Some differences must be anticipated between drop behavior in this simplified setup compared to behavior in ME. Drops are of the millimeter scale whereas in industrial ME, they are in the order of the micrometer or tens of micrometers. Also, drop interactions which could occur between drops formed at adjacent pores (described in the literature review in 1.3.3.2.) are not taken into account in this configuration, due to the presence of only one drop generated at a time. Finally, the continuous phase is stationary. As a result, we study only the impact of vibration on the drops without having an effect of the shear induced by continuous phase flow. This is the purpose of further work described in chapter 5 and Appendices 4 and 5, on the second setup described in section 2 of this chapter.

From this first simplified setup, we expect to gain insight on the impact of vibration on drop generation in transversally vibrating ME, keeping in mind that some effects have been neglected. In addition, the work performed on this setup will generally improve the understanding of partially bound drop behavior submitted to high-amplitude axial oscillations. As was seen in the last section of the literature review (3.3), the comprehension on this subject is limited and in particular, little experimental work has been performed.

1.2. Parameters investigated

1.2.1. System parameters

Oil-in-water emulsions are produced throughout our experiments. The different phases we used are detailed below and summarized in 1.2.1.4, with their physicochemical properties.

1.2.1.1. Reference system

The reference dispersed, organic phase is dodecane (99 vol%, Fisher Scientific). Dodecane is an alkane with a molecular formula $C_{12}H_{26}$ (fig. 2.5). It has a molar mass of $170.34 \text{ g}\cdot\text{mol}^{-1}$ and a density at 20°C of 0.753, according to the supplier data. Experimentally, the same density was measured (see method in 3.1.2) with a relative error of 0.5%.

The reference continuous, aqueous phase is distilled water. Its density is of 0.997 at 25°C [132]. Experimental values (see method in 3.1.2) were in accordance with the literature value with a relative error of 0.2%.

This combination of dodecane and distilled water constitutes the reference system.

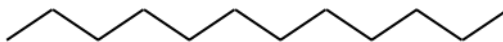


Figure 2.5: Representation of a dodecane molecule.

1.2.1.2. *Systems with varying phase viscosities*

To investigate the impact of the dispersed phase viscosity, paraffin (Fisher Scientific) is added to the dispersed phase at 25 wt% or 50 wt% (systems 3 and 4, respectively, the continuous phase being distilled water). Adding paraffin increases the dispersed phase viscosity, without significantly impacting the interfacial tension or the dispersed phase density (table 2.1). Paraffin is constituted of a mixture of alkanes, so it is made up of molecules from the same molecular group as dodecane. Paraffin and dodecane are thus easily miscible.

Glycerol (98 vol%, Fisher scientific) is added to the continuous phase at 50 wt% to study the influence of the continuous phase viscosity (system 5, with the dispersed phase being dodecane). Indeed, glycerol added to distilled water increases the continuous phase viscosity. The formula for glycerol is $C_3H_8O_3$, with three hydroxyl groups, as shown in fig. 2.6. Glycerol was chosen as it is a simple solution (no mixtures of molecules), which is miscible in the continuous, water phase. However, we must point out that the continuous phase density and system interfacial tension are impacted by the addition of glycerol (table 2.1).

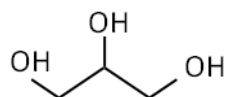


Figure 2.6: Representation of a glycerol molecule.

1.2.1.3. *Systems with varying surface tension*

When investigating the impact of surface tension on drop generation, a surfactant (SDS, 85 wt%, Acros Organics) is added to the continuous phase at 0.1 wt% or 2 wt% (systems 1 and 2, respectively, the dispersed phase being dodecane). Adding SDS leads to a decrease in the interfacial tension of the system. SDS, represented in fig. 2.7, is an anionic surfactant which has a molar mass of $288.38 \text{ g}\cdot\text{mol}^{-1}$. Its HLB value is reported to be 40 [133]. It is very hydrophilic, adapted to the generation of oil drops in an aqueous phase, as is the case in our experiments.

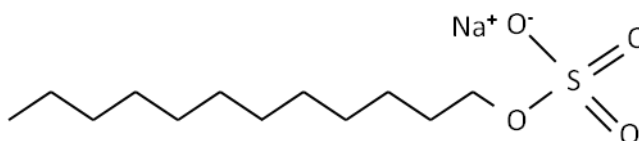


Figure 2.7: Representation of an SDS molecule.

1.2.1.4. Summary of the systems studied and properties

Table 2.1 sums up the systems tested as well as their properties. For pure solutions, *i.e.*, distilled water and dodecane, density and viscosity values were obtained from the literature. For other solutions (mixtures), densities and viscosities were measured (see 3.1.2 and 3.1.3). The interfacial tension between the continuous and dispersed phase were also determined experimentally for all the systems (see 3.1.1).

Table 2.1: Different systems investigated and their physicochemical properties.

System	Dispersed phase 'dp'	η_{dp} (mPa.s)	ρ_{dp} (kg.m ⁻³)	Continuous phase 'cp'	η_{cp} (mPa.s)	ρ_{cp} (kg.m ⁻³)	γ (mN.m ⁻¹)
Reference	Dodecane	1.34	750	Distilled water	0.89	997	50.7 ± 3.5 ^a
System 1	Dodecane	1.34	750	Distilled water & SDS (0.1 wt%)	0.89	997 ± 1.4 ^a	19.0 ± 0.6 ^{a,b}
System 2	Dodecane	1.34	750	Distilled water & SDS (2 wt%)	0.89	1001 ± 1.2 ^a	5.4 ± 0.5 ^{a,b}
System 3	Dodecane (75 wt%) & paraffin (25 wt%)	1.79 ± 0.23 ^a	772 ± 1.4 ^a	Distilled water	0.89	997	53.5 ± 2.4 ^a
System 4	Dodecane (50 wt%) & paraffin (50 wt%)	3.24 ± 0.42 ^a	790 ± 1.1 ^a	Distilled water	0.89	997	50.0 ± 1.2 ^a
System 5	Dodecane	1.34	750	Distilled water (50 wt%) & glycerol (50 wt%)	4.18 ± 0.54 ^c	1119 ± 1.3 ^a	37.0 ± 3.9 ^a
System 6	Dodecane	1.34	750	Distilled water (50 wt%) & glycerol (50 wt%) & SDS (2 wt%)	4.18 ± 0.54 ^c	1119 ± 1.3 ^a	4.3 ± 0.6 ^a

^a experimentally measured values (methods described in 3.1.1, 3.1.2 and 3.1.3)

^b experimentally measured interfacial tensions at the intermediate plateau as described in the supplementary material in section 2.9.1 of chapter 4

1.2.2. Process parameters

As was seen in 1.2.1, the impact of the physicochemical properties of the system (interfacial tension and phase viscosities) were investigated. In addition, various process parameters were studied. These include the inner pore diameter of the nozzle, the dispersed phase flow velocity and the vibration parameters (frequency and amplitude), the latter which constitute the focus of this work.

1.2.2.1. Capillary inner pore diameter

The inner pore diameter of the capillary tube D_p was measured by the method described in 3.2.1. For this first experimental setup, pore sizes of $D_p = 0.11$ mm, 0.32 mm, 0.35 mm and 0.75 mm were investigated. The reference pore diameter was $D_p = 0.32$ mm as this is the diameter for which the phenomena we studied were most observable and repeatable. Hence, when investigating the impact of phase viscosities or for system 1, trials were only performed on this pore diameter.

1.2.2.2. Dispersed phase flow rate

Different dispersed phase flow velocities were investigated depending on the pore diameter. The flow rates investigated ranged from $q = 1.2 \mu\text{L}\cdot\text{s}^{-1}$ to $19.1 \mu\text{L}\cdot\text{s}^{-1}$. For almost each pore diameter and system, two dispersed phase flow rates at least were tested, one being approximately double the other. These results are reported specifically in Appendix 3.

We underline that the flow in the capillary is always laminar. The associated Reynolds numbers for the different flow rates range from $\text{Re}_{\text{cap}} = 3$ to 33. Re_{cap} is the Reynolds number inside the capillary tube, defined by $\text{Re}_{\text{cap}} = \rho_{dp} v_{dp} D_p / \eta_{dp}$, with $v_{dp} = 4q / (\pi D_p^2)$ being the mean dispersed phase velocity in the nozzle.

1.2.2.3. Vibration parameters

For each set of parameters investigated (system and process parameters), experiments were performed for different forcing frequencies and amplitudes of vibration. Forcing frequencies tested ranged from 30 Hz to 150 Hz, with amplitudes being swept between 0 mm and 1 mm at most for each frequency. The maximum amplitude tested was often less than 1 mm due to the vibrating exciter limitations. Indeed, the maximum amplitude which can be reached depends on the frequency set (the higher the frequency, the lower the maximum reachable amplitude) due to mechanical damping.

For trials from 30 Hz to 100 Hz, intervals of 10 Hz were applied. Above 100 Hz, intervals varied depending on the pore diameter tested. The limitations of the vibrating exciter do not enable us to observe the phenomena we focus on above 150 Hz for $D_p = 0.32$ mm or 110 Hz and 120 Hz for $D_p = 0.11$ mm and $D_p = 0.75$ mm, respectively.

1.3. Experimental methods

First, the syringe and flexible, plastic tube are filled with distilled water to remove all air bubbles in the dispersed phase supply system. The setup is then filled with 70 mL of continuous phase. Afterwards, the syringe which was previously filled with distilled water is switched with a syringe filled with the dispersed phase. During the swap, care is taken to avoid the formation of any new air bubbles. We note that when the continuous phase contains the surfactant SDS, the concentration in the continuous phase is calculated to account for the 1 mL of distilled water originally in the flexible, plastic tube which will end up inside the tank. After having set up the experiment, the camera focus and light intensity are adjusted to produce a sufficiently clear, contrasted and centered image on the capillary tube. The image is saturated to simplify image analysis (see 3.4.1). The laser sensor is also adjusted to the centre of its measurement range, to be able to measure amplitudes of up to the maximum of its range (1 mm).

Once this is completed, the syringe pump is activated and experimentation begins. A trial without vibration is first performed with drop size measurement. This enables to check that the setup was adequately cleaned (see 3.3.2) and that the continuous phase is not contaminated by remaining surfactants or dust particles. It also enables to check that no air bubbles or leaks are present in the setup. Additionally, this step constitutes a control experiment, to compare with the results of drops formed with vibration.

Then, different vibration parameters are applied. The forcing frequency is set and an amplitude sweep is performed, from low to high amplitudes, by gradually increasing the tension set on the signal generator (fig. 2.2). Image acquisition is performed for each amplitude tested, taking care to have an acquisition at the threshold where the phenomena we investigate occur (at this point, drop size decreases suddenly). This protocol is repeated for each forcing frequency investigated.

The syringe pump is constantly active so as to avoid interrupting the dispersed phase flux. If the flux is stopped, the dispersed phase is retracted back towards the flexible plastic tube due to pressure fluctuations in the tube. Continuous phase is retracted into the tubing at the same time. The two phases then mix inside the reservoir which is present in the central part of the setup (between the input tube and the capillary). After this occurs, it becomes complicated to recreate a pure, uninterrupted dispersed phase flux.

Once all data has been acquired, all apparatus is switched off, the setup is emptied and filled with the cleaning agent for 24h (see 3.3).

1.4. Summary of the trials performed

Many combinations of parameters were tested to understand and model drop generation under high-amplitude axial oscillations, exposed in chapters 3 and 4 and in Appendix 3. Table 2.2 summarizes the trials performed, by reporting the different dispersed phase flow rates tested for each system and capillary inner pore diameter for which a certain range of frequencies and amplitudes were studied. For each combination, trials were carried out at least in triplicate.

Table 2.2: Summary of the parameters investigated for each system.

	$D_p = 0.11 \text{ mm}$ $f = 30 \text{ to } 110 \text{ Hz}$ $A = 0 \text{ to } \geq A_{th}$	$D_p = 0.32 \text{ mm}$ $f = 30 \text{ to } 150 \text{ Hz}$ $A = 0 \text{ to } \geq A_{th}$	$D_p = 0.35 \text{ mm}$ $f = 30 \text{ to } 150 \text{ Hz}$ $A = 0 \text{ to } \geq A_{th}$	$D_p = 0.75 \text{ mm}$ $f = 30 \text{ to } 120 \text{ Hz}$ $A = 0 \text{ to } \geq A_{th}$
Reference system ($\gamma = 50.7 \text{ mN.m}^{-1}$, $\eta_{dp} = 1.34 \text{ mPa.s}$, $\eta_{cp} = 0.89 \text{ mPa.s}$)	$q = 2.2 \text{ }\mu\text{L.s}^{-1}$, $q = 3.1 \text{ }\mu\text{L.s}^{-1}$	$q = 2.4 \text{ }\mu\text{L.s}^{-1}$, $q = 3.6 \text{ }\mu\text{L.s}^{-1}$, $q = 6.1 \text{ }\mu\text{L.s}^{-1}$, $q = 14.4 \text{ }\mu\text{L.s}^{-1}$	$q = 3.8 \text{ }\mu\text{L.s}^{-1}$, $q = 6.4 \text{ }\mu\text{L.s}^{-1}$	$q = 9.6 \text{ }\mu\text{L.s}^{-1}$
System 1 ($\gamma = 19.0 \text{ mN.m}^{-1}$)		$q = 2.4 \text{ }\mu\text{L.s}^{-1}$, $q = 3.6 \text{ }\mu\text{L.s}^{-1}$		
System 2 ($\gamma = 5.4 \text{ mN.m}^{-1}$)	$q = 1.2 \text{ }\mu\text{L.s}^{-1}$, $q = 2.3 \text{ }\mu\text{L.s}^{-1}$	$q = 1.2 \text{ }\mu\text{L.s}^{-1}$, $q = 2.4 \text{ }\mu\text{L.s}^{-1}$, $q = 3.6 \text{ }\mu\text{L.s}^{-1}$, $q = 6.1 \text{ }\mu\text{L.s}^{-1}$	$q = 3.8 \text{ }\mu\text{L.s}^{-1}$, $q = 6.4 \text{ }\mu\text{L.s}^{-1}$	$q = 9.6 \text{ }\mu\text{L.s}^{-1}$, $q = 19.1 \text{ }\mu\text{L.s}^{-1}$
System 3 ($\eta_{dp} = 1.79 \text{ mPa.s}$)		$q = 2.4 \text{ }\mu\text{L.s}^{-1}$, $q = 3.6 \text{ }\mu\text{L.s}^{-1}$		
System 4 ($\eta_{dp} = 3.24 \text{ mPa.s}$)		$q = 2.4 \text{ }\mu\text{L.s}^{-1}$, $q = 3.6 \text{ }\mu\text{L.s}^{-1}$		
System 5 ($\eta_{cp} = 4.18 \text{ mPa.s}$)		$q = 2.4 \text{ }\mu\text{L.s}^{-1}$, $q = 3.6 \text{ }\mu\text{L.s}^{-1}$		
System 6 ($\eta_{cp} = 4.18 \text{ mPa.s}$, $\gamma = 4.3 \text{ mN.m}^{-1}$)		$q = 2.4 \text{ }\mu\text{L.s}^{-1}$, $q = 3.6 \text{ }\mu\text{L.s}^{-1}$		

2. Setup with continuous phase flow

In order to further approach industrial conditions of vibrating ME and better describe drop detachment mechanisms, a new setup was designed and built to investigate the impact of continuous phase flow (fig. 2.9). Again, CAD representations of this setup are given in Appendix 2. This setup is that used to obtain the results established in chapter 5 and in Appendices 4 and 5. Again, a single drop is formed through a capillary which can undergo forced, axial vibrations. Also, continuous phase is pumped through the setup perpendicularly to the vibration. Therefore, the setup better mimics industrial conditions, with the combination of the impact of vibration and shear induced by the continuous phase cross-flow. The remaining differences are the drop size scale and the absence of drop interactions at adjacent pores.

2.1. Experimental setup

2.1.1. Setup description

The setup consists in a PVC cell (fig. 2.9(a)), with inside it a pseudo rectangular channel containing a thin, fused silica capillary tube in its centre (fig. 2.8(a)) (TSP, Photon Lines). The inner pore diameter $D_p = 0.32$ mm of the capillary was measured by the method described in 3.2.1. In order for the dispersed phase to be forced through the capillary, a microfluidic system was devised (fig. 2.8) and is described below.

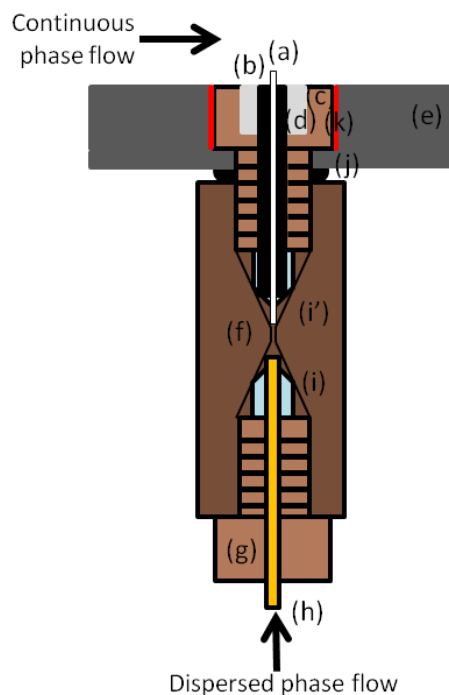


Figure 2.8: Schematic representation of the dispersed phase feeding system: (a) fused silica capillary; (b) sleeve; (c) fitting for sleeve; (d) silicon; (e) part of the bottom of the PVC cell; (f) NanoTight Union; (g) fitting; (h) PEEK tube; (i) and (i') olives; (j) rubber seal; (k) Teflon.

The capillary is placed inside a sleeve (fig. 2.8(b)) (F-243, Cluzeau Info Labo) for support, as the sleeve is more rigid than the capillary. The sleeve and capillary are then placed inside a

fitting (fig. 2.8(c)) (F-333NX, Cluzeau Info Labo). The empty space at the top of the fitting is filled with silicon (fig. 2.8(d)) providing a flat and continuous surface compared to the bottom of the PVC cell. This avoids creating vortices in the continuous phase flow inside the channel. The fitting is positioned in a dedicated space at the bottom of the PVC cell (fig. 2.8(e)) and screwed into a NanoTight Union (fig. 2.8(f)) (P-779, Cluzeau Info Labo). On the other side of the union, a similar fitting (fig. 2.8(g)) is linked to a PEEK tube (fig. 2.8(h)) (1538, Cluzeau Info Labo). This system enables to force the dispersed phase from the PEEK tube through the capillary without leaks and with a connection which can withstand high pressures induced by high dispersed phase flow (notably in the case where jetting is investigated).

Olives (fig. 2.8(i) and (i')) are placed at the end of the fittings to make the system hermetic: the dispersed phase only flows through the PEEK and capillary tubes. A rubber seal (fig. 2.8(j)) is placed between the fitting and the bottom of the PVC cell, to avoid continuous phase leaks outwards or air leaks inwards. Teflon (fig. 2.8(k)) is also introduced in the narrow gap between the fitting in the PVC cell to avoid fluid circulation out of the desired path.

A 2.5 mL stainless steel syringe is filled with the dispersed phase and fixed on a syringe pump (PHD ULTRA, Harvard Apparatus). The dispersed phase is forced from the syringe through the rigid PEEK tube (fig. 2.9(b)) into the capillary, as described above, at a constant flow rate q (see 3.2.2). The rigidity of both the syringe and tube limit pressure fluctuations which could occur. This enables us to switch off the syringe pump between each image acquisition without the dispersed phase flux being affected.

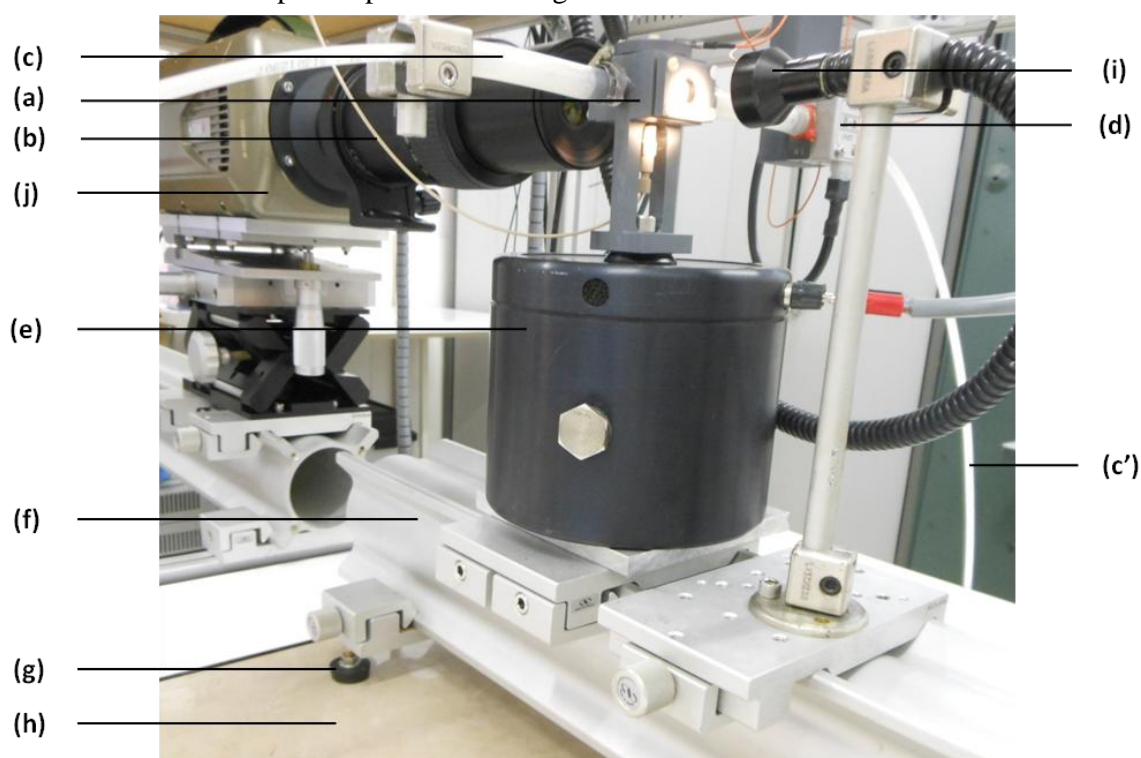


Figure 2.9: Photograph of the experimental setup with continuous phase flow: (a) PVC cell; (b) PEEK tube for dispersed phase flow; (c) and (c') plastic tubing for continuous phase flow; (d) flowmeter; (e) vibrating exciter; (f) steel profile; (g) rubber support; (h) anti-vibration table; (i) cold light source; (j) high-speed camera mounted with macro lens.

The setup cell is linked on both sides to plastic tubing, which transports the continuous phase from a container into the cell and back to the container (closed cycle) (fig. 2.9(c) and (c')). The container is closed to avoid any dust or other particles from contaminating the continuous phase, which could affect the interfacial tension. A magnetic gear pump (MDG M15T3B, Iwaki Co.) is used to pump the continuous phase from the container through the setup and back. The input tube (from the container to the setup) is placed at the bottom of the container. The output tube (from the setup to the container) spills out the fluid at the top of the container. Therefore, dispersed phase drops formed and taken away in the return flow are not recirculated and remain at the top of the continuous phase inside the container, due to differences in density.

The flow is monitored with a flowmeter (OVAL MIII LSF41, OVAL Corporation) (fig. 2.9(d)), which measures the flow rate at which the fluid is pumped through the setup. It is placed just at the exit of the setup cell. This flowmeter can measure flow rates from 2.0 to 100.0 L.h⁻¹ with water as the continuous phase. The flow rate it measures is displayed on a displayer (PAX 1, Serv' Instrumentation) which enables us to adjust the flow rate during experimentation to the desired values and maintain this rate, with a precision between 0.1 and 5% depending on the flow rate. From the flow rate, we know the fluid velocity inside the cell due to a calibration using particle image velocimetry (PIV) (see 2.1.3).

The setup cell is mounted on a vibrating exciter (type 4809, Brüel & Kjaer) (fig. 2.9(e)) which enables to induce vibrations parallel to the capillary axis. In this case, drop oscillations are distorted due to the continuous phase flow. As in the previous setup, the capillary is driven with a sinusoidal motion x_{cap} function of time t : $x_{cap} = A \sin(2\pi ft)$. A is the amplitude of vibration and f the forcing frequency. The method employed to control these vibration parameters is detailed in 2.1.2. In this setup, there is no free surface, although small air bubbles are sometimes trapped at the top of the cell.

The vibrating exciter is fixed onto a large steel profile (fig. 2.9(f)), placed on rubber supports (fig. 2.9(g)). This block is positioned on an anti-vibration table (fig. 2.9(h)). As a result, the setup is well isolated from external vibrations. The block also enables to ballast the vibrating exciter. In order to limit external vibrations from impacting the setup, all apparatus other than the light source were placed on a separate rack, which was independent of the anti-vibration table.

The same halogen cold light source (KL 2500 LCD, Schott) (fig. 2.9(i)) illuminates the system as in the previous setup. The high-speed camera (Phantom v310) is mounted with a different macro lens (Macro MP-E 65mm f/2.8, Canon) (fig. 2.9(j)) and the Phantom 675.2 software is used to capture drop generation images. These are acquired with different resolutions (ranging from 640×480 px² to 1024×512 px²) and different acquisition rates (ranging from 300 fps to 10300 fps) depending on the trials carried out. The images are then analysed by the method described in 3.4 to obtain data including drop size.

We specify that similarly to the previous setup, the cell contains two transparent windows (made of optical glass) on either side to be able to visualise the phenomena inside the channel.

2.1.2. Vibration control

We control and measure the amplitude of vibration using the following setup. A miniature CCLD accelerometer (type 4517, Brüel & Kjaer) is linked to a vibration control system (LDS LASER_{USB}, Brüel & Kjaer), which we control using the Shaker Control software. First, the accelerometer is calibrated using a calibration exciter (4294, Brüel & Kjaer). Then, the accelerometer is fixed firmly on the setup with wax. A bubble spirit level is used to ensure that the accelerometer surface is parallel to the setup. As a result, the measured amplitudes correspond to an axial displacement. The setup vibrations off axis were characterised with two accelerometers on both sides of the setup when an imposed vibration of 0.1 mm at frequencies of 50 Hz to 200 Hz was generated. The sideways vibrations were in the order of 10 µm, which corresponds to 10% of the imposed vibration. Thus we consider that the setup vibrates axially.

Once in place, a feedback loop occurs, illustrated in fig. 2.10. The desired vibration characteristics are sent from the computer software to the LDS LASER system (target signal). The LDS LASER sends the target signal to the power amplifier (type 2718, Brüel & Kjaer), which itself sends the amplified target signal to the vibrating exciter. The accelerometer fixed on the setup measures the resulting acceleration and sends the measured signal through the LDS LASER back to the computer software. The software adjusts the signal sent to the vibrating exciter. This is repeated (feedback loop) until the setup vibrates at the target signal.

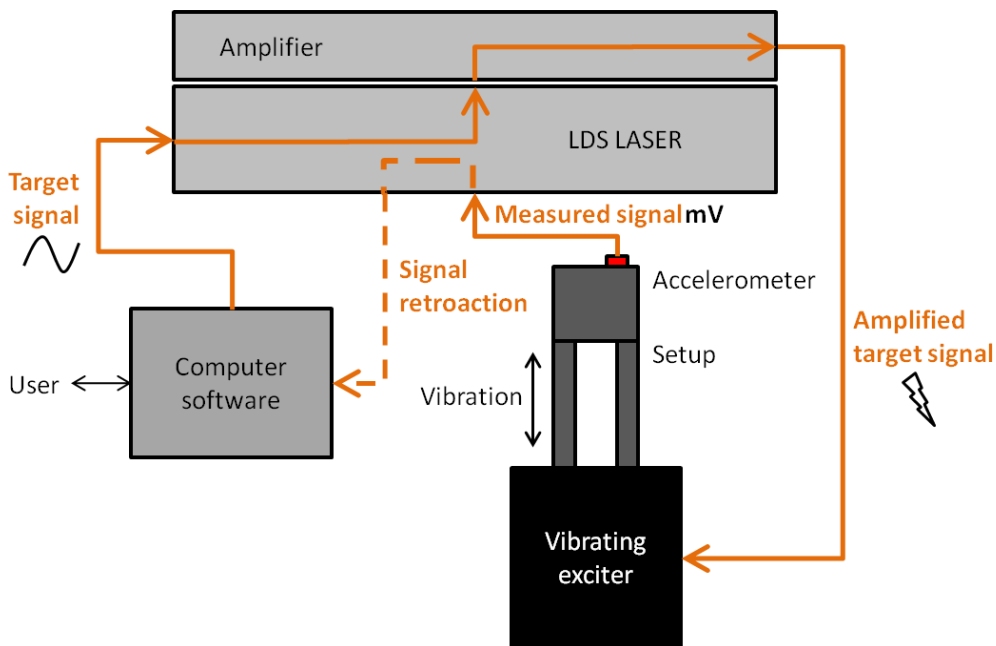


Figure 2.10: Schematic representation of the feedback loop for vibration amplitude control.

This system enables to control and to measure the setup (thus capillary) vibration amplitudes directly, accurately and in real time, avoiding any problems of parasite vibrations. Therefore, the setup with the vibrating exciter type 4809 was not characterised as was the type 4810 with the first setup, as described in 1.1.3.

In order to make the most of the vibrating exciter vibration range, the two tubes carrying the continuous phase linked to the setup cell are flexible. Therefore, the vibrating motion is not hindered. The flexible tubes are then linked to rigid tubing at equal distances from the setup, in order for the vibrations to remain symmetrical.

We also characterised parasite vibrations on the steel profile on which the vibrating exciter was fixed, for an imposed vibration of 0.1 mm at frequencies of 50 Hz to 200 Hz. The parasite vibration amplitudes were below 5 μm . Therefore, the setup is well fixed.

2.1.3. Continuous phase flow velocity inside the channel: PIV

The flow rate through the setup is known, however the setup cell channel has a complicated geometry. As a result, the fluid velocity inside the channel cannot be calculated simply from the flow rate. Therefore, particle image velocimetry (PIV) was performed to obtain the continuous phase velocity inside the channel as a function of the flow rate.

Polyamid Seeding Particles (PSP) with a mean particle diameter of 5 μm were used, which is large enough to be visualised and small enough to obtain satisfactory results when performing adaptive PIV. This particle size also has an advantage as it does not obstruct the flowmeter. These hydrophobic PSP particles were first dispersed by a magnetic stirrer into distilled water with SDS (0.5 wt%), to obtain a homogenous solution. This solution was then pumped through the setup for different flow rates to calibrate the system.

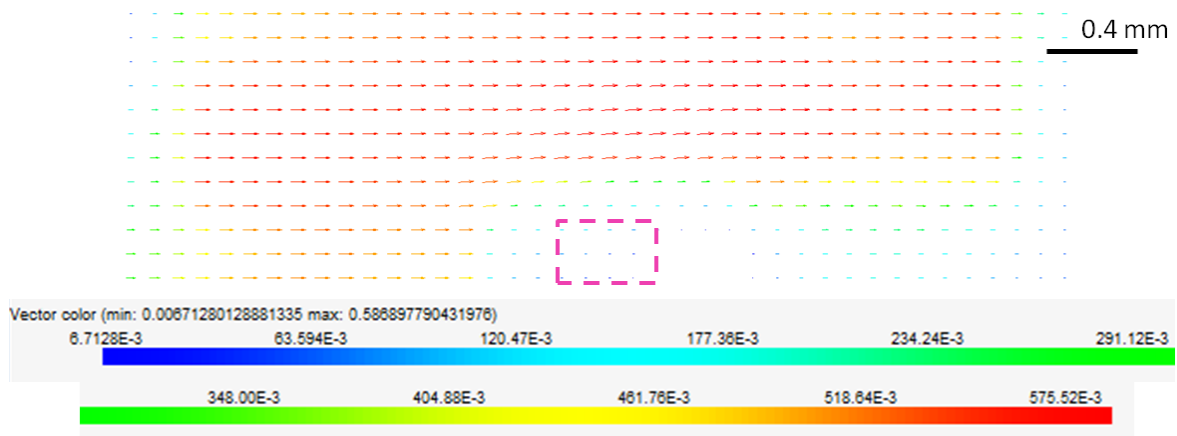


Figure 2.11: Average velocity vectors in the setup cell channel for a flowrate of 45.3 L.h⁻¹. Flow velocity scale in m.s⁻¹. Capillary outline with a dashed pink line.

The PIV software (DynamicStudio, Dantec Dynamics) was used to acquire and analyse 50 images obtained per trial (set flow rate). The same image acquisition equipment (high speed camera, macro lens and light source) was used as in the setup description. A resolution of 1280 x 400 px² was set, in single frame mode, with an acquisition frequency of 6559 Hz. Adaptive PIV was performed with a final grid step size of 16 x 16 px². The images were calibrated using the external diameter of the capillary, given by the supplier ($433 \pm 2 \mu\text{m}$). From the 50 images, an average vector plot was calculated. It represents the flow velocity profile in the channel (fig.

2.11), which corresponds to laminar flow. This was repeated in triplicate in order to have robust results, with velocities obtained used in further calculations.

Near the edges of the image (fig. 2.11), the flow seems slower than in the centre. This is due to the difference in lighting, however velocities used for calculations are those above the capillary, where lighting was uniform. The measurements were made at a distance above the capillary corresponding to the centre of a drop which would be formed for the continuous phase flow rate considered. We thus note that drop size measurements as a function of the continuous phase flow were performed before the PIV trials.

For high continuous phase flow velocities, *i.e.*, above 45.3 L.h⁻¹, bubbles appear because of the gear pump combined with the presence of surfactant in the fluid. In this case, an average vector plot was not calculated as it would underestimate the average fluid velocity (inside bubbles, a velocity of 0 m.s⁻¹ is measured). Instead, the same analysis as above was performed but on one representative image without bubbles. This was again performed in triplicate, *i.e.*, for three images, for robustness. Again, the resulting profiles indicate an overall laminar flow.

A summary of the results of the PIV calibration are illustrated in fig. 2.12. We find the following scaling law to obtain the continuous phase velocity from the set flow rate:

$$v_{cp} = 0.0278q_{cp}^{0.783} \quad (2.2)$$

with v_{cp} the continuous phase velocity (m.s⁻¹) and q_{cp} its flow rate (L.h⁻¹). We find an uncertainty of 0.00188 and 0.0180 for the coefficient and exponent, respectively (see 3.5 for calculation method).

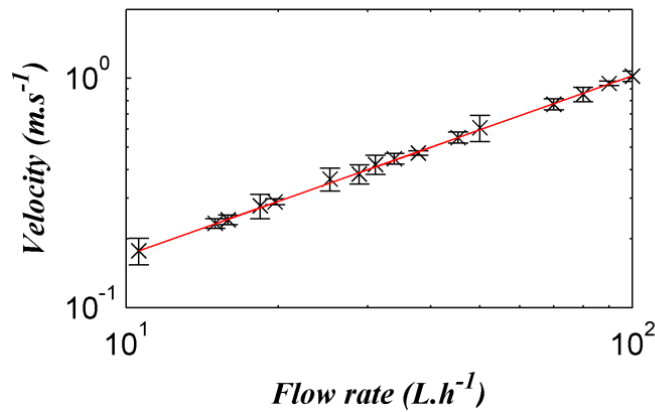


Figure 2.12: Continuous phase flow velocity in the channel as a function of the set flow rate.

2.2. Parameters investigated

2.2.1. System parameters

For this second setup, we explored the impact of the interfacial tension and dispersed phase viscosity, thus we studied the following systems, whose physicochemical properties are reported in table 2.1 in 1.2.1.4:

- A reference system, with dodecane drops formed into distilled water (see 1.2.1.1)
- Two systems with varying interfacial tensions, with SDS added at 0.1 wt% or 2 wt% to distilled water (systems 1 and 2, respectively) (see 1.2.1.3)
- Two systems with varying dispersed phase viscosities, with paraffin added at 25 wt% or 50 wt% to dodecane (systems 3 and 4, respectively) (see 1.2.1.2).

For trials with surfactant (systems 1 and 2), we prepared the setup, switched on the gear pump, left the continuous phase to flow for 5 minutes at 50 L.h^{-1} and collected some continuous phase from the container to measure its interfacial tension with dodecane, by the method described in 3.1.1. Indeed, distilled water is trapped in the tubes and cell during the rinsing stage of cleaning. This means that the continuous phase is thereafter diluted. We find surface tensions of $22.3 \text{ mN.m}^{-1} \pm 1.1$ and $6.6 \text{ mN.m}^{-1} \pm 0.4$ for systems 1 and 2, respectively.

2.2.2. Process parameters

We tested a capillary with an inner pore diameter of $D_p = 0.32 \text{ mm}$, as measured by the method described in 3.2.1. This enables to have drops large enough for observation and renders the results comparable with those from the previous setup. We did not investigate the impact of other pore diameters due to time constraints. This could be the purpose of further work, especially considering that in ME, pore sizes are in the order of the micron.

Various continuous and dispersed phase flow rates were investigated, depending on the type of trials performed. Therefore, the different values applied are detailed directly in the experimental methods section below and are summarized in table 2.3 in section 2.4.

2.3. Experimental methods

2.3.1. Protocol

The syringe is filled with the dispersed phase and attached to the PEEK tube with a stainless steel Swagelok fitting. The PEEK tube is linked to the union fitting, itself leading to the capillary (see 2.1.1). Then, the continuous phase container is filled with the continuous phase and the input and output tubes positioned in the container, at the bottom and top, respectively. Some continuous phase must be injected manually into the input tube so that the gear pump can begin to pump the continuous phase (no air in the tubes).

Once in place, the gear pump (thus continuous phase flow) is switched on. Any air bubbles remaining in the large flexible tubes on either side of the PVC cell are eliminated by pressing

the tubes. The bubbles are then carried away by the flow. We note that the setup cell must sometimes be pre-filled manually with continuous phase before switching on the gear pump in order to avoid air bubbles from being trapped at the windows of the cell.

The camera focus and light are adjusted, with the capillary positioned at the side of the image to optimize the time that the drops are visible on the screen as they are carried away with the flow. The accelerometer is fixed on the setup, ensuring it is level with the setup surface with a bubble spirit level.

Once the setup is ready, the syringe pump is activated. Different types of experiments are carried out, described below. After experimentation, the cleaning agent replaces the continuous phase in the container and is circulated through the setup for 5 min at 50 L.h⁻¹. Then, the cleaning agent is left inside the setup without circulation for 24h. Afterwards, the setup is thoroughly rinsed in an open circuit by circulating distilled water.

2.3.2. Trials with continuous phase flow only

Trials with continuous phase flow only (no vibration) are performed to obtain drop size as a function of the continuous phase flow velocity. This also enables to compare experiments between them, to check that the setup was properly cleaned each time.

These trials are carried out for the different systems described in 2.2.1, for $D_p = 0.32$ mm. The continuous phase flow velocity is set and ranges between different values depending on the system, reported in table 2.3 in the column “Cross-flow: dripping”. For all of these trials, drops are generated with a dispersed phase velocity of $v_{dp} = 0.031$ m.s⁻¹.

For the reference system, five dispersed phase flow velocities were tested in total. The four supplementary ones compared to the 0.031 m.s⁻¹ previously described are $v_{dp} = 0.016$, 0.063, 0.14 and 0.21 m.s⁻¹ (see table 2.3).

For all of these trials, the resulting drop size is measured as an average of six drops. These trials were performed at least in triplicate (on different days).

2.3.3. Trials with continuous phase flow and vibration

Similar trials were performed than in the first setup, although the impact of vibration was here combined with the impact of the continuous phase cross-flow. For these trials, a forcing frequency was set (between 140 Hz to 200 Hz, with steps of 10 Hz), at the same time as the continuous phase was flowing.

The reference system was investigated, for $D_p = 0.32$ mm. The dispersed phase velocity was set at $v_{dp} = 0.031$ m.s⁻¹ and the continuous phase flow velocity was either $v_{cp} = 0.23$ m.s⁻¹ or 0.40 m.s⁻¹. An amplitude sweep was carried out from low to high amplitudes for each frequency, the highest amplitude being 0.25 mm. The vibration amplitude was increased until the phenomena we investigate are observed. These trials were not so conclusive and the results are exposed in the Appendix 4. The summary of the tests performed are reported in table 2.3, in the column “Cross-flow with vibration: dripping to stretching”.

2.3.4. Dripping to jetting transition

The dripping to jetting transition is investigated on this setup. In the literature review (2.2.2.4.), it was seen that although some experiments have been performed, few satisfactory models exist to predict the transition in this configuration.

To do so, the continuous phase flow is set and the dispersed phase flow is gradually increased, until a continuous jet is formed. Jetting is defined when the ratio between the elongated neck length L_n and detached drop diameter D_d is above 1 ($L_n/D_d > 1$), as did Meyer and Crocker (2009) [69] or Pathak (2011) [70]. The elongated neck length is measured from the capillary surface to the base of the drop. In our case, this ratio must be verified for at least 6 consecutive drops for us to consider the jetting regime to be established.

This method is carried out for $D_p = 0.32$ mm, with continuous phase velocities which range between different values depending on the system (see table 2.3). The flowmeter could not measure higher continuous phase flow rates than 100 L.h^{-1} , *i.e.*, $v_{cp} = 1.03 \text{ m.s}^{-1}$. The dispersed phase flow velocity is increased until the transition occurs and it is of maximum $v_{dp} = 0.73 \text{ m.s}^{-1}$ due to the syringe pump limitations. The associated Reynolds numbers in the capillary tube for all the flow rates tested range from $\text{Re}_{\text{cap}} = 7.4$ to 130.4 (which corresponds to laminar flow). The summary of the tests performed are given in table 2.3 in the column “Dripping to jetting”.

2.3.5. Dripping to jetting transition with vibration

The impact of vibration on the dripping to jetting transition was also examined, although this is still at a preliminary stage. In the literature review (2.2.3.2.), it was seen that little experimental data and no models exist on vibration applied to jetting, and none to our knowledge in the current configuration which mimics ME.

The continuous phase flow rate and dispersed phase flow rate are set such that the dispersed phase forms a jet in conditions without vibration. That is, for the reference system, the continuous phase flow velocity is set at $v_{cp} = 0.23 \text{ m.s}^{-1}$ and the dispersed phase flow velocity is either $v_{dp} = 0.62 \text{ m.s}^{-1}$ or 0.66 m.s^{-1} . Then, a frequency is set (between 80 Hz and 240 Hz) and a downwards amplitude sweep is performed. The highest amplitudes were such that the maximum acceleration for each frequency reached around 200 m.s^{-1} . This is close to the limit of the vibrating exciter possibilities keeping in mind the weight of the setup. The impact on the drop diameter and the drop generation mode are investigated.

For these trials, the reference system was investigated and a few trials were performed on system 4, all for $D_p = 0.32$ mm. All trials performed are reported in table 2.3, in the column “Dripping to jetting with vibration”. Further work could be performed on this subject, with a wider range of systems or pore diameters as well as flow rates which could be investigated.

2.4. Summary of the trials performed

The different trials carried out on the second experimental setup are summarized in table 2.3, with the parameters tested given as a function of the focus of the investigation. All trials were carried out for $D_p = 0.32$ mm.

Table 2.3: Summary of the trials performed on the second setup.

	Cross-flow: dripping		Cross-flow with vibration: dripping to stretching	Dripping to jetting	Dripping to jetting with vibration
	v_{cp} (m.s ⁻¹)	v_{dp} (m.s ⁻¹)	$f = 140 - 200$ Hz $A = 0$ to $\geq A_{th}$	v_{cp} (m.s ⁻¹) (* v_{dp})	$v_{cp} = 0.23$ m.s ⁻¹
Reference system ($\gamma = 50.7$ mN.m ⁻¹ , $\eta_{dp} = 1.34$ mPa.s, $\eta_{cp} = 0.89$ mPa.s)	0.18 - 0.55	0.016, 0.031, 0.063, 0.14 and 0.21	$v_{cp} = 0.23$ or 0.40 m.s ⁻¹ $v_{dp} = 0.031$ m.s ⁻¹	0.17 - 1.03	$v_{dp} = 0.62$ or 0.66 m.s ⁻¹ $f = 80$ to 240 Hz $A = 0$ to $200/4\pi^2 f^2$
System 1 ($\gamma = 22.3$ mN.m ⁻¹)	0.11 - 0.50	0.031		0.17 - 0.59	
System 2 ($\gamma = 6.6$ mN.m ⁻¹)	0.10 - 0.40	0.031		0.17 - 0.40	
System 3 ($\eta_{dp} = 1.79$ mPa.s)	0.11 - 0.55	0.031		0.23 - 1.03	
System 4 ($\eta_{dp} = 3.24$ mPa.s)	0.10 - 0.60	0.031		0.23 - 0.94	$v_{dp} = 0.69$ m.s ⁻¹ $f = 80$ to 600 Hz $A = 0$ to $200/4\pi^2 f^2$

* For the dripping to jetting transition, v_{dp} is increased gradually from 0 m.s⁻¹ until the value where the transition is observed. It reaches up to 0.73 m.s⁻¹ at most.

3. General methods

3.1. System characterisation

3.1.1. Surface tension measurement

The dynamic interfacial tension γ was measured for all systems in triplicate using the rising drop method with a tensiometer (Tracker, I.T. Concept, Teclis). This method consists in equating the Laplace pressure with the hydrostatic pressure induced by gravity. From this, numerical shape calculation is performed and optimised until obtaining the real drop shape, giving γ . The densities of both phases must therefore be known to implement this method and were given as those measured experimentally, exposed in table 2.1.

For each system, the dynamic interfacial tension γ was measured as a function of time t for at least 30 s and plotted as a function of $1/\sqrt{t}$ (fig. 2.13), as did Serrien and Joos (1990) [134] and Deshiikan *et al.* (1998) [8]. We then used the method of Deshiikan *et al.* to estimate an intermediate plateau interfacial tension for systems with SDS, as detailed in the supplementary material in section 2.9.1 in chapter 4. The corresponding values are those reported for γ in table 2.1.

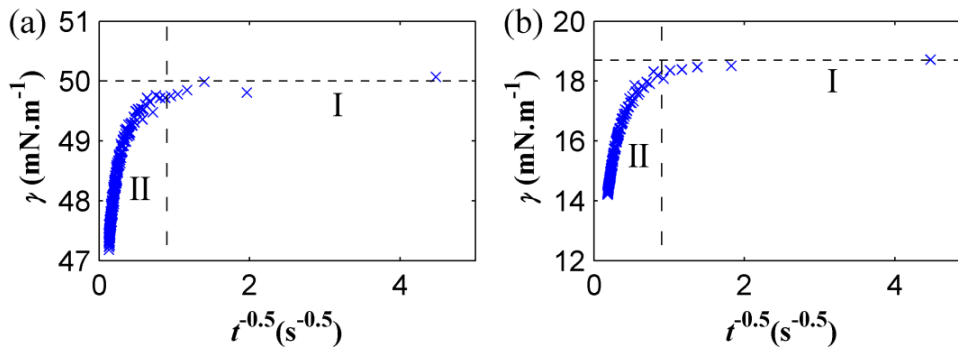


Figure 2.13: Dynamic interfacial tension as a function of $1/\sqrt{t}$, for (a) the reference system; (b) system 1. I: plateau region; II: slight decrease region.

For the reference system or systems 3, 4 and 5, we used the same method as that exposed in the supplementary material in 2.9.1 of chapter 4, even though these systems contain no surfactant. Indeed, we obtain the same type of curve for these systems than for those with SDS (fig. 2.13(a)). In this case, we infer that the initial plateau (I) gives the clean interface surface tension value and that this corresponds to our experimental value when drops form (short times). Then, there is a slight decrease region (II) before attaining the true equilibrium value at long times. We attribute this to impurities in the system, which lead to a decrease in γ . From this method, we find a clean dodecane-water interfacial tension of $50.7 \text{ mN}\cdot\text{m}^{-1} \pm 3.5$, in accordance with data reported in the literature, such as $51.2 \text{ mN}\cdot\text{m}^{-1}$ by Deshiikan *et al.* (1998) or $52 \text{ mN}\cdot\text{m}^{-1}$ by Bonfillon *et al.* (1994) [8,135]. Thus it is reasonable to use the same measurement method as for the systems with SDS. Also, it enables our results to be comparable between the systems.

The overall uncertainty was calculated by eq. (2.12) of 3.5.2. Drops were always large enough so that Bond numbers were above 0.1, which reduces errors. We estimate the maximum error due to verticality at $e = 0.4\%$ for eq. (2.14), which corresponds to 1° deviation from verticality. The maximum error due to optical deformation is $e = 1.7\%$ and that due to noise is $e = 2.7\%$, also used in eq. (2.14) (errors given by the supplier). We estimate an extra type B uncertainty $U_{B,plateau}$ which is the error when reading the plateau value. Typically, errors vary from $0.1 \text{ mN}\cdot\text{m}^{-1}$ to $0.8 \text{ mN}\cdot\text{m}^{-1}$, depending on how clear the curve is.

3.1.2. Density measurement

The density of the different solutions was measured in triplicate at room temperature. To do so, the liquid contained in a volumetric pipette of 10 mL with two marks was weighed (0.2 vol% error), using a digital scale with a 0.01 g precision. The overall uncertainty was calculated from eq. (2.12) of 3.5.2. The type B uncertainty was due to the weighing resolution, calculated from eq. (2.15) by considering that a 0.01 g precision corresponds to $1 \text{ kg}\cdot\text{m}^{-3}$ and due to the pipette precision, calculated from eq. (2.14). The results and overall maximum uncertainties are reported in table 2.1.

3.1.3. Viscosity measurement

The dynamic viscosities η of systems 3, 4 and 5 were measured in triplicate with a Ubbelohde type viscosimeter (AVS310, Schott-Geräte) at 25.1°C . The principle of this apparatus is that the time t for the liquid to pass through a known, capillary section is measured. This enables to calculate the dynamic viscosity η through Poiseuille's law by:

$$\eta = k(t - HC)\rho \quad (2.3)$$

with k the viscosimeter constant which accounts for the capillary dimensions (radius and length) given by the supplier, t the time measured by the apparatus, HC a kinetic energy correction which depends on the capillary used, also given by the supplier and ρ the system density measured experimentally as described in 3.1.2.

Type 0a capillaries were used with an inner diameter of 0.53 mm, as these capillaries are recommended for viscosity measurements from 0.8 to 5 mPa.s. This range of dynamic viscosities corresponds to those of all the systems investigated. The constant of the capillary used was $k = 0.004935$. HC is a function of t , the function being given by the supplier.

We specify that the temperature was monitored by a water bath filled with distilled water, keeping in mind that a 0.1°C error induces a maximum error of 0.6% in viscosity measurement. The systems measured were always placed in the water bath during 10 min before measurement for temperature equilibration to occur between the system and the water bath.

The overall uncertainty was calculated from eq. (2.12) of 3.5.2. Two type B uncertainties were considered: one due to a temperature error and one due to apparatus resolution. The former was calculated by eq. (2.14) considering a temperature difference of 0.1°C maximum, so $e = 0.6\%$, as given by the supplier. An error of 12.9% was considered for the error in

resolution, applied to eq. (2.15). This value was estimated by considering the error between the viscosity measurement of water compared to the data for the dynamic viscosity of water commonly reported.

3.2. Process characterisation

3.2.1. Pore size measurement

The pore size of the capillary tubes was measured accurately by optic microscopy (LSM 700 confocal microscope, Zeiss) (fig. 2.14 and fig. 2.15), to obtain the inner pore diameter D_p used in calculations throughout the work. As can be seen in fig. 2.14(a) or (c) ($D_p = 0.11$ mm or $D_p = 0.35$ mm, respectively), the pore section is circular and the diameter is easily deduced. For fig. 2.14(b) or (d)) ($D_p = 0.32$ mm or $D_p = 0.75$ mm, respectively), the pores have an oval section. The pore diameter is obtained by a geometric mean of the major and minor axes. The changes in pore section must be kept in mind as they may affect drop detachment, as was exposed for microchannel ME or in CFD models for ME. Also, the cracks observed at the surface around the pores result from the cutting of the capillary, with a diamond sawing machine (Accutom-2, Struers). These are especially present in fig. 2.14(c) or fig. 2.14(d) ($D_p = 0.35$ mm or $D_p = 0.75$ mm, respectively).

Measurements were also performed on the second setup, to check the tube inner diameter in comparison with those given by the supplier (fig. 2.15). The tube was cut with a ceramic blade, orientated at 45° . From this, we obtain a clear cut of the tube at 90° to its axis. As a result, the pore edges are smoother and the pore is more circular than for the glass capillaries cut with a diamond sawing machine. The pore opening should therefore not have an impact on drop formation for the second setup.

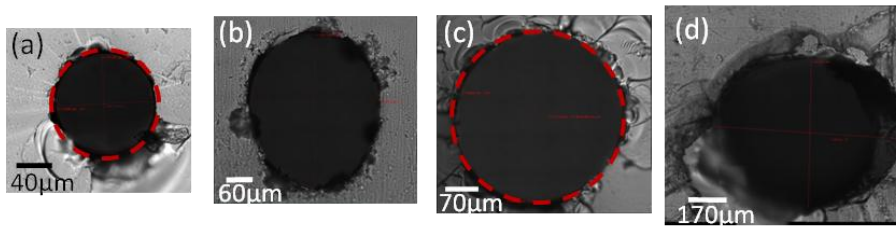


Figure 2.14: Optic microscopy images for the capillary tube pores at the surface for the first experimental setup: (a) $D_p = 0.11$ mm; (b) $D_p = 0.32$ mm; (c) $D_p = 0.35$ mm; (d) $D_p = 0.75$ mm. Circular pores circled with a dashed red line.

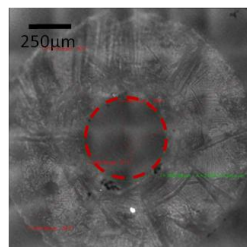


Figure 2.15: Optic microscopy image for the fused silica capillary tube pore at the surface for the second experimental setup. Pore circled with a dashed red line.

3.2.2. Dispersed phase flow control

For the first setup, the dispersed phase was fed through the tube and capillary with a syringe pump (R-99, Razel Instruments). The syringe pump was calibrated using a 12 mL plastic syringe filled with dodecane. The pump has an accuracy within 2% and a reproducibility within 0.5%.

Another syringe pump (PHD ULTRA, Harvard Apparatus) was used to study the impact of phase viscosities with the first setup of section 1 or for all experiments with the second setup of section 2. A 2.5 mL stainless steel syringe was used and entered in the syringe pump parameters, which enables to directly control the desired flow rate (no calibration necessary). This pump has an accuracy within 0.25% and a reproducibility within 0.05%.

3.3. Cleaning protocol

As was exposed in the literature review (in section 1.3.3.2.), in ME, membrane wettability is important to control drop generation. In order to form oil in water drops (as is the case presently), the surface must be hydrophilic. This avoids the oil from spreading as it exits the pore. Hence, the contact angle between water and the capillary surface must be close to 0° throughout experiments.

3.3.1. Protocol

A repeatable, cleaning protocol was designed to render the glass capillary hydrophilic before each experiment. This enables to form dodecane drops in water and allows experiments to be comparable as the surface is repeatedly cleaned to the same state. Also, due to the hydrophilic nature of the surface, the capillary outer diameter will not impact drop formation.

To design the protocol, we used glass slides to mimic our glass capillary. We spread 0.1 mL of dodecane on the glass slides, as dodecane will experimentally come into contact with the glass capillary surface. The soiled glass slides were soaked for different times in 30 mL Mucosal solution (Merz) at 3 vol % \pm 0.3%. Mucosal is an alkaline cleaning agent containing phosphates (>30 vol%), anionic surfactants (<5 vol%) and zwitterionic surfactants. The glass slides were then abundantly rinsed with distilled water and dried with a hair-dryer for one minute to avoid deposits on the surface. Afterwards, water drops were deposited on the surface and the contact angle was measured with the tensiometer (Tracker, I.T. Concept, Teclis) at room temperature. For each slide, five drops were deposited at different spots and an average contact angle was obtained. Each trial was reproduced in triplicate.

The average contact angles are illustrated in fig. 2.16. The limit detection angle of the tensiometer is of 10° . Therefore, for contact angles below 10° , we attributed a default angle of 5° . We consider that the glass surface is clean for a reproducible contact angle below 20° , as described by P. Chartier (1997) [136]. We conclude that our glass surface is clean after 24 h of immersion, as this is when the average contact angle is repeatedly below 20° .

Further trials were carried out by placing the Mucosal solution and slide on a magnetic stirrer, in order to attempt to reduce the immersion time. However, the time necessary to render

the slides hydrophilic was not reduced (it was even increased to above 24 h). Therefore, the method without stirring was maintained.

The cleaning protocol is thus to immerse the setup in 3 vol% Mucosol solution after testing for 24 h. Then, the setup is rinsed abundantly with distilled water just before experimentation.

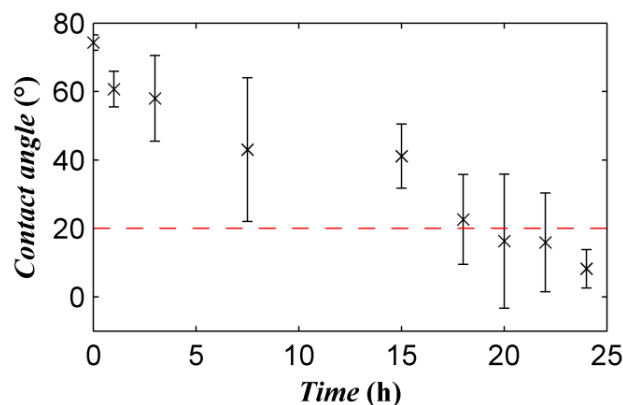


Figure 2.16: Average contact angle of a water drop on the glass slide immersed in 3 vol% Mucosol solution, for different times.

3.3.2. Verification

From the drop diameters obtained without vibration on the first setup, we calculate the *in situ* interfacial tensions by applying Tate's law as described in the literature review in 2.3.1.1 (eq. (1.28)), with the Harkins Brown correction factor. We confirm that the setup was adequately cleaned (no surfactants left) for each experiment by comparing these experimental values with those measured in a clean system and reported in table 2.1. This is described in detail in chapter 4.

By taking into consideration the measurement uncertainties, we find relative errors between the *in situ* interfacial tensions and the clean interfacial tensions mainly below 10 %. When relative errors were too high and experimental interfacial tensions were lower than expected, we considered that the setup had not been sufficiently rinsed and that the cleaning agent surfactants interfered with drop generation. We therefore did not include the results of these trials in our analysis.

3.3.3. Impact of time

We cleaned the setup with the designed protocol. Then, for the first setup described in section 1, we continuously generated dodecane drops through the pore without vibration for 30 min, with a constant dispersed phase flow rate ($4.3 \mu\text{L}\cdot\text{s}^{-1}$). Drop size formed without vibration did not vary significantly in time: a 1.4 % decrease in drop diameter was found between $t = 0$ and 30 min. We conclude that the wettability is not changed enough during setup operation to impact drop size. Thus, drops formed throughout the whole experiment can be compared.

We also verified this by making drops size measurements without vibration before and after actual experiments, which corresponds to a longer time than 30 min and drew the same conclusions.

3.4. Image analysis

3.4.1. Image adjustment

The lighting was adjusted experimentally to create an adequate contrast between the drop and the surrounding continuous phase for image analysis. The best contrast is obtained with a saturated image, as can be observed in fig. 2.17(a). An exposure of 100 μs was set on the camera software (Phantom 675.2) with an extreme dynamic range (EDR) of 0 μs to maintain the saturated image.

As can be seen from fig. 2.17, the inner pore diameter for the first setup cannot be used to set the scale as it is too small compared to the image width, which would lead to large errors. We thus use the outer pore diameter as the reference length to set the scale. This length was measured accurately by using an electronic slide gauge (0.3% precision). For the second setup of section 2, the outer capillary diameter was also used to set the scale, given by the supplier (0.9% precision).



Figure 2.17: Steps for image analysis, with images from the first setup: (a) original image; (b) binary image; (c) border filling and analysis.

In fig. 2.17(a), a black ring is apparent at the drop border, which we consider as part of the drop (included in drop size measurement). The refractive index of dodecane which forms the drop ($n_{dp} = 1.42$) is higher than that of the continuous water phase ($n_{cp} = 1.33$). Thus, light behind the drop is deviated towards its centre, leading to a black ring at the interface.

This is confirmed by the model developed and illustrated in fig. 2.18. The light beams arrive from the left, are refracted when entering the drop and exit the drop on the right, being deviated again at the drop exit. The light beams which are tangent to the drop edge continue straight, without being deviated. The double arrows show the zones where no light beams arrive at the exit of the drop (that is, in between the tangent beams and the refracted beams). These zones correspond to a shadow zone, leading to the apparent black ring.

For the two different drop sizes illustrated in fig. 2.18 (3 mm and 1 mm diameter), we experimentally measure a ring diameter of 0.3 mm and 0.1 mm, respectively. This is in accordance with the ring diameters obtained from simulations, of 0.28 mm and 0.18 mm, respectively. Therefore, it is reasonable to consider the black ring as part of the drop.

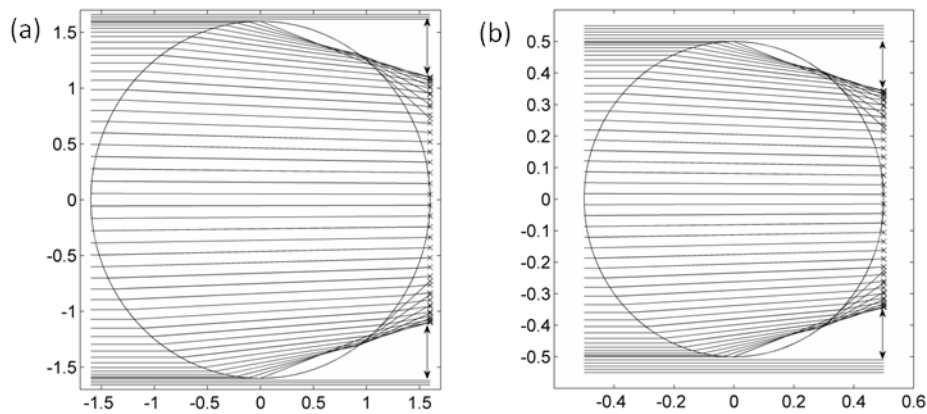


Figure 2.18: Light refraction for dodecane drops in water: (a) large drop (3 mm diameter); (b) small drop (1 mm diameter). Shadow zones (double arrows).

3.4.2. Drop dimensions analysis

Images obtained during trials were analysed using the ImageJ public domain software [137]. We obtained data including the average detached drop diameters D_d , axial drop elongations L , the position of the drop centre of mass X_d compared to the nozzle surface and the elongated neck length L_n during jetting.

On the first setup of section 1, the maximum relative standard deviations in drop diameter range from 1 to 7%. On the second setup of section 2, relative standard deviations are of on average 3.4%, 8.7% and 7.7% in dripping, jet widening and narrowing, respectively.

3.4.2.1. Detached drop diameter

The method used to measure the detached drop diameters is illustrated in fig. 2.17. The images are made binary. Then, the outlines are filled and particle size analysis is performed. The analysis is limited to objects having a circularity larger than 0.9, with the circularity defined as $O = 4\pi\bar{A}/P^2$, with \bar{A} the surface area and P the perimeter. O ranges from 0 (infinitely elongated polygon) to 1 (circle), thus 0.9 corresponds to a circular shape. A minimal size of at least 0.05 px² is also defined. Both of these criteria enable us to measure the spherical drop surface area and avoid measuring dust particles or shadows.

For a given drop, we analyze ten images to obtain an average surface area. From this, we deduce the equivalent drop diameter for one drop (we obtain the diameter from the surface area by considering that the surface area corresponds to that of a perfect circle). We repeat this method on at least five different drops for the same experimental conditions, to obtain an overall average drop diameter.

On the second setup, especially in jetting mode, drops were not always monodispersed. For these experiments, six drop sizes were measured by the method described above. However, the image contrast did not always allow this method to be used. In the case where it was impossible, drop diameters were measured manually. Three diameters were measured per drop

to obtain an average diameter, which was again done for six different drops for the same experimental conditions. This led to an overall average drop diameter.

3.4.2.2. Bound drop diameter

We use the detached drop diameter in future calculations rather than the bound drop diameter, as we saw previously that the analysis method is rather simple. In a few cases, on the first setup, we estimated the bound drop volume using the Guldinus theorem (assuming that the drop is axisymmetric) which gives the attached drop volume V :

$$V = \bar{A}2\pi r_d \quad (2.4)$$

with \bar{A} the surface area of half of the drop and r_d the distance between the axis and centre of mass of the half drop $x_{1/2}$, illustrated in fig. 2.19.

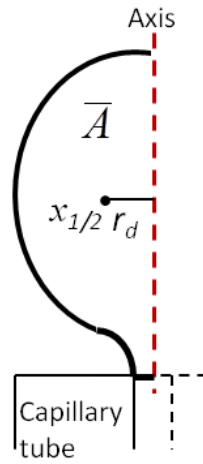


Figure 2.19: Dimensions to estimate the bound drop diameter from the Guldinus theorem. \bar{A} half drop area, $x_{1/2}$ centre of mass of the half drop, r_d distance from the axis to $x_{1/2}$.

From this, we deduced the volume-equivalent sphere diameter:

$$D_d = \left(\frac{6V}{\pi}\right)^{1/3} \quad (2.5)$$

We found a relative difference between bound and detached drop diameters of -3% to 7%. This is in the order of drop diameter uncertainty which is of maximum 7%, so it is reasonable to assimilate the diameter of the attached drop just before detachment to the detached drop diameter. Therefore, to simplify image analysis, the detached drop diameter was used through the work.

We assume that we can also estimate the bound drop diameter by the detached drop diameter on the second setup with cross-flow in the dripping mode limit. In jetting mode however, this is not possible as dispersed phase visually remains attached to the fluid neck at break off. However, only the detached drop diameter was of interest in this setup, thus the volume of fluid in the elongated neck (jet) was not estimated.

3.4.2.3. Other drop lengths

In addition to the drop diameter, other distances including the drop length L , maximum drop length L_{max} (fig. 2.21) and the elongated neck length during jetting L_n (fig. 2.21) were measured, in the case of the bound drop.

Drop length and maximum length were measured manually from the limit of the capillary surface to the tip of the drop apex for the first setup of section 1 (fig. 2.21). For each experimental condition, these lengths were measured on three different drops at the same stage of drop detachment to obtain an overall average length.

For the jetting trials on the second setup of section 2, neck length was also measured manually, from the capillary surface to the bottom limit of the drop, where the neck was attached (fig. 2.20). This was performed for the six different drops on which drop size measurement was performed, to obtain six different L_n/D_d ratios, to establish whether the drop generation was in dripping or jetting mode.

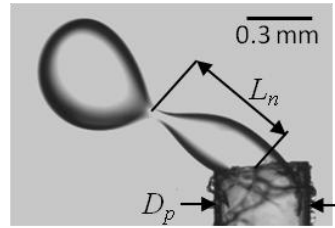


Figure 2.20: Drop before break off in jetting mode for the reference system (second setup), $v_{cp} = 0.73 \text{ m.s}^{-1}$, $v_{dp} = 0.24 \text{ m.s}^{-1}$. Characteristic lengths: elongated neck length L_n , pore diameter D_p .

3.4.2.4. Position of the drop centre of mass

The position of the drop centre of mass for the first setup of section 1 was obtained by a similar method as that to measure the drop diameter. First, the drop was selected in a frame with the lower frame limit at the capillary surface. The image was made binary, the outlines were filled and particle analysis was performed, with no condition on particle size nor circularity. Care was taken so as to avoid any other particles (dust, lighting artefact) from appearing in the selected frame. From this particle analysis, we obtain the position of the centre of mass of the bound drop for the given capillary surface level. We repeat this method for all the capillary positions to obtain the variation of the centre-of-mass position in time, relatively to the capillary surface.

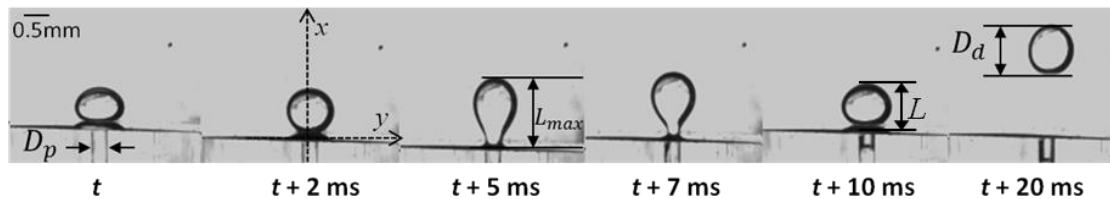


Figure 2.21: Drop formation in time for the reference system for the first setup, $D_p = 0.32 \text{ mm}$, $q = 3.6 \text{ } \mu\text{L.s}^{-1}$, $f = 100 \text{ Hz}$, $A = 0.210 \text{ mm}$. Characteristic lengths: drop length L , maximum drop length L_{max} and drop diameter D_d .

3.4.3. Drop formation time

Drop formation time is measured by counting the number of images between two successive drops at the same stage of drop formation, *e.g.* the point of detachment. By dividing the number of images by the acquisition frequency set on the high speed camera, drop formation time is obtained. An average of three to five times is made. This time can be verified by mass conservation, knowing the dispersed phase flow rate and drop diameters produced. This can also put to light whether there are leaks in the dispersed phase supply system.

We note that when drops are submitted to vibration, from the drop formation time obtained above, we can also calculate the number of oscillations necessary for drop generation. This is done by dividing the formation time by the forcing frequency.

3.5. Data analysis

3.5.1. Analysis of curve fits

When analyzing the fits of curves presenting power laws (*e.g.* drop diameter or amplitude as a function of the forcing frequency), we performed an uncertainty analysis on the slopes. To do so, we transformed the data from a power law to a linear law, followed by a variable change:

$$y = kx^\xi \rightarrow \ln(y) = \ln(k) + \xi \ln(x) \rightarrow Y = k' + \xi X \quad (2.6)$$

On the linearised equation with the variable change, we perform a linear regression. First, a simple linear regression (SLR) based on the least-squares method is applied. Then, a maximum likelihood method provided by Thirumalai, Singh and Ramesh (2011) according to the method of York *et al.* (2004) is used [138,139]. The experimental points are weighted according to their uncertainty. The weighting is taken as the inverse of the variance for the measured data (represented on the y -axis):

$$w_{Y,i} = \frac{1}{\sigma_{Y,i}^2} \quad (2.7)$$

with $\sigma_{Y,i}$ the standard deviation calculated for the point i . A uniform weighting of $w_{X,i} = 0.1$ is applied to each points for the x -axis, which corresponds to the set parameter, *i.e.*, forcing frequency. The arbitrary value will not impact the results as the weighting is uniform.

Then, the coefficient ξ is iteratively calculated by eq. (2.8) taking the previous coefficient ξ of the SLR as a starting point. Iterations are performed until the difference between the previous value and new value reaches a certain tolerance level (in this case 10^{-8}):

$$\xi = \frac{\sum W_i j_i V_i}{\sum W_i j_i U_i} \quad (2.8)$$

with $W_i = w_{X,i} w_{Y,i} / (w_{X,i} + \xi^2 w_{Y,i})$, $U_i = X_i - \bar{X}$, $V_i = Y_i - \bar{Y}$ and $j_i = W_i U_i / w_{Y,i} + \xi V_i / w_{X,i}$. We specify that \bar{X} and \bar{Y} are the average weighted values of X and Y , respectively. From this value of ξ obtained, the value of k' of eq. (2.6) is calculated simply by:

$$k' = \bar{Y} - \xi \bar{X} \quad (2.9)$$

The uncertainties σ on ζ and k' are then established, by eq. (2.10) and (2.11), respectively.

$$\sigma_{\zeta} = \sqrt{\frac{1}{\sum W_i u_i^2}} \quad (2.10)$$

with $u_i = X_i - \sum W_i(\bar{X} + j_i)/\sum W_i$ which corresponds to the differences between the experimental points and the weighted adjusted points.

$$\sigma_{k'} = \sqrt{\frac{1}{\sum W_i} + \sigma_{\xi}^2 \frac{\sum W_i(\bar{X} + j_i)}{\sum W_i}} \quad (2.11)$$

From these results, we can therefore estimate to what extent our power law fit exponent is significant and can compare different experimental fits between them.

3.5.2. Uncertainties calculations

The overall uncertainties U_o obtained for system characterization measurements of section 3.1. and reported in table 2.1 were calculated by the GUM approach (NF ENV 13005) [140]:

$$U_o = \sqrt{U_A^2 + \sum U_{B,i}^2} \quad (2.12)$$

with U_A the type A uncertainty and $U_{B,i}$ the different type B uncertainties.

U_A is obtained by:

$$U_A = t \frac{\sigma}{\sqrt{n}} \quad (2.13)$$

with σ the standard deviation of the mean measured value, n the number of measurements made for the parameter considered and t the Student coefficient if 40 or fewer measurements are made (t varies inversely to n).

Different type B uncertainties exist. The type B uncertainties due to the apparatus were calculated by:

$$U_{B,apparatus} = \frac{e\bar{X}}{\sqrt{3}} \quad (2.14)$$

with e the errors given by the supplier, which we detail for each parameter measured (when relevant) in sections 3.1.1 to 3.1.3 and \bar{X} the average measured value.

The type B uncertainties due to an error in resolution were calculated by:

$$U_{B,resolution} = \frac{e\bar{X}}{\sqrt{12}} \quad (2.15)$$

with e which we estimate, again described for each parameter in sections 3.1.1 to 3.1.3 and \bar{X} the average measured value.

Additional type B uncertainties may also be added and are described directly in sections 3.1.1 to 3.1.3 as they are specific to each measured value.

4. Conclusions

The first setup designed exposed in section 1 of this chapter enabled us to study the behaviour of a bound drop submitted to high-amplitude axial oscillations, in liquid-liquid systems. In this configuration, the outer phase is stationary. On this setup, we investigated the impact of system parameters (interfacial tension, continuous and dispersed phase viscosities) as well as the impact of process parameters (pore diameter, dispersed phase flow velocity, frequencies and amplitudes of vibration) on drop generation. The mechanisms involved in drop detachment are presented in chapter 3 and the model proposed to accurately account for the transition in drop generation regime put to light is presented in chapter 4. Supplementary unpublished results are presented in Appendix 3.

The second setup exposed in section 2 of this chapter allowed us to investigate the impact of cross-flow on drop generation as well as the impact of cross-flow coupled with vibrations. On this setup, we investigated the impact of the continuous and dispersed phase flow velocities, interfacial tension and dispersed phase viscosity on drop generation in simple cross-flow, in dripping mode. This is described in chapter 5. We then considered the impact of added vibrations, detailed in Appendix 4. We pursued the work on this second setup to consider the dripping to jetting transition in simple cross-flow, described in chapter 5 (varying the interfacial tension, dispersed phase viscosity and both flow velocities). We extended this work to consider the dripping to jetting transition when coupled with vibrations. These results are presented in Appendix 5. These trials lead the way to further possible research.

Chapter 3: Impact of axial vibrations on drop generation in dripping mode

1. Preamble

As exposed in the literature review in section 1.3.3., membrane emulsification (ME) has been extensively investigated since its development in the 1990s, with the study of the impact of many different parameters (process, formulation and membrane parameters). However, the impact of vibration (both longitudinal and transversal) on the process has only recently been studied, as described in 1.3.4. In transversally vibrating ME, which is the process that we aim at understanding, little experimentation has been performed. Also, no models exist to describe drop generation in this process in dripping mode with the imposed vibrations, as seen in 1.3.4.2. Additionally, experimental work is rare in the simpler case of drop generation in dripping mode when submitted to high-amplitude axial oscillations (exposed in 3.3.3.).

Therefore, the aim of this chapter is to experimentally investigate the impact of high-amplitude axial oscillations on drop detachment in dripping mode. Indeed, we can assimilate a drop formed in transversally vibrating ME to this configuration. To do so, we study a simple design with a single, millimetre-scale drop generated inside an outer, immiscible, stationary liquid phase. The experimental setup and protocol employed as well as the trials carried out are described in detail in section 1 of the materials and methods chapter (chapter 2). Some of the methods applied, such as image analysis or the setup cleaning method, are also exposed in chapter 2, in section 3.

From these results, two drop generation modes (dripping and stretching) were put to light. The qualitative mechanisms which lead to the transition from dripping to stretching mode are proposed. In addition, a simple model (either force-based or elongation-based) has been developed to grossly explain the transition.

The mechanisms and simple models are described in this third chapter, made up of a letter published in *EPL* (reference: *EPL*, 111 (2015) 44004, doi 10.1209/0295-5075/111/44004). The letter was received on the 23rd of June 2015, accepted in final form on the 9th of August 2015 and published online on the 4th of September 2015. The PACS (Physics and Astronomy Classification Scheme) attributed to this work were:

47.55.db – Drop and bubble formation

47.55.df – Breakup and coalescence

47.35.Pq – Capillary waves.

An erratum was also published (reference: *EPL*, 114 (2016) 59901, doi 10.1209/0295-5075/114/59901). We directly made the erratum amendments in this chapter.

We note that the results concerning the impact of dispersed phase flux which are mentioned in this chapter but reported as “not shown” are shown in chapter 4 and in Appendix 3.

2. Good vibrations - Transition in drop generation from an immersed capillary tube

A. Bertrandias, H. Duval, J. Casalinho and M. L. Giorgi

Laboratoire de Génie des Procédés et Matériaux (LGPM), CentraleSupélec, Université Paris Saclay
- Grande voie des vignes, 92295 Châtenay-Malabry, France

2.1. Abstract

We experimentally investigate single drop formation from a vibrating capillary tube immersed in a second immiscible liquid. At set forcing frequencies, significantly smaller drops are generated when a threshold amplitude is reached. We show that a drop grows and resonates in first mode once the drop resonance frequency and the forcing frequency coincide. The drop then detaches by a stretching mode if its elongation ratio exceeds a critical value, function of the drop to pore diameter ratio. The detached drop diameter is well described by the Bisch *et al.* expression for bound drop resonance frequency. Otherwise, the drop grows, leaves the first mode resonance range and detaches at a larger size by dripping. The threshold and drop diameters are well predicted by a simple LFHO-based model.

2.2. Introduction

Controlling drop breakup is key for industries performing emulsification such as the food, pharmaceutical and chemical industries. Indeed, drop size and distribution affect emulsion rheological properties and stability. Membrane emulsification (ME) consists in forcing a dispersed phase through a porous membrane. The drops are directly generated on the other side of the membrane into a continuous flowing phase, which exerts shear on the drops [1]. ME is commonly operated in dripping (drop by drop) mode.

In recent years, a few attempts were made to couple ME with vibration to better control drop detachment, thus drop size [2-4]. Most investigations concern longitudinal vibrations (see [2] and references therein). In these studies, the shear stress experienced by the drop is mainly due to the membrane oscillation and drop size is controlled by the peak shear stress at the membrane surface. The drop size does not depend on the membrane excitation frequency apart from its influence on shear stress [2]. ME coupled with transversal vibrations (perpendicular to the membrane surface) has been less studied [3,4]. In this case, membrane vibration induces axial vibrations of the drops. Arnaud found a strong decrease in drop size when the membrane (mean pore size of 0.8 μm) was excited at a frequency of 15 kHz (unknown forcing amplitude). The peak of the volume-weighted drop size distribution was shifted from 30 μm without vibration to 10 μm with vibration [3]. The mechanisms at hand were not explained [3,4].

However, axial oscillations of bound drops undergoing forced vibrations have been extensively investigated since the pioneering experimental work of Bisch *et al.* [5]. Strani and Sabetta examined the case of small linearised oscillations and found an additional vibration mode ($n = 1$) for the bound drop, associated with the translation motion of the centre of mass

of the drop [6]. It is reminded that the $n = 2$ mode is the first vibration mode for a free drop as established by Lamb [7]. The response of drops undergoing large-amplitude vibrations has been studied by DePaoli *et al.* and Wilkes and Basaran [8,9]. They showed that bound drops behave as soft nonlinear oscillators and can exhibit hysteretic responses. Finally, Wilkes and Basaran and Kim studied drop detachment in air under strong forcing [10,11]. Wilkes and Basaran examined drop ejection from an oscillating rod using computational fluid dynamics. They found that above a critical forcing amplitude, a pendant drop (with a pinned contact line) breaks up and a primary drop is ejected [10]. Kim experimentally studied the fall-off of a pendant drop (with a free contact line) from a smooth solid vibrating surface. Kim found that the vibration amplitude inducing fall-off is minimal when the forcing frequency and resonance frequency of the drop coincide [11].

In order to understand the effect of vibration on drop detachment in ME, we focus on a simplified configuration where rising drops form from an axially vibrating capillary tube into an unbounded liquid under gravity. A dedicated transparent setup has been designed to observe drop formation. Contrarily to cross-flow ME, there is no continuous phase flow and the membrane reduces to a single pore, *i.e.*, the capillary tube, so potential interactions between drops at adjacent pores are avoided. Drops are constantly fed dispersed phase, thus their size increases with time whereas in the studies on drop oscillation mentioned above, the drop size is set. The aim of the present paper is to study drop generation assisted by axial oscillations, so as to identify the different regimes and the mechanisms involved depending on the excitation parameters.

2.3. Experimental setup

Oil-in-water emulsions were formed with dodecane (99%, viscosity $\eta_d = 1.34$ mPa.s at 25°C, density $\rho_d = 750$ kg.m⁻³ at 25°C) as the dispersed phase and distilled water (viscosity $\eta_c = 0.89$ mPa.s at 25°C, density $\rho_c = 997$ kg.m⁻³ at 25°C) as the continuous, aqueous phase. The interfacial tension was of $\gamma = 46.0 \pm 2.1$ mN.m⁻¹ as measured by the rising drop method with a tensiometer (Tracker, I.T. Concept, Teclis), averaged between 10 s and 20 s after drop formation.

A single-pore vibrating setup has been designed to observe drop formation (fig. 3.1). The setup consists in a transparent tank filled with 70 mL of stationary aqueous phase, in which a glass capillary tube is placed. The dispersed phase is fed through the capillary with a syringe pump (R-99, Razel Instruments). For the pore diameter $D_p = 0.32$ mm, three dispersed phase flow rates are tested: $q = 2.5$ $\mu\text{L.s}^{-1}$, 4.3 $\mu\text{L.s}^{-1}$ and 6.5 $\mu\text{L.s}^{-1}$. When the influence of D_p is investigated, dispersed phase flow rates are set at $q = 2.2$ $\mu\text{L.s}^{-1}$, 6.5 $\mu\text{L.s}^{-1}$, 6.9 $\mu\text{L.s}^{-1}$ and 10.1 $\mu\text{L.s}^{-1}$ (accuracy within 2%) for $D_p = 0.11$ mm, 0.32 mm, 0.35 mm and 0.75 mm respectively. The flow in the capillary is laminar as the associated Reynolds numbers lie between $\text{Re}_{\text{cap}} = 5$ and $\text{Re}_{\text{cap}} = 22$ (with $\text{Re}_{\text{cap}} = \rho_d v_d D_p / \eta_d$ and $v_d = 4q / (\pi D_p^2)$, the dispersed phase velocity).

The capillary is fixed on a vibrating exciter (Bruel & Kjaer 4810) and is driven with a sinusoidal motion function of time: $x = (1/2)A_{pp} \sin(2\pi ft)$. The vibration is parallel to the capillary tube axis, so drops undergo axial vibrations. Forcing frequencies are $f = 30$ Hz to 150 Hz (10 Hz intervals until 100 Hz, variable intervals above depending on D_p). Peak-to-peak amplitudes range from $A_{pp} = 0$ mm to 2 mm, measured by an LED sensor (M5L/2, Bullier International), with an uncertainty in the order of 10 μ m.

A halogen cold light illuminates the system. A high-speed camera (Phantom v310) mounted with a macro lens (AF Zoom-Micro Nikkor 70-180mm f/4.5-5.6D ED, Nikon) captures drop formation images with a resolution of 800×600 pixels. Acquisition frequency is set at 10 times the forcing frequency and at 100 fps for trials without vibration. The images are analysed using ImageJ with the scale set by the capillary outside diameter. Data are provided including average drop diameters D_d and axial drop elongations. The maximum relative errors are of 7%, mainly due to statistical dispersion, as the error due to image resolution is of 1%. Experiments were carried out in triplicate and the error bars in the figures correspond to statistical dispersion.

After experimentation, the setup is cleaned with a surfactants solution (3 vol%, Mucosol, Merz) and thoroughly rinsed with distilled water. As a result, the glass surface is hydrophilic and the capillary outside diameter does not influence dodecane drop detachment.

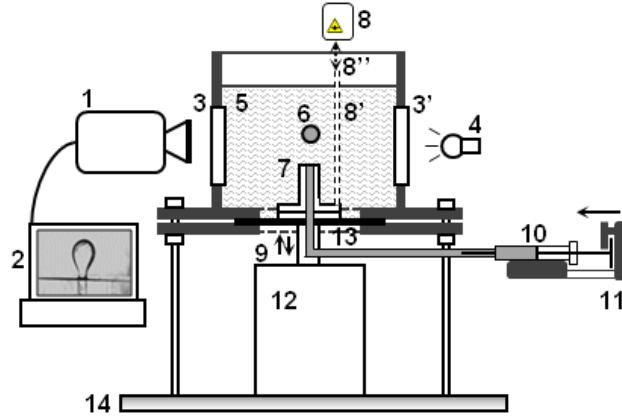


Figure 3.1: Experimental setup: 1, high speed camera; 2, computer; 3 and 3', windows; 4, light source; 5, continuous phase; 6, dispersed phase; 7, glass capillary; 8, 8' and 8'', LED sensor, emerging rod and distance measured; 9, vibrating motion; 10, syringe; 11, syringe pump; 12, exciter; 13, flexible seal; 14, optical table.

2.4. Drop detachment mode without vibration

Without vibration, experiments are in dripping mode for the dispersed phase flow rates and pore diameters tested. Indeed, a drop by drop formation is observed, with the drops formed close to the capillary tip.

In dripping mode, detachment occurs when buoyancy F_b exceeds the maximum capillary force $F_Y^{max} = \pi D_p \gamma$ that the drop neck can withstand without breaking, as stated by Tate's law [12]:

$$F_b = \mathcal{F}_{HB} F_Y^{max}, \text{ i.e., } (\rho_c - \rho_d) \frac{\pi}{6} D_d^3 g = \mathcal{F}_{HB} \pi D_p \gamma \quad (3.1)$$

with \mathcal{F}_{HB} the Harkins Brown correction factor, introduced to account for the fraction of liquid volume which remains attached to the capillary tip after drop break off [13].

Theoretical drop diameters were calculated from eq. (3.1) using the factor \mathcal{F}_{HB} proposed by Mori [14]. They were compared to those measured. The relative differences between calculated and measured diameters vary between -7% and 5% depending on pore diameters and dispersed phase flow rates. It is in the order of drop diameter uncertainty.

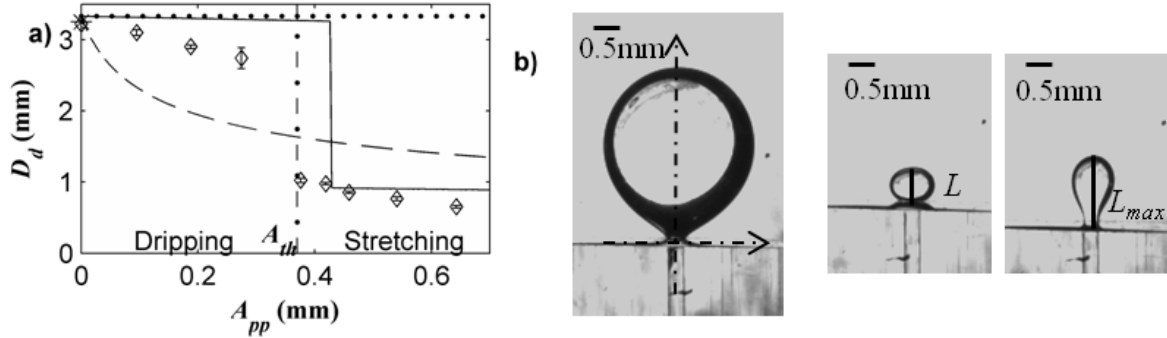


Figure 3.2: (a) Drop diameter D_d depending on the peak-to-peak capillary amplitude A_{pp} for $f = 100$ Hz, $D_p = 0.32$ mm, $q = 4.3 \mu\text{L}\cdot\text{s}^{-1}$: (\diamond) measurements, measured amplitude threshold (dash-dotted line), (*) estimates from eq. (3.1), estimates from the balance $F_b = F_Y^{max}$ (dotted line), estimates from the balance $F_b + F_{exc}^{peak} = F_Y^{max}$ (dashed line), estimates from eq. (3.9) (solid line). (b) Drop image just before detachment in dripping mode (left, $A_{pp} = 0.095$ mm), in stretching mode (centre and right, $A_{pp} = 0.419$ mm).

2.5. Detachment modes with vibration

Amplitude sweeps from low to high amplitudes were carried out at set forcing frequencies. For $f = 30$ Hz to $f = 150$ Hz, two modes of detachment are observed, characterized by large or small drops. These modes are separated by a threshold amplitude A_{th} (fig. 3.2). For other frequencies, the transition could not be observed due to limitations of the vibrating exciter. This was also the case above 110 Hz and 120 Hz for $D_p = 0.11$ mm and 0.75 mm respectively.

For $A_{pp} < A_{th}$, drops detach at large sizes, close to those for drops formed without vibration ($A_{pp} = 0$). As A_{pp} increases, drop size decreases and an increasing deformation of the drop interface is seen. However drops still detach in dripping mode (fig. 3.2(b), left). The large apparent black ring inside the drop (fig. 3.2(b), left) is due to the differences in the refractive index of dodecane ($n_d = 1.42$) and water ($n_c = 1.33$).

For $A_{pp} \geq A_{th}$, enhanced drop detachment occurs: smaller monodispersed drops are generated at a faster rate than in dripping mode. A decrease of 45% (for $f = 30$ Hz) to 76% (for $f = 150$ Hz) in drop diameter is observed at A_{th} compared to without vibration. Beyond the threshold, drop diameters continue to decrease with increasing A_{pp} . Drops are elongated at breakup in this mode (fig. 3.2(b), right). This was named the stretching mode.

2.6. Threshold

The higher the forcing frequency, the lower the threshold amplitude (fig. 3.3). The threshold amplitude roughly scales as f^{-1} for $D_p = 0.32$ mm and 0.35 mm. For $D_p = 0.75$ mm, no scaling law emerges. For $D_p = 0.11$ mm, the threshold amplitude is around twice higher compared to other pore diameters and scales as $f^{-2/3}$. Dispersed phase flux does not significantly affect A_{th} (not shown).

The diameters of the drops generated at A_{th} decrease with increasing forcing frequency (fig. 3.4). Furthermore, it appears that drop diameters scale as $f^{-1/2}$ for all pore diameters. Also, as expected, the larger the pore diameter, the larger the drops produced. Lastly, as the dispersed phase flux increases, a slight increase in drop diameter is observed (not shown). It is attributed to the extra dispersed phase fed to the drop during necking.

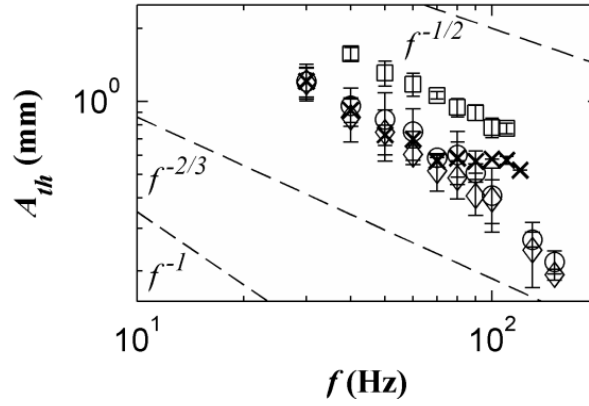


Figure 3.3: Threshold amplitude depending on the forcing frequency: (\square) $D_p = 0.11$ mm, $q = 2.2 \mu\text{L}\cdot\text{s}^{-1}$, (\diamond) $D_p = 0.32$ mm, $q = 6.5 \mu\text{L}\cdot\text{s}^{-1}$, (\circ) $D_p = 0.35$ mm, $q = 6.9 \mu\text{L}\cdot\text{s}^{-1}$, (\times) $D_p = 0.75$ mm, $q = 10.1 \mu\text{L}\cdot\text{s}^{-1}$.

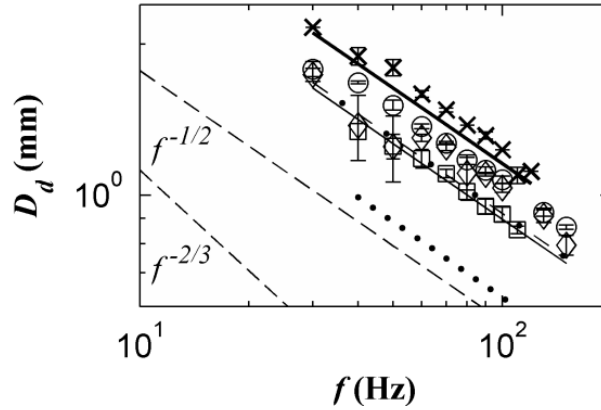


Figure 3.4: Drop diameter depending on the forcing frequency: (\square) $D_p = 0.11$ mm, $q = 2.2 \mu\text{L}\cdot\text{s}^{-1}$, (\diamond) $D_p = 0.32$ mm, $q = 6.5 \mu\text{L}\cdot\text{s}^{-1}$, (\circ) $D_p = 0.35$ mm, $q = 6.9 \mu\text{L}\cdot\text{s}^{-1}$, (\times) $D_p = 0.75$ mm, $q = 10.1 \mu\text{L}\cdot\text{s}^{-1}$. Estimates from eq. (3.9): $D_p = 0.11$ mm (dotted line), $D_p = 0.32$ mm (dash-dotted line), $D_p = 0.35$ mm (solid line), $D_p = 0.75$ mm (thick solid line).

2.7. Resonance

In the moving non-inertial frame of reference where the capillary is still (axes defined in fig. 3.2(b)), the forces exerted on the drop due to the capillary motion are the inertial force and the associated Archimedes' thrust. We note that, in the present setup, the continuous phase above the capillary and its support is accelerated by the exciter, as shown by Faraday waves at the free surface. Thus, the resulting excitation force reads

$$F_{exc} = (\rho_c - \rho_d) \frac{\pi}{6} D_d^3 a_{cap} \quad (3.2)$$

with $a_{cap} = (1/2)A_{pp} \omega^2 \sin(\omega t + \pi)$ the capillary acceleration in the laboratory inertial frame and $\omega = 2\pi f$ the forcing pulsation. Hence, the peak excitation force is

$$F_{exc}^{peak} = (\rho_c - \rho_d) \frac{\pi}{12} D_d^3 \omega^2 A_{pp} \quad (3.3)$$

A Tate-like model based on the balance between the maximum driving force of drop detachment ($F_b + F_{exc}^{peak}$) and the restoring capillary force F_Y^{max} is represented in fig. 3.2(a). \mathcal{F}_{HB} is omitted as it is a first-order correction. This simple model does not account for the experimental results as the sudden jump in drop diameter is not predicted. Additionally, the measured drop diameters in stretching mode are significantly lower than the predicted diameters.

Drop generation footage reveals that as a drop grows, its length L (measured from capillary tip to drop apex, fig. 3.2(b), centre) oscillates and it elongates more just before enhanced detachment. In addition, we found a strong correlation between drop diameter at A_{th} and forcing frequency (fig. 3.4). These elements suggest that drop resonance is involved in enhanced detachment.

Figure 3.5 presents typical variations of drop length L with time t (arbitrary time origin) for $A_{pp} < A_{th}$. These variations coincide with the drop apex motion in the capillary frame. Figure 3.5 simultaneously shows the displacement x of the capillary tip in the laboratory inertial frame. We observe that mean drop length increases as dispersed phase is constantly fed to the drop. Drop length oscillates around the mean due to the excitation force F_{exc} . Drop oscillation amplitude is significantly lower than the capillary one. Indeed, the amplitude of the drop excitation force per mass unit is lower than the capillary acceleration amplitude, by a factor $\phi = (\rho_c - \rho_d)/\rho_d = 0.325$. From $t \cong 0.12$ s, the drop oscillation amplitude increases until a maximum reached at $t \cong 0.21$ s, then decreases. From $t \cong 0.12$ s to 0.26 s, drop oscillation amplitudes are higher than outside this area. This relates a resonance zone (RZ) of the drop. Resonance may be involved in stretching mode as drop sizes in the RZ are close to detached drop sizes at A_{th} .

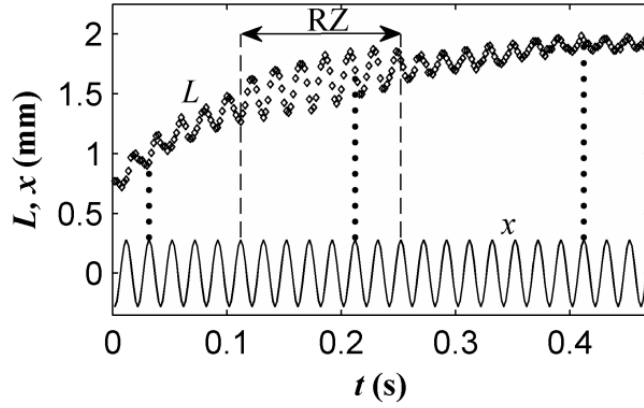


Figure 3.5: (\diamond) Drop length L , capillary displacement x (solid line), approximate boundaries of the resonance zone RZ (dashed line), phase shift estimation guidelines (dotted line): $f = 50$ Hz, $D_p = 0.32$ mm, $A_{pp} = 0.56$ mm $< A_{th} = 0.88$ mm, $q = 4.3$ $\mu\text{L}\cdot\text{s}^{-1}$.

Drop shapes in the resonance zone (fig. 3.2(b), centre and right) correspond to the shapes reported by Bisch *et al.* [5] for the $n = 1$ vibration mode of bound drops. A simple empirical formula for mode 1 resonance frequency f_r is given by Bisch *et al.* [5]:

$$f_r = \frac{1}{2\pi} \sqrt{\frac{6K\gamma \sqrt{D_p}}{\pi\rho_d D_d^2}} \quad (3.4)$$

with $K = 9$ for any two immiscible fluids with equal densities. In our experiments, densities are close as $\rho_c/\rho_d = 1.3$. Equation (3.4) was established for drop to pore diameter ratios of 1.3 to 7. In our case, the ratios are of 1.3 to 12.3. We note that the scaling law followed by the drop diameter at A_{th} , *i.e.* $D_d \sim f^{-1/2}$, is consistent with eq. (3.4). In comparison, if a bound drop resonated exactly as a free drop, the drop diameter would scale as $f^{-2/3}$ [7].

From eq. (3.4), we calculate the resonance frequency of the drops detached at A_{th} . The diameter of the resonating bound drop is assimilated to the detached drop diameter. These frequencies concur well with the experimental forcing frequencies (fig. 3.6). We conclude that once a drop reaches a critical size such that its resonance frequency and the forcing frequency coincide, it resonates in mode 1 and detaches if the capillary oscillation amplitude exceeds A_{th} .

For $D_p = 0.11$ mm, the calculated frequencies are lower than the forcing frequencies (fig. 3.6). Indeed, drop to pore diameter ratios range from 7.5 to 12.3, which is above where eq. (3.4) was validated. The calculations of Strani and Sabetta [6] show that the bound drop first resonance frequency scales as $f_r \sim D_d^\alpha$ where α varies from -2.9 to -1.75 when the drop to pore diameter ratios vary from 1.3 to 7, respectively. They show that eq. (3.4) underestimates the resonance frequency when $D_d/D_p > 7$, which is consistent with the deviation seen for $D_p = 0.11$ mm.

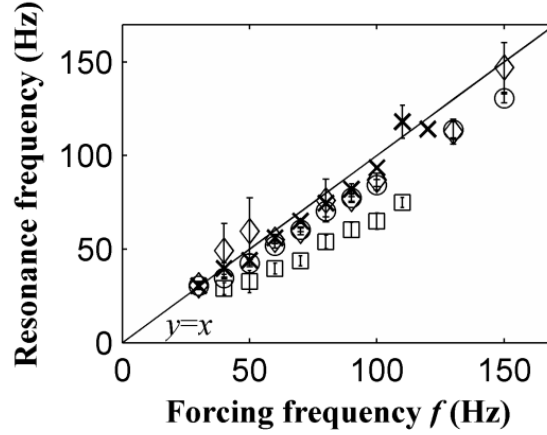


Figure 3.6: Calculated mode 1 resonance frequency [5] versus set experimental frequency: (□) $D_p = 0.11$ mm, $q = 2.2$ $\mu\text{L}\cdot\text{s}^{-1}$, (◇) $D_p = 0.32$ mm, $q = 6.5$ $\mu\text{L}\cdot\text{s}^{-1}$, (○) $D_p = 0.35$ mm, $q = 6.9$ $\mu\text{L}\cdot\text{s}^{-1}$, (x) $D_p = 0.75$ mm, $q = 10.1$ $\mu\text{L}\cdot\text{s}^{-1}$.

We suppose that the resonating bound drop behaves as a linearly forced harmonic oscillator (LFHO) with moderate damping and that drop growth is slow enough to consider steady-state oscillations. Before the RZ, the drop is so small that its resonance frequency is notably greater than the forcing frequency f . In this case, the LFHO model [15] predicts that drop oscillations are in phase with the excitation force (we remind that the excitation force $F_{exc}(t)$ is in phase opposition with the capillary motion $x(t)$) and that the drop oscillation amplitude should be small compared to the forcing amplitude. However, as the support below the drop is open, part of the drop volume is free to oscillate in and out of the capillary, leading to higher oscillation amplitudes than expected. After the RZ, the drop is so large that its resonance frequency is notably lower than f . Then, the LFHO model [15] predicts that drop oscillations are in phase opposition with the excitation force and that the drop oscillation amplitude is close to the forcing amplitude, *i.e.* ϕA_{pp} when f is large enough. At resonance, drop oscillation amplitudes are maximal and the phase shift is equal to $\delta = -\pi/2$ (fig. 3.5), which is in accordance with the LFHO model [15].

In fig. 3.5, the RZ is wide as drop size increases slowly with the dispersed phase flow rates used: the drop diameter increase per oscillation is of about 1.3% in the RZ.

When the drop does not detach in the RZ, it grows and detaches at a larger size in dripping mode, at 2.36 s in the example in fig. 3.5 (not shown). At this point, drop oscillations (which became weak) increase again, but with a lesser amplitude than in the RZ. This is attributed to the excitation of a higher resonance mode of the drop. This explains why in the dripping mode, drop diameter steadily decreases as A_{pp} increases.

2.8. Force-based analysis

To account for the transition from dripping to stretching mode, we propose a model where the drop is described as a LFHO and the condition for drop detachment is expressed with a force-based criterion. The system is certainly nonlinear since oscillations can be large enough

to induce drop detachment [8,9]. However, it is expected that the main features of the transition can be understood from this approximation.

The bound drop is subjected to a restoring capillary force, made up of a stationary and oscillatory part. The stationary part balances the buoyancy force and can be expressed as

$$F_Y^{stat} = -\frac{\pi}{6}D_d^3(\rho_c - \rho_d)g \quad (3.5)$$

The oscillatory part responds to the excitation force. According to the LFHO model, this part reads

$$F_Y^{osc} = -\frac{\pi}{6}D_d^3\rho_d\omega_1^2x_d(t) \quad (3.6)$$

with ω_1 the mode 1 eigenpulsation of the bound drop without damping and $x_d(t)$ the displacement of the centre of mass of the drop. We assume that the buoyancy force negligibly affects the drop eigenpulsation and damping constant. Indeed, the drop Bond number, $Bo_d = (\rho_c - \rho_d)g(D_d/2)^2/\gamma$, in the RZ is significantly lower than 1. Assuming quasi-steady-state oscillations, the drop centre-of-mass motion is given by $x_d(t) = (1/2)A_d(\omega) \sin(\omega t + \delta)$ with the peak-to-peak amplitude

$$A_d(\omega) = \frac{\omega^2\phi A_{pp}}{\sqrt{(\omega_1^2 - \omega^2)^2 + 4\beta^2\omega^2}} \quad (3.7)$$

where ω_1 is related to ω_r (resonance pulsation) by the expression $\omega_r^2 = \omega_1^2 - 2\beta^2$, with $\omega_r = 2\pi f_r$ (f_r the resonance frequency) and β the damping constant. For moderate damping, $\omega_r \cong \omega_1$ and the peak-to-peak amplitude of the steady-state oscillations at resonance is given by $A_d^r \cong Q(\phi A_{pp})$ with the quality factor $Q = \omega_1/(2\beta)$.

We first estimated Q from eq. (3.8) given by Bisch *et al.* [5], which relates β to the resonance frequency f_r and to the phase properties (valid for $\eta_d/\rho_d > \eta_c/\rho_c$ as is our case):

$$\beta/f_r = 4.5 \times 10^3(\eta_d/\rho_d) + 2.32 \times 10^5(\eta_c/\rho_c) \quad (3.8)$$

We found $Q = 14.6$. On the other hand, at set f , we measured the maximum amplitude A_d^{max} of the drop centre-of-mass motion in the RZ (for $A_{pp} < A_{th}$). We estimated Q by $A_d^{max}/(\phi A_{pp})$ and found significantly lower values than from eq. (3.8). For example, in the conditions of fig. 3.2, $A_d^{max}/(\phi A_{pp}) = 4.5$. This ratio is independent of A_{pp} : it depends on the other operating parameters. The difference between measured and calculated values is attributed to the fact that the drop does not spend enough time in the RZ to reach steady state.

The drop detaches when the overall restoring force reaches the maximum retaining capillary force

$$\frac{\pi}{6}D_d^3 \left((\rho_c - \rho_d)g + \frac{1}{2}\rho_d\omega_1^2A_d^{\#}(\omega) \right) = \pi D_p \gamma \quad (3.9)$$

where $A_d^\#(\omega) = \min(A_d(\omega), A_d^{max})$ since the drop does not spend enough time in the RZ to reach amplitudes exceeding A_d^{max} . As an example, D_d is calculated from eq. (3.9) for growing drops in the conditions of fig. 3.2(a), with $A_d^{max} = 4.5\phi A_{pp}$ and β from eq. (3.8). Results are shown by the solid line in fig. 3.2(a). The transition from dripping to stretching is well reproduced. The model from eq. (3.9) was applied with $A_d^{max}/(\phi A_{pp})$ estimated between 80 Hz and 100 Hz for each D_p (for $A_{pp} < A_{th}$). Results are shown in fig. 3.4. The model is in good agreement with the experiments except for $D_p = 0.11$ mm. However, the discrepancy is coherent with the one observed for $D_p = 0.11$ mm in fig. 3.6 and is explained in the same manner.

Above A_{th} , drop size decreases with increasing A_{pp} because the detachment criterion is satisfied earlier in the RZ (for $\omega_1 > \omega$). The model overestimates drop sizes above A_{th} , attributed to nonlinear effects [8,9]. A downwards shift in resonance frequency occurs when increasing A_{pp} for soft nonlinear oscillators [16]. Below A_{th} , drop sizes are also overestimated: a resonance mode higher than mode 1 is excited and this is not taken into account in eq. (3.9).

We note that the present model does not account for the scaling $A_{th} \sim \omega^{-1}$ observed in fig. 3.3 since eq. (3.9) under steady-state assumption leads to $A_{th} \sim \omega^{-1/2}$. The LFHO assumption is too simplified to capture all the features of the transition. Also, the transient stage and nonlinear effects are not modeled.

2.9. Elongation-based analysis

Similarly to Wilkes and Basaran [10], we also examined the maximum length reached by the drop prior to its detachment. At A_{th} , we measured the maximum drop length L_{max} and defined the elongation ratio as the maximum drop length divided by the detached drop diameter. Dimensional analysis shows that L_{max}/D_d should essentially depend on the drop to pore diameter ratio D_d/D_p , since the physicochemical properties are set.

We report elongation ratio values as a function of D_d/D_p (fig. 3.7) for all tested forcing frequencies and pore diameters. Although the statistical dispersion is significant, the larger the drops are compared to the pore, the lower the critical elongation ratio needed for detachment. On average, the critical elongation ratios decrease from about 1.4 to 1.1 when D_d/D_p varies from 1.4 to 12.

The decreasing trend can be explained by the results of Strani and Sabetta [6]. Indeed, they reported that when the drop to pore diameter ratio tends to infinity, the $n = 1$ vibration mode degenerates into a zero-frequency rigid motion. Thus, for a large but finite D_d/D_p , the drop essentially experienced a rigid motion with the deformation mainly localised at the neck. This explains the lower drop elongation ratios for $D_p = 0.11$ mm.

For $D_p = 0.75$ mm, critical elongation ratios are below the trend. It is attributed to the fact that, for $D_p = 0.75$ mm, drop breakup occurred partly inside the tube rather than at the surface.

Then, the measured method for L_{max} (from capillary tip to apex) underestimates the real drop length.

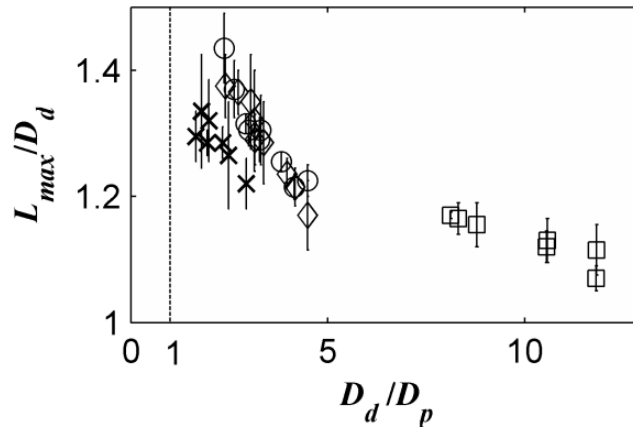


Figure 3.7: Elongation ratio function of drop to pore diameter ratio ($f = 30 \text{ Hz} - 150 \text{ Hz}$):
 $(\square) D_p = 0.11 \text{ mm}$, $(\diamond) D_p = 0.32 \text{ mm}$, $(\circ) D_p = 0.35 \text{ mm}$, $(\times) D_p = 0.75 \text{ mm}$.

The comparison with the simulation results of Wilkes and Basaran [10] are difficult since in their results, only a drop fraction is ejected. Moreover, the drop equivalent diameter is smaller than D_p . The closest case to our study is a D_d/D_p value slightly lower than 1. In this case, a critical elongation ratio of the order of 2 is reported, consistent with our results. According to their simulation snapshots, drop deformation creates pressure gradients inside the drop, leading to flow out of the neck, pinch-off and thus drop detachment. A similar scenario is expected in our experiments.

2.10. Conclusion

Drop generation from a vibrating tube exhibits a transition from dripping to stretching mode when increasing the forcing amplitude at a set forcing frequency. In stretching mode, drops are significantly smaller from a threshold amplitude and above. During drop growth, the bound drop resonates in first mode once its resonance frequency and the forcing frequency coincide. It detaches by a so-called stretching mode if its elongation ratio exceeds a critical value, function of the drop to pore diameter ratio. The main features of this transition, *i.e.* threshold and drop diameter, can be described by a simple LFHO model using the expression of Bisch *et al.* for bound drop resonance frequency.

2.11. Acknowledgements

We thank J. Trubuil and T. Martin for their help with designing and manufacturing the experimental setup.

3. Additional information

3.1. Harkins-Brown correction factor

The volume of a detached drop V_d is smaller than the volume of the pendant drop just before detachment V_p , because part of the liquid volume stays attached to the capillary tip after detachment. The two volumes are related by

$$V_d = \frac{\pi}{6} D_d^3 = \mathcal{F}_{HB} V_p \quad (3.A11)$$

with \mathcal{F}_{HB} the Harkins-Brown correction factor ($\mathcal{F}_{HB} \leq 1$). Tate's law expresses the balance between the buoyancy and capillary forces for the pendant drop:

$$(\rho_c - \rho_d) V_p g = \pi D_p \gamma \quad (3.A12)$$

By combining eq. (A11) and (A12), we rewrite Tate's law to find eq. (3.1), which contains the detached drop diameter D_d (measured experimentally). \mathcal{F}_{HB} is calculated knowing the pore diameter and the detached drop volume.

3.2. Factor ϕ

In the non-inertial frame of reference (where the capillary is still), the excitation force exerted on the drop by the capillary motion is that given in eq. (3.2), with a_{cap} the capillary acceleration in the inertial, laboratory frame of reference.

In the non-inertial frame of reference (where the capillary is still), the excitation force per mass unit that the drop is subjected to reads

$$\overrightarrow{a_{eff}} = \frac{F_{exc}}{\rho_d \frac{\pi}{6} D_d^3} = \frac{(\rho_c - \rho_d)}{\rho_d} \overrightarrow{a_{cap}} = \phi \overrightarrow{a_{cap}} \quad (3.A13)$$

This is less than the capillary acceleration, as $\phi = (\rho_c - \rho_d)/\rho_d = 0.325$. Consequently, the effective capillary displacement is $x_{eff} = \phi x$. From this, we note that in fig. 3.5, drop oscillations should actually be compared to x_{eff} rather than x .

3.3. Tate-like model

In the published erratum, we added why the Tate-like model based on peak excitation force rapidly underestimates drop diameters in dripping mode by the following description.

Let us consider a large drop after the resonance zone (RZ). Its eigenpulsation is typically much smaller than the forcing pulsation. The detachment criterion (eq. (3.9) presented in the letter) simplifies under the assumption $\omega_1 \ll \omega$

$$D_d^3 \rho_d \phi \left[\frac{\omega_1^2 A_{pp}}{2} + g \right] > 6 D_p \gamma \quad (3.A14)$$

to be compared with the Tate-like model:

$$D_d^3 \rho_d \phi \left[\frac{\omega^2 A_{pp}}{2} + g \right] > 6D_p \gamma \quad (3.A15)$$

Since $\omega \gg \omega_1$ in dripping mode, we deduce that the Tate-like model based on peak excitation force then underestimates drop diameters.

4. References

- [1] T. Nakashima, M. Shimizu and M. Kukizaki, « Membrane Emulsification by Microporous Glass », *Key Engineering Materials*, 61–62, p. 513–516, 1992.
- [2] Holdich R. G., Dragosavac M. M., Vladislavljevic G. T. and Kosvintsev S. R., « Membrane emulsification with oscillating and stationary membranes », *Ind. Eng. Chem. Res.*, 49 (8), p. 3810–3817, 2010.
- [3] C. Arnaud, « Procédé et dispositif de fabrication d'une dispersion ou d'une émulsion », European patent EP 1 551 540 B1, 2006.
- [4] E. Lepercq-Bost, « Etude d'un procédé d'émulsification par membrane vibrante: compréhension des mécanismes, modélisation et optimisation », PhD Thesis, Ecole Centrale Paris, p. 224–233, 2008.
- [5] C. Bisch, A. Lasek and H. Rodot, « Comportement hydrodynamique de volumes liquides sphériques semi-libres en apesanteur simulée », *J. Méc. Théor. Appl.*, 1, p. 165–183, 1982.
- [6] M. Strani M. and F. Sabetta, « Free vibrations of a drop in partial contact with a solid support », *J. Fluid Mech.*, 141, p. 233–247, 1984.
- [7] H. Lamb, *Hydrodynamics*, 6th Edition (Cambridge University Press, Cambridge, UK), p. 473–475, 1932.
- [8] D. W. DePaoli, J. Q. Feng, O. A. Basaran, et T. C. Scott, « Hysteresis in forced oscillations of pendant drops », *Phys. Fluids*, 7, p. 1181–1183, 1995.
- [9] E. D. Wilkes et O. A. Basaran, « Hysteretic response of supported drops during forced oscillations », *J. Fluid Mech.*, 393, p. 333–356, 1999.
- [10] E. D. Wilkes et O. A. Basaran, « Drop Ejection from an Oscillating Rod », *J. Colloid Interface Sci.*, 242, p. 180–201, 2001.
- [11] H.-Y. Kim, « Drop fall-off from the vibrating ceiling », *Phys. Fluids*, 16, p. 474–477, 2004.
- [12] T. Tate, « On the magnitude of a drop of liquid formed under different circumstances », *Phil. Mag.*, 27, p. 176–180, 1864.
- [13] W. D. Harkins and F. E. Brown, « The determination of surface tension (free surface energy), and the weight of falling drops: the surface tension of water and benzene by the capillary height method », *J. Am. Chem. Soc.*, 41, p. 499–524, 1919.
- [14] Y. H. Mori, « Harkins-brown correction factor for drop formation », *AIChE J.*, 36, p. 1272–1274, 1990.
- [15] E. Butikov, *Simulations of Oscillatory Systems* (CRC Press, Taylor & Francis Group), p. 38–45, 2015.
- [16] E. D. Wilkes et O. A. Basaran, « Forced oscillations of pendant (sessile) drops », *Phys. Fluids*, 9, p. 1512–1528, 1997.

Chapter 4: Model for drop generation in dripping mode with axial vibrations

1. Preamble

The main aim of this work is to understand drop generation in transversally vibrating membrane emulsification in dripping mode. Indeed, it was seen in the literature review in section 1.3.4. that this has not been extensively studied nor understood. To do this, we assimilate a drop formed in this process to a bound drop undergoing high-amplitude forced oscillations. This configuration has also not been thoroughly experimentally studied (as described in 3.3.3. of the literature review). Consequently, we first investigated this configuration on one system (dodecane-distilled water without surfactant) and one parameter (pore diameter), with the results exposed in chapter 3.

In chapter 3, we showed that above a threshold amplitude of vibration, drop generation undergoes a transition from dripping to stretching mode, with significantly smaller drops formed in the latter mode. The mechanisms put to light are that bound drop grows and resonates in first mode once its eigenfrequency (as given by Bisch *et al.*) coincides with the forcing frequency. During resonance, if the drop elongation ratio exceeds a critical value, it detaches in stretching mode. We proposed a simple LFHO model in chapter 3 to account for the threshold amplitude and resulting drop diameter. This model grossly accounts for the transition.

In this fourth chapter, we develop a more complex model which accounts for the drop dynamics in time and for additional damping which occurs due to the film of liquid between the drop and nozzle surface. This model enables to predict drop diameters at the threshold and especially enables to account for threshold amplitude values, which had previously never been done to our knowledge. We validate the model by further experimental work for different pore diameters, dispersed phase velocities, interfacial tensions and dispersed phase viscosities. The experimental setup used to do so is the same as that employed in chapter 3. It is described in detail in section 1 of the materials and methods chapter (chapter 2).

This chapter is made up of an article published in *Physics of Fluids* (reference: *Phys. Fluids*, 28 (2016) 102103, doi 10.1063/1.4964378). The letter was received on the 10th of June 2016, accepted in final form on the 20th of September 2016 and published online on the 12th of October 2016.

We note that not all experimental results were included due to publishing space limitations: complementary results obtained are exposed and analysed in Appendix 3.

2. Drop generation from a vibrating nozzle in an immiscible liquid-liquid system

A. Bertrandias, H. Duval, J. Casalinho and M. L. Giorgi

Laboratoire de Génie des Procédés et Matériaux (LGPM), CentraleSupélec, Université Paris Saclay
- Grande voie des vignes, 92295 Châtenay-Malabry, France

2.1. Abstract

Drop generation from an axially vibrating nozzle exhibits a transition in drop diameter when varying the vibration amplitude. Below a threshold amplitude, forcing has essentially no effect on drop size and drops form in dripping mode. Above the threshold, drop size is controlled by forcing: drops detach at resonance, *i.e.*, when the first eigenfrequency of the growing drop coincides with the forcing frequency. We experimentally study the impact of the nozzle inner diameter, dispersed phase flow rate, interfacial tension and dispersed phase viscosity on this transition. Drop diameter is well correlated to the mode 1 eigenfrequency of Strani and Sabetta for a drop in partial contact with a spherical bowl. We propose a transient model to describe drop dynamics until detachment. The drop is modelled as a linearly forced harmonic oscillator, with the eigenfrequency of Strani and Sabetta. Since the dispersed phase does not wet the nozzle tip, an additional damping coefficient is introduced to account for the viscous dissipation in the film of continuous phase between the drop and nozzle surface. The model adequately reproduces the effect of the different parameters on the threshold amplitude.

2.2. Introduction

Inducing vibration to jets or drops can be used to control breakup, thus drop size. Vibration is applied for example in ink jet printing, spray coating or vibrating cross-flow membrane emulsification, the latter having motivated our research. We focus on transversal vibrations, where drops undergo axial oscillations. For a membrane with a mean pore diameter of 0.8 μm , Arnaud found a decrease in the peak of the volume-weighted drop size distribution (from 30 μm to 10 μm) at a forcing frequency of 15 to 20 kHz compared to without vibration [1]. Thus, vibrating the membrane in this process impacts drop size but mechanisms for drop detachment were not explained [1,2]. To obtain a fine control on drop size, understanding the physics of drop vibration and detachment is necessary.

Oscillations of liquid drops have been extensively studied since the pioneering work of Lord Rayleigh [3]. He calculated the eigenmodes of a free inviscid, incompressible drop in a vacuum, in absence of gravity and for small-amplitude oscillations. The eigenmodes are characterized by two integers: a polar wavenumber $n \geq 2$ and an azimuthal wavenumber $m \in [-n; n]$. In this study, we focus on axisymmetric modes ($m = 0$). Rayleigh showed that the eigenfrequencies depend on n , the liquid density, interfacial tension and drop size [3]. Drop eigenfrequencies scale as $D_d^{-3/2}$, with D_d the drop diameter. Lamb generalized this theory by

calculating the eigenpulsation of a drop in a surrounding fluid and found the same relationship $f \sim D_d^{-3/2}$ [4].

Rodot *et al.* [5] and Bisch *et al.* [6] investigated drops partially bound to a rod, submitted to controlled vibration. The drop was immersed in immiscible liquids of equal density, with its contact line pinned on the rod edge. A large range of liquid couples were examined and the first eigenfrequency was found to depend on the support diameter, drop diameter, drop density and surface tension. The first resonance frequency scales as D_d^{-2} and not as $D_d^{-3/2}$ such as for the free drop. Then, Strani and Sabetta (hereafter denoted S&S) studied linear oscillations of a liquid drop in an outer fluid, in partial contact with a spherical bowl under inviscid and zero-gravity assumptions [7]. The presence of the support increases the eigenfrequencies for modes $n \geq 2$, but an additional low-frequency mode appears. This is the $n = 1$ eigenmode, associated with the displacement of the bound drop center of mass. When the support reduces to a single point, the $n = 1$ mode degenerates to a zero-frequency rigid motion of the drop. S&S noted that the mode 1 eigenfrequency may be approximated over intervals by D_d^α with α varying between -2.9 and -1.75 for drop to support diameter ratios of 1.3 to 7, respectively [7]. This is consistent with $\alpha = -2$ proposed by Bisch *et al.* [6]. Also, S&S [7] computed frequencies were in agreement with Bisch *et al.* [6] data, but resonance frequencies were overpredicted by 20% (reduced to 10% by accounting for viscous effects [8]). However, both models (inviscid [7] and viscous [8]) overpredicted resonance frequencies for large support to drop diameter ratios, attributed to nonlinear effects, not taken into account in the models. Smithwick and Boulet [9] studied the first resonance frequency of mercury drops on glass (pinned contact line) under partial vacuum and compared their data to the calculations of S&S [7]. A maximum error of 3.3% was found.

Bostwick and Steen [10] and Vejrazka *et al.* [11] studied linear oscillations of a drop supported on a ring. Bostwick and Steen noted that the center-of-mass motion is partitioned among all the eigenmodes but the $n = 1$ mode is its main carrier [10]. Vejrazka *et al.* found that for small support to drop diameter ratios, the frequency response of the drop is independent of the constraint (bowl or ring) [11]. Abi Chebel *et al.* [12] and Vejrazka *et al.* [11] examined drop oscillations driven by imposed periodic volume variations. The frequency response is independent of the forcing type as long as the support to drop diameter ratio is small [11]. Lastly, Noblin *et al.* studied bound drop oscillations with mobile instead of pinned contact lines: a decrease in resonance frequency was found [13]. The transition from a pinned to mobile contact line occurred above a critical forcing amplitude. In that case, the variation of the contact angle exceeds the contact angle hysteresis.

Previous studies explored linear oscillations. Wilkes and Basaran (hereafter denoted W&B) used computational fluid dynamics (CFD) to study large-amplitude axisymmetric oscillations of a viscous bound drop on a rod (pinned contact line) [14]. They found that the drop resonance frequency varies slightly with amplitude at high Ohnesorge numbers (Oh, expressed in section 2.6.2) but decreases significantly with amplitude at low Oh, Oh being the ratio of a

viscicapillary to an inertial-capillary time scale. Resonance frequency also decreases as the Bond number (Bo , expressed in section 2.3.3) increases. Bo compares the gravity to capillary forces. The maximum drop deformation, observed at resonance, increases with forcing amplitude and Bo and decreases with Oh and n . DePaoli *et al.* experimentally studied pendant drops in air under high-amplitude forcing and observed hysteresis, characteristic of soft nonlinearities [15]. At a set forcing amplitude (resp. frequency), a larger response amplitude appeared at lower frequencies (resp. amplitudes) when a downwards frequency (resp. amplitude) sweep was performed *vs.* an upwards sweep. W&B numerically gave the critical forcing amplitude for the onset of hysteresis for different Oh [16]. This value could be as low as 3% of the rod radius (drop and rod radii of the same order). Calculations were also performed for drops hanging from a tube: the first resonance frequency is slightly higher when the support is a tube, the hysteresis range is shifted to higher values of forcing frequency and the deformation at resonance is higher.

For high enough forcing amplitudes, drops detach from the support. W&B used CFD to simulate drop ejection from a rod (pinned contact line) [17]. Above a critical amplitude, the bound drop ruptures: a primary drop is ejected from the liquid remaining on the rod. The variations of the critical amplitude as a function of the forcing pulsation have a V-shape (the minimum corresponds to drop resonance). For a set rod diameter, the critical amplitude increases when Oh decreases or when the bound drop volume decreases. Critical amplitudes range from 25% to 80% of the rod radius. Kim experimentally studied the detachment of a pendant drop from a smooth vibrating plate in air (mobile contact line) [18]. The variations of the critical amplitude as a function of the forcing frequency have a W-shape. Kim [18] found that the minima concord well with the $n = 1$ and $n = 2$ modes of the bound drop as calculated by S&S [7]. Again, the minima correspond to drop resonance. The agreement between data and calculations of S&S [7] is remarkable as the contact line mobility is different and experimental oscillation amplitudes are beyond the linear regime.

Resonance also triggered drop detachment in previous work of the authors, where different pore diameters were studied for one system (dodecane-water without surfactant) [19]. Drops were formed through a vibrating nozzle continuously fed with dodecane, immersed in the stationary immiscible water phase. This enabled to gain insight into transversally vibrating membrane emulsification in a simplified configuration. We found that at a set forcing frequency, smaller drops were generated above a threshold forcing amplitude: a growing drop detached prematurely when its first resonance frequency (as given by Bisch *et al.*) and the forcing frequency coincided. However, the threshold was higher than expected, attributed to the fact that the bound drop did not spend enough time in the resonance range to reach steady-state resonance. The generation mode forming the smaller drops was named the “stretching mode”. Below the threshold, larger drops were formed in dripping mode.

The aim of this work is to study the mutual effect of forcing parameters and system properties on drop generation from a vibrating nozzle. We also aim to further model drop generation modes by accounting for drop growth and motion as a function of time. We

emphasize that studies on vibrated growing drops are rare [19] compared to those on constant-volume drops [5-18] and that previous work concerned only one system and parameter [19]. In the following, we first describe our setup. We present the dripping to stretching transition and propose a simple framework to approach it. Then, we discuss the effect of nozzle inner diameter, dispersed phase flow rate, interfacial tension and dispersed phase viscosity on the transition. We examine the effect of these parameters on (i) the threshold amplitude for the stretching mode and (ii) the resulting drop diameters. We further analyze our results by comparing them to S&S calculations [7]. Finally, we propose a simple transient model to describe drop dynamics until detachment and compare the model predictions to experiments.

2.3. Experimental setup

2.3.1. Materials

We call the reference system a system whose continuous and dispersed phases are distilled water and dodecane (99%, Fisher Scientific), respectively. To study the impact of interfacial tension, a surfactant (SDS (Sodium dodecyl sulfate), 85%, Acros Organics) is added to the continuous phase at 0.1 wt% or 2 wt% (named systems 1 and 2, resp.). To study the impact of dispersed phase viscosity, paraffin (Fisher Scientific) is added to the dispersed phase at 25 wt% or 50 wt% (named systems 3 and 4, resp.). A system with an increased continuous phase viscosity was also tested (supplementary material in section 2.9.4). The so-called reference system and system 1 to 4 properties are given in table 4.1. The viscosities η and densities ρ of the mixtures were measured in triplicate, the former with a Ubbelohde type viscosimeter (AVS310, Schött-Gerade) at 25.1°C. The interfacial tension γ was measured in triplicate by the rising drop method with a tensiometer (Tracker, I.T. Concept, Teclis). For systems 1 and 2, γ is determined by the method explained in the supplementary material in section 2.9.1. Table 4.1 values report an intermediate plateau interfacial tension. We consider that the plateau value gives an adequate estimation of the interfacial tension when drops form (see supplementary material in section 2.9.2).

Table 4.1: Properties of the different systems investigated.

System	Dispersed phase 'dp'	η_{dp} (mPa.s)	ρ_{dp} (kg.m ⁻³)	Continuous phase 'cp'	η_{cp} (mPa.s)	ρ_{cp} (kg.m ⁻³)	γ (mN.m ⁻¹)
Reference	Dodecane	1.34	750	Distilled water	0.89	997	50.7 ± 3.5 ^a
1	Dodecane	1.34	750	Distilled water and SDS (0.1 wt%)	0.89	997 ± 1.4 ^a	19.0 ± 0.6 ^{a,b}
2	Dodecane	1.34	750	Distilled water and SDS (2 wt%)	0.89	1001 ± 1.2 ^a	5.4 ± 0.5 ^{a,b}
3	Dodecane (75 wt%) and paraffin (25 wt%)	1.79 ± 0.23 ^a	772 ± 1.4 ^a	Distilled water	0.89	997	53.5 ± 2.4 ^a
4	Dodecane (50 wt%) and paraffin (50 wt%)	3.24 ± 0.42 ^a	790 ± 1.1 ^a	Distilled water	0.89	997	50.0 ± 1.2 ^a

^a the tabulated value is measured experimentally.

^b the tabulated value corresponds to the dynamic interfacial tension measured at the intermediate plateau.

2.3.2. Experimental setup

The setup, illustrated in prior work [19], is summarized in fig. 4.1. A single glass capillary (nozzle) of inner diameter D_p emerges into a tank with the stationary continuous phase. Two pore diameters are presently tested: $D_p = 0.32$ mm and $D_p = 0.11$ mm. The dispersed phase is supplied through the pore at a flow rate $q = 1.1 \mu\text{L}\cdot\text{s}^{-1}$ to $14.4 \mu\text{L}\cdot\text{s}^{-1}$ (PHD Ultra Syringe Pump, Harvard Apparatus), leading to mean flow velocities $v_{dp} = 4q/(\pi D_p^2)$. Reynolds numbers for the flow in the nozzle are of $\text{Re}_{\text{cap}} = 3.0$ to 32.8 ($\text{Re}_{\text{cap}} = \rho_{dp} v_{dp} D_p / \eta_{dp}$) (laminar flow). The nozzle is fixed on a vibrating exciter (Bruel & Kjaer 4810) which induces a sinusoidal motion x_{cap} in time t : $x_{\text{cap}} = A \sin(2\pi ft)$. A is the forcing amplitude measured by a laser sensor (M5L/2, Bullier Automation) with a precision in the order of $10 \mu\text{m}$. f is the forcing frequency set on the signal generator (33512B Arbitrary Waveform Generator, Agilent). Vibrations are parallel to the nozzle axis, so drops undergo axial oscillations.

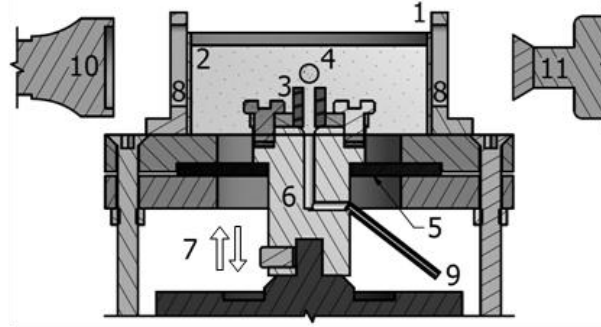


Figure 4.1: Cross-section side view of the setup by CAD: 1, tank; 2, continuous phase; 3, glass capillary (nozzle); 4, dispersed phase drop; 5, flexible seal; 6, central element fixed on the vibrating exciter; 7, axial, vibrating motion; 8, windows; 9, dispersed phase supply system; 10, light source; 11, high-speed camera with macro lens.

In the moving non-inertial frame of reference where the nozzle is still (axes in fig. 4.2), the forces exerted on the drop due to nozzle motion are the inertial force and associated Archimedes' thrust. We note that the continuous phase above the nozzle and support is accelerated by the exciter, shown by Faraday waves at the free surface. The resulting excitation force is:

$$F_{\text{exc}} = (\rho_{cp} - \rho_{dp}) \frac{\pi}{6} D_d^3 a_{\text{cap}} \quad (4.1)$$

with D_d the bound drop diameter and $a_{\text{cap}} = A \omega^2 \sin(\omega t + \pi)$ the nozzle acceleration in the laboratory inertial frame ($\omega = 2\pi f$ is the forcing pulsation). Drop formation is recorded with a high-speed camera (v310, Phantom) and macro lens (AF Zoom-Micro Nikkor 70-180mm f/4.5-5.6D ED, Nikon). The acquisition frequency is ten times the forcing frequency or 100 fps for trials without vibration. The resolution is 800×600 px². We extract data with ImageJ [20] including average detached drop diameters D_d , axial drop elongations L and the position of the drop center of mass X_d compared to the nozzle surface. Images were calibrated (36 px/mm)

using the outer diameter (7.86 ± 0.01 mm for $D_p = 0.32$ mm) of the nozzle. The main output data are resumed in fig. 4.2.

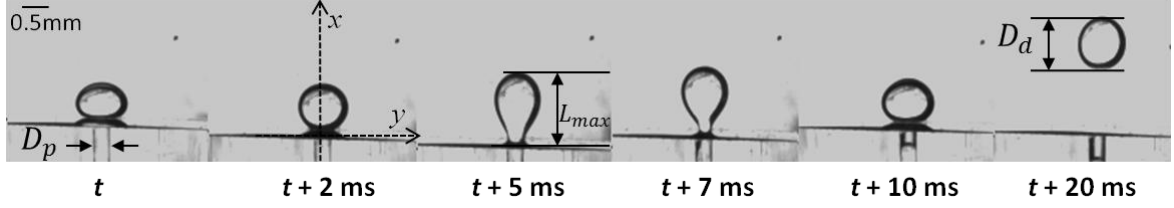


Figure 4.2: Visual summary of the output data. Drop detaching in stretching mode in time t for the reference system, $D_p = 0.32$ mm, $q = 3.6 \mu\text{L}\cdot\text{s}^{-1}$, $f = 100$ Hz, $A = 0.209$ mm.

2.3.3. Experimental protocol

The tank is filled with the continuous phase and the tube and syringe with the dispersed phase. The syringe pump is activated and drop diameters are measured without vibration. Drops are formed in dripping mode. We calculate Bond numbers Bo and Weber numbers We as Clanet and Lasheras [21]: we find $Bo = [(\rho_{cp} - \rho_{dp})gD_p^2/2\gamma]^{1/2}$ (with g the gravitational acceleration) from 1.7×10^{-2} to 1.5×10^{-1} and $We = \rho_{dp}v_{dp}^2D_p/\gamma$ from 4.5×10^{-3} to 2.8×10^{-1} . These values are below the critical We for the transition to jetting (at the given Bo), confirming the setup operates in dripping mode. From the drop diameters obtained without vibration, we calculate the *in situ* interfacial tensions by Tate's law [22]:

$$(\rho_{cp} - \rho_{dp}) \frac{\pi}{6} D_d^3 g = \mathcal{F}_{HB} \pi D_p \gamma \quad (4.2)$$

Drop detachment occurs when buoyancy (left-hand side of Eq. (4.2)) exceeds the maximum capillary force $F_Y^{max} = \pi D_p \gamma$ that the drop neck can resist without breaking. D_d is the detached drop diameter. \mathcal{F}_{HB} is the Harkins Brown correction factor [23]: it accounts for the fraction of liquid volume which stays attached to the nozzle after drop detachment. We use the \mathcal{F}_{HB} factor of Mori [24]. The *in situ* interfacial tension is then compared to the measured one (table 4.1), to ensure the setup is adequately cleaned.

Then, vibration is applied. A forcing frequency is set and an upwards amplitude sweep is performed. Measurements are made at different amplitudes, ensuring one is always made at the threshold where a transition in drop generation occurs (see 2.4 for details on the transition). This is repeated for frequencies from 30 to 150 Hz. From 30 to 100 Hz, 10 Hz intervals are applied. Above 100 Hz, intervals vary depending on the pore diameter. The vibrating exciter limitations do not enable us to observe the stretching mode above 150 Hz for $D_p = 0.32$ mm and 110 Hz for $D_p = 0.11$ mm. After trials, a cleaning agent at 3 vol% (Mucosol, Merz) fills the setup for 24h and it is rinsed with distilled water leading to a hydrophilic glass surface. Then, the organic dispersed phase does not wet the nozzle and the outer nozzle diameter does not influence drop detachment.

For each test condition (*i.e.*, physicochemical system, pore diameter, dispersed phase flow rate and forcing frequency), three trials are carried out to determine the transition threshold. For

each trial, six detached drops are studied. For each drop, ten images are analyzed. We checked that the accuracy of the diameter measurement from ten different snapshots of a given drop is sub-pixel. For a given trial, we noted variations up to 2 px at most in diameter from one drop to another. In the figures displaying drop diameters, the error bars correspond to the relative standard deviation in drop diameters: it ranges between 1% to 7% depending on the test conditions.

2.4. Transition from dripping to stretching mode

Figure 4.3 shows typical variations of the drop diameter as a function of the forcing amplitude at a set forcing frequency f . The drop diameter falls (by 63%) at a threshold amplitude A_{th} . The same behavior occurs for all systems. For the reference system, a relative decrease in drop diameter of 45% to 76% was found at A_{th} compared to without vibration depending on f , for all pore diameters. For system 2, similar values were found: 29% to 73%. This fall at A_{th} corresponds to a transition in the drop generation regime. For $A < A_{th}$, drops detach in dripping mode and their diameter is close to the diameter of the drop formed without vibration: detachment is buoyancy-controlled. For $A > A_{th}$, the drop detaches when its mode 1 eigenfrequency coincides with f and when it reaches a critical elongation ratio: detachment is controlled by the excitation force. Figure 4.2 shows how a drop elongates at resonance (characteristic mode 1 resonance shape) and detaches. We named this the “stretching mode” [19]. It should be noted that there is an amplitude interval where both modes coexist. The threshold amplitude A_{th} is defined as the upper bound of that interval, when all drops are generated in stretching mode.

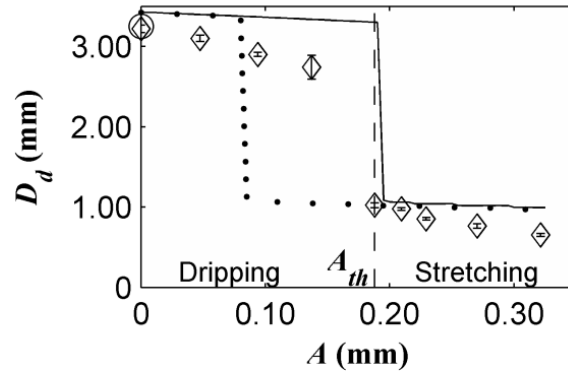


Figure 4.3: Transition from dripping to stretching mode: generated drop diameter as a function of the forcing amplitude for the reference system, $D_p = 0.32$ mm, $f = 100$ Hz, $q = 3.6 \mu\text{L}\cdot\text{s}^{-1}$. (\diamond) Experimental data; experimental threshold (dashed line); (O) theoretical drop size without vibration from Eq. (4.2); simulation results of section 2.6.3, Eq. (4.14) (dotted line); of section 2.6.4, Eq. (4.17) with $\alpha = -1.9$, $\mathcal{C} = 4.4$ (solid line).

We proposed a simple model to describe the main features of stretching mode [19]. Below, we recall its main arguments and derive scaling laws to provide a framework to analyze our experimental results in section 2.5. The vibrating bound drop is considered as a linearly forced

harmonic oscillator (LFHO) with moderate damping [25]. Drop growth is considered slow enough for oscillations to reach steady state. We are aware that these assumptions are strong since the system is probably no longer linear when oscillations are such that the drop detaches and the process remains transient. However they are required to develop the following scaling laws. A simple analytical expression of the mode 1 eigenfrequency f_1 of a bound drop has been empirically established by Bisch *et al.* [6] for D_d/D_p of 1.3 to 7 and fluids of equal densities:

$$f_1 = \frac{1}{2\pi} \sqrt{\frac{6k\gamma \sqrt{D_p}}{\pi\rho_{dp} D_d^2}} \quad (4.3)$$

k is a constant that should depend on the fluid density ratio, with $k = 9$ for fluids of equal densities. D_d is the resonating bound drop diameter, which we assimilate to the detached drop diameter. Bisch *et al.* [6] also propose an empirical expression for the damping coefficient β :

$$\beta/f_1 = a(\eta_{dp}/\rho_{dp}) + b(\eta_{cp}/\rho_{cp}) \quad (4.4)$$

with $a = 4.5 \times 10^3$ and $b = 2.32 \times 10^5$ if $\eta_{dp}/\rho_{dp} > \eta_{cp}/\rho_{cp}$ and $a = 1.57 \times 10^5$ and $b = 4.5 \times 10^4$ if $\eta_{dp}/\rho_{dp} < \eta_{cp}/\rho_{cp}$. We assume Eq. (4.3) and (4.4) can be reasonably applied to our trials as the density ratio ρ_{cp}/ρ_{dp} is in the order of 1 (it ranges from 1.26 to 1.33). Also, we neglect the effect of buoyancy on f_1 and β .

From Eq. (4.2) and (4.3), omitting \mathcal{F}_{HB} , we deduce the minimum forcing frequency above which a growing drop may detach in stretching mode (if $A > A_{th}$):

$$f_{1,min} = \frac{k^{1/2}}{2 \times 6^{1/6} \pi^{3/2}} \frac{|\rho_{cp} - \rho_{dp}|^{2/3} g^{2/3}}{\gamma^{1/6} D_p^{1/6} \rho_{dp}^{1/2}} \quad (4.5)$$

The minimum forcing frequency is around 8 Hz for $D_p = 0.32$ mm for the reference system and 14 Hz for $D_p = 0.11$ mm for system 2. This is smaller than the lower bound of the frequency range investigated. Consequently, drops may detach in stretching mode.

Whatever the mode (dripping or stretching), the drop detaches when the restoring capillary force F_γ exceeds the maximum capillary force F_γ^{max} . Under LFHO assumption, F_γ reads:

$$F_\gamma = \frac{\pi}{6} D_d^3 \rho_{dp} \omega_1^2 x_d(t) \quad (4.6)$$

with ω_1 the eigenpulsation of the bound drop without damping. x_d is the displacement of the drop center of mass with respect to its rest position (absence of buoyancy and excitation forces). The force-based detachment criterion can be easily recast into an elongation-based criterion:

$$x_d(t) \geq \frac{6D_p\gamma}{D_d^3\rho_{dp}\omega_1^2} \quad (4.7)$$

The displacement of the drop center of mass x_d is made up of a stationary part due to buoyancy and an oscillatory part due to the excitation force. Assuming quasi steady state, x_d reads:

$$x_d(t) = \frac{\phi g}{\omega_1^2} + A_d \sin(\omega t + \delta) \quad (4.8)$$

with $\phi = (\rho_{cp} - \rho_{dp})/\rho_{dp}$, δ the phase shift and A_d the amplitude given by the well-known expression [25]:

$$A_d = \frac{\omega^2 \phi A}{\sqrt{(\omega_1^2 - \omega^2)^2 + Q^{-2} \omega_1^2 \omega^2}} \quad (4.9)$$

Q is the quality factor given by $Q = \omega_1/(2\beta)$. Since β is given by Eq. (4.4), Q depends only on the phase densities and viscosities. A_d is maximum when $\omega_1(D_d) = \omega(1 - 1/(2Q^2))^{1/2}$, *i.e.*, $\omega_1(D_d) \cong \omega$ for moderate damping. In that case, A_d simplifies to $A_d \cong Q\phi A$.

In dripping mode, the drop has left the resonance range and its eigenfrequency is much lower than the forcing frequency. Then, buoyancy dominates: Eq. (4.7) and (4.8) reduce to Eq. (4.2) (omitting \mathcal{F}_{HB}). In stretching mode, the drop detaches at resonance ($\omega_1 \cong \omega$). Its diameter is thus:

$$D_d \cong \left(\frac{6k\gamma D_p}{\pi\rho_{dp}} \right)^{1/4} \frac{1}{\sqrt{\omega}} \quad (4.10)$$

An estimate of the threshold amplitude may be derived from the above equations neglecting buoyancy and assuming that the detachment criterion is satisfied at an oscillation peak:

$$A_{th} \cong \left(\frac{\pi}{k} \right)^{3/4} \left(\frac{6D_p\gamma}{\rho_{dp}} \right)^{1/4} \frac{1}{Q\phi\sqrt{\omega}} \quad (4.11)$$

As a result, D_d and A_{th} should both scale as $\omega^{-1/2}$, *i.e.*, $f^{-1/2}$.

2.5. Impact of process parameters and system properties

In this section, we study the effect of process parameters (pore diameter, dispersed phase flow rate) and system properties (interfacial tension, dispersed phase viscosity) on the dripping to stretching transition. Threshold amplitudes A_{th} are determined from an amplitude sweep and drop diameters at A_{th} from image analysis. Error bars are generally large for threshold amplitudes partly due to measurement errors and partly due to the difficulty to repeatedly estimate the threshold.

2.5.1. Influence of pore diameter

Figure 4.4 reports the variations of the threshold amplitude and generated drop diameter as a function of the forcing frequency for two pore diameters, *i.e.*, $D_p = 0.11$ mm and 0.32 mm (more pore diameters were tested in another paper in the case of the reference system [19]). Threshold amplitude variations with forcing frequency are monotonous (fig. 4.4(a)) and do not exhibit the V- or W-shape reported by W&B [17] or Kim [18], respectively. In the latter cases,

bound drop volume (thus eigenfrequencies) are fixed, independently of f . On the contrary, in our setup, the drop grows until its eigenfrequency coincides with f .

The threshold amplitude decreases as the forcing frequency increases (fig. 4.4(a)), in accordance with Eq. (4.11). Eq. (4.11) predicts a $f^{-1/2}$ scaling but our data scale differently: $f^{-0.71\pm 0.07}$ for $D_p = 0.11$ mm and $f^{-1.05\pm 0.13}$ for $D_p = 0.32$ mm. Also, thresholds are twice higher for $D_p = 0.11$ mm than for $D_p = 0.32$ mm. This contradicts the expected $D_p^{1/4}$ scaling (Eq. (4.11)). We return to this in section 2.6.

The drop diameter decreases with increasing forcing frequency (fig. 4.4(b)). The $f^{-1/2}$ scaling predicted by Eq. (4.10) was verified for four pore diameters ranging from 0.11mm to 0.75mm [19]: we specifically find $f^{-0.48\pm 0.03}$ for $D_p = 0.11$ mm and $f^{-0.48\pm 0.04}$ for $D_p = 0.32$ mm. The larger the pore diameter, the larger the drops produced. However, from experimental data [19], it is difficult to conclude on the relevance of the predicted $D_p^{1/4}$ scaling as the deviation of the data to the $D_p^{1/4}$ scaling is large (0% to 31%, depending on f).

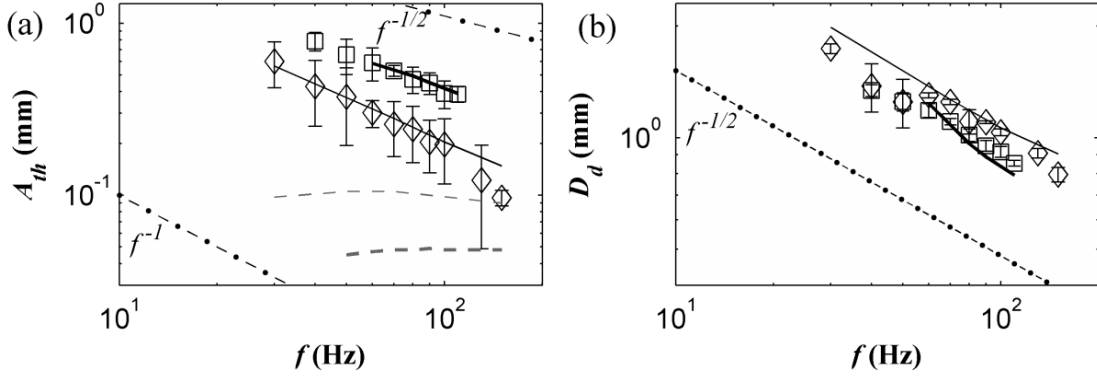


Figure 4.4: Impact of pore size on (a) threshold amplitude A_{th} and (b) drop diameter at A_{th} , for the reference system. (\square) $D_p = 0.11$ mm, $q = 2.2 \mu\text{L}\cdot\text{s}^{-1}$; (\diamond) $D_p = 0.32$ mm, $q = 6.1 \mu\text{L}\cdot\text{s}^{-1}$. Simulations from Eq. (4.14) of section 2.6.3 (dashed line); Eq. (4.17) of section 2.6.4 (solid line): $D_p = 0.11$ mm (thick); $D_p = 0.32$ mm (thin).

2.5.2. Influence of dispersed phase flow rate

Four dispersed phase flow rates q were applied to the reference system, for $D_p = 0.32$ mm: $q = 2.5 \mu\text{L}\cdot\text{s}^{-1}$, $4.3 \mu\text{L}\cdot\text{s}^{-1}$, $6.5 \mu\text{L}\cdot\text{s}^{-1}$ and $14.4 \mu\text{L}\cdot\text{s}^{-1}$. Threshold amplitudes and drop diameters do not vary significantly with these flow rates according to the error bars (see supplementary material in section 2.9.3). This is consistent with Eq. (4.10) and (4.11). For higher flow rates, this parameter could become significant. A drop may no longer have time to reach large-amplitude oscillations at resonance for stretching mode. Also, a transition to jetting would occur [21,26,27] (out of the scope of this paper).

When q increases from 2.5 to $14.4 \mu\text{L}\cdot\text{s}^{-1}$, the mean number of oscillations between two drops at $f = 100$ Hz decreases from 28 to 4. As the threshold is little affected by q in the investigation range, we infer that the steady-state oscillation regime is reached in just a few oscillations.

2.5.3. Influence of interfacial tension

Experiments were carried out for the reference system and systems 1 and 2 ($\gamma = 50.7 \text{ mN.m}^{-1}$, 19.0 mN.m^{-1} and 5.4 mN.m^{-1} , resp.) for $D_p = 0.32 \text{ mm}$. The threshold amplitude scaling is not significantly affected by γ : $f^{-0.95 \pm 0.08}$ for system 1 and $f^{-0.95 \pm 0.26}$ for system 2 compared to $f^{-1.05 \pm 0.13}$ for the reference system (fig. 4.5(a)). However, it is not in accordance with the predicted $f^{-1/2}$ scaling (Eq. (4.11)). Higher SDS concentrations result in lower interfacial tensions, leading to lower threshold amplitudes for a drop to detach in stretching mode (fig. 4.5(a)). This is in qualitative agreement with Eq. (4.11) but it is difficult to conclude on the relevance of the predicted $\gamma^{1/4}$ scaling, as the deviation of the data to this scaling is large (8% to 32%, depending on f).

The $f^{-1/2}$ scaling of the drop diameter is maintained when the interfacial tension is decreased from 50.7 mN.m^{-1} to 5.4 mN.m^{-1} (fig. 4.5(b)): we find $f^{-0.48 \pm 0.01}$ for system 1 and $f^{-0.49 \pm 0.02}$ for system 2. Smaller drops are generated for lower interfacial tensions. The drop diameter roughly scales as $\gamma^{1/4}$ in accordance with Eq. (4.10) (deviations of 1% to 18%, depending on f).

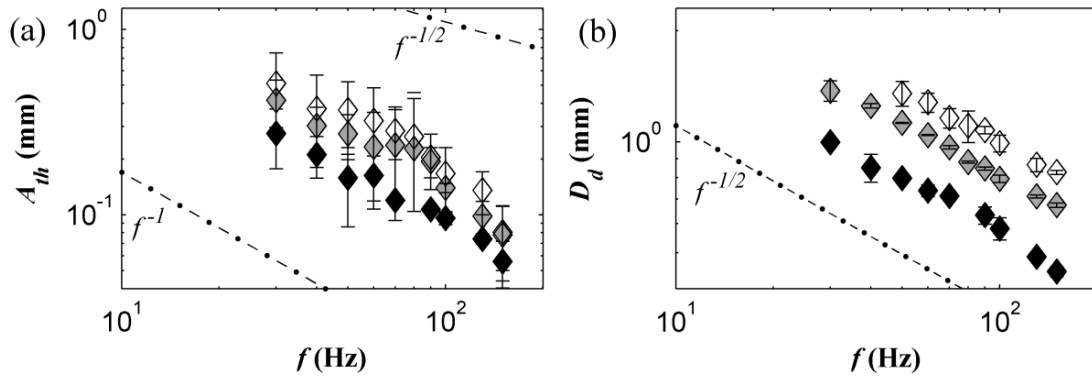


Figure 4.5: Impact of interfacial tension on (a) threshold amplitude A_{th} and (b) drop diameter at A_{th} , for $D_p = 0.32 \text{ mm}$, $q = 3.6 \text{ μL.s}^{-1}$. (◇) Reference system; (◊) system 1; (◆) system 2.

2.5.4. Influence of dispersed phase viscosity

Experiments were carried out for the reference system and systems 3 and 4 ($\eta_{dp} = 1.34 \text{ mPa.s}$, 1.79 mPa.s and 3.24 mPa.s , resp.) for $D_p = 0.32 \text{ mm}$. Threshold amplitudes A_{th} increase when η_{dp} increases (fig. 4.6(a)), as in W&B calculations [17]. When changing the reference system for system 3 (resp. 4), η_{dp} increases by 34% (resp. 142%) and A_{th} increases by 28% to 79% (resp. 62% to 133%). The effect of η_{dp} is stronger than expected. Indeed, when the reference system is changed for system 4, the quality factor Q decreases from 14.6 to 13.9 (Eq. (4.4)), leading to a theoretical 5% increase in A_{th} (Eq. (4.11)). In addition, the f^{-1} scaling with the reference system is not conserved for systems 3 and 4: we find $f^{-1.25 \pm 0.07}$ for system 3 and $f^{-0.73 \pm 0.12}$ for system 4. Thus, these results do not agree with the predicted $f^{-1/2}$ scaling (Eq. (4.11)). η_{dp} does not significantly impact drop diameter (fig. 4.6(b)), in agreement with Eq. (4.10) (valid for moderate damping).

As mentioned above, a system with a greater continuous phase viscosity was also studied: results and analysis are reported in supplementary material in section 2.9.4.

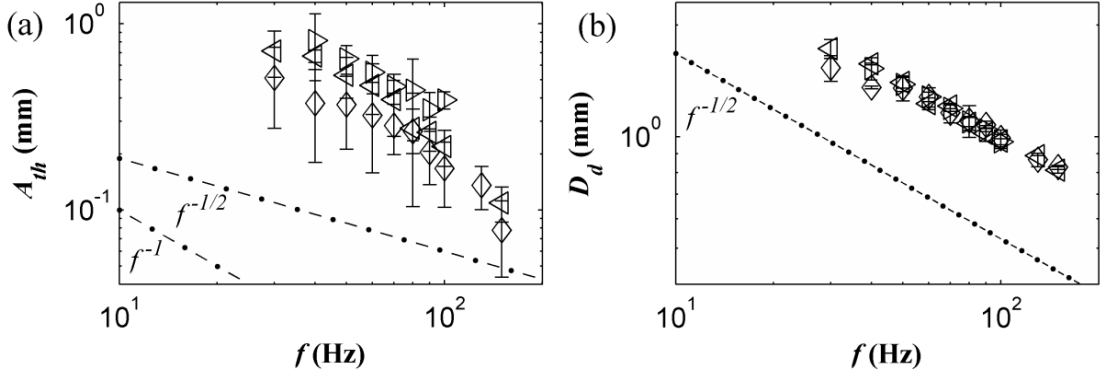


Figure 4.6: Impact of dispersed phase viscosity on (a) threshold amplitude A_{th} and (b) drop diameter at A_{th} , for $D_p = 0.32$ mm, $q = 6.1$ $\mu\text{L}\cdot\text{s}^{-1}$. (◇) Reference system; (◁) system 3; (▷) system 4.

2.6. Further analysis

In this section, we synthesize drop diameter data of section 2.5. Then, we analyze the elongation ratio for detachment. Finally, we propose a LFHO model that better reflects the A_{th} data.

2.6.1. Mode 1 resonance

Drop diameters at the threshold are consistent with the detachment at resonance when the bound drop mode 1 eigenfrequency coincides with the forcing frequency. To quantify the discrepancy between our data and Eq. (4.3) of Bisch *et al.* [6], we plot the dimensionless forcing pulsation (our data) and dimensionless drop eigenpulsation (Eq. (4.3)) against the drop to pore diameter, for different pore diameters and interfacial tensions (fig. 4.7(a)) and dispersed phase viscosities (fig. 4.7(b)). Pulsations are made dimensionless by $(8\gamma/(\rho_{dp}D_d^3))^{1/2}$ and are labeled with a * exponent.

Our data are well represented by Eq. (4.3) of Bisch *et al.* [6] (dashed line) until $D_d/D_p = 5$. For $D_d/D_p > 5$, our data are markedly above the Bisch *et al.* curve [6]. As stated, Eq. (4.3) was validated until $D_d/D_p = 7$. As the validity of the Bisch *et al.* [6] law is restricted, we consider the theoretical results of S&S established for any D_d/D_p and density ratio [7,8]. They analyzed the axisymmetric vibrations of a liquid drop in an outer fluid, in partial contact with a spherical bowl (see fig. 4.8) under the assumptions of zero gravity, negligible viscous effects and small surface deformations. Their calculated eigenfrequency f_n of mode n is:

$$f_n = \frac{1}{2\pi} \sqrt{\frac{8\gamma}{D_d^3 \rho_{dp} \lambda_n}} \quad (4.12)$$

with λ_n the eigenvalue for mode n , function of the support angle Θ and phase density ratio.

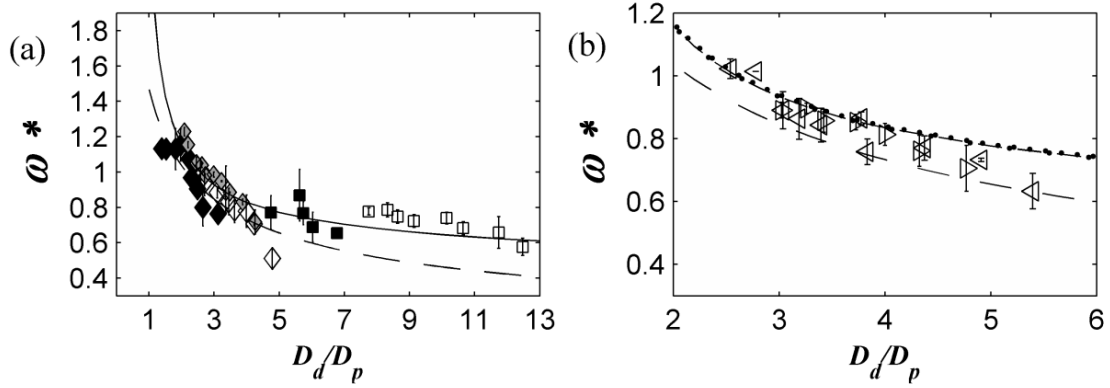


Figure 4.7: Dimensionless forcing pulsation depending on the drop to pore diameter. (a) For different interfacial tensions and pore diameters: reference system (white); system 1 (grey); system 2 (black). (\square) $D_p = 0.11$ mm; (\diamond) $D_p = 0.32$ mm. (b) For different dispersed phase viscosities, $D_p = 0.32$ mm: (\triangleleft) system 3; (\triangleright) system 4. Curve of the dimensionless eigenpulsation from: Eq. (4.3) of Bisch *et al.* [6] (dashed line); Eq. (4.12) of S&S [7] for the reference system (solid line), system 3 (dash-dotted line) and system 4 (dotted line).

Assuming fig. 4.8 is a reasonable simplification of our drop, we estimate $\Theta = \arcsin(D_p/D_d)$. We calculate λ_1 with Smithwick and Boulet's method [9] derived from the work of S&S [7], using densities and interfacial tensions of table 4.1. Our data are better fitted by the model of S&S [7] than by the law of Bisch *et al.* [6] (fig. 4.7(a) and (b)), notably for $D_d/D_p \geq 7$. As in Kim's [18] work, agreement between our data and S&S [7] calculations is remarkable as the binding constraint is different.

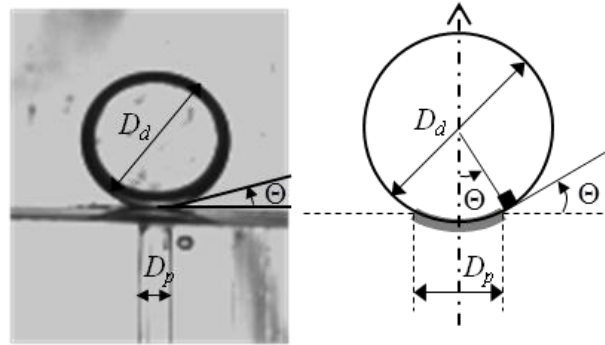


Figure 4.8: Analogy between the present drop bound to a nozzle (left) and a drop in partial contact with a solid spherical cap (right) as defined by S&S [7,8].

2.6.2. Critical elongation ratio

A critical elongation ratio L_{max}/D_d function of the drop to pore diameter ratio leads to drop detachment [17,19]. We measured L_{max}/D_d for all parameters tested (fig. 4.9), L_{max} being taken from the nozzle tip to the drop apex. The points lie roughly on the same curve (fig. 4.9), confirming that a drop detaches in stretching mode once a critical elongation is reached. Also, we see that the critical elongation ratio is essentially a function of D_d/D_p .

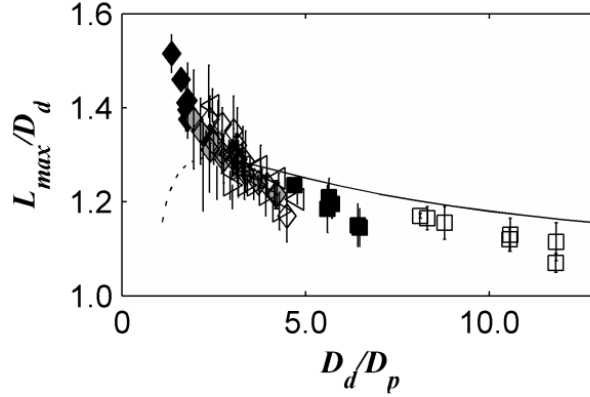


Figure 4.9: Drop elongation ratio function of the drop to pore diameter. Reference system (white); system 1 (grey); system 2 (black). (\square) $D_p = 0.11$ mm; (\diamond) $D_p = 0.32$ mm; (\blacktriangleleft) system 3, $D_p = 0.32$ mm; (\blacktriangleright) system 4, $D_p = 0.32$ mm. Curve from Eq. (4.13) (dashed and solid lines).

We remind that physicochemical properties vary for systems 1 to 4 compared to the reference system. L_{max}/D_d should depend on the viscosity ratio $\zeta = \eta_{dp}/\eta_{cp}$ and on the Ohnesorge number $Oh = \eta_{dp}/[\rho_{dp}\gamma(D_p/2)]^{1/2}$. The viscosity ratios we tested ($\zeta = 1.5$ to 3.6) may not vary enough to have an impact on L_{max}/D_d . For a free drop submitted to shear, Stone *et al.* found that breakup occurs above a critical elongation ratio, function of ζ but for $\zeta = 0.1$ to 1 , the critical elongation ratio did not vary significantly [28]. Similarly, we find Oh from 1.7×10^{-2} to 5.3×10^{-2} . These values may be too close to observe a difference in L_{max}/D_d , although for a free drop submitted to shear, these values are sufficiently different to obtain a twofold increase in aspect ratio [29].

We return to the elongation-based criterion for stretching mode (Eq. (4.7)). Let us note x_d^{max} the displacement of the drop center of mass when the drop axial elongation is L_{max} . In the limit $D_d \gg D_p$, we may consider that drop deformation is entirely localized in the neck. In that case, an estimation of x_d^{max} is given by $(L_{max} - D_d)$ and L_{max}/D_d roughly reads:

$$\frac{L_{max}}{D_d} \cong 1 + \frac{3}{4} \lambda_1 \left(\frac{D_d}{D_p} \right)^{-1} \quad (4.13)$$

The curve from Eq. (4.13) (solid line) is plotted against our data (fig. 4.9). For high drop to pore diameter ratios, critical elongation ratios are well estimated by Eq. (4.13), in accordance with S&S [7] or Bostwick and Steen [10]: for large D_d/D_p , the bound drop essentially experiences a rigid motion with deformation localized at the neck. For low D_d/D_p , Eq. (4.13) is no longer valid (dashed line) and drop deformation is rather uniform. From fig. 4.9, we deduce that the transition from the uniform deformation regime to the localized deformation regime occurs around $D_d/D_p \cong 3$. In our setup, the neck of the bound drop preexists (without vibration) contrary to in the configuration of S&S [7]. Thus, deformation is more quickly localized (they find values for the transition in the order of 10).

2.6.3. Oscillation model with the transient

The effects of process parameters and system properties on drop diameter concord with the scaling laws of section 2.4 but threshold amplitude variations are not well predicted. Thus we developed a finer model which describes drop growth and motion as a function of time. We still consider the drop as a LFHO as it probably provides the most simple framework to study growing drop oscillations. In the moving non-inertial frame of reference where the nozzle is still, the differential equation of motion of the drop center of mass reads:

$$\ddot{x}_d + 2\beta\dot{x}_d + \omega_1^2 x_d = \phi\omega^2 A \sin(\omega t + \pi) + \phi g \quad (4.14)$$

Drop mode 1 eigenpulsation ω_1 is given by Eq. (4.12) of S&S [7] and calculated using Smithwick and Boulet's method [9]. The damping coefficient β is estimated from the empirical Eq. (4.4) of Bisch *et al.* [6]. We suppose drop growth is slow enough for Eq. (4.14) to hold at every moment. The drop diameter increases in time t according to:

$$D_d(t) = \left(D_d^3(0) + \frac{6}{\pi} qt \right)^{1/3} \quad (4.15)$$

ω_1 and β depend on D_d , so vary with time as well. Equation (4.14) is solved numerically by the fourth order Runge-Kutta method. The integration time step is $0.01f^{-1}$. We begin calculations with $D_d(0) = 1.01 \times D_p$ as ω_1 is not defined for $D_d/D_p \leq 1$. We fix initial conditions of $x_d(0) = \phi g/\omega_1^2$ and $\dot{x}_d(0) = 0$. Figure 4.3 reports simulation results (dotted line) with A ranging from 0 to 0.325 mm (increment of 0.005 mm) for one data set on the reference system (a typical drop center-of-mass simulated motion close to the threshold is shown in supplementary material in section 2.9.5). Drop size at the transition is well predicted but it is overestimated far from the transition. Moreover, the threshold amplitude is underestimated: in this example, the predicted value is twice lower than experimentally.

In the example of fig. 4.4(a), we see that threshold values from the model (dashed lines) are well below experimental ones. Since the present model accounts for the transient (contrary to the model [19] briefly reported in section 2.4), these discrepancies cannot be attributed to the time spent by the bound drop in its resonance range as advanced earlier [19]. This is consistent with the experimental results of section 2.5.2 which show that the dispersed phase flow rate little affects the threshold amplitude. The effect of the frequency on the amplitude variations is also not well predicted. Finally, the effect of the pore diameter is opposite to experimentally: threshold amplitudes from the model are higher for $D_p = 0.32$ mm whereas in trials, threshold amplitudes are higher for $D_p = 0.11$ mm. We infer that damping is underestimated in this model and the effect of D_d/D_p is not well described.

2.6.4. Oscillator model with additional friction term β_{film}

We estimate the quality factor Q by $(L_{\text{max}} - D_d)/\phi A$ for bound drops at different amplitudes at $f = 100$ Hz (reference system). We find lower values than from Eq. (4.4) (around 3 times). Damping is higher than expected, even for amplitudes of the drop excitation force as

low as 0.015 mm (9% of the drop radius, well below A_{th}). Q is constant below the threshold amplitude A_{th} , so we assume that at A_{th} and below, nonlinear effects are weak and do not explain the higher damping.

Our system undergoes additional friction compared to configurations in the literature [6,7,11]. As the dispersed phase does not wet the nozzle tip, there is a wedge between the drop and nozzle surface, containing continuous liquid phase (fig. 4.8). Assuming $x_d(t)/D_d \ll D_p/D_d \ll 1$, an estimate of the wedge angle θ is given by D_p/D_d . When the drop oscillates, θ oscillates. The continuous phase in the wedge is driven outwards (inwards, resp.) when θ decreases (increases) with time. The viscous friction associated with the film flow leads to an extra friction term in the LFHO model of the oscillating drop. We note β_{film} the damping coefficient associated with the friction in the film and propose the following expression (see Appendix in 2.8 for details):

$$\beta_{\text{film}} = \mathcal{C} \frac{\eta_{cp}}{\rho_{dp}} \frac{D_p^\alpha}{D_d^{\alpha+2}} \quad (4.16)$$

\mathcal{C} is dimensionless. We infer \mathcal{C} depends only on the viscosity ratio η_{dp}/η_{cp} and α depends on the deformation regime (“uniform” or “localized”). The differential equation of motion of the drop center of mass now reads:

$$\ddot{x}_d + 2(\beta + \beta_{\text{film}}) \dot{x}_d + \omega_1^2 x_d = \phi \omega^2 A \sin(\omega t + \pi) + \phi g \quad (4.17)$$

We solve Eq. (4.17) by the same procedure as for Eq. (4.14). α and \mathcal{C} are identified from experimental threshold amplitudes since the slope of the curve $A_{th}(f)$ is related to α and the curve is translated up or down by increasing or decreasing \mathcal{C} , respectively. α and \mathcal{C} values are summarized in table 4.2.

α was determined by fitting simulation results to the data $A_{th}(f)$ for the reference system with $D_p = 0.32$ mm and $D_p = 0.11$ mm. We needed to introduce two distinct values of α depending on D_d/D_p . For $D_d/D_p \leq 5$, the data (obtained with $D_p = 0.32$ mm) are well represented with $\alpha = -1.9$. For $D_d/D_p > 5$, the data ($D_p = 0.11$ mm) are better represented with $\alpha = -1.4$.

When $\alpha = -1.9$ (resp. $\alpha = -1.4$), the viscous force per length unit of pore circumference that acts against the drop oscillations scales as $\theta^{-2.9}$ (resp. $\theta^{-2.4}$). In the case where a viscous force opposes a contact line movement, the dependence on the wedge angle is weaker: the force per length unit of the contact line scales as θ^{-1} . Indeed, the wedge angle is constant and the wedge translates parallel to the surface whereas in this case, the wedge angle varies, inducing the liquid flow in the wedge.

Table 4.2: Identified values of coefficients α and \mathcal{C} for β_{film} .

D_d/D_p	≤ 5			≥ 5
α	-1.9			-1.4
η_{dp}/η_{cp}	1.5	2	3.6	1.5
\mathcal{C}	4.4	6.0	7.4	8.2

The dispersed to continuous phase viscosity ratio is of 1.5, 2 and 3.6 for the reference system, systems 3 and 4, respectively. We determined \mathcal{C} for the different ratios by fitting simulation results to the data $A_{th}(f)$ (with α previously identified). \mathcal{C} increases monotonously from 4.4 to 7.4 when η_{dp}/η_{cp} increases from 1.5 to 3.6. We logically expect that at a set η_{cp} , the viscous friction in the film increases with η_{dp}/η_{cp} (drop interface becomes less and less mobile).

Figure 4.3 shows that the threshold amplitude is well reproduced by adding β_{film} (solid line). Drop diameter at the transition is also well predicted. However, drop diameters are still overestimated far from the transition. Above A_{th} , this may be due to nonlinear effects. A downwards shift in resonance frequency occurs when increasing A for soft nonlinear oscillators [15,16]. Therefore, at the set forcing frequency, smaller drops which would usually resonate at higher frequencies resonate and detach in stretching mode [19]. Below A_{th} , overestimation is attributed to the excitation of a higher resonance mode than mode 1. This is not taken into account in Eq. (4.14) or (4.17).

When β_{film} is included, the effect of the frequency on amplitude variations is well described (fig. 4.4(a), solid lines). The effect of the pore diameter on the threshold is also well accounted for (fig. 4.4(a)). Below 60 Hz, no clear threshold appeared in simulations for $D_p = 0.11$ mm. (fig. 4.4(a)). We expect the drop behaves as an overdamped oscillator. Experimentally, the threshold is less sharp however exists.

We note that simulations for systems 1 and 2 were performed with \mathcal{C} and α identified on the reference system, since the viscosity ratios are the same. Threshold amplitudes and drop diameters are relatively well predicted for these systems from the model (grey and black points, fig. 4.10).

Overall, the theoretical threshold amplitudes from the modified LFHO model well reproduce experimental ones (fig. 4.10(a)) and drop diameters are also well accounted for (fig. 4.10(b)).

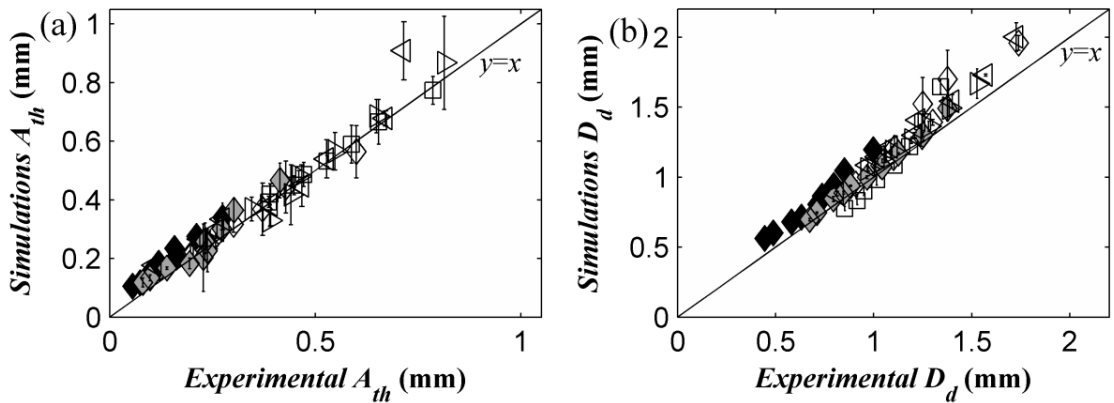


Figure 4.10: Simulation and experimental values for different forcing frequencies for (a) threshold amplitudes A_{th} and (b) drop diameters at A_{th} . Reference system (white); system 1 (grey); system 2 (black). (\square) $D_p = 0.11$ mm; (\diamond) $D_p = 0.32$ mm; (\blacktriangleleft) system 3, $D_p = 0.32$ mm; (\blacktriangleright) system 4, $D_p = 0.32$ mm.

2.7. Conclusion

Studies on vibrated growing drops are rare [19] compared to those on constant volume drops [5-18]. In addition, few studies focus on vibrated drops where detachment occurs from the surface [17-19]. In the present work, we studied drop growth and detachment from an axially vibrating nozzle. We studied the impact of forcing parameters as well as nozzle inner diameter, dispersed phase flow rate, interfacial tension and dispersed phase viscosity. At a set forcing frequency, we observed a transition in drop diameter when increasing the forcing amplitude: above a threshold, drops detach at resonance, *i.e.*, when the first eigenfrequency of the growing drop coincides with the forcing frequency. Below the threshold, larger drops detach in dripping mode, driven by buoyancy. The diameter of the drops formed above the threshold is very well correlated to the mode 1 eigenfrequency calculated by S&S [7]. We remind that the eigenfrequency depends on the support and drop diameters, phase densities and interfacial tension. The agreement between our results and calculations of S&S [7,8] is remarkable as the binding constraint is different.

We examined the critical elongation ratio for drop detachment, which depends on the drop to pore diameter. We discerned two deformation regimes: for low D_d/D_p , a uniform deformation regime and for larger D_d/D_p , a localized deformation regime (limited to the neck). The neck preexists, so the latter regime appears earlier than in the configuration of S&S [7,8]. We proposed a transient model to account for the threshold amplitude variations. To our knowledge, critical amplitudes for drop ejection have not been accounted for before. We modelled the growing drop as a LFHO, with the eigenfrequency of S&S [7,8]. Since the dispersed phase does not wet the nozzle, we introduced an extra damping coefficient to account for the viscous dissipation in the film of continuous phase between the drop and nozzle surface. The friction force is described as a power law of the pore to drop diameter ratio. The exponent depends on the deformation regime and the multiplier constant on the viscosity ratio. Our model well reproduces the experimental threshold amplitudes and resulting drop diameters.

In further work, it would be interesting to study drop generation when axial vibration is coupled to the shear stress exerted by a circulating phase, to approach vibrating membrane emulsification conditions.

2.8. Appendix: additional friction term β_{film}

We consider a drop attached to the nozzle inner edge (fig. 4.11). We suppose that the drop diameter is large compared to the nozzle inner diameter and that the drop shape (at rest) can be approached by a spherical cap of angle $(\pi - \Theta)$. Θ is the angle of the wedge formed between the drop at rest and the nozzle surface. Θ is given by $\Theta = \arcsin(D_p/D_d) \cong D_p/D_d$.

When the drop is submitted to vibrations, we consider that it may be described by a truncated ellipsoid of revolution that oscillates between prolate and oblate shapes. The wedge angle varies with time as the drop oscillates. Its instantaneous value is $\theta(t) \cong (1 + 4 x_d(t)/D_d) D_p/D_d$ in the limit of small drop deformations. The continuous phase in the wedge

is driven outwards (inwards, resp.) when θ decreases (increases, resp.) with time. The viscous friction associated with the film flow in the wedge leads to an additional friction term in the LFHO model of the oscillating drop. We note F_{film} the corresponding friction force that acts against drop axial oscillations. Under the assumption $x_d(t)/D_d \ll D_p/D_d \ll 1$, we infer that F_{film} depends on η_{cp} , η_{dp} , D_p , D_d and \dot{x}_d . From dimensional arguments, we deduce:

$$\frac{F_{\text{film}}}{\eta_{cp} D_p \dot{x}_d} = \mathcal{F} \left(\frac{\eta_{dp}}{\eta_{cp}}, \frac{D_p}{D_d} \right) \quad (4. A1)$$

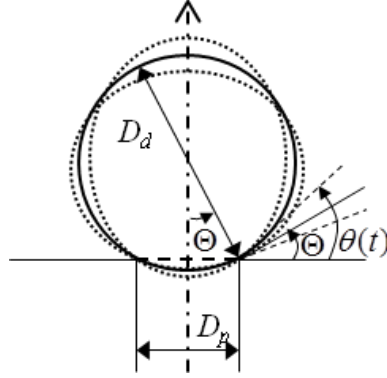


Figure 4.11: Sketch of an attached drop oscillating between prolate and oblate shapes.

In the case of a viscous force that opposes a contact line movement, the vicinity of the contact line is usually described as a wedge with a well-defined dynamic contact angle. The force per length unit of the contact line is proportional to the liquid viscosity and is inversely proportional to the dynamic contact angle. In analogy to this, we seek a law in the generic form:

$$\frac{F_{\text{film}}}{\eta_{cp} D_p \dot{x}_d} = \mathcal{G} \left(\frac{\eta_{dp}}{\eta_{cp}} \right) \times \left(\frac{D_p}{D_d} \right)^{\alpha'} \quad (4. A2)$$

with D_p/D_d the wedge angle and \mathcal{G} a function of η_{dp}/η_{cp} . We note that, for a moving contact line, the wedge angle is constant and the wedge translates parallel to the surface whereas in our case, the wedge angle varies, leading to the liquid flow in the wedge. We deduce the expression of the damping coefficient β_{film} (associated with F_{film}) appearing in Eq. (4.17):

$$\beta_{\text{film}} = \mathcal{C} \left(\frac{\eta_{dp}}{\eta_{cp}} \right) \times \frac{\eta_{cp}}{\rho_{dp}} \frac{D_p^{\alpha'+1}}{D_d^{\alpha'+3}} = \mathcal{C} \left(\frac{\eta_{dp}}{\eta_{cp}} \right) \times \frac{\eta_{cp}}{\rho_{dp}} \frac{D_p^\alpha}{D_d^{\alpha+2}} \quad (4. A3)$$

where $\mathcal{C} = \mathcal{C}(\eta_{dp}/\eta_{cp})$ depends on the dispersed to continuous phase viscosity ratio.

2.9. Supplementary material

See supplementary material for insight on: 2.9.1, the interfacial tension at the intermediate plateau; 2.9.2, the characteristic time to reach this plateau; 2.9.3, the figures for the influence of dispersed phase flow rate; 2.9.4, the figures and analysis for the influence of the continuous phase viscosity and 2.9.5, the drop center-of-mass motion with respect to the nozzle surface.

2.9.1. Interfacial tension at the intermediate plateau

SDS adsorption occurs in three steps on a dodecane-water interface [30,31]. First, interfacial tension decreases rapidly with SDS adsorption by diffusion. Then, a plateau occurs (quasi-static equilibrium). SDS is no longer adsorbed due to electrical repulsion as the interface is charged, SDS being anionic. Once the potential barrier is overcome (after thousands of seconds), interfacial tension reduces further to reach the equilibrium value. Plateau values are higher than equilibrium values.

For each system, the dynamic interfacial tension (γ) was measured as a function of time (t) with a tensiometer using the rising drop method. As Deshiikan *et al.* [31], the variations of the dynamic interfacial tension were plotted as a function of $1/\sqrt{t}$ (fig. 4.A1). For systems with SDS, two distinct regions I and II are revealed, respectively: a plateau or a slow decrease in interfacial tension at early times followed by a steep decrease at long times. The former region (I) corresponds to the intermediate plateau. We note that region I is preceded by another region (very early times) where the interfacial tension falls from a value close to the interfacial tension without surfactant to the plateau value. This is not seen on fig. 4.A1 as this phenomenon is too fast to be captured by our tensiometer. Furthermore, region II is followed, after thousands of seconds, by a plateau corresponding to the equilibrium interfacial tension. This is not seen on fig. 4.A1 as we stop measurements after 500 s. According to the method of Deshiikan *et al.* [31], we estimate the intermediate plateau interfacial tension by extrapolating for $t \rightarrow \infty$ ($1/\sqrt{t} \rightarrow 0$) the straight line of region I.

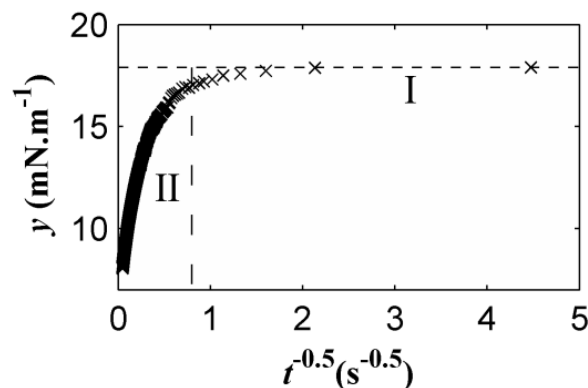


Figure 4.A1. Dynamic interfacial tension as a function of $1/\sqrt{t}$, for system 1.

2.9.2. Characteristic time to reach the intermediate plateau

According to Bonfillon *et al.* [32] for SDS at the dodecane-water interface under equilibrium conditions, the surface pressure, Π , can be related to the surface surfactant concentration, Γ , by:

$$\Pi = \gamma_0 - \gamma = -\frac{n}{2}k_B T \Gamma_\infty \ln\left(1 - \frac{\Gamma}{\Gamma_\infty}\right) + n k_B T \Gamma \quad (4.B1)$$

with γ_0 the equilibrium interfacial tension without surfactant, γ the equilibrium value with surfactant, Γ_∞ the limiting surfactant adsorption at equilibrium and n equal to 2 for SDS entirely ionized at the surface. Bonfillon *et al.* [32] report $\Gamma_\infty = 1.5 \times 10^{18} \text{ m}^{-2}$ for SDS at the dodecane-water interface. Following Deshiikan *et al.* [31], we assume Eq. (4.B1) provides a good estimate of Γ for surface pressures under dynamic conditions. Thus, the surface surfactant concentration at the plateau denoted Γ_1 can be deduced from the measurement of γ_0 and the estimation of the interfacial tension γ_1 at the plateau.

Assuming that surfactant transfer is purely diffusive at early times and that the subsurface surfactant concentration remains small enough compared to its bulk concentration far from the surface, the short-time variations of Γ are given by:

$$\Gamma = 2 \sqrt{\frac{\mathcal{D}t}{\pi}} C \quad (4.B2)$$

with C the bulk free-surfactant concentration far from the surface and \mathcal{D} the bulk diffusion coefficient of the surfactant ions [32]. Lindman *et al.* [33] report $\mathcal{D} = 6 \times 10^{-11} \text{ m}^2 \cdot \text{s}^{-1}$ for the self-diffusion coefficient of SDS. We deduce the characteristic time τ_{diff} to reach the intermediate plateau:

$$\tau_{diff} = \frac{\pi \Gamma_1^2}{4 \mathcal{D} C^2} \quad (4.B3)$$

For system 1, the surfactant concentration ($0.85 \text{ g} \cdot \text{L}^{-1}$) is significantly lower than the CMC, as the CMC of SDS in water is $2 \text{ g} \cdot \text{L}^{-1}$, *i.e.*, $4.18 \times 10^{24} \text{ m}^{-3}$ (SDS molar mass: $M_{\text{SDS}} = 288.4 \text{ g} \cdot \text{mol}^{-1}$) [32]. Neglecting the formation of aggregates, the free-surfactant concentration far from the surface is $C = 1.77 \times 10^{24} \text{ m}^{-3}$. Measurements give $\gamma_0 - \gamma_1 = 31.7 \text{ mN} \cdot \text{m}^{-1}$. From this, we find $\Gamma_1 = 1.44 \times 10^{18} \text{ m}^{-2}$ and $\tau_{diff} = 8.7 \times 10^{-3} \text{ s}$. For system 2, the surfactant concentration ($17 \text{ g} \cdot \text{L}^{-1}$) is about an order of magnitude greater than the CMC. We consider that the free-surfactant concentration far from the surface is close to the CMC, *i.e.*, $C \approx 4.18 \times 10^{24} \text{ m}^{-3}$. Since $\gamma_0 - \gamma_1 = 45.3 \text{ mN} \cdot \text{m}^{-1}$, we find $\Gamma_1 = 1.5 \times 10^{18} \text{ m}^{-2}$ and $\tau_{diff} = 1.7 \times 10^{-3} \text{ s}$.

For experiments with system 1 (resp. 2), drop formation time ranges from 0.044 s (resp. 0.013 s) to 0.378 s (resp. 0.145 s), depending on the forcing parameters. As calculated above, $\tau_{diff} = 8.7 \times 10^{-3} \text{ s}$ (resp. $\tau_{diff} = 1.7 \times 10^{-3} \text{ s}$). The characteristic time is significantly lower than the drop formation time (5 to 85 times), so we consider that the measured plateau value gives an adequate estimation of the interfacial tension when drops form.

When the interface is submitted to vibrations, mass transfer is expected to be enhanced and the characteristic time to reach the intermediate plateau should be shorter. In fact, Gomaa *et al.* [34] showed that vibration led to a faster decrease in interfacial tension, due to an increase in the surfactant transfer rate. The higher the forcing frequency, the faster the decrease.

Clift *et al.* [35] mention several mass transfer studies of free oscillating liquid drops suspended in a second immiscible liquid and propose an empirical equation for the Sherwood number Sh_{cp} characterizing the solute (surfactant) mass transfer in the continuous phase. We assume this equation still holds for an attached drop oscillating at its eigenfrequency f_1 :

$$Sh_{cp} = 1.2 \sqrt{\frac{D_d^2 f_1}{\mathcal{D}}} \quad (4.B4)$$

with D_d the diameter of the volume-equivalent sphere according to Clift *et al.* [35] We approximate this diameter by that of the detached drop in stretching mode. Besides, the continuous phase Sherwood number Sh_{cp} is defined as [35]:

$$Sh_{cp} = [\overline{kS}/S_d] \frac{D_d}{\mathcal{D}} \quad (4.B5)$$

with \overline{kS} the time averaged transfer coefficient-area product and S_d the surface area of the volume-equivalent sphere. As a first approximation, we neglect the neck of the drop and consider that S_d and the attached drop surface area are both equal to πD_d^2 . Then, an estimate of the characteristic time to reach the plateau when diffusion is coupled to convection is given by:

$$\tau_{dc} = \frac{\Gamma_1 \pi D_d^2}{\overline{kS} C} = \frac{\Gamma_1}{1.2 C \sqrt{f_1} \mathcal{D}} \quad (4.B6)$$

From Eq. (4.B3) and (4.B6), we define the characteristic frequency f_c above which a significant mass transfer enhancement is expected:

$$f_c \approx \frac{\mathcal{D} C^2}{\Gamma_1^2} \quad (4.B7)$$

For systems 1 and 2, f_c is estimated at 84 Hz and 466 Hz, respectively. As the forcing frequency was between 30 Hz and 150 Hz, slight mass transfer enhancement is expected for system 1.

2.9.3. Influence of dispersed phase flow rate: figures

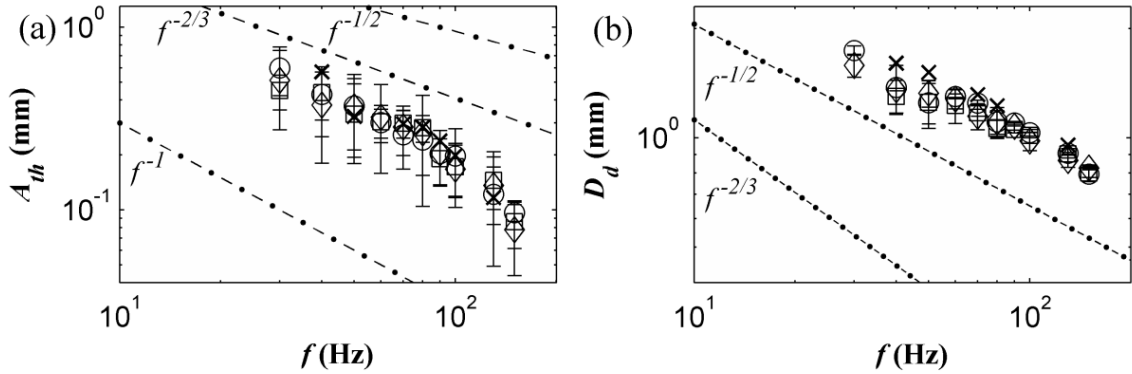


Figure 4.C1: Impact of dispersed phase flow rate on (a) threshold amplitude A_{th} and (b) drop diameter at A_{th} , for the reference system, $D_p = 0.32$ mm. (\square) $q = 2.4$ $\mu\text{L}\cdot\text{s}^{-1}$; (\diamond) $q = 3.6$ $\mu\text{L}\cdot\text{s}^{-1}$; (\circ) $q = 6.1$ $\mu\text{L}\cdot\text{s}^{-1}$; (\times) $q = 14.4$ $\mu\text{L}\cdot\text{s}^{-1}$.

2.9.4. Influence of continuous phase viscosity: figures and analysis

The system with an increased continuous phase viscosity is named system 5. The dispersed phase is dodecane. The continuous phase is 50 wt% distilled water with 50 wt% glycerol (98 vol%, Fisher Scientific). We find $\eta_{cp} = 4.18 \pm 0.54$ mPa.s, $\rho_{cp} = 1119 \pm 1.3$ $\text{kg}\cdot\text{m}^{-3}$ and $\gamma = 37.0 \pm 3.9$ $\text{mN}\cdot\text{m}^{-1}$.

Threshold amplitudes A_{th} are curiously unchanged for system 5 compared to the reference system (fig. 4.D1(a)), although the damping coefficient is doubled (Eq. (4.4)). η_{cp} is not the only property that varies. According to Eq. (4.11), the 27% decrease in interfacial tension may reduce A_{th} by 8% and the 12% increase in continuous phase density may further reduce it by 33% (ϕ increases from 0.33 to 0.49). At the same time, the increase in η_{cp} should double A_{th} (Q is halved). These contradictory effects seem to compensate even if we roughly predict that the latter effect should dominate.

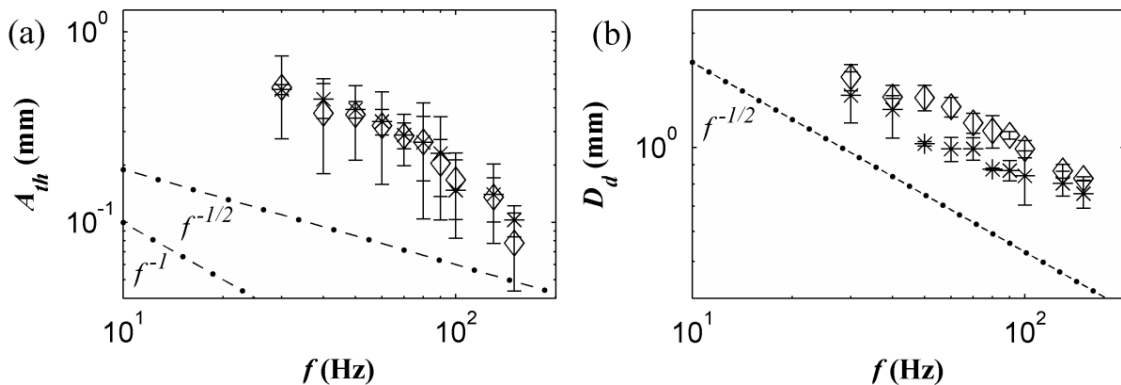


Figure 4.D1: Impact of continuous phase viscosity on (a) threshold amplitude A_{th} and (b) drop diameter at A_{th} , for $D_p = 0.32$ mm, $q = 6.1$ $\mu\text{L}\cdot\text{s}^{-1}$. (\diamond) Reference system; ($*$) System 5.

Drop diameter decreases markedly (14% to 17%) with increasing η_{cp} (fig. 4.D1(b)), opposite to expected. Damping may be roughly taken into account in Eq. (4.10) by introducing a correction factor $(1 - 1/(2Q^2))^{-1/4}$. This factor is slightly above 1, leading to a theoretical drop diameter increase of less than 1%. Lastly, the drop diameter scaling is of $f^{-0.32 \pm 0.03}$ instead of $f^{-1/2}$ for other systems.

The Bisch *et al.* [6] law (valid for fluids of equal densities) overestimates the drop eigenpulsation for system 5 (dashed line, fig. 4.D2), which exhibits the largest phase density contrast (1.49). This is not sufficient to explain the discrepancies, as the S&S [7,8] model also overestimates system 5 data (2% to 26% discrepancy, solid line, fig. 4.D2), even though this model is valid for different densities.

The overestimation cannot be solely attributed to the inviscid assumption: S&S [8] calculations with viscous effects led to a reduction of only about 6% in the eigenfrequency ($\sim 3\%$ for the drop diameter) with respect to the inviscid case. Nonlinearity is not a convincing explanation either. W&B [14] showed that nonlinear effects are promoted at low Ohnesorge numbers Oh. Oh is lower for the reference system than system 5 and the reference system is well described by S&S calculations [7,8].

For high η_{cp} , the drop can no longer be modeled as isolated in an infinite medium as for S&S [7,8]. Confinement affects the continuous phase flow around the drop, thus the hydrodynamic force exerted on it. Also, vibration is applied to the flexible seal (not the whole tank). For high η_{cp} , the surrounding phase next to the fluid column above the seal increasingly impacts the flow pattern above the seal, thus around the drop. As a result, we cannot model the data for this system with the model developed in section 2.6.4. It was thus excluded from the main results in the paper.

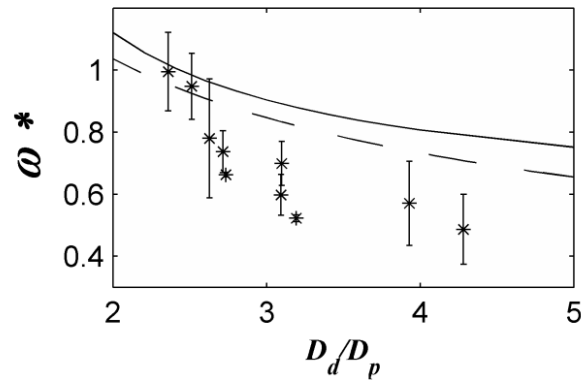


Figure 4.D2: Dimensionless forcing pulsation depending on the drop to pore diameter, for $D_p = 0.32$ mm, (*) system 5. Curve of the dimensionless eigenpulsation from: Eq. (4.3) of Bisch *et al.* [117] (dashed line); Eq. (4.12) of S&S [112] for system 5 (solid line).

2.9.5. Drop center-of-mass motion with respect to the nozzle surface

An example of the drop center-of-mass simulated motion (without β_{film}) with respect to the capillary surface (dashed line, fig. 4.E1) is plotted against the measured one (points, fig. 4.E1). In the trial, the amplitude is set at the threshold and the drop detaches at resonance, at 0.07 s. The drop center-of-mass motion is the superposition of two motions, *i.e.*, a slow monotonous motion due to drop growth (and to a lesser extent to buoyancy) and a rapid oscillatory motion due to the excitation force. The phase shift between the drop (oscillatory motion) and the vibrating exciter is well described, in accordance with the LFHO model [25], as described previously [19]. However, drop oscillation amplitude close to resonance is overestimated whereas it is underestimated before resonance.

Figure 4.E1 also shows the drop center-of-mass simulated motion when β_{film} is included (solid line). β_{film} further damps drop oscillations leading to a better agreement near resonance between simulations and measurements. However, before resonance, oscillation amplitudes from the model are again significantly lower than in experiments. As the support below the drop is open, part of the drop volume is free to oscillate in and out of the nozzle, leading to higher oscillation amplitudes. The relative impact of this phenomenon on drop oscillation amplitude is more important when the drop is small. This is not taken into account by either model.

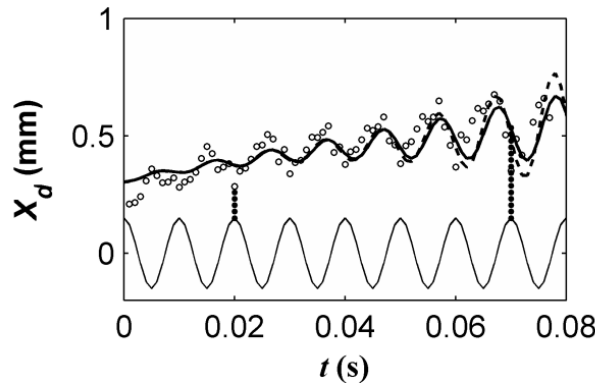


Figure 4.E1: Position of the drop centre of mass in time with respect to the capillary surface X_d for reference system, $D_p = 0.32$ mm, $f = 100$ Hz, $A = 0.150$ mm, $q = 6.1 \mu\text{L}\cdot\text{s}^{-1}$. (o)

Experimental data; capillary motion (thin solid line); theoretical curve from Eq. (4.14) (dashed line); Eq. (4.17) with $\alpha = -1.9$, $C = 4.4$ (thick solid line).

2.10. Acknowledgements

We thank J. Trubuil and T. Martin for their insight and work on the setup design, manufacturing and improvement.

3. Additional information

3.1. Initial conditions for the model

A more relevant initial condition on the centre-of-mass velocity than the one we used described in 2.6.3 would be $\dot{x}_d(0) = -\omega^3 \phi A / \omega_1^2$.

We consider that at $t = 0$, $\omega_1 \gg \omega$ as the drop is initially small and we consider that the drop undergoes steady-state forced oscillations. Thus, at $t = 0$, according to the LFHO model, the drop is in phase opposition with the capillary motion. From eq. (4.7), we therefore find:

$$\dot{x}_d(t) = \omega A_d \cos(\omega t - \pi) \quad (4. A11)$$

By replacing A_d in eq. (4.A11) by the expression of eq. (4.8), keeping in mind the assumption $\omega_1 \gg \omega$, we obtain:

$$\dot{x}_d(t) = \frac{\omega^3}{\omega_1^2} \phi A \cos(\omega t - \pi) \quad (4. A12)$$

For $t = 0$, we therefore find $\dot{x}_d(0) = -\omega^3 \phi A / \omega_1^2$, which would a more appropriate initial condition on the centre-of-mass velocity. However, we found that the initial conditions only have a weak effect on the final results (threshold amplitudes and drop diameters).

4. References

- [1] C. Arnaud, « Procédé et dispositif de fabrication d'une dispersion ou d'une émulsion », European patent EP 1 551 540 B1, 2006.
- [2] E. Lepercq-Bost, « Etude d'un procédé d'émulsification par membrane vibrante: compréhension des mécanismes, modélisation et optimisation », PhD Thesis, Ecole Centrale Paris, p. 224–233, 2008.
- [3] Lord Rayleigh, « On the Capillary Phenomena of jets », *Proc. R. Soc. Lond.*, 29, p. 71–97, 1879.
- [4] H. Lamb, *Hydrodynamics*, 6th Edition (Cambridge University Press, Cambridge, UK), p. 473–475, 1932.
- [5] H. Rodot, C. Bisch and A. Lasek, « Zero-gravity simulation of liquids in contact with a solid surface », *Acta Astronaut.*, 6, p. 1083–1092, 1979.
- [6] C. Bisch, A. Lasek and H. Rodot, « Comportement hydrodynamique de volumes liquides sphériques semi-libres en apesanteur simulée », *J. Méc. Théor. Appl.*, 1, p. 165–183, 1982.
- [7] M. Strani M. and F. Sabetta, « Free vibrations of a drop in partial contact with a solid support », *J. Fluid Mech.*, 141, p. 233–247, 1984.
- [8] M. Strani and F. Sabetta, « Viscous oscillations of a supported drop in an immiscible fluid », *J. Fluid Mech.*, 189, p. 397–421, 1988.
- [9] R. W. Smithwick III and J. A. Boulet, « Vibrations of Microscopic Mercury Droplets on Glass », *J. Colloid Interface Sci.*, 130 (2), p. 588–596, 1989.
- [10] J. B. Bostwick and P. H. Steen, « Capillary oscillations of a constrained liquid drop », *Phys. Fluids*, 21, 032108, 2009.
- [11] J. Vejrazka, L. Vobecka and J. Tihon, « Linear oscillations of a supported bubble or drop », *Phys. Fluids*, 25, 062102, 2013.
- [12] N. Abi Chebel, F. Risso and O. Masbernat, « Inertial modes of a periodically forced buoyant drop attached to a capillary », *Phys. Fluids*, 23, 102104, 2011.
- [13] X. Noblin, A. Buguin and F. Brochard-Wyart, « Vibrated sessile drops: Transition between pinned and mobile contact line oscillations », *Eur. Phys. J. E*, 14, p. 395–404, 2004.
- [14] E. D. Wilkes et O. A. Basaran, « Forced oscillations of pendant (sessile) drops », *Phys. Fluids*, 9, p. 1512–1528, 1997.
- [15] D. W. DePaoli, J. Q. Feng, O. A. Basaran, et T. C. Scott, « Hysteresis in forced oscillations of pendant drops », *Phys. Fluids*, 7, p. 1181–1183, 1995.
- [16] E. D. Wilkes et O. A. Basaran, « Hysteretic response of supported drops during forced oscillations », *J. Fluid Mech.*, 393, p. 333–356, 1999.
- [17] E. D. Wilkes et O. A. Basaran, « Drop Ejection from an Oscillating Rod », *J. Colloid Interface Sci.*, 242, p. 180–201, 2001.
- [18] H.-Y. Kim, « Drop fall-off from the vibrating ceiling », *Phys. Fluids*, 16, p. 474–477, 2004.
- [19] A. Bertrandias, H. Duval, J. Casalinho and M.-L. Giorgi, « Good vibrations —Transition in drop generation from an immersed capillary tube », *EPL*, 111, 44004, 2015.

- [20] W.S. Rasband, ImageJ, U. S. National Institutes of Health, Bethesda, Maryland, USA, <http://imagej.nih.gov/ij/>, 1997–2014.
- [21] C. Clanet and J.C. Lasheras, « Transition from dripping to jetting », *J. Fluid Mech.*, 383, p. 307–326, 1999.
- [22] T. Tate, « On the magnitude of a drop of liquid formed under different circumstances », *Phil. Mag.*, 27, p. 176–180, 1864.
- [23] W. D. Harkins and F. E. Brown, « The determination of surface tension (free surface energy), and the weight of falling drops: the surface tension of water and benzene by the capillary height method », *J. Am. Chem. Soc.*, 41, p. 499–524, 1919.
- [24] Y. H. Mori, « Harkins-brown correction factor for drop formation », *AIChE J.*, 36, p. 1272–1274, 1990.
- [25] E. Butikov, *Simulations of Oscillatory Systems* (CRC Press, Taylor & Francis Group), p. 38–45, 2015.
- [26] G. F. Scheele and B. J. Meister, « Drop formation at low velocities in liquid-liquid systems: Part II. Prediction of jetting velocity », *AIChE J.*, 14 (1), p. 15–19, 1968.
- [27] R. F. Meyer and J. C. Crocker, « Universal Dripping and Jetting in a Transverse Shear Flow », *Phys. Rev. Lett.*, 102, 194501, 2009.
- [28] H. A. Stone, B. J. Bentley, and L. G. Leal, « An experimental study of transient effects in the breakup of viscous drops », *J. Fluid Mech.*, 173, p. 131–158, 1986.
- [29] A. A. Castrejón-Pita, J. R. Castrejón-Pita, and I. M. Hutchings, « Breakup of Liquid Filaments », *Phys. Rev. Lett.*, 108, 074506, 2012.
- [30] A. Bonfillon and D. Langevin, « Viscoelasticity of Monolayers at Oil-Water Interfaces », *Langmuir*, 9, p. 2172–2177, 1993.
- [31] S. R. Deshiikan, D. Bush, E. Eschenazi and K. D. Papadopoulos, « SDS, Brij58 and CTAB at the dodecane-water interface », *Colloids and Surfaces A: Physicochem. Eng. Aspects*, 136, p. 133–150, 1998.
- [32] A. Bonfillon, F. Sicoli and D. Langevin, « Dynamic surface tension of ionic surfactant solutions », *J. Colloid Interface Sci.*, 168, p. 497–504, 1994.
- [33] B. Lindman, M.-C. Puyal, N. Kamenka, R. Rymden and P. Stilbs, « Tracer self-diffusion studies of micelle formation of a short-chain ionic surfactant, sodium n-octanoate », *J. Phys. Chem.*, 88 (1), p. 53–57, 1984.
- [34] H. G. Gomma, J. Liu and J. Zhu, « Experimental and theoretical analysis of emulsification characteristics using a high porosity microscreen under oscillatory shear conditions », *Colloids and Surfaces A: Physicochem. Eng. Aspects*, 456, p. 160–168, 2014.
- [35] R. Clift, J. Grace and M. E. Weber, *Bubbles, Drops and Particles* (Dover Publications, Inc.) p.191–197, 2005.

Chapter 5: Transition from dripping to jetting

1. Preamble

From chapters 3 and 4 and Appendix 3, further insight has been gained into drop behaviour submitted to high-amplitude oscillations, with a stationary outer phase. We experimentally studied this for different dispersed phase velocities, interfacial tensions, phase viscosities and forcing parameters. We proposed a model to account for the threshold amplitudes for the onset of the stretching mode (where significantly smaller drops are produced) and to account for the resulting drop sizes. We remind that this work aimed at understanding drop generation in transversally vibrating membrane emulsification, in dripping mode.

In membrane emulsification, drops are actually generated into a cross-flowing phase. In order to approach this configuration, a completely new experimental setup was conceived and built, described in section 2 of the materials and methods chapter (chapter 2). It enables to form a drop through a nozzle into cross-flow. Membrane emulsification is generally operated in dripping mode but in certain conditions, a transition from dripping to jetting occurs (see 2.2.2. of the literature review). The dripping to jetting transition has been widely studied for liquids in air and in coflowing or flow-focusing devices. However, in cross-flow such as in ME, the transition has not been widely investigated and no comprehensive models were proposed (see 2.2.2.4.).

Therefore, this fifth chapter aims at understanding the dripping to jetting transition in cross-flow. First, we consider drops formed in dripping mode in cross-flow. We then experimentally focus on the dripping to jetting transition, for different continuous phase cross-flow velocities, interfacial tensions and dispersed phase viscosities. From this, we describe two regimes within the jetting mode. We further propose a comprehensive model to account for the dripping to jetting transition, that is, we account for the jetting velocities and drop diameters at the transition.

This chapter is made up of an article which will be submitted in the near future.

We note that the impact of the combination of vibration and cross-flow in dripping mode has also been studied and is described in Appendix 4. Indeed, these trials further approach vibrating membrane emulsification conditions (vibration and cross-flow), in dripping mode.

We also began to study the impact of the combination of vibration and cross-flow in jetting mode, described in Appendix 5. It was not included in this chapter as the study is at its preliminary stage. However, interesting results were obtained and perspectives for further research emerge from this work.

2. Dripping to jetting transition for cross-flowing liquids

A. Bertrandias, H. Duval, J. Casalinho and M. L. Giorgi

Laboratoire de Génie des Procédés et Matériaux (LGPM), CentraleSupélec, Université Paris Saclay
- Grande voie des vignes, 92295 Châtenay-Malabry, France

2.1. Abstract

We experimentally study drops formed from a nozzle into an immiscible, cross-flowing phase. Depending on the operating conditions, drops are generated either in dripping or jetting mode. We investigate the impact of the continuous and dispersed phase velocities, dispersed phase viscosity and interfacial tension on the drop generation mode and size. We find that a dripping to jetting transition (DJT) takes place at a critical inner Weber number, function of the outer capillary and Ohnesorge numbers. Two jetting regimes occur depending on the phase velocity ratio. When the continuous phase velocity is significantly greater (resp. lower) than the dispersed phase velocity, jet narrowing (resp. widening) occurs. In jet widening, the critical inner Weber number depends little on the outer capillary number whereas in jet narrowing, it sharply decreases as the outer capillary number increases. We propose a comprehensive model to describe the DJT based on the attached drop equation of motion, similarly to Clanet and Lasheras. The model satisfactorily predicts the DJT and the effect of the outer capillary number on the critical inner Weber number. It also well accounts for the drop diameter in jet narrowing.

2.2. Introduction

Membrane emulsification is an industrial process used to generate emulsions by forcing a dispersed phase through an inorganic, porous membrane into a continuous cross-flowing phase [1]. This process is usually operated in dripping (drop by drop) mode. The shear stress exerted by the continuous phase controls drop formation, so drag and the retaining capillary force are the main forces involved. In dripping mode, the drop diameter decreases with increasing shear stress, while remaining greater than the membrane pore size. A first estimate of the drop diameter may be given by a simple torque balance about the pore edge [2].

More recently, alternative fabrication methods based on microfluidics have appeared, such as flow-focusing and coflowing devices. These devices commonly operate in dripping or jetting (continuous jet) mode [3-6]. In jetting mode, the liquid thread breaks up by Plateau-Rayleigh instabilities. In certain operating conditions, drops much smaller than the nozzle diameter may be produced. The same trend is expected for membrane emulsification operated in jetting mode. Thus, it is of high interest to study the dripping to jetting transition (DJT) in this process.

A DJT can occur if the liquid thread exiting the nozzle grows to a length comparable to its radius and if the pinch-off time is larger than the thread growth time [7]. The simplest case is the dripping faucet, where a dispersed phase flows from a nozzle into a stagnant, immiscible outer phase. Smith and Moss studied mercury jets into gases and found that above a critical

velocity (named the jetting velocity), the liquid exits the nozzle as a jet [8]. They proposed an empirical expression for the jetting velocity, which can be recovered from a simple balance between the jet momentum flux and the retaining capillary force. Scheele and Meister investigated the DJT for fifteen liquid-liquid couples and established the jetting velocity from a force balance, which further includes the excess pressure force [9]. The maximum error between their data and predictions is of 30.2%. Richards *et al.* studied drop formation before and after the DJT by computational fluid dynamics (CFD) [10] and obtained drop sizes that compare well with Scheele and Meister's data [9]. Clanet and Lasheras studied the DJT for water flowing from a stainless steel nozzle into air and found that the DJT occurs at a critical inner Weber number We_{in} function of Bond numbers (Bo , Bo_o) [11]. We_{in} compares the inner momentum to the capillary force. It is built with the nozzle inner diameter and mean dispersed phase velocity in the nozzle. Bo and Bo_o compare buoyancy to the retaining capillary force. Bo (resp. Bo_o) is built with the nozzle inner (resp. outer) diameter. When the dispersed phase does not wet the nozzle, only Bo is relevant. Clanet and Lasheras [11] extended Taylor's model [12] for the recession of a free, liquid edge. Their model, adapted to drop recession and growth, predicts the jetting velocities. Their calculations are in good agreement with their own data and Scheele and Meister's data [9] (maximum error of 13.7% and 20%, resp.).

In coflowing liquids, Cramer *et al.* examined the critical continuous phase velocity for the DJT [13]. They found that it decreases for increasing dispersed phase flow rates or viscosity ratios $\zeta = \eta_{dp}/\eta_{cp}$ and for decreasing interfacial tensions. Utada *et al.* proposed a state diagram of the DJT in coflowing liquids in a $Ca_{out}-We_{in}$ space [3]. Ca_{out} compares the viscous force (exerted by the outer fluid) to the capillary force. It is built with the nozzle inner diameter, the outer (continuous) phase viscosity and velocity. Two jetting regimes occur depending on the fluid velocity ratio. If the outer velocity is greater than the inner one, the inner liquid is stretched by the outer fluid and jet narrowing occurs. If the outer velocity is lower than the inner one, the outer fluid slows the inner fluid and jet widening occurs [3,4]. In jet widening, Castro-Hernández *et al.* showed that inertial or viscous forces drove the DJT depending on the inner Reynolds number Re_{in} (built with the mean dispersed phase velocity and nozzle inner diameter) [4]. They proposed a unified scaling to predict drop size in both the widening and narrowing regimes (relative errors of 30%). Chen *et al.* studied both regimes by CFD [14]. They noted that drop detachment in jet widening is due to high pressures in the neck whereas in jet narrowing, it is due to velocity differences between the front and rear ends of the neck (linking the drop to the thread).

Two spatiotemporal instabilities may occur in coflowing liquids: an absolute instability (A), with disturbances advected up- and downstream or a convective instability (C), with advection only downstream [15,16]. Linear stability analysis was performed for confined coflowing liquids. Concentric cylindrical capillaries [17] and rectangular channels [18] were studied at low Reynolds numbers. Analysis was extended to when liquid inertia is not negligible [19]. A/C regions were typically provided as a function of the inner and outer phase flow rates. The A (resp. C) region coincides with the dripping (resp. jetting) region identified experimentally.

Stability analysis was also performed for unbounded coflowing liquids: jet widening was reported as absolutely unstable and jet narrowing as convectively unstable. The widening regime was actually assimilated to a dripping regime, with drops formed at the end of the fluid thread [20].

Compared to coflowing liquids, the DJT in membrane emulsification (*i.e.*, for cross-flowing liquids) was very little investigated: Meyer and Crocker [21] performed experiments whereas Pathak [22] examined the DJT by CFD. For both, membrane emulsification was mimicked by forcing a dispersed phase through a single, circular pore of a plane wall sheared by a continuous phase flow. Meyer and Crocker found that the state diagram of the DJT depends on We_{in} and Ca_{out} , but also on the inner Ohnesorge number Oh_{dp} (ratio of the viscocapillary to inertial-capillary time scale) [21]. Both authors proposed a correlation for the DJT by replacing Bo and Bo_o by Ca_{out} in Clanet and Lasheras' DJT criterion [11] and by adjusting coefficients. However, no comprehensive models were developed in this configuration [21,22].

The aim of this work is to study drop generation in cross-flow. The setup consists in a nozzle, which forms dispersed phase drops into a continuous cross-flowing phase. Both dripping and the DJT are studied for various phase velocities, interfacial tensions and dispersed phase viscosities. Dripping data are used to identify the drag force experienced by a drop attached to the nozzle. Then, a physical model is proposed to predict the jetting velocities and drop diameters at the DJT. This enables to gain insight on drop formation in membrane emulsification and more generally on the DJT for cross-flowing liquids.

2.3. Experimental

The systems investigated are reported in table 5.1. η_{dp} and η_{cp} are the dispersed and continuous phase viscosities, respectively, ρ_{dp} and ρ_{cp} are the dispersed and continuous phase densities, respectively and γ is the interfacial tension. η_{dp} was measured at 25.1°C, with a Ubbelohde viscosimeter (AVS310, Schött-Gerade) and γ was measured for all systems by the rising drop method, with a tensiometer (Tracker, I.T. Concept, Teclis).

Table 5.1: Investigated system composition and physicochemical properties.

System and symbol	Dispersed phase 'dp'	η_{dp} (mPa.s)	ρ_{dp} (kg.m ⁻³)	Continuous phase 'cp'	η_{cp} (mPa.s)	ρ_{cp} (kg.m ⁻³)	γ (mN.m ⁻¹)
Reference (◇)	Dodecane	1.34	750	Distilled water	0.89	997	50.7 ± 3.5 ^a
1 (◆)	Dodecane	1.34	750	Distilled water and SDS (0.1 wt%)	0.89	997 ± 1.4 ^a	22.3 ± 0.5 ^{a,b}
2 (♦)	Dodecane	1.34	750	Distilled water and SDS (2 wt%)	0.89	1001 ± 1.2 ^a	6.6 ± 0.2 ^{a,b}
3 (◁)	Dodecane (75 wt%) and paraffin (25 wt%)	1.79 ± 0.23 ^a	772 ± 1.2 ^a	Distilled water	0.89	997	53.5 ± 2.4 ^a
4 (▷)	Dodecane (50 wt%) and paraffin (50 wt%)	3.24 ± 0.42 ^a	790 ± 1.1 ^a	Distilled water	0.89	997	50.0 ± 1.2 ^a

The tabulated values ^a are measured experimentally; ^b correspond to those at the intermediate plateau (see [23,24]).

An original setup was designed (fig. 5.1). It consists in a cell with a horizontal channel through which the continuous phase flows. A vertical nozzle of inner diameter $D_p = 0.32$ mm emerges into the channel. The continuous phase is pumped in a closed cycle by a gear pump (MDG M15T3B, Iwaki Co.), perpendicular to the nozzle axis (cross-flow). The flow rate is adjusted (OVAL MIII LSF41, OVAL Corporation) with a $0.1 \text{ L}\cdot\text{h}^{-1}$ precision. The dispersed phase is forced through the nozzle with a syringe pump (PHD ULTRA, Harvard Apparatus) at a volumetric flow rate q_{dp} (accuracy $\leq 0.25\%$), giving a mean dispersed phase velocity in the nozzle v_{dp} . A cold light (KL 2500 LCD, Schott) illuminates the setup. A high-speed camera (v310, Phantom) allowing up to 3250 fps at full resolution ($1280 \times 800 \text{ px}^2$) is mounted with a macro lens (Macro MP-E 65mm f/2.8, Canon) of magnification $\times 5$. Images are captured through the cell windows and are analysed with ImageJ to obtain data such as drop size D_d , with the scale (238 px/mm) set by the nozzle outer diameter ($433 \pm 2 \mu\text{m}$). Average relative standard deviations in drop diameters are of 3.4%, 8.7% and 7.7% in dripping, jet widening and narrowing, respectively.

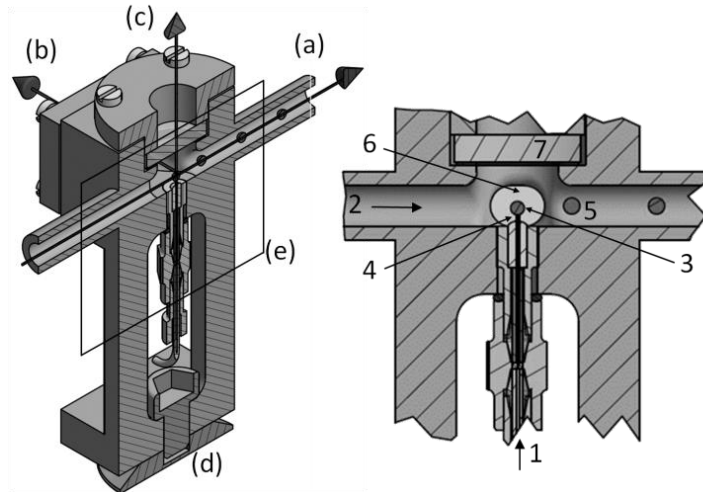


Figure 5.1: Cell cross-section by CAD (to scale). Cell (left): (a) continuous phase flow axis; (b) optical axis; (c) dispersed phase flow axis; (d) cell binding point; (e) frame for zoom. Zoom in the cell (right): 1, dispersed phase inlet (microfluidic system); 2, continuous phase flow; 3, growing drop; 4, nozzle; 5, formed drop carried away; 6, optical glass window; 7: window for user.

In order to obtain the so-called unperturbed continuous phase velocity at the location of the bound drop center of mass (denoted v_{cp}), the continuous phase flow is analyzed by particle image velocimetry (PIV), without dispersed phase injection (see supplementary material in 2.8.1, fig. 5.A1). Analysis is performed for the range of continuous phase volumetric flow rates q_{cp} tested in this work. The average continuous phase velocity is essentially uniform above the nozzle except in a thin adjacent layer (see supplementary material in 2.8.1, fig. 5.A2). We theoretically estimate the boundary-layer thickness at a distance $D_p/2$ from the leading edge of the nozzle [25] for all q_{cp} and find a thickness of 0.06 mm for the highest q_{cp} to 0.2 mm for the lowest q_{cp} : the boundary-layer thickness is always small compared to the minimum drop

diameter formed at the given q_{cp} (0.302 mm and 1.019 mm, resp.). The drop is thus mainly located above the shear layer that develops above the nozzle. This differs from Meyer and Crocker's [21] or Pathak's [22] work, where the drop is entirely located in the shear flow set up by the continuous phase flowing parallel to the plane wall. In the following, the continuous phase velocity v_{cp} seen by a growing drop corresponds to the velocity measured in the uniform flow above the shear layer.

Drop formation by dripping is studied as a function of the continuous phase velocity v_{cp} seen by the growing drop. The parameters tested are reported in table 5.2 (dripping trials). We consider that the Reynolds number characteristic of the continuous phase flow in the channel inside the cell is close to the Reynolds number in the cylindrical tubes on the sides of the cell, in series with this channel (see fig. 5.1). We find $Re = 4\rho_{cp}q_{cp}/\pi D_t\eta_{cp}$ from 330 to 3300, with D_t the tube diameter. According to Morrison [25], the continuous phase flow entering the cell is laminar ($Re < 2100$) or transitional ($2100 < Re < 3300$). The inner Reynolds number $Re_{in} = 4\rho_{dp}q_{dp}/\pi D_p\eta_{dp}$ ranges from 2 to 38, so the dispersed phase flow is laminar in the nozzle.

Then, the DJT is studied. The v_{cp} values tested are given in table 5.2 (DJT trials) and the dispersed phase velocity v_{dp} is increased slowly until the DJT. The onset of jetting is defined as in the literature [21,22]: it occurs when $L_n/D_d > 1$, with L_n the thread length prior to drop break off (from the nozzle surface to the drop base) and D_d the detached drop diameter. We obtain jetting velocities with a precision of 2.9 to 7.7% in jet widening and 2.6 to 11.1% in jet narrowing (due to the chosen increment in dispersed phase flux). Re_{in} ranges from 7 to 130, so the dispersed phase flow is laminar in the nozzle. In the tubes on the sides of the cell, Re ranges from 330 to 6600, so for the highest q_{cp} , *i.e.* v_{cp} , the continuous phase flow is turbulent in the channel [25].

After a series of trials (either PIV or dripping and DJT trials), the cell is filled with 3 vol% Mucosol (Merz) for 24h and is rinsed with distilled water. The nozzle surface is then hydrophilic: the organic dispersed phase does not wet the nozzle surface, so its outer diameter does not impact drop generation.

Table 5.2: Operating conditions investigated.

System	Dripping trials		DJT trials
	v_{cp} (m.s ⁻¹)	v_{dp} (m.s ⁻¹)	v_{cp} (m.s ⁻¹)
Reference	0.18 - 0.55	0.016, 0.031, 0.063, 0.14, 0.21	0.17 - 1.03
1	0.11 - 0.50	0.031	0.17 - 0.59
2	0.10 - 0.40	0.031	0.17 - 0.40
3	0.11 - 0.55	0.031	0.23 - 1.03
4	0.10 - 0.60	0.031	0.23 - 0.94

2.4. Drop generation by dripping with cross-flow

Drop diameters D_d were measured as a function of the continuous phase velocity v_{cp} (fig. 5.2), at constant $v_{dp} = 0.031 \text{ m.s}^{-1}$. As v_{cp} increases, D_d decreases due to the increasing shear exerted by the continuous phase flow. Drop diameters scale as $v_{cp}^{-0.62}$ to $v_{cp}^{-0.80}$, depending on the system. A lower interfacial tension γ leads to smaller drops (systems 1 and 2, fig. 5.2). The capillary force decreases with γ , so a drop detaches earlier, also found by Xu *et al.* [26]. No significant impact on D_d is seen with the dispersed phase viscosity η_{dp} (possibly a slight decrease in D_d with increasing η_{dp}) (fig. 5.2). In membrane emulsification, Timgren *et al.* [27] numerically found a decrease in drop size with a thousand-fold increase in η_{dp} , expected as the drag coefficient then notably increases [28]. In our case, the difference may not be large enough to significantly impact drop size.

The influence of v_{dp} was also tested on the reference system (not shown). We find that v_{dp} does not impact drop diameter, as found for a stationary outer phase [29] or in cross-flow [26]. For these trials, drops form in dripping mode. $Ca_{out} = \eta_{cp} v_{cp} / \gamma$ ranges from 3.1×10^{-3} to 9.7×10^{-3} , $We_{in} = \rho_{dp} D_p v_{dp}^2 / \gamma$ from 1.1×10^{-3} to 2.0×10^{-1} and $Oh_{dp} = \eta_{dp} / \sqrt{\rho_{dp} D_p \gamma} = 1.2 \times 10^{-2}$. This is in fact in the dripping region of the state diagram reported in the literature [21,22].

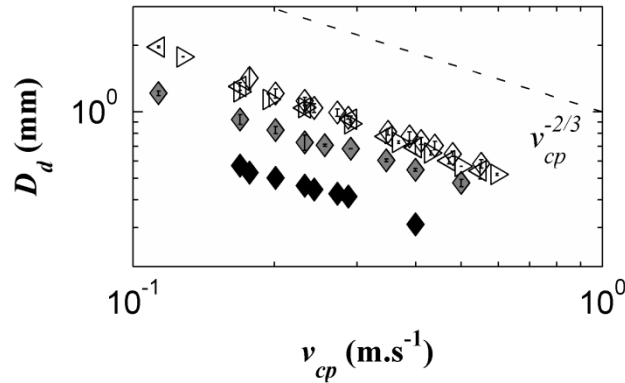


Figure 5.2: Drop diameter D_d function of the continuous phase velocity v_{cp} , $v_{dp} = 0.031 \text{ m.s}^{-1}$.

See table 5.1 for symbols.

In order to account for the drop diameter scaling observed in dripping mode, we consider that drag and the retaining capillary force are the main forces involved. Buoyancy is neglected since the buoyancy to drag force ratio is on average less than 5%. As Peng and Williams [2], we assume that the drop subjected to the forces discussed above stays spherical and rotates about the nozzle edge until detachment. The fraction of the drop that could remain attached to the nozzle tip after break off is neglected. The torque balance (TB) about the nozzle edge reads:

$$\frac{\pi D_d^2}{4} C_D \frac{\rho_{cp}}{2} v_{cp}^2 \frac{D_d}{2} = \pi D_p \gamma \frac{D_p}{2} \quad (5.1)$$

with C_D the drag coefficient. In eq. (5.1), we neglect the velocity of the drop center of mass v_d . Indeed, if we assume that in dripping mode, the main contribution to the drop center of mass

motion is due to drop growth, a rough estimate of v_d is given by $v_d(t) \approx 0.5(dD_d/dt)$, where D_d increases in time according to $D_d(t) = (6qt/\pi)^{1/3}$. For all systems and phase velocities tested, we find $v_d \ll v_{cp}$ (38 to 589 times). We further rearrange eq. (5.1) as:

$$\frac{D_d}{D_p} = k \left(\frac{\text{Oh}_{cp}}{\text{Ca}_{out}} \right)^{2/3} \quad (5.2)$$

with $k = [8/C_D]^{1/3}$ and $\text{Oh}_{cp} = \eta_{cp}/\sqrt{\rho_{cp}D_p\gamma}$ the outer Ohnesorge number. We note that eq. (5.2) may also be written as $D_d/D_p = k \text{We}_{out}^{-1/3}$, with We_{out} the outer Weber number, built with the continuous phase velocity. If we assume that C_D is approximately constant (corresponding to the Newton regime), from eq. (5.2), we find that the drop diameter scales as $v_{cp}^{-2/3}$. This is in good agreement with our experimental data ($v_{cp}^{-0.62}$ to $v_{cp}^{-0.80}$). However, this scaling differs from the one found by Meyer and Crocker [21], *i.e.* $D_d/D_p \sim \text{Ca}_{out}^{-1/2}$. In their trials, drops are entirely located in the shear layer that develops along the plane wall and their diameters seem better described by a force balance.

For a solid sphere in an infinite fluid, the Newton regime holds for particle Reynolds numbers $\text{Re}_p = \rho_{cp}v_{cp}D_d/\eta_{cp}$ from 10^3 to 10^5 [25]. In this range, $C_D \approx 0.4$. In our case, $\text{Re}_p = 92$ to 360 , so C_D may vary. We estimate C_D from eq. (5.1) and find that C_D decreases with increasing Re_p (data points, fig. 5.3). Our C_D values are higher than reported for a viscous sphere in an infinite fluid by Feng and Michaelides [30] (dashed line, fig. 5.3). Indeed, in our trials, the drop is not isolated but bound to a nozzle. We propose to model the variations of C_D as a function of Re_p by the law of eq. (5.3), in the form obtained by Abraham for a solid sphere [31]:

$$C_D = C_0 \left(1 + \frac{\delta_0}{\text{Re}_p^{1/2}} \right)^2 \quad (5.3)$$

We perform a weighted least squares minimization to identify the free coefficients of eq. (5.3) from the data of the reference system, systems 1 and 2. These systems are characterized by a viscosity ratio $\zeta = 1.5$, with $\text{Re}_p = 92$ to 360 . We find $C_0 = 0.14$ and $\delta_0 = 17.7$. The data are well described by the adjusted law (solid line, fig. 5.3). In the Stokes limit ($\text{Re}_p \ll 1$), eq. (5.3) reads $C_D \approx C_0\delta_0^2/\text{Re}_p \approx 45/\text{Re}_p$ close to the drag coefficient of a solid sphere at a wall in creeping flow, *i.e.* $C_D \approx 1.7 \times (24/\text{Re}_p) \approx 41/\text{Re}_p$ [32]. We only retain that the order is satisfactory as our drop deviates from a solid sphere and the coefficients were adjusted far from the Stokes regime.

For system 3 ($\zeta = 2.0$) and 4 ($\zeta = 3.6$), we cannot carry out the above method since our trials do not cover a wide range of Re_p for these viscosity ratios. We assume that C_D are not significantly different than from eq. (5.3) fitted on systems with $\zeta = 1.5$, consistently with the analysis of fig. 5.2. In section 2.5, eq. (5.3) will be used to estimate the drag force experienced by a drop near the DJT.

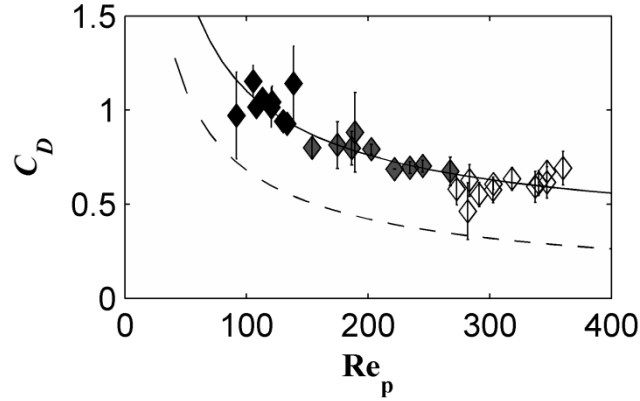


Figure 5.3: Drag coefficient C_D function of the particle Reynolds number Re_p . Experimental results from eq. (5.1), see table 5.1 for symbols. Feng and Michaelides predictions for $\zeta = 1.5$ (dashed line); our fit from eq. (5.3) with $C_0 = 0.14$ and $\delta_0 = 17.7$ (solid line).

2.5. Dripping to jetting transition (DJT)

2.5.1. Experimental results

For a set system and continuous phase velocity v_{cp} , the DJT is reached for a critical dispersed phase velocity (corresponding to the jetting velocity for the given v_{cp}). We remind that the onset of jetting is defined when the length of the liquid thread connecting the drop to the nozzle reaches the drop diameter (see section 2.3). Typical snapshots of dripping and jetting are reported in fig. 5.4. We note that in fig. 5.4(a) and (b), the first image on the left represents “strict” dripping (as studied in section 2.4), with a drop rotating about the nozzle edge.

As in coflowing liquids [3,4,14], when the DJT is reached, two jetting regimes may be observed. When $v_{cp} \lesssim v_{dp}$, the liquid thread is on average thicker than the nozzle inner diameter (fig. 5.4(a), last image): this is the widening regime. On the contrary, when $v_{cp} \gtrsim v_{dp}$, the liquid thread gets thinner from the nozzle to the drop (fig. 5.4(b), last image): this is the narrowing regime. Curiously, Meyer and Crocker did not distinguish these regimes in their paper [21].

In jet widening, we also see that the thread undergoes surface oscillations (see supplementary material in 2.8.2, fig. 5.B1). These oscillations are essentially stationary in space. According to Utada *et al.* who studied jet widening in coflowing liquids, this behavior is characteristic of an absolute instability [20]. To quantify this, as Utada *et al.* [20], we examine the variations of the neck diameter (between the thread and growing drop) as a function of time (see supplementary material in 2.8.2, fig. 5.B2). The neck diameter oscillates about its mean with an increasing amplitude until pinch off and subsequent drop detachment. The oscillation frequency is around 350 Hz for the reference system, consistent with the inertial-capillary time scale of this system.

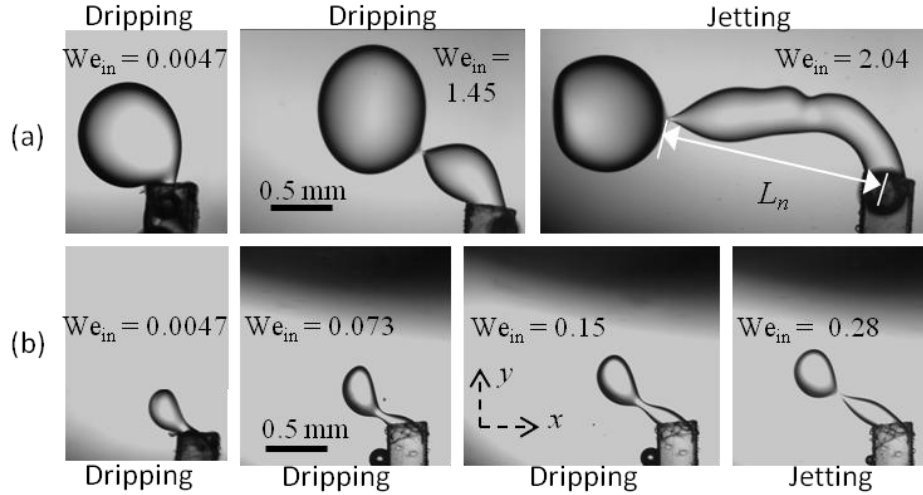


Figure 5.4: Reference system snapshots ($Oh_{cp} = 7.0 \times 10^{-3}$): (a) jet widening, $Ca_{out} = 5.1 \times 10^{-3}$; (b) jet narrowing, $Ca_{out} = 1.3 \times 10^{-2}$. Continuous phase flow from right to left.

As for coflowing or cross-flowing liquids [3,21,22], we represent the DJT in the $Ca_{out}-We_{in}$ space. We remind that We_{in} is the inner Weber number ($We_{in} = \rho_{dp} D_p v_{dp}^2 / \gamma$) and Ca_{out} the outer capillary number ($Ca_{out} = \eta_{cp} v_{cp} / \gamma$). Figure 5.5(a) presents the variations of We_{in} built with the jetting velocity as a function of Ca_{out} , for the five systems of table 5.2. The curves exhibit a plateau for lower Ca_{out} values and a sudden decrease for higher Ca_{out} . They are similar in shape to the curves established by Meyer and Crocker [21] and Pathak [22]. We associate the plateau with jet widening and the sudden decrease with jet narrowing. For all systems, at the plateau, We_{in} is in the order of 1, in the order of magnitude reported for jet widening in coflow [3]. Our plateau values are also similar to those of Meyer and Crocker [21] and Pathak [22]. The transition between widening and narrowing occurs at a critical value of Ca_{out} , such that $v_{cp} \approx v_{dp}$. This value is denoted Ca^* for the reference system in fig. 5.5(a).

The same trends, *i.e.* a plateau followed by a marked decrease, are obtained for the drop diameters formed at the DJT as a function of Ca_{out} (fig. 5.5(b)). The variations in drop diameters at the DJT as a function of Ca_{out} were not reported before [21,22]. In jet widening, we expect that the drop diameter is controlled by a balance between the jet momentum and the retaining capillary force. In jet narrowing, the drop diameter should be controlled by a balance between the drag force experienced by the drop and the capillary force. As the continuous phase velocity increases, the thread gets thinner leading to a lower retaining capillary force, thus smaller drops.

As the interfacial tension γ decreases between the reference system, system 1 and 2, the plateau value for We_{in} decreases and the transition from jet widening to narrowing is shifted towards higher Ca_{out} . This result, to which we shall return, was not reported before. The influence of γ on the DJT was not examined in detail in cross-flow [21,22].

In our trials, the dispersed phase viscosity η_{dp} does not affect the jetting velocity since the data for the reference system, system 3 and 4 collapse onto a unique curve (fig. 5.5(a)). This is

in good agreement with Meyer and Crocker's results [21]. They found that the jetting velocity does not vary significantly with the inner Ohnesorge number $Oh_{dp} = \eta_{dp}/\sqrt{\rho_{dp}D_p\gamma}$ while Oh_{dp} is below 3×10^{-2} . Indeed, while $Oh_{dp} \ll 1$, the pinch-off time scale is in the order of the inertial-capillary time scale, thus it does not depend on η_{dp} . This corresponds to our experimental range: Oh_{dp} increases from 1.2×10^{-2} to 2.9×10^{-2} as η_{dp} increases from 1.34 to 3.24 mPa.s. Drop diameters are also unaffected by η_{dp} (fig. 5.5(b)).

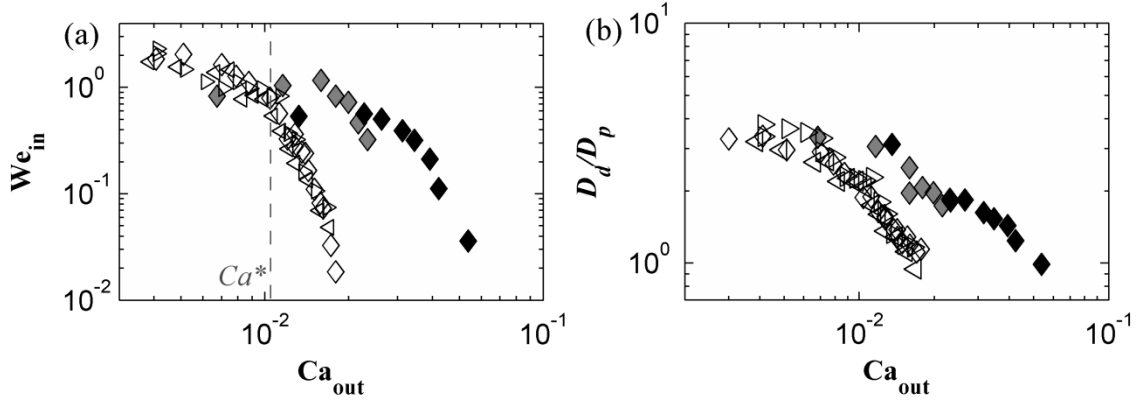


Figure 5.5: Characteristic values at the DJT, see table 5.1 for symbols: (a) We_{in} function of Ca_{out} . Widening to narrowing limit Ca^* for the reference system (dashed line); (b) Drop to pore diameter ratio D_d/D_p function of Ca_{out} .

According to Utada *et al.* [3] and Meyer and Crocker [21], our DJT curves should overlap in the $Ca_{out}-We_{in}$ space since $Oh_{dp} \ll 1$. However, as stated before, our DJT curves are shifted towards higher Ca_{out} as the interfacial tension decreases. We attribute this to the hydrodynamic regime of the drag force experienced by a growing drop. Indeed, the particle Reynolds number Re_p ranges from 114 to 424 in our DJT trials. These values are much higher than those reported by Utada *et al.* [3] and Meyer and Crocker [21]. Thus, the drag force in our trials rather corresponds to the Newtonian regime than to the Stokes regime. Since the ratio of the drag to capillary force is in the order of $(Ca_{out}/Oh_{cp})^2 = We_{out}$ under Newton regime assumption (as opposed to Ca_{out} under Stokes approximation), we plot We_{in} as a function of Ca_{out}/Oh_{cp} (see supplementary material in 2.8.3). We remind that Oh_{cp} is the outer Ohnesorge number ($Oh_{cp} = \eta_{cp}/\sqrt{\rho_{cp}D_p\gamma}$). We find that reference system and system 1 and 2 data then actually collapse in the narrowing regime.

2.5.2. Model

The DJT criteria proposed by Pathak [22] and Meyer and Crocker [21] are not adapted to our case. Indeed, in our trials, the growing drops are mainly located above the shear layer adjacent to the nozzle tip (see section 2.3) and the particle Reynolds number is far from the Stokes regime (see section 2.5.1). Figure 5.D1 (supplementary material in 2.8.4) shows the discrepancy between our DJT data for the reference system and previous authors' DJT criteria [21,22]. We remind that these criteria are semi-empirical since these authors simply replaced

Bo and Bo_o , the Bond numbers built with the nozzle inner and outer diameters, by Ca_{out} in Clanet and Lasheras' criterion [11] and adjusted the coefficients to fit their data. In this section, we propose a comprehensive model to account for the jetting velocity and drop diameters at the DJT.

Firstly, the footage shows that thread dynamics occur essentially along the x -axis (fig. 5.4): the drop forms at the end of a thread that tends to align with the continuous phase flow. Thus, we approximate our configuration by a coflow configuration (fig. 5.6). A force balance is now more relevant than a torque balance since the drop can no longer be considered as a sphere rotating about the nozzle edge.

We revisit Clanet and Lasheras' approach developed for a liquid injected downwards into a stagnant gas under gravity [11] and amend the drop equation of motion to consider coflowing liquids. We thus add a drag force induced by the continuous flowing phase since η_{cp} is orders of magnitude higher than the dynamic viscosity of air and we account for the added mass effect since $\rho_{cp} \sim \rho_{dp}$. We neglect buoyancy since for the largest drops (obtained in the widening regime), the buoyancy to capillary force ratio is lower than 3%.

In Clanet and Lasheras' scenario [11], drops are generated as follows: a first drop detaches (at $x = 0$ in fig. 5.6), leaving a thread behind that recedes at a velocity dx/dt , due to surface tension effects. During recession, a mass (drop) M forms (sphere in fig. 5.6). It recedes until it reaches a distance x_{max} (closer to the nozzle, fig. 5.6). The mass then progresses the other way, once momentum and drag overcome surface tension effects. It is assumed that pinch off begins at x_{max} . From that point, the drop no longer grows. The drop travels a distance l_d until detachment. If $x_{max} > l_d$, dripping occurs. Oppositely, if $x_{max} < l_d$, the detachment point advances each time, leading to jetting.

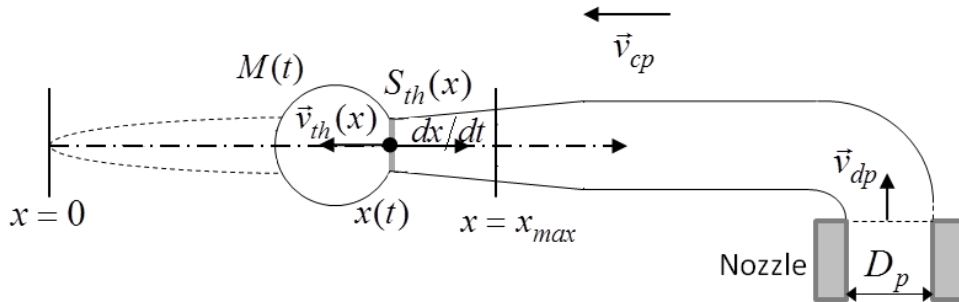


Figure 5.6: Model configuration with the different variables involved.

The mass $M(t)$ of the drop is given by

$$M(t) = \frac{\pi}{4} D_p^2 \rho_{dp} v_{dp} t + \rho_{dp} \int_0^{x(t)} S_{th}(x') dx' \quad (5.4)$$

We remind that v_{cp} and v_{dp} are velocity moduli. $S_{th}(x)$ is the thread cross-section at the location x . $S_{th}(x)$ is related to $v_{th}(x)$, the mean fluid velocity modulus in the thread at the location x , by $q_{dp} = S_{th}(x)v_{th}(x)$. The variations of the mean dispersed phase velocity v_{th} along the thread depend on the continuous phase shear stress.

The drop equation of motion during recession reads:

$$\frac{d}{dt} \left[(M(t) + M_a(t)) \frac{dx}{dt} \right] = \pi D_{th}(x) \gamma - \rho_{dp} q_{dp} \left(\frac{dx}{dt} + v_{th}(x) \right) - \frac{\pi}{4} D_m^2(t) C_D \frac{\rho_{cp}}{2} \left(v_{cp} + \frac{dx}{dt} \right)^2 \quad (5.5)$$

The left-hand side of eq. (5.5) corresponds to the drop effective inertia and includes $M_a(t)$ the added mass due to the surrounding continuous phase. We suppose that the added mass is equal to half of the displaced volume of continuous phase, as for a solid sphere in an infinite medium. It is thus given by $M_a(t) = 0.5M(t)\rho_{cp}/\rho_{dp}$. The first term on the right-hand side of eq. (5.5) is the retaining capillary force, with $D_{th}(x)$ the thread diameter at the location x . The second term is the jet momentum flux entering the drop. The last term is the drag force, in which the frontal area corresponds to that of a sphere with the given mass. The drop mass diameter is given by:

$$D_m(t) = \left[\frac{6 M(t)}{\pi \rho_{dp}} \right]^{1/3} \quad (5.6)$$

In the drag force, the drag coefficient $C_D(\text{Re}_p)$ is estimated from eq. (5.3), with the coefficients adjusted before and Re_p is built with $D_m(t)$ (eq. (5.6)) and the relative velocity $|v_{cp} + dx/dt|$. At the DJT, we find $\text{Re}_p = 114$ to 424 (estimated with the experimental D_d and v_{cp}). This is in the same range as where the coefficients of eq. (5.3) were adjusted. However, eq. (5.3) was established for drops detaching in dripping mode: we here neglect the deviations in C_D that may arise at the DJT when the thread linking the drop to the nozzle is larger. We assume that C_D essentially depends on the drop mass diameter and the particle Reynolds number and little on the drop shape details.

x_{max} is determined from the numerical integration of system (5.4-5.6) (see Appendix in 2.7). As stated above, the DJT occurs at $x_{max} = l_d$. l_d is the detachment distance by pinch off, such that:

$$\int_0^{l_d} \frac{dx}{v_{th}(x)} = \tau_n \quad (5.7)$$

τ_n is the necking time or pinch-off time (in the order of the inertial-capillary time), given by:

$$\tau_n = k' \left[\frac{D_j^3(x_{max}) \rho_{dp}}{8\gamma} \right]^{1/2} \quad (5.8)$$

We estimate $k' \approx 8.26 \pm 0.43$ by Clanet and Lasheras' method [11]: we measure the neck diameter variations in dripping mode as a function of time during pinch off, we fit the variations to an exponential form to find τ_n and we plot $1/\tau_n$ as a function of $\tau_c = [8\gamma/D_p^3\rho_{dp}]^{1/2}$. This was done for the reference system, systems 1 and 2 (see supplementary material in 2.8.5). These systems differ only by their interfacial tension and are characterized by a viscosity ratio $\zeta = 1.5$. We find τ_n 2.6 times higher than Clanet and Lasheras for a liquid

in air [11], which depicts a lower instability growth rate. This is in agreement with results reported in the literature: Rayleigh found a growth rate (made dimensionless by τ_c) of 0.34 for an inviscid liquid in air [33]. On the other hand, Funada and Joseph found a growth rate 1.3 to 4.8 times lower for water in benzene ($\zeta = 1.5$) in the range of our Re_{in} , from a fully viscous analysis [34].

Returning to the model, the jetting velocity at a set v_{cp} is obtained as follows (see Appendix in 2.7 for details): v_{dp} is scanned and for each v_{dp} , the system (5.4-5.6) is integrated as a function of time, until $x = x_{max}$. If x_{max} coincides with l_d (eq. (5.7)), the corresponding v_{dp} value is the jetting velocity at the given v_{cp} . The resulting drop diameter is deduced from eq. (5.6): $D_d \approx D_m(t_{max})$, where t_{max} is the time taken for the mass to travel from 0 to x_{max} . This method may be repeated for each v_{cp} tested to reproduce our experimental results.

2.5.3. Comparison with experiments

To implement the above model, we must describe the mean dispersed phase velocity along the thread. Two limit cases will be considered: (1) the thread diameter and mean velocity are negligibly affected by the continuous phase flow in both jetting regimes and (2) the mean thread velocity quickly reaches the continuous phase velocity in the narrowing regime.

2.5.3.1. Uniform nozzle-sized thread

First, we consider the simplest scenario where the thread diameter is not affected by the continuous phase in either jetting regime. In this case, we assume $v_{th}(x) = v_{dp}$ and $D_{th}(x) = D_p$ from $x = 0$ to x_{max} . Then, the thread cross-section reads $S_{th}(x) = \pi D_p^2/4$. We call this the uniform nozzle-sized thread limit. We solve system (5.4-5.6) under this assumption by the method described in the Appendix. The results are reported in fig. 5.7 (solid lines).

The variations of the critical inner Weber number We_{in} function of the outer capillary number Ca_{out} are satisfactorily reproduced (fig. 5.7(a), solid lines). The same conclusion may be drawn for the variations of the dimensionless drop diameter as a function of Ca_{out} (fig. 5.7(b), solid lines). Furthermore, the effect of the interfacial tension on the transition is well accounted for.

The model predicts a plateau in jet widening (for small Ca_{out}), but in our experiments, the plateau is more pronounced and extends for higher Ca_{out} . Furthermore, in jet widening, We_{in} and especially D_d are overpredicted. The difference in plateau values for We_{in} between the reference system and system 2 is also not reproduced (fig. 5.7(a)). We checked that the differences in plateau values cannot be attributed to the relative effect of buoyancy. We attribute them to the thread surface oscillations (see supplementary material in 2.8.2), which affect the retaining capillary force and pinch-off time. These oscillations cannot be accounted for in the framework of the present model.

Lastly, we note that We_{in} and D_d are overestimated at high Ca_{out} for the reference system (and systems 3 and 4, not shown in fig. 5.7). This may be explained by the narrowing of the

thread which becomes significant at high v_{cp} but is neglected in the present case. In the next section (2.5.3.2), we attempt to take this effect into account.

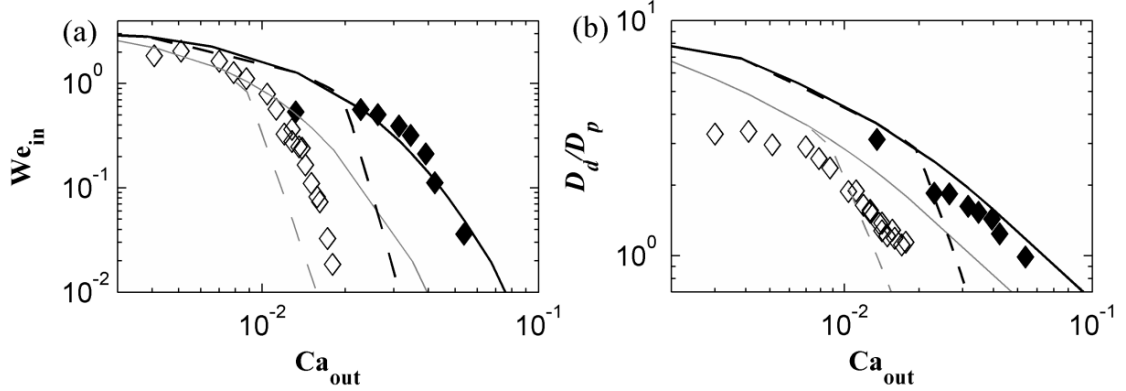


Figure 5.7: Characteristic values at the DJT, see table 5.1 for symbols. (a) We_{in} function of Ca_{out} ; (b) Drop to pore diameter ratio D_d/D_p function of Ca_{out} . Simulation results for the reference system (grey); system 2 (black). Uniform nozzle-sized thread limit of section 2.5.3.1 (solid line); maximal narrowing limit of section 2.5.3.2 (dashed line).

2.5.3.2. Maximal narrowing

We measure the thread diameter for the reference system in the narrowing regime: it decreases by less than 10% for $v_{cp} \leq 0.73 \text{ m}\cdot\text{s}^{-1}$ ($Ca_{out} = 1.3 \times 10^{-2}$) but decreases by more than 50% for the highest v_{cp} . In the latter case, narrowing effects can no longer be neglected and our hypothesis $D_{th}(x) = D_p$ of section 2.5.3.1 is no longer valid.

We suppose that the momentum diffusion across the thread is rapid and fully efficient in the narrowing regime. In this case, we may consider that if $v_{cp} > v_{dp}$, the thread is characterized by $v_{th}(x) = v_{cp}$, $D_{th}(x) = D_p(v_{dp}/v_{cp})^{1/2}$ and $S_{th}(x) = \pi D_{th}^2(x)/4$ from $x = 0$ to x_{max} . This gives the maximal narrowing limit. According to Castro-Hernandez *et al.*, maximal narrowing is observed when $Re_{in} < 1$ [4]. In our trials, $Re_{in} = 7$ to 130, so their assumption is not strictly applicable. However, it will give us an overestimate of the narrowing effect on the DJT and drop diameter. If $v_{cp} < v_{dp}$ (jet widening), we still neglect the effect of the continuous phase on the thread size and assume that $D_{th}(x) = D_p$ and $v_{th}(x) = v_{dp}$, as in section 2.5.3.1.

As before, we solve system (5.4-5.6) under these new assumptions (see Appendix) and we report the results in fig. 5.7 (dashed lines). For the reference system (and systems 3 and 4, not shown), our data for We_{in} and D_d in jet narrowing lie in between the maximal narrowing limit (dashed lines, fig. 5.7(a) and (b)) and the uniform nozzle-sized thread limit (solid lines, fig. 5.7(a) and (b)).

We note that the data for system 2 are surprisingly well described by the uniform nozzle-sized thread limit. This is probably due to the compensation of different errors related to the uniform nozzle-sized approximation, the use of the drag coefficient estimated in the dripping regime and the assumption that forces act only along the x -axis.

2.6. Conclusions

While the dripping to jetting transition (DJT) is well documented for liquid-air [8,11] or liquid-liquid coflow [3,4,13,14], liquid-liquid cross-flow [21,22] has received little attention and no comprehensive model was proposed to describe the DJT in this configuration. Also, drop diameters specifically at the DJT were either not measured or not reported [21,22].

In the present work, we studied liquid-liquid cross-flow for different phase velocities, interfacial tensions and dispersed phase viscosities. Contrary to previous work [21,22], the growing drops are mainly located above the shear layer that develops above the nozzle. Furthermore, since the inner Ohnesorge number (characteristic of the dispersed phase flow) is much lower than 1, drop pinch-off is controlled by the inertial-capillary time scale.

In strict dripping, we found that the drop diameter is well described by a simple torque balance about the nozzle edge, taking into account the drag force experienced by the drop and the retaining capillary force. This result was used to estimate the drag coefficient for an attached drop as a function of the particle Reynolds number.

The DJT occurs at a critical inner Weber number function of the outer capillary and Ohnesorge numbers. Two jetting regimes occur (widening and narrowing) depending on the phase velocity ratio. In jet widening (when the dispersed phase velocity is greater than the continuous phase one), the critical inner Weber number depends little on the outer capillary number whereas in the narrowing regime, it sharply decreases as the outer capillary number increases. Furthermore, when the outer Ohnesorge number increases, the transition between widening and narrowing is shifted to higher values of the outer capillary number. The hydrodynamic regime of the drag force experienced by a growing drop is actually inertial and not viscous.

We proposed to model the DJT in liquid-liquid cross-flow by revisiting an approach originally developed by Clanet and Lasheras for a liquid injected into a stagnant gas under gravity. The model describes the recession dynamics and the growth of the drop until pinch off. In the present case, the driving force for drop detachment is not buoyancy but the drag force exerted by the continuous phase flow. We distinguished two limit cases for the thread profile that exits the nozzle and enters the drop: a uniform nozzle-sized thread limit and a maximal narrowing limit. Jetting velocities and drop diameters measured at the DJT in jet narrowing are well accounted for and lie in between model predictions in the two limit cases. Furthermore, the effect of the outer Ohnesorge number on the DJT is well reproduced. In jet widening, the agreement is less satisfactory. Discrepancies are attributed to thread surface oscillations which appear in jet widening. However, we may conclude that the main features of the DJT in cross-flow are captured which highlights the insight and the robustness of Clanet and Lasheras' original model.

2.7. Appendix

For a set v_{cp} , the jetting velocity is obtained by an iterative procedure. v_{dp} is varied with a $0.001 \text{ m}\cdot\text{s}^{-1}$ increment. For each v_{dp} value, the recession dynamics of a growing drop is computed by integrating system (5.4-5.6) using the fourth order Runge-Kutta method. The initial conditions are $D_d(0) = 0$ and $x(0) = 0$. According to eq. (5.5), $\dot{x}(0)$ is then given by eq. (5.A1) for the uniform nozzle-sized thread limit and by eq. (5.A2) for the maximal narrowing limit.

$$\dot{x}(0) = -\frac{v_{dp}}{2} \left(1 + \frac{\rho_{dp}}{\rho_e}\right) + \frac{1}{2} \left(v_{dp}^2 \left(1 - \frac{\rho_{dp}}{\rho_e}\right)^2 + \frac{16\gamma}{D_p \rho_e} \right)^{1/2} \quad (5.A1)$$

$$\dot{x}(0) = -\frac{v_{cp}}{2} \left(1 + \frac{\rho_{dp}}{\rho_e}\right) + \frac{1}{2} \left(v_{cp}^2 \left(1 - \frac{\rho_{dp}}{\rho_e}\right)^2 + \frac{16\gamma(v_{dp}/v_{cp})^{1/2}}{D_p \rho_e} \right)^{1/2} \quad (5.A2)$$

with $\rho_e = \rho_{dp} + \rho_{cp}/2$. Integration is performed until the drop stops and changes direction. That point is denoted x_{max} . The above iterative procedure is stopped as soon as $x_{max} = l_d$, the latter calculated from eq. (5.7). At this point, the v_{dp} value corresponds to the jetting velocity.

2.8. Supplementary material

See supplementary material for insight on: 2.8.1, continuous phase flow analysis using Particle Image Velocimetry (PIV); 2.8.2, oscillations in jet widening; 2.8.3, collapsed data in jet narrowing; 2.8.4, comparison with Pathak's and Meyer and Crocker's DJT criteria; 2.8.5, estimation of the necking time.

2.8.1. Continuous phase flow analysis using Particle Image Velocimetry (PIV)

The continuous phase flow is analyzed by Particle Image Velocimetry (PIV) (without dispersed phase injection) in order to find the unperturbed continuous phase velocity v_{cp} at the location of the bound drop center of mass. To do so, a $5 \text{ }\mu\text{m}$ -Polyamid Seeding Particles solution (with a small amount of surfactant to disperse the particles) is pumped through the cell, with 50 images analyzed per flow rate (DynamicStudio, Dantec Dynamics), at least in triplicate. The camera, lens and light source are those of section 2.3. We use a resolution of $1280 \times 400 \text{ px}^2$ and an acquisition frequency of 6559 Hz. Adaptive PIV is performed with a final grid step size of $16 \times 16 \text{ px}^2$.

We investigate the different continuous phase volumetric flow rates q_{cp} tested in the present work. For each q_{cp} , we obtain an average velocity vector map (fig. 5.A1). The continuous phase velocity v_{cp} seen by a growing drop is determined from the map by the following method. We report the velocity component along the x -axis as a function of the position above the capillary y (fig. 5.A2). We note that this is done for a position x corresponding to the centre of the nozzle. We see that the continuous phase velocity above the nozzle is essentially

uniform, except for in a thin adjacent layer, corresponding to the boundary-layer. As mentioned in section 2.3, in our case, drops are mainly located above this layer. As a result, we consider that the continuous phase velocity v_{cp} seen by a growing drop corresponds to the velocity measured in the uniform flow above the shear layer. Therefore, in the example of fig. 5.A2, we consider that $v_{cp} = 0.57 \text{ m.s}^{-1}$.

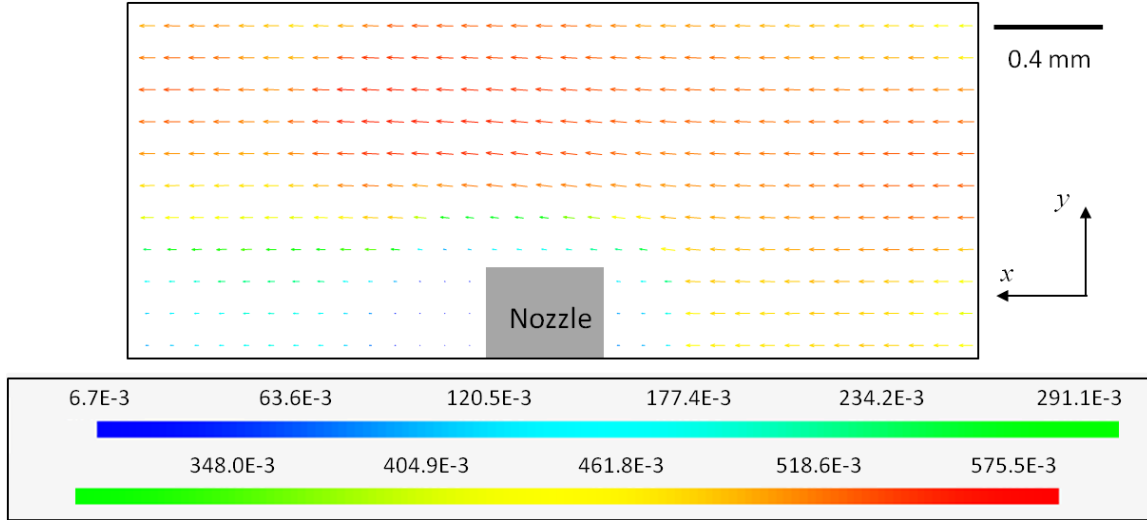


Figure 5.A1: Average velocity vector map in the centre of the cell channel at a continuous phase flow rate of 45.3 L.h^{-1} . Velocity scale below in m.s^{-1} ; nozzle tip superimposed in grey.

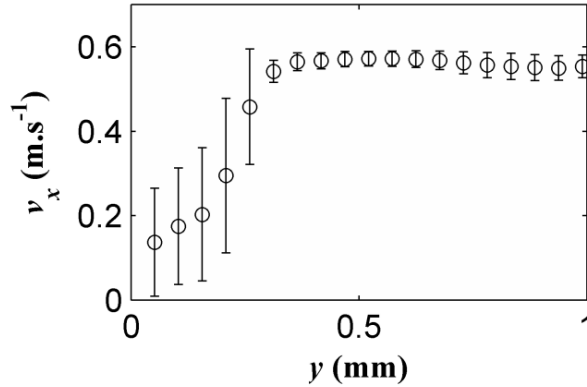


Figure 5.A2: Velocity component along the x -axis function of the position above the capillary y , for the example of fig. 5.A1.

2.8.2. Oscillations in jet widening

In fig. 5.B1, we show a chronological sequence of snapshots for a jet formed in the widening regime, for the reference system. From this, we can see the complex behavior of the thread, with surface oscillations which occur. These oscillations seem stationary in space. According to Utada *et al.* who studied jet widening in coflowing liquids, this behavior is characteristic of an absolute instability [20].

As Utada *et al.* [20], we further quantified these oscillations by focusing on the drop neck (between the drop and the thread). We measured the drop neck diameter variations in time (fig. 5.B2). It can be seen that the neck diameter oscillates about its mean with an increasing

amplitude until pinch-off, followed by drop detachment. The oscillation amplitude grows more rapidly for the reference system (black points, fig. 5.B2) than for system 1 (grey points, fig. 5.B2).

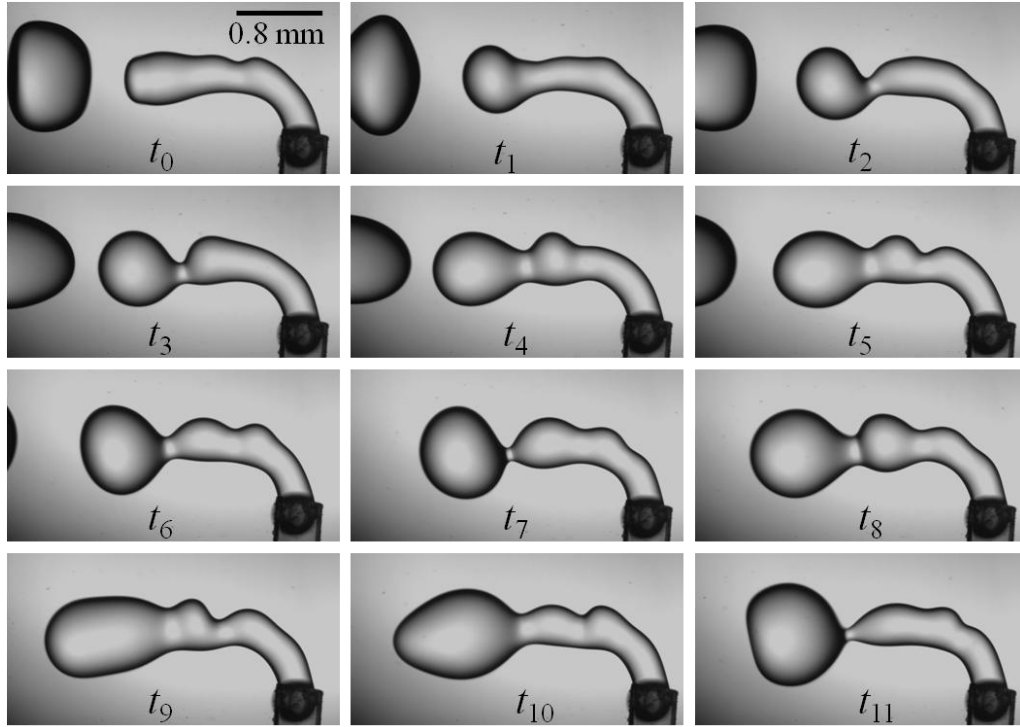


Figure 5.B1: Illustration of thread surface oscillations in jet widening: snapshots for the reference system ($Oh_{cp} = 7.0 \times 10^{-3}$), $We_{in} = 2.04$, $Ca_{out} = 5.1 \times 10^{-3}$. t_0 is the initial point, taken just after the previous drop detachment, $t_n = t_{n-1} + 656 \mu s$ and finally, the current drop detaches between t_{11} and t_{12} .

From various curves such as in fig. 5.B2, we estimate the neck oscillation frequency f_c for the reference system (350 Hz), system 1 (164 Hz) and system 2 (72 Hz). This gives characteristic growth times $\tau_c = 1/f_c$. We find that the necking time τ_n as calculated in section 2.5.2 is in the order of τ_c . τ_n is 1.4 to 2.5 times higher than τ_c , depending on the system.

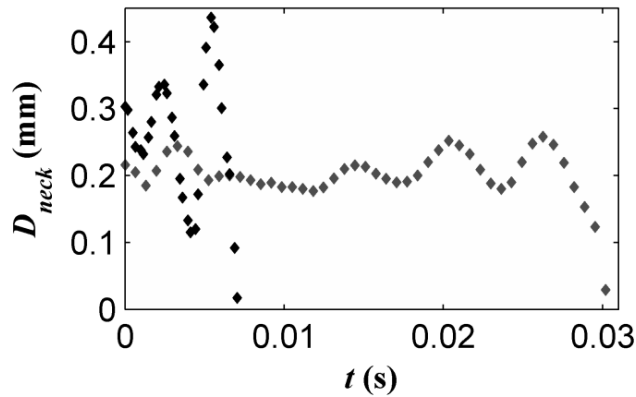


Figure 5.B2: Drop neck diameter variations in time for: reference system, $We_{in} = 2.04$ and $Ca_{out} = 5.1 \times 10^{-3}$ (black); system 1, $We_{in} = 0.82$ and $Ca_{out} = 6.8 \times 10^{-3}$ (grey).

2.8.3. Collapsed data in jet narrowing

In section 2.5.1, we noted that the transition from jet widening to narrowing is shifted towards higher Ca_{out} values as the interfacial tension decreases. This trend was not reported before. However, in our trials, the drag force experienced by a growing drop corresponds to that for an inertial flow since the particle Reynolds number Re_p ranges from 114 to 424. This is far from the Re_p range of Pathak's [22] cross-flow simulations, Meyer and Crocker's [21] cross-flow experiments or Utada *et al.*'s [20] coflow experiments. Indeed, Re_p ranges from about 10 to 50 in Pathak's simulations, from 2 to 150 in Meyer and Crocker's trials and from 2 to 10 in Utada *et al.*'s experiments. These Re_p ranges are much closer to creeping flow than ours.

Under Newton regime assumption, the ratio of the drag force to the capillary force is in order of $(Ca_{out}/Oh_{cp})^2 = We_{out}$ (as opposed to Ca_{out} under Stokes approximation). We therefore propose to plot the critical inner Weber number We_{in} as a function of Ca_{out}/Oh_{cp} (fig. 5.C1): it appears that our data in fact collapse in the narrowing regime.

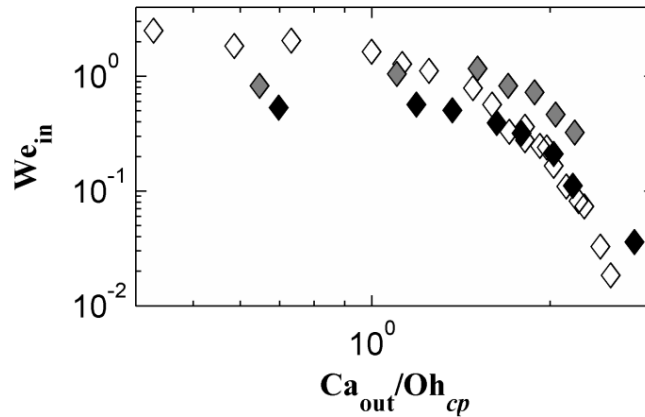


Figure 5.C1: We_{in} function of Ca_{out}/Oh_{cp} , see table 5.1 for symbols.

2.8.4. Comparison with Pathak's and Meyer and Crocker's DJT criteria

Figure 5.D1 presents the DJT data obtained for the reference system in the $Ca_{out}-We_{in}$ space, together with Pathak's [22] and Meyer and Crocker's [21] DJT criteria. The outer capillary number in Pathak's criterion is originally built with the mean continuous phase velocity (ratio of the volumetric flow rate to the channel section for the continuous phase flow). To calculate Pathak's criterion, we presently assimilate the mean continuous phase velocity to v_{cp} , the velocity effectively seen by a growing drop. The outer capillary number in Meyer and Crocker's criterion is built with the continuous phase wall shear rate and the nozzle inner diameter. To calculate Meyer and Crocker's criterion, we consider that the continuous phase velocity at the distance D_p from the nozzle tip is close to v_{cp} .

Figure 5.D1 shows that the reference system data are not satisfactorily described by Pathak's criterion (dashed line), nor by Meyer and Crocker's criterion (solid line). Two main reasons may be advanced: (i) in our trials, the growing drop is mainly located above the shear layer adjacent to the nozzle tip whereas in the previous authors' work, the drop is entirely located in

the shear layer; (ii) the hydrodynamic regime of the drag force experienced by the drop differs between our experiments and Pathak's simulations and Meyer and Crocker's trials (see supplementary material in 2.8.3).

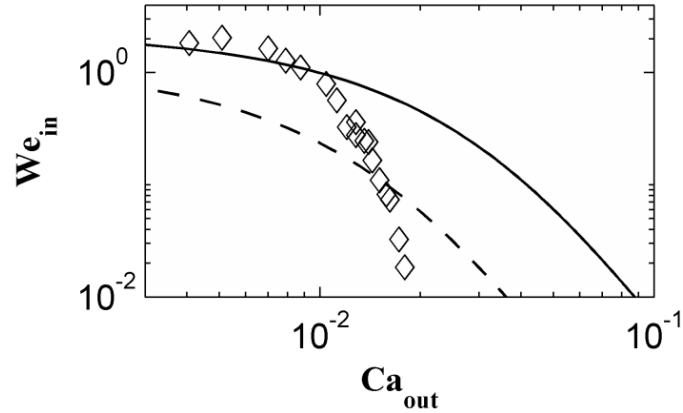


Figure 5.D1: We_{in} function of Ca_{out} at the DJT, see table 5.1 for symbols. Pathak's DJT criterion (dashed line); Meyer and Crocker's DJT criterion (solid line).

2.8.5. Estimation of the necking time

By the same method as Clanet and Lasheras, we estimate the characteristic necking time τ_n of a drop formed in dripping mode [11]. We measure the neck diameter variations in time and fit our data with an exponential function in the form $D_{neck}/D_p = 1 - e^{-(t-t_0)/\tau_n}$ (example given in fig. 5.E1), where t_0 is the moment of drop detachment.

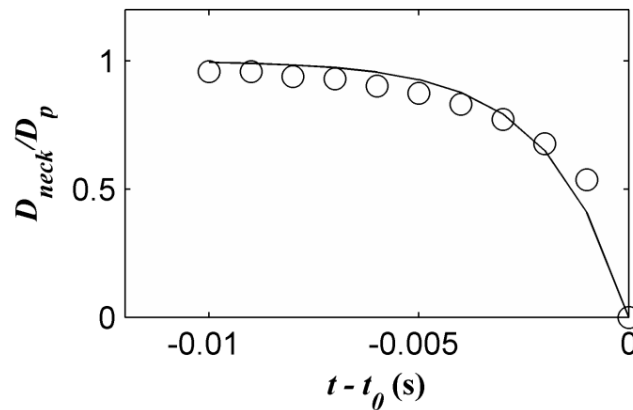


Figure 5.E1: Evolution of the dimensionless neck width (D_{neck}/D_p) in time: (o) reference system data, for $v_{cp} = 0.39 \text{ m.s}^{-1}$ and $v_{dp} = 0.031 \text{ m.s}^{-1}$; exponential fit with $\tau_n = 0.0019 \text{ s}$ (solid line).

We carry out this method for three trials on the reference system, for different (low) continuous phase velocities v_{cp} . We repeat this method for systems 1 and 2, again in dripping mode and for low v_{cp} . We report our results in fig. 5.E2 to determine the expression of the necking time τ_n .

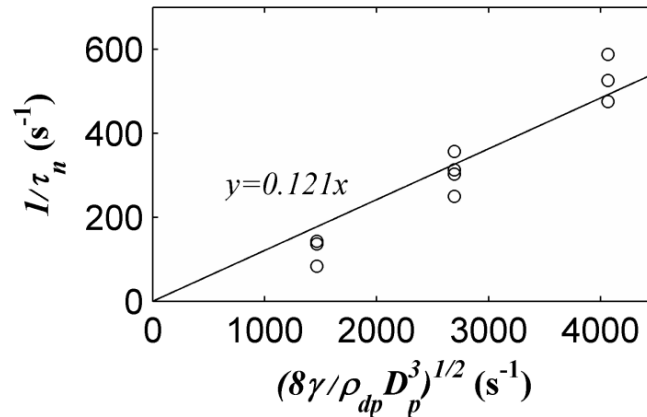


Figure 5.E2: Necking growth rate function of $(8\gamma/D_p^3\rho_{dp})^{1/2}$, obtained on the reference system ($v_{cp} = 0.18$ to 0.44 $\text{m}\cdot\text{s}^{-1}$), system 1 ($v_{cp} = 0.11$ to 0.35 $\text{m}\cdot\text{s}^{-1}$) and system 2 ($v_{cp} = 0.10$ to 0.20 $\text{m}\cdot\text{s}^{-1}$), with $v_{dp} = 0.031$ $\text{m}\cdot\text{s}^{-1}$. Fit passing through the origin (solid line).

2.9. Acknowledgements

We thank T. Martin and J. Trubuil for their contribution in designing the setup and for their work on the setup manufacturing.

3. Additional information

3.1. Influence of the dispersed phase viscosity

As described in 2.4, we tested the impact of the dispersed phase velocity on drop generation in dripping mode, for the reference system. No impact was found on the drop diameters produced, thus results were not presented. They are shown below in fig. 5.AI1.

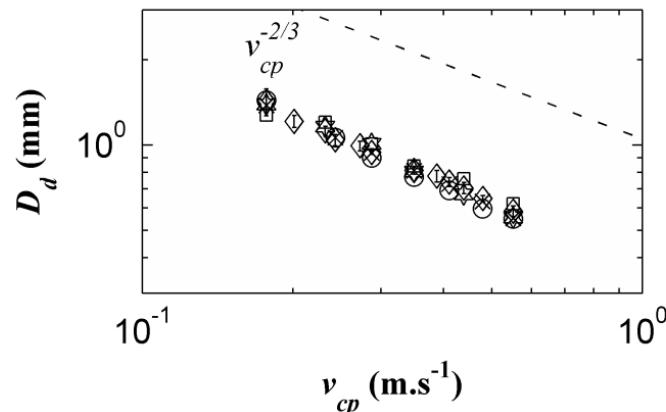


Figure 5.AI1: Drop diameter function of the continuous phase velocity for different dispersed phase velocities, for the reference system. (o) $v_{dp} = 0.016$ $\text{m}\cdot\text{s}^{-1}$; (\diamond) $v_{dp} = 0.031$ $\text{m}\cdot\text{s}^{-1}$; (x) $v_{dp} = 0.063$ $\text{m}\cdot\text{s}^{-1}$; (\star) $v_{dp} = 0.14$ $\text{m}\cdot\text{s}^{-1}$; (\square) $v_{dp} = 0.21$ $\text{m}\cdot\text{s}^{-1}$.

4. References

- [1] T. Nakashima, M. Shimizu, and M. Kukizaki, « Membrane Emulsification by Microporous Glass », *Key Engineering Materials*, 61–62, p. 513–516, 1992.
- [2] S. J. Peng and R. A. Williams, « Controlled production of emulsions using a crossflow membrane: Part I: Droplet formation from a single pore », *Chem. Eng. Res. Des.*, 76 (8), p. 894–901, 1998.
- [3] A. S. Utada, A. Fernandez-Nieves, H. A. Stone and D. A. Weitz, « Dripping to Jetting Transitions in Coflowing Liquid Streams », *Phys. Rev. Lett.*, 99 (9), 094502, 2007.
- [4] E. Castro-Hernández, V. Gundabala, A. Fernández-Nieves and J. M. Gordillo, « Scaling the drop size in coflow experiments », *New J. Phys.*, 11 (7), 075021, 2009.
- [5] A. M. Gañán-Calvo, « Jetting–dripping transition of a liquid jet in a lower viscosity co-flowing immiscible liquid: the minimum flow rate in flow focusing », *J. Fluid Mech.*, 553 (1), p. 75–84, 2006.
- [6] S. L. Anna, N. Bontoux and H. A. Stone, « Formation of dispersions using “flow focusing” in microchannels », *Appl. Phys. Lett.*, 82 (3), p. 364–366, 2003.
- [7] A. S. Utada, « Monodisperse Double Emulsions Generated from a Microcapillary Device », *Science*, 308 (5721), p. 537–541, 2005.
- [8] S. W. J. Smith and H. Moss, « Experiments with Mercury Jets », *Proc. R. Soc. Math. Phys. Eng. Sci.*, 93 (652), p. 373–393, 1917.
- [9] G. F. Scheele and B. J. Meister, « Drop formation at low velocities in liquid-liquid systems: Part II. Prediction of jetting velocity », *AIChE J.*, 14 (1), p. 15–19, 1968.
- [10] J. R. Richards, A. N. Beris and A. M. Lenhoff, « Drop formation in liquid–liquid systems before and after jetting », *Phys. Fluids*, 7 (11), p. 2617–2630, 1995.
- [11] C. Clanet and J. C. Lasheras, « Transition from dripping to jetting », *J. Fluid Mech.*, 383, p. 307–326, 1999.
- [12] G. I. Taylor, « The dynamics of thin sheets of fluids. III. Disintegration of fluid sheets », *Proc. R. Soc. Lond. A*, 253 (1274), p. 313–321, 1959.
- [13] C. Cramer, P. Fischer and E. J. Windhab, « Drop formation in a co-flowing ambient fluid », *Chem. Eng. Sci.*, 59 (15), p. 3045–3058, 2004.
- [14] Y. Chen, L. Wu and C. Zhang, « Emulsion droplet formation in coflowing liquid streams », *Phys. Rev. E*, 87 (1), 013002, 2013.
- [15] S. J. Leib and M. E. Goldstein, « Convective and absolute instability of a viscous liquid jet », *Phys. Fluids*, 29 (4), p. 952–954, 1986.
- [16] P. Huerre and P. A. Monkewitz, « Local and Global Instabilities in Spatially Developing Flows », *Annu. Rev. Fluid Mech.*, 22 (1), p. 473–537, 1990.
- [17] P. Guillot, A. Colin, A. S. Utada and A. Ajdari, « Stability of a Jet in Confined Pressure-Driven Biphasic Flows at Low Reynolds Numbers », *Phys. Rev. Lett.*, 99 (10), 104502, 2007.
- [18] P. Guillot, A. Colin and A. Ajdari, « Stability of a jet in confined pressure-driven biphasic flows at low Reynolds number in various geometries », *Phys. Rev. E*, 78 (1), 016307, 2008.

- [19] M. A. Herrada, A. M. Gañán-Calvo and P. Guillot, « Spatiotemporal instability of a confined capillary jet », *Phys. Rev. E*, 78 (4), 046312, 2008.
- [20] A. S. Utada, A. Fernandez-Nieves, J. M. Gordillo and D. A. Weitz, « Absolute Instability of a Liquid Jet in a Coflowing Stream », *Phys. Rev. Lett.*, 100 (1), 014502, 2008.
- [21] R. F. Meyer and J. C. Crocker, « Universal Dripping and Jetting in a Transverse Shear Flow », *Phys. Rev. Lett.*, 102, 194501, 2009.
- [22] M. Pathak, « Numerical simulation of membrane emulsification: Effect of flow properties in the transition from dripping to jetting », *J. Membr. Sci.*, 382 (1–2), p. 166–176, 2011.
- [23] S. R. Deshiikan, D. Bush, E. Eschenazi and K. D. Papadopoulos, « SDS, Brij58 and CTAB at the dodecane-water interface », *Colloids Surf. Physicochem. Eng. Asp.*, 136 (1), p. 133–150, 1998.
- [24] A. Bertrandias, H. Duval, J. Casalinho and M. L. Giorgi, « Drop generation from a vibrating nozzle in an immiscible liquid-liquid system », *Phys. Fluids*, 28, 102103, 2016.
- [25] F. A. Morrison, *An introduction to fluid mechanics* (Cambridge University Press), p. 622–628, 2013.
- [26] J. Xu, G. Luo, G. Chen and J. Wang, « Experimental and theoretical approaches on droplet formation from a micrometer screen hole », *J. Membr. Sci.*, 266 (1–2), p. 121–131, 2005.
- [27] A. Timgren, G. Trägårdh and C. Trägårdh, « Effects of cross-flow velocity, capillary pressure and oil viscosity on oil-in-water drop formation from a capillary », *Chem. Eng. Sci.*, 64 (6), p. 1111–1118, 2009.
- [28] R. Clift, J. Grace and M. E. Weber, *Bubbles, Drops and Particles* (Dover Publications, Inc.) p.125–135, 2005.
- [29] A. Bertrandias, H. Duval, J. Casalinho and M. L. Giorgi, « Good vibrations —Transition in drop generation from an immersed capillary tube », *EPL*, 111 (4), 44004, 2015.
- [30] Z.-G. Feng and E. E. Michaelides, « Drag Coefficients of Viscous Spheres at Intermediate and High Reynolds Numbers », *J. Fluids Eng.*, 123 (4), p. 841–849, 2001.
- [31] F. F. Abraham, « Functional Dependence of Drag Coefficient of a Sphere on Reynolds Number », *Phys. Fluids*, 13 (8), p. 2194–2195, 1970.
- [32] M. E. O’Neill, « A sphere in contact with a plane wall in a slow linear shear flow », *Chem. Eng. Sci.*, 23 (11), p. 1293–1298, 1968.
- [33] Rayleigh, « On the instability of jets », *Proceeding Lond. Math. Soc.*, 10, p. 4–13, 1878.
- [34] T. Funada and D. D. Joseph, « Viscous potential flow analysis of capillary instability », *Int. J. Multiph. Flow*, 28 (9), p. 1459–1478, 2002.

Conclusion

Conclusions

The initial aim of our work was to understand the detachment mechanisms for drops in transversally vibrating membrane emulsification. Indeed, C. Arnaud (2006) and E. Lepercq-Bost (2008) found that in certain conditions, vibration led to a significant decrease in drop size compared to without vibration. However, the mechanisms remained unknown.

To understand these mechanisms, we first studied a simplified configuration with a dedicated experimental setup to observe the impact of vibration (only) on drop generation. It consisted in a single capillary tube (nozzle) through which the dispersed phase was forced, forming drops into a stationary, continuous phase. We studied the impact of pore diameter, interfacial tension, dispersed phase velocity, dispersed and continuous phase viscosities as well as the forcing parameters of the axially vibrating nozzle (frequency and amplitude).

For a set forcing frequency, significantly smaller drops are produced above a threshold amplitude. We named this the stretching mode. We found that a drop grows and resonates in first mode (centre-of-mass motion mode) once its first eigenfrequency coincides with the forcing frequency. The drop dynamics were described by modelling the drop as a linearly forced harmonic oscillator (LFHO), with the first eigenfrequency of Strani and Sabetta (1984) and the damping coefficient of Bisch *et al.* (1982). An additional damping coefficient was introduced to account for the viscous dissipation in the film of continuous phase between the drop and the nozzle surface (as the drop does not wet the nozzle tip). A criterion for detachment was established: a drop detaches when the restoring capillary force exceeds the maximum capillary force. From this, if the centre-of-mass motion from the LFHO model (thus forcing amplitude, for a set forcing frequency) exceeds a certain value, the drop detaches at resonance, with its size controlled by the forcing frequency. This leads to the production of the smaller drops observed in stretching mode. Otherwise, the drop continues to grow and detaches in dripping mode at larger sizes, essentially controlled by buoyancy.

Overall, our model well accounts for experimental threshold amplitudes and resulting drop sizes in the range of viscosities and interfacial tensions tested, except for the system with an increased continuous phase viscosity. We note that from the model, we account for drop sizes obtained by C. Arnaud in industrial vibrating membrane emulsification.

We then experimentally studied drop formation from a nozzle into continuous phase cross-flow with a second, specifically developed setup. This enabled to approach the industrial process, as cross-flow induces drop generation in dripping mode due to the drag exerted. In the

previous setup, buoyancy induced detachment in the absence of vibration rather than shear, as the continuous phase was stationary. We studied the impact of the interfacial tension, dispersed phase viscosity, both phase velocities and forcing parameters of the axially vibrating nozzle.

With cross-flow (no vibration), drop diameters are well described by a torque balance. In the trials of E. Lepercq-Bost, a torque balance well accounts for one of the peaks of drops formed without vibration. With cross-flow and vibration, no significant difference was found compared to the results with vibration but without cross-flow (previous setup), due to setup limitations. We demonstrated the importance of well adjusting the combination of cross-flow velocity and forcing parameters to control drop size by the stretching mode. In E. Lepercq-Bost trials, the cross-flow was too high for the set forcing parameters to obtain the stretching mode.

The dripping to jetting transition in cross-flow was then investigated. Without vibration, the transition depended on the inner Weber number, function of the outer capillary and Ohnesorge numbers. Two jetting regimes occurred depending on the phase velocity ratio (jet widening and narrowing). We developed a model based on the drop equation of motion to predict the dripping to jetting transition. We compared the receding distance travelled by the drop to the detachment distance by pinch off. When the distance travelled is smaller than the detachment distance by pinch off, the detachment point advances each time, leading to jetting. The jetting velocity was determined when the two distances became equal and we deduced the resulting drop diameter. We applied the model to two limit cases in jet narrowing: a uniform-sized jet or maximal narrowing (the uniform-sized jet limit was always applied in jet widening). In jet narrowing, our data lie in between the two limit cases, so the model is satisfactory. In jet widening, jetting velocities and drop sizes are overpredicted due to the complex jet profile. With vibration, a delay in the dripping to jetting transition was observed. This leads to a better control on drop size due to the transition back to dripping, and even to stretching, depending on the forcing amplitude. In the trials of E. Lepercq-Bost, vibration simply led to the appearance of a peak smaller than the pore diameter, which we attribute to satellite drop formation.

In conclusion, we explained drops sizes obtained in the trials of C. Arnaud and E. Lepercq-Bost with the mechanisms and models proposed. More generally, this work enabled to gain insight on bound drop generation under high-amplitude forcing as well as on the dripping to jetting transition in cross-flow (for liquid-liquid systems). These topics had not been previously extensively studied nor understood. For both topics, we proposed models which were novel and satisfactory as they well accounted for most experimental results. We highlight the importance of understanding the mechanisms for drop detachment to be able to adjust operating parameters in vibrating membrane emulsification and as a result, control emulsion drop sizes.

Perspectives

Various perspectives emerge from this work, either to refine the models proposed or to gain further understanding on the topics studied:

- It would be interesting to calculate the eigenfrequency of a bound drop including the viscous dissipation in the film between the drop and nozzle surface. This would enable to gain insight on the data for the highest continuous phase viscosity.
- Also, experiments could be performed on an industrial membrane, for a broad range of systems and vibrating conditions compared to the two initial trials of C. Arnaud and E. Lepercq-Bost. This would enable to further validate our model and see the questions which remain. It should be noted that optimizing the continuous phase flow in the industrial process is necessary, to avoid drops from being formed by both dripping and jetting modes and thus avoid bimodal drop size distribution.
- Concerning the dripping to jetting transition, a more refined model could be developed based on the model we presented. In particular, this model could take into account the real jet profile with narrowing effects.
- The impact of axial vibrations on dripping was investigated in detail but the impact on jetting was only looked into briefly. It would be interesting to further study this, as it seems that vibration delays the transition from dripping to jetting.
- Finally, satellite drop formation when vibration is applied could be investigated, to optimize the conditions where they are suppressed. Indeed, satellite drops have less well controlled sizes and lead to a bimodal drop size distributions.

Appendix 1: Surfactant molecules formulae

The formulae for the different surfactants mentioned in the literature review in section 1.1.4. are represented here. The formulae have been taken from the ThermoFisher Scientific and Sigma-Aldrich websites (<https://www.thermofisher.com/> and <http://www.sigmaaldrich.com/>), consulted on the 26th of July 2016.

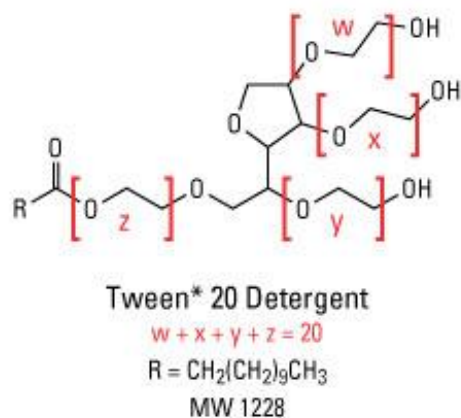


Figure A1.1: Tween 20 (Polysorbate 20).

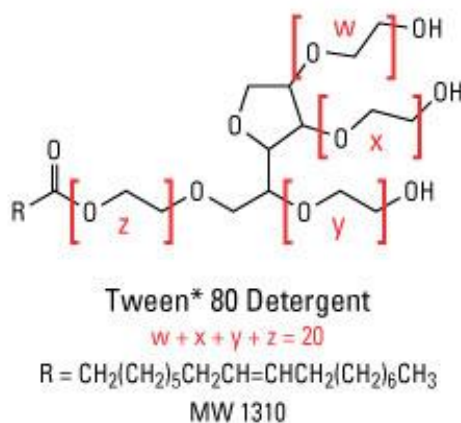


Figure A1.2: Tween 80 (Polysorbate 80).

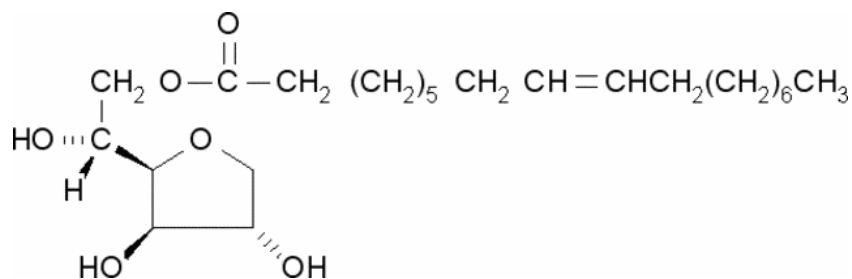


Figure A1.3: Span 80 (Sorbitane monooleate).

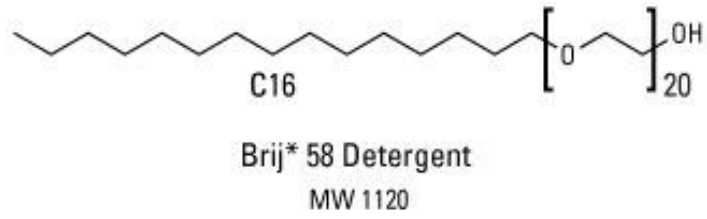


Figure A1.4: Brij 58 (Polyethylene glycol hexadecyl ether).

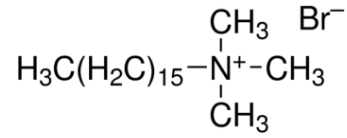


Figure A1.5: CTAB (Cetyl trimethylammonium bromide).

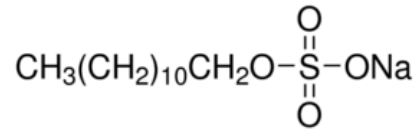


Figure A1.6: SDS (Sodium dodecyl sulphate).

Appendix 2: CAD of the experimental setups

1. Setup 1: single drop formation into a stationary outer phase

This setup corresponds to that described in section 1 of chapter 2 and which was used to obtain the results of chapters 3, 4 and Appendix 3.

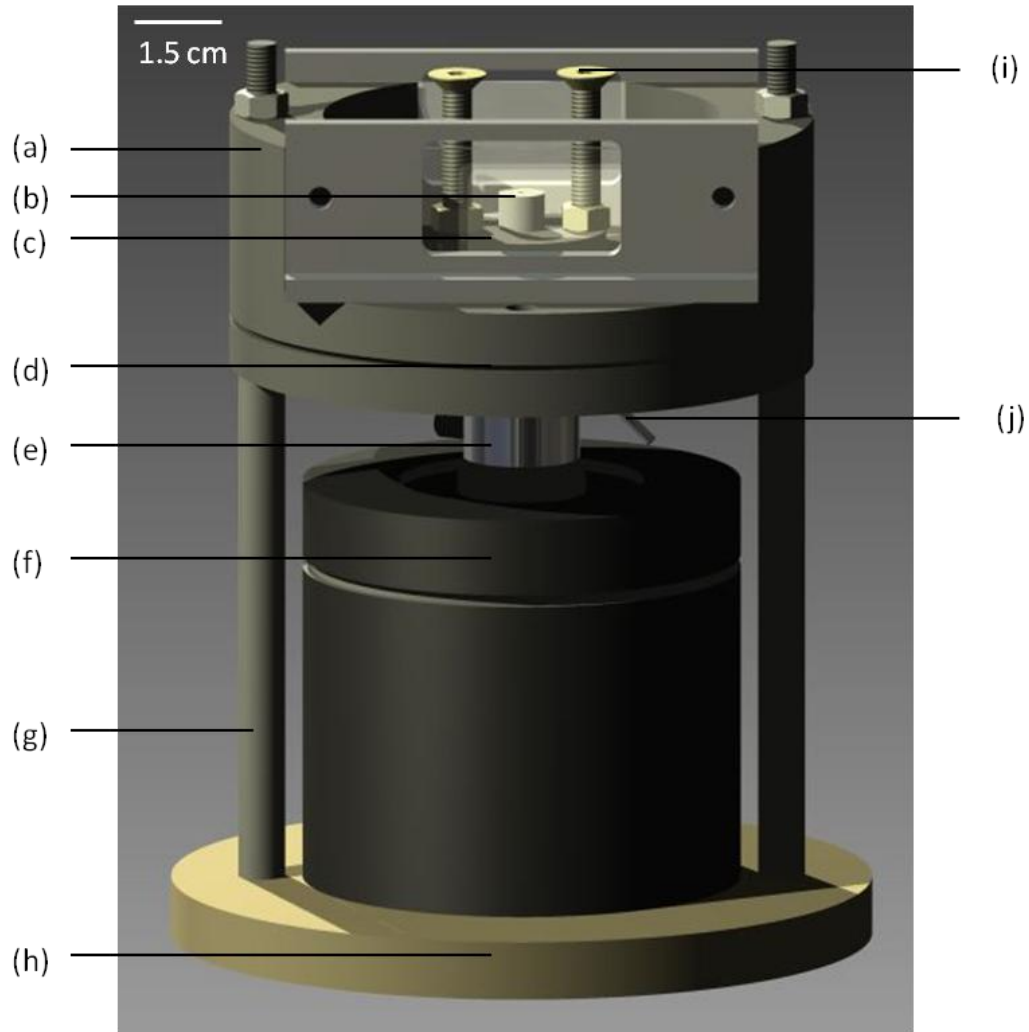


Figure A2.1: CAD designed by Joel Casalinho of the entire setup (to scale). (a) Tank; (b) capillary tube (nozzle); (c) window for image acquisition; (d) position of rubber seal between the upper and lower parts of the tank; (e) central element linking the capillary to the vibrating exciter; (f) vibrating exciter; (g) setup support; (h) bottom support placed on the anti-vibration table; (i) screw to support capillary and for amplitude displacement measurement; (j) dispersed phase influx element.

2. Setup 2: single drop formation into cross-flow

This setup corresponds to that described in section 2 of chapter 2 and which was used to obtain the results of chapter 5 and Appendices 4 and 5.

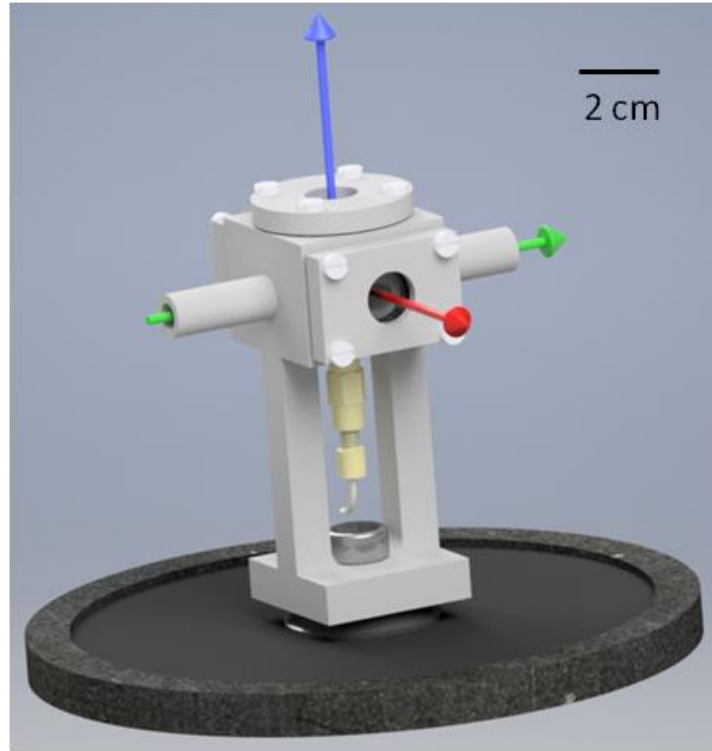


Figure A2.2: CAD designed by Joel Casalinho of the entire cell, fixed onto the vibrating exciter (to scale). Dispersed phase flow direction and vibration axis (blue arrow); continuous phase flow axis (green arrow); optical axis (red arrow).

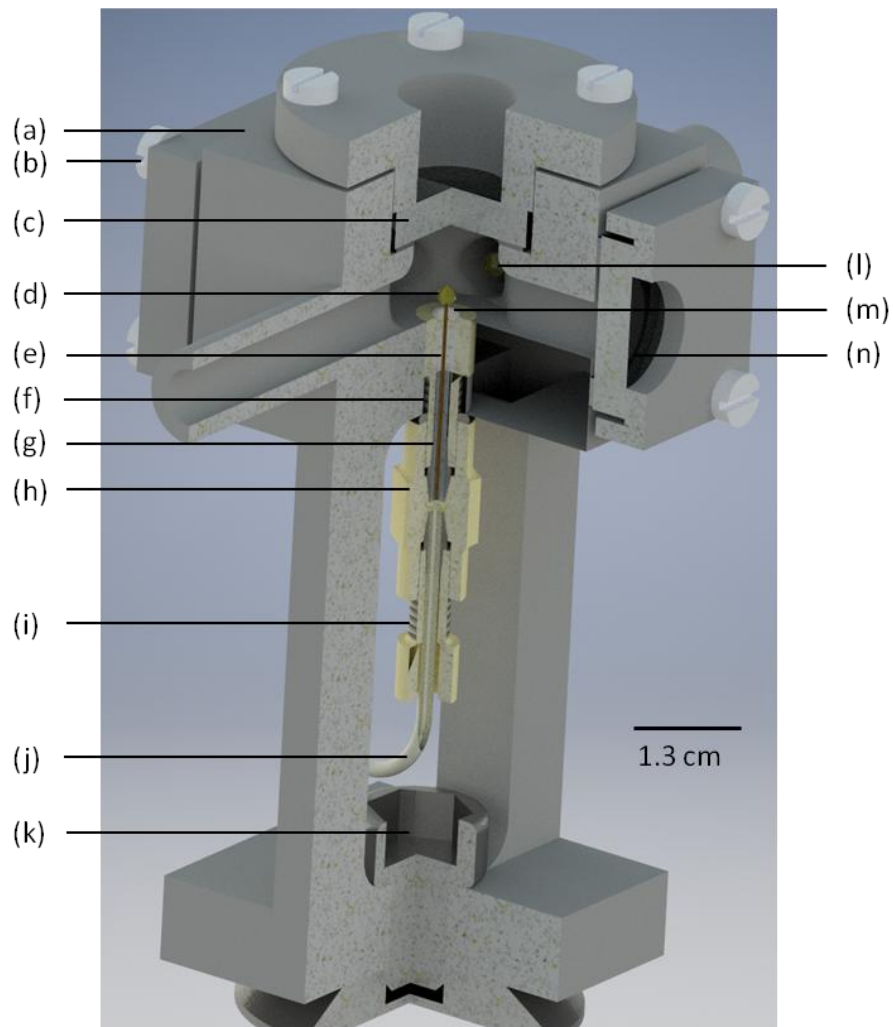


Figure A2.3: CAD designed by Joel Casalinho of the cross-section of the inside of the cell (to scale). (a) cell; (b) screws to close the setup; (c) window for user observation; (d) drop in formation; (e) capillary tube (nozzle); (f) screw for microfluidic system (downstream); (g) sleeve; (h) connector; (i) screw for microfluidic system (upstream); (j) tube for dispersed phase influx; (k) screw to fix cell on vibrating exciter; (l) drop carried away by the continuous phase flow; (m) silicon; (n) window for image acquisition.

Appendix 3: Complementary results on drop generation in stretching mode with a stationary outer phase

1. Complementary experimental results

In chapters 3 and 4, not all experimental results were exposed due to space constraints for publishing. Here, we present the complementary results followed by a short analysis.

1.1. Impact of dispersed phase flow rate

For most of the experimental conditions tested (pore size, system, vibration parameters), at least two dispersed phase flow rates were applied. The experimental results are presented in this section, depending on the system.

1.1.1. Reference system

For the reference system, in chapter 4, we showed data for different dispersed phase flow rates for the reference pore diameter ($D_p = 0.32$ mm). For this system, we also tested two flow rates for $D_p = 0.11$ mm and 0.35 mm. The highest flow rate (red) was 1.4 times and 1.7 times the lowest flow rate (blue), respectively. Considering the error bars, threshold amplitudes and drop diameters for $D_p = 0.11$ mm are not affected by the flow rate, for the rates investigated (fig. A3.1(a) and (b)). This confirms results found for $D_p = 0.32$ mm in chapter 4. The chapter 4 model results (yellow lines) show that this is expected. For fig. A3.2 to A3.6, model results will not be plotted such as in fig. A3.1, in order to render the figures more readable.

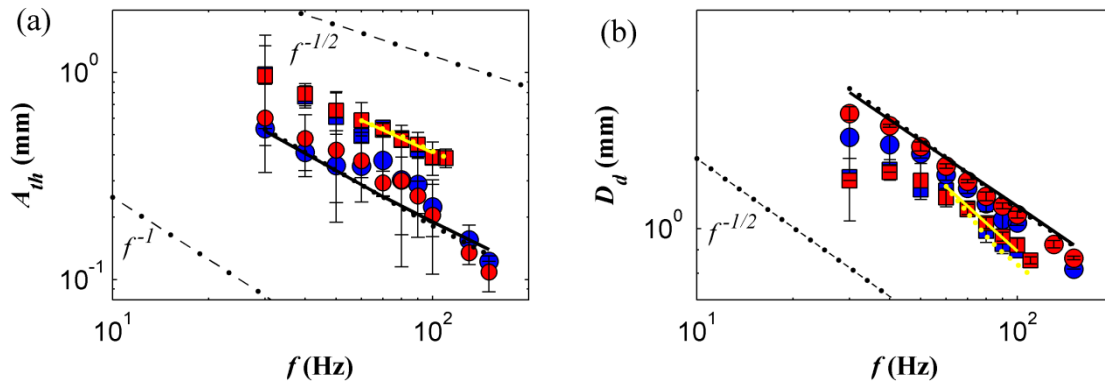


Figure A3.1: Impact of dispersed phase flow rate on (a) threshold amplitude A_{th} and (b) drop diameter at A_{th} , for the reference system. (\square) $D_p = 0.11$ mm, $q = 2.2 \mu\text{L}\cdot\text{s}^{-1}$ (blue), $q = 3.1 \mu\text{L}\cdot\text{s}^{-1}$ (red); (\circ) $D_p = 0.35$ mm, $q = 3.8 \mu\text{L}\cdot\text{s}^{-1}$ (blue), $q = 6.4 \mu\text{L}\cdot\text{s}^{-1}$ (red). Simulations from eq. (4.17) of chapter 4: $D_p = 0.11$ mm, $\alpha = -1.4$, $\mathcal{C} = 8.2$ (yellow); $D_p = 0.35$ mm, $\alpha = -1.9$, $\mathcal{C} = 4.4$ (black). Lowest flow rates (dotted line); highest flow rates (solid line).

For $D_p = 0.35$ mm, threshold amplitudes are also unaffected (fig. A3.1(a)), as expected from the chapter 4 model (black lines). However, there is a relative increase of between 0.1% and 12.7% in drop diameter when the flow rate is increased (red circles vs. blue circles) (fig. A3.1(b)). We consider that this is due to extra dispersed phase fed to the drop during necking, with necking time assimilated to the time for one oscillation to occur. Therefore, we estimate the extra volume fed to the drop by:

$$V_n = \frac{q_{high\ flow\ rate} - q_{low\ flow\ rate}}{f} \quad (A3.1)$$

We add this value to the drop size obtained at the low flow rate to estimate the drop size at the higher flow rate. Relative errors in drop diameter of 1.5% to 10.1% are found compared to trials. It is reasonable to assimilate part of the increase in drop size with increasing dispersed phase flux to an extra volume of dispersed phase fed to the drop during necking. This is not taken into account by the model, which explains that no difference in drop size is expected.

1.1.2. System 2

For system 2, as for the reference system (chapter 4), we studied the impact of four dispersed phase flow rates for $D_p = 0.32$ mm: $q = 1.2 \mu\text{L}\cdot\text{s}^{-1}$, $2.4 \mu\text{L}\cdot\text{s}^{-1}$, $3.6 \mu\text{L}\cdot\text{s}^{-1}$ and $6.1 \mu\text{L}\cdot\text{s}^{-1}$. Again, when considering the error bars, threshold amplitudes are not significantly affected by the flow rate in the trial range (fig. A3.2(a)). An average relative increase in drop diameter of 24.2% is observed at $6.1 \mu\text{L}\cdot\text{s}^{-1}$ (black points) compared to $1.2 \mu\text{L}\cdot\text{s}^{-1}$ (red points) (fig. A3.2(b)). We attribute part of this to the extra dispersed phase fed to the drop during necking. Indeed, from the same method as above, we find relative errors between calculated and experimental drop sizes of 0% to 14% for the highest flow rate.

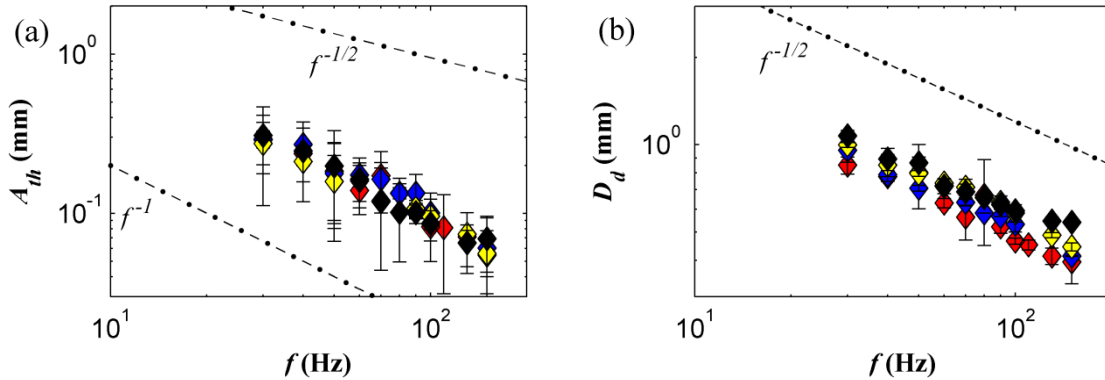


Figure A3.2: Impact of dispersed phase flow rate on (a) threshold amplitude A_{th} and (b) drop diameter at A_{th} , for system 2, $D_p = 0.32$ mm. $q = 1.2 \mu\text{L}\cdot\text{s}^{-1}$ (red); $q = 2.4 \mu\text{L}\cdot\text{s}^{-1}$ (blue); $q = 3.6 \mu\text{L}\cdot\text{s}^{-1}$ (yellow); $q = 6.1 \mu\text{L}\cdot\text{s}^{-1}$ (black).

For system 2, we also investigated the impact of two flow rates for $D_p = 0.35$ mm and 0.75 mm. The highest dispersed phase flow rate (red) was 1.7 and 2.0 times the lowest rate (blue), respectively. Threshold amplitudes are unaffected by the dispersed phase flow rate for both pore diameters when considering the error bars (fig. A3.3(a)). Drop diameters are also unaffected for $D_p = 0.35$ mm (fig. A3.3(b)). This confirms previous findings.

For $D_p = 0.75$ mm, a relative increase in drop diameter between 17.0% and 51.1% is found above 70 Hz for the highest flow rate (red crosses) compared to the lowest flow rate (blue crosses). For the highest flow rate, drops are larger than expected. From the footage, it is seen that a drop which detaches by resonance remerges with the dispersed phase in the tube before

actually detaching. Therefore, extra dispersed phase is fed to the drop after the mergence. These results are therefore not representative of the phenomena we investigate.

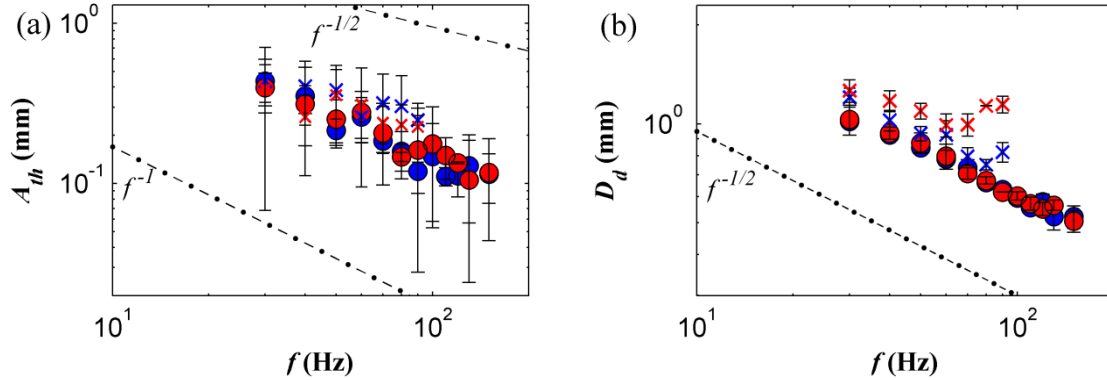


Figure A3.3: Impact of dispersed phase flow rate on (a) threshold amplitude A_{th} and (b) drop diameter at A_{th} , for system 2. (o) $D_p = 0.35$ mm, $q = 3.8$ $\mu\text{L}\cdot\text{s}^{-1}$ (blue); $q = 6.4$ $\mu\text{L}\cdot\text{s}^{-1}$ (red); (x) $D_p = 0.75$ mm, $q = 9.6$ $\mu\text{L}\cdot\text{s}^{-1}$ (blue), $q = 19.1$ $\mu\text{L}\cdot\text{s}^{-1}$ (red).

1.1.3. Other systems

For the other systems, *i.e.*, systems 1, 3, 4 and 5, we tested two flow rates for $D_p = 0.32$ mm. The highest (red) was 1.5 times the lowest (blue) for system 1 and 1.7 times for the other systems. Threshold amplitudes are not significantly affected by the flow rate when considering the error bars, for the rates tested (fig. A3.4(a)), confirming previous findings. Drop diameters are not affected for systems 1, 3 and 4, as the relative increase in drop diameter is maximum 7.2% (in the order of drop diameter uncertainty) (fig. A3.4(b)).

For system 5, a relative increase in drop diameter between -7.2% and 24.8% is found depending on the frequency (red *vs.* blue stars). It is surprising that drops generated at low flow rates can be larger than at high flow rates. Error bars are especially large for these trials, so we cannot conclude on the impact of the flow rate (fig. A3.4(b)). As exposed in chapter 4, this system is complex and further work remains to be performed on it to grasp its behaviour.

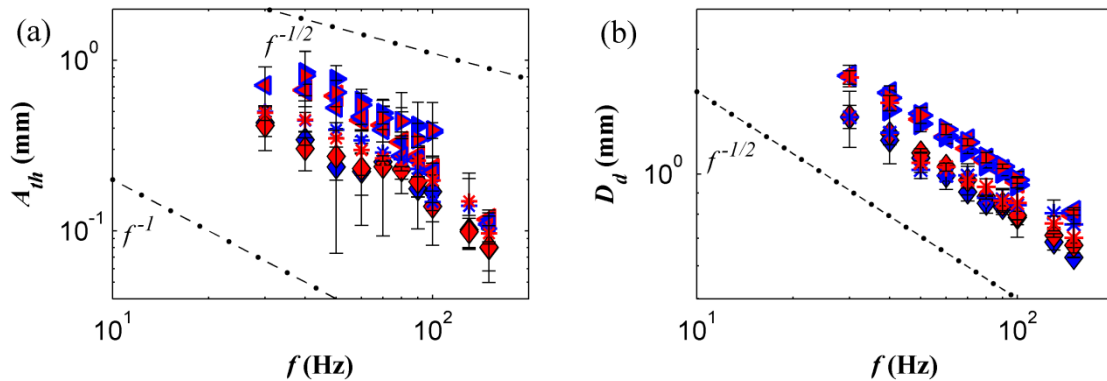


Figure A3.4: Impact of dispersed phase flow rate on (a) threshold amplitude A_{th} and (b) drop diameter at A_{th} . (\diamond) System 1: $q = 2.4$ $\mu\text{L}\cdot\text{s}^{-1}$ (blue), $q = 3.6$ $\mu\text{L}\cdot\text{s}^{-1}$ (red); (\triangleleft) System 3: $q = 2.5$ $\mu\text{L}\cdot\text{s}^{-1}$ (blue), $q = 4.3$ $\mu\text{L}\cdot\text{s}^{-1}$ (red); (\triangleright) System 4: $q = 2.5$ $\mu\text{L}\cdot\text{s}^{-1}$ (blue), $q = 4.3$ $\mu\text{L}\cdot\text{s}^{-1}$ (red); (*) System 5: $q = 2.5$ $\mu\text{L}\cdot\text{s}^{-1}$ (blue), $q = 4.3$ $\mu\text{L}\cdot\text{s}^{-1}$ (red).

1.1.4. Conclusions

Threshold amplitudes were unaffected by the different flow rates. This confirms results of chapters 3 and 4, where only the reference system and pore diameter were detailed. Drop diameters were also unaffected, as described before, except in a few cases, where an increase in drop diameter occurred with increased flow rates. This was partly attributed to the extra dispersed phase fed to the drop during necking.

1.2. Impact of the pore diameter

The impact of the pore diameter was illustrated in chapters 3 and 4 for the reference system. Trials were also performed for the four pore diameters for system 2. Threshold amplitudes decrease with increasing forcing frequency, with a scaling of $f^{-0.52 \pm 0.09}$, $f^{-0.80 \pm 0.05}$ and $f^{-0.76 \pm 0.05}$ for $D_p = 0.11$ mm, 0.32 mm and 0.35 mm, respectively (fig. A3.5(a)). The values of the exponent are lower in absolute value than for the reference system for each pore diameter. For $D_p = 0.75$ mm, the scaling is less clear (fig. A3.5(a)), as was already the case for the reference system. Also, as for the reference system, threshold amplitudes are higher for $D_p = 0.11$ mm (fig. A3.5(a)).

Drop diameters vary as $f^{-0.4 \pm 0.05}$, $f^{-0.49 \pm 0.02}$ and $f^{-0.47 \pm 0.03}$ for $D_p = 0.11$ mm, 0.32 mm and 0.35 mm, respectively, in accordance with the expected $f^{-1/2}$ scaling. Again, no clear law emerges for $D_p = 0.75$ mm (fig. A3.5(b)). The larger the pore diameter, the larger the drops formed. The drop diameter roughly scales as $D_p^{1/4}$ (deviation of 5 % to 14% depending on f), in better agreement with expectations than for the reference system.

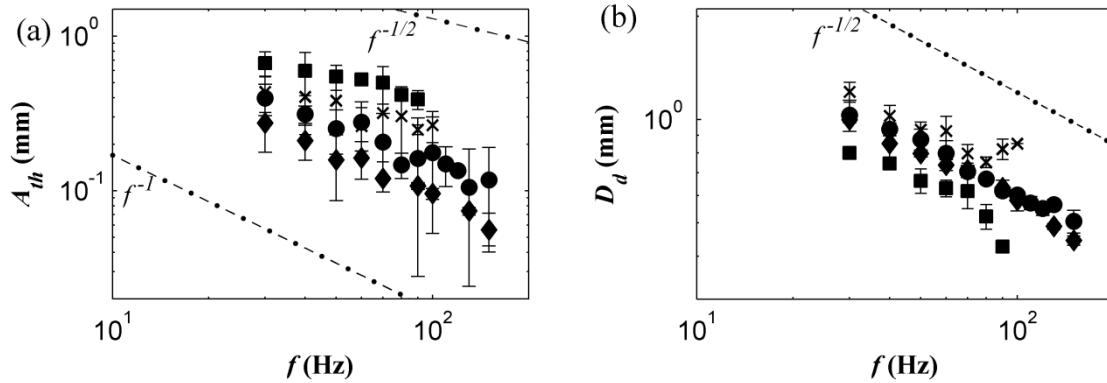


Figure A3.5: Impact of pore diameter on (a) threshold amplitude A_{th} and (b) drop diameter at A_{th} , for system 2. (\square) $D_p = 0.11$ mm, $q = 1.1 \mu\text{L}\cdot\text{s}^{-1}$; (\diamond) $D_p = 0.32$ mm, $q = 3.6 \mu\text{L}\cdot\text{s}^{-1}$; (\circ) $D_p = 0.35$ mm, $q = 6.4 \mu\text{L}\cdot\text{s}^{-1}$; (\times) $D_p = 0.75$ mm, $q = 9.6 \mu\text{L}\cdot\text{s}^{-1}$.

1.3. Impact of the continuous phase viscosity

The impact of the continuous phase viscosity was studied for a system with surfactant. That is, the equivalent of system 5 was tested with 2% SDS, referred to as system 6. The interfacial tension is of $\gamma = 4.3 \text{ mN}\cdot\text{m}^{-1} \pm 0.4$. The density and viscosity are those of system 5 ($\rho_{cp} = 1119$

kg.m⁻³, $\eta_{cp} = 4.18$ mPa.s). System 6 (increased η_{cp} and 2 wt% SDS) was thus compared to system 2 (2 wt% SDS) to observe the impact of the continuous phase viscosity.

Threshold amplitudes are unaffected by the continuous phase viscosity by considering the error bars (fig. A3.6(a)). We find a scaling of $f^{-1.14 \pm 0.11}$ for system 6 compared to $f^{-0.80 \pm 0.05}$ for system 2.

Drop sizes at the threshold are not significantly different for $f > 80$ Hz. Below 70 Hz, drops are smaller with increasing η_{cp} (fig. A3.6(b)). This was also found for system 5 with an increased η_{cp} compared to the reference system (chapter 4). Drop sizes scale as $f^{-0.32 \pm 0.03}$ for system 6 which differs from the usual $f^{-1/2}$ scaling. However, for system 5 with an increased η_{cp} but without surfactant, the scaling was similar ($f^{-0.32 \pm 0.03}$).

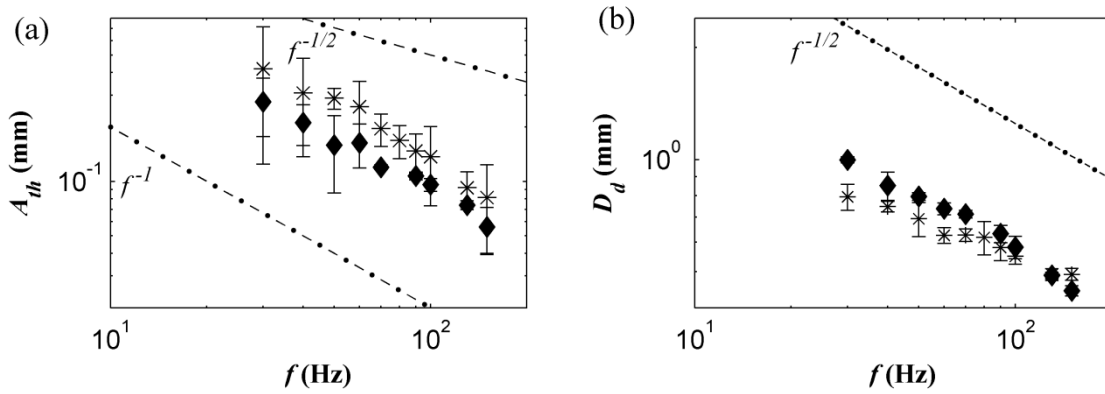


Figure A3.6: Impact of the continuous phase viscosity on (a) threshold amplitude A_{th} and (b) drop diameter at A_{th} , for $D_p = 0.32$ mm, $q = 3.6$ $\mu\text{L}\cdot\text{s}^{-1}$. (◇) System 2, $\eta_{cp} = 0.89$ mPa.s; (*) System 6, $\eta_{cp} = 4.18$ mPa.s.

2. Brief analysis of the results

In this section, we perform a similar analysis as to in chapter 4 on the complementary results, to confirm the validity of our model.

2.1. Dimensionless frequency

We plot the dimensionless forcing pulsation (data for systems 2 and 6) and dimensionless drop eigenpulsation (dashed line for Bisch *et al.* [117], solid line for Strani and Sabetta [141]) against the drop to pore diameter (fig. A3.7). We do not plot the results for the different dispersed phase flow rates, as we saw in section 1 that it had little impact on drop size. Points without error bars correspond to a single measurement (not in triplicate).

As found previously, our data are well represented by the law of Bisch *et al.* until $D_d/D_p = 5$. Above this value, data are better represented by the law of Strani and Sabetta. Similarly to without surfactant, the law of Strani and Sabetta overestimates system 6 (increased continuous phase viscosity) data, though the difference between the data and predictions is lower than for system 5. The complementary results are in accordance with those of chapter 4.

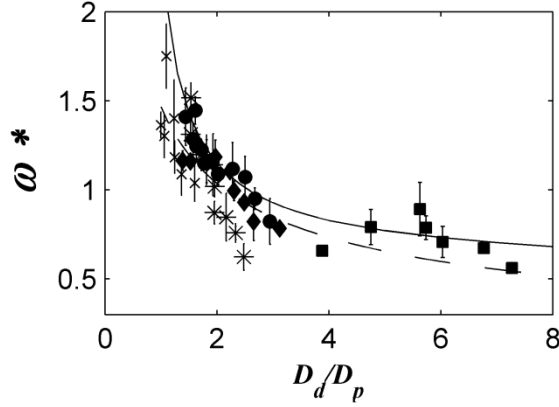


Figure A3.7: Dimensionless forcing pulsation depending on the drop to pore diameter. System 2: (\square) $D_p = 0.11$ mm, $q = 1.1 \mu\text{L}\cdot\text{s}^{-1}$; (\diamond) $D_p = 0.32$ mm, $q = 3.6 \mu\text{L}\cdot\text{s}^{-1}$; (\circ) $D_p = 0.35$ mm, $q = 6.4 \mu\text{L}\cdot\text{s}^{-1}$; (\times) $D_p = 0.75$ mm, $q = 9.6 \mu\text{L}\cdot\text{s}^{-1}$. (*) System 6, $D_p = 0.32$ mm, $\eta_{cp} = 4.18$ mPa.s, $q = 3.6 \mu\text{L}\cdot\text{s}^{-1}$. Curve of the dimensionless eigenpulsation from: eq. (4.3) in chapter 4 of Bisch *et al.* (dashed line); eq. (4.12) in chapter 4 of Strani and Sabetta (solid line).

2.2. Predictions from the full model

We predict the threshold amplitudes and drop diameters for the data presented in section 1.2. using the model from eq. (4.17) exposed in chapter 4. We include β_{film} , with \mathcal{C} and α which were adjusted on the reference system for $D_p = 0.32$ mm. Therefore, the simulation results presented constitute a prediction. The results are summarized in fig. A3.8.

We do not simulate results of section 1 as the dispersed phase velocity does not have a significant impact on the results, as seen from fig. A3.1. Also, we do not simulate system 6 data, similarly to system 5, as different behavior arises. For system 2, for $D_p = 0.11$ mm, no clear threshold emerged below 70 Hz (experimentally, a threshold was present although weak). The system behaves as an overdamped oscillator.

From fig. A3.8, we see that simulations relatively well predict the experimental threshold amplitudes, when taking into account the error bars (fig. A3.8(a)). There is often an overprediction, which was already found on the reference pore diameter for system 2 in chapter 4. For $D_p = 0.75$ mm, drops are formed partly inside the nozzle, so additional friction occurs which is not taken into account by the model, explaining why threshold amplitudes are highly underestimated.

Drop diameters are also relatively well predicted by the model (fig. A3.8(b)), with drop sizes that are generally slightly overpredicted, as found in chapter 4. For $D_p = 0.75$ mm, predictions are less accurate however as seen above, different behavior occurs due to the large size of the nozzle inner diameter.

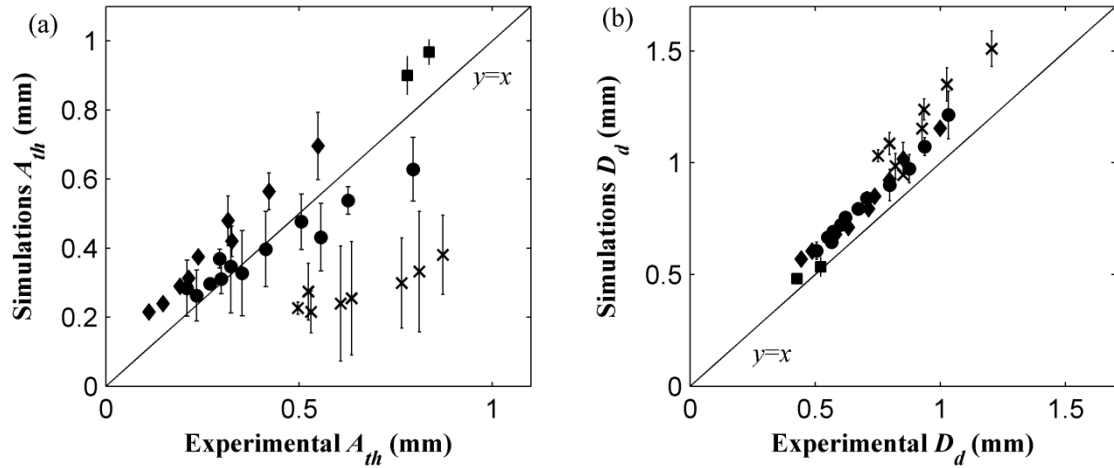


Figure A3.8: Simulation and experimental values for different forcing frequencies for (a) threshold amplitudes A_{th} and (b) drop diameters at A_{th} , for system 2. (\square) $D_p = 0.11$ mm, $q = 1.1 \mu\text{L}\cdot\text{s}^{-1}$; (\diamond) $D_p = 0.32$ mm, $q = 3.6 \mu\text{L}\cdot\text{s}^{-1}$; (\circ) $D_p = 0.35$ mm, $q = 6.4 \mu\text{L}\cdot\text{s}^{-1}$; (\times) $D_p = 0.75$ mm, $q = 9.6 \mu\text{L}\cdot\text{s}^{-1}$.

2.3. Conclusions

To conclude, the complementary data is in accordance with the data presented in chapters 3 and 4. The differences, in particular the scaling laws for threshold amplitudes as a function of the forcing frequency, are accounted for by the model (eq. (4.17) of chapter 4), from which we adequately reproduce most threshold amplitudes and drop diameters. We remind that results for a system with an increased continuous phase viscosity show different behavior compared to the other systems (confirmed here). Further work remains to describe systems with an increased continuous phase viscosity.

Appendix 4: Drops simultaneously submitted to vibration and cross-flow

1. Experimental methods: choice of the investigation range

The impact of vibration combined with the impact of the shear induced by the continuous phase cross-flow was investigated, to approach transversally vibrating ME conditions.

1.1. Choice of the continuous phase flow rate

For the reference system and pore diameter, we applied two cross-flow velocities: $v_{cp} = 0.23 \text{ m.s}^{-1}$ and 0.40 m.s^{-1} . We set a forcing frequency $f = 100 \text{ Hz}$ and performed an amplitude sweep from 0 to 0.2 mm. We measured resulting drop diameters (fig. A4.1).

For the high cross-flow velocity (red points), there is no significant change in drop diameter with increasing forcing amplitude. The initial drop size generated without vibration is already smaller than the theoretical size for first mode resonance (star). Therefore, the drop detaches due to shear before it can begin to resonate. In fact, the drop eigenfrequency is much larger than the forcing frequency. It ranges from 175 Hz to 226 Hz as calculated by the equation of Bisch *et al.* (which can reasonably be applied as $\rho_{cp}/\rho_{dp} = 1.33$ and $D_d/D_p = 2.0$ to $2.3 < 5$). In order to possibly observe the stretching mode, $f > 226 \text{ Hz}$ would have to be applied. For these frequencies, the vibrating exciter cannot deliver sufficiently high amplitudes to observe the stretching mode. Thus, lower continuous phase flow rates must be employed.

Consequently, we set $v_{cp} = 0.23 \text{ m.s}^{-1}$ (white points). The initial drop size is 13.8% larger than the theoretical size for mode 1 resonance (star), so drops should be able to detach in stretching mode. The threshold for stretching mode is not clear (fig. A4.1): we expect it lies between $A = 0.05 \text{ mm}$ and 0.075 mm . The initial drop size is too close to the theoretical drop size at resonance to be able to distinguish the stretching mode clearly.

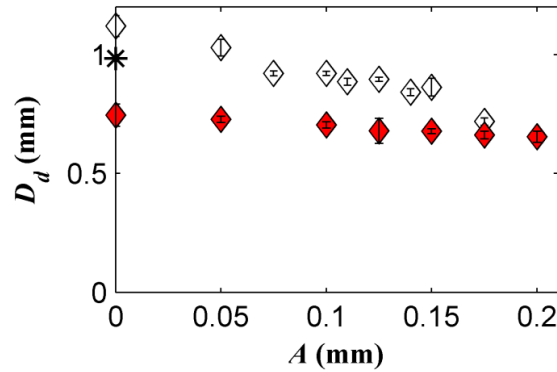


Figure A4.1: Drop diameter as a function of the forcing amplitude, for the reference system with $D_p = 0.32 \text{ mm}$, $f = 100 \text{ Hz}$, $q = 2.5 \text{ }\mu\text{L.s}^{-1}$. $v_{cp} = 0.23 \text{ m.s}^{-1}$ (white); $v_{cp} = 0.40 \text{ m.s}^{-1}$ (red); (*) theoretical drop size at resonance for $f = 100 \text{ Hz}$ according to the Bisch *et al.* law.

Similarly to Eq. (4.5) in chapter 4, omitting \mathcal{F}_{HB} , we establish the minimum forcing frequency above which a growing drop may detach in stretching mode (if $A > A_{th}$):

$$f_{1,min} = \frac{6^{1/2} \times k^{1/2} \rho_{cp}^{2/3} c_d^{2/3} v_{cp}^{4/3}}{8\pi^{3/2} \gamma^{1/6} D_p^{5/6} \rho_{dp}^{1/2}} \quad (\text{A4.1})$$

In this case, the drop diameter produced due to the inertial drag force (rather than buoyancy) is compared to that due to resonance of Eq. (4.3) in chapter 4. For the example of fig. A4.1, for $v_{cp} = 0.40 \text{ m.s}^{-1}$, we estimate the minimum frequency at around 170 Hz from Eq. (A4.1). Thus, it was in fact not possible to observe the stretching mode in this example, where the forcing frequency was set at $f = 100 \text{ Hz}$.

1.2. Choice of the vibration parameters

We performed upwards amplitude sweeps for $f > 140 \text{ Hz}$, with $v_{cp} = 0.23 \text{ m.s}^{-1}$. Then, initial drop diameters without vibration were 34.8% higher than the theoretical size at resonance, enabling to see the threshold more easily. This is shown on one example at $f = 150 \text{ Hz}$: the threshold is visualised at $A = 0.1 \text{ mm}$ (fig. A4.2). A_{th} is clear, although of course less than in the first setup, where initial drop diameters were much larger due to the absence of cross-flow (in the conditions of fig. A4.2, the initial drop diameter without vibration is of 3.14 mm).

Thus, forcing frequencies of 140 Hz to 200 Hz were applied, with steps of 10 Hz. Below 140 Hz, the stretching mode was not clear. Above 200 Hz, sufficient amplitudes could not be reached for the stretching mode due to vibrating exciter limitations.

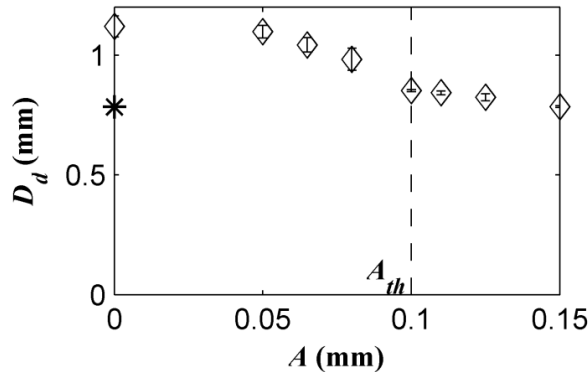


Figure A4.2: Drop diameter as a function of the vibration amplitude, for the reference system with $D_p = 0.32 \text{ mm}$, $f = 150 \text{ Hz}$, $q = 2.5 \text{ }\mu\text{L.s}^{-1}$, $v_{cp} = 0.23 \text{ m.s}^{-1}$. (*) Theoretical drop size at resonance for $f = 150 \text{ Hz}$ according to the Bisch *et al.* law.

2. Results and analysis

Drop diameters in stretching mode should not be significantly affected with cross-flow compared to with a stationary outer phase. The drop detaches when it resonates, *i.e.*, when its eigenfrequency coincides with the forcing frequency. Therefore, the drop will always have the same size. However, the threshold amplitude for the onset of the stretching mode may be affected by the cross-flow. Indeed, the drag force induced by the continuous phase cross-flow will participate in drop dynamics, hence affect its detachment.

An amplitude sweep was performed until drop size was such that the drop eigenfrequency coincided with the forcing frequency with a relative error of less than 15%. This determined the

threshold for the stretching mode. The resulting average drop eigenfrequencies at the threshold (calculated by the law of Bisch *et al.* using the experimental detached drop diameter) are plotted against the forcing frequency (fig. A4.3).

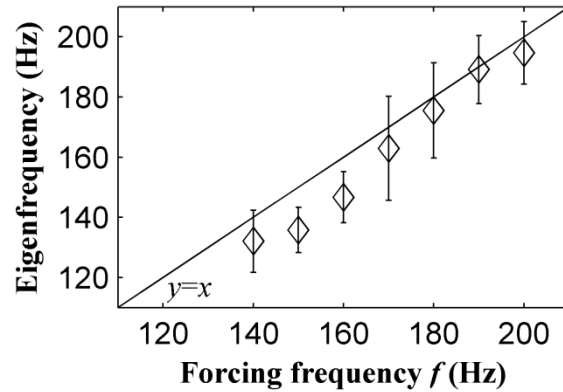


Figure A4.3: Drop eigenfrequency at the threshold calculated by the law of Bisch *et al.* versus the forcing frequency: reference system, $D_p = 0.32$ mm, $q = 2.5$ $\mu\text{L}\cdot\text{s}^{-1}$, $v_{cp} = 0.23$ $\text{m}\cdot\text{s}^{-1}$.

Threshold amplitudes for the stretching mode are plotted against the forcing frequency (white points, fig. A4.4) and compared to those obtained in the absence of cross-flow on the first setup (blue points). Forcing frequencies tested only slightly overlap, so simulation results from the model of chapter 4 established on the first setup without cross-flow is also shown (dashed line). It remains difficult to compare results due to the narrow overlapping range.

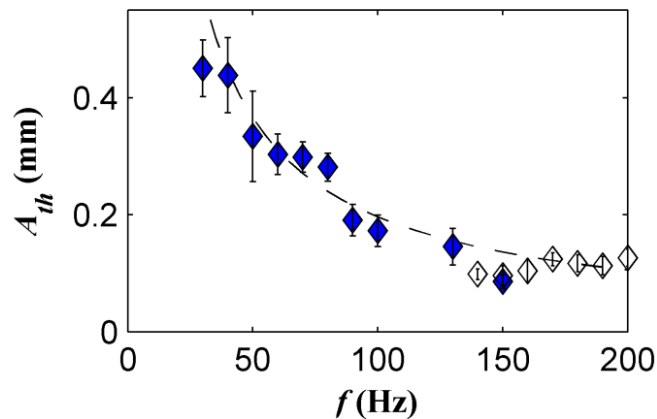


Figure A4.4: Threshold amplitudes as a function of the forcing frequency: reference system, $D_p = 0.32$ mm, $q = 2.5$ $\mu\text{L}\cdot\text{s}^{-1}$. Results from setup 1 without cross-flow (blue); from setup 2 with $v_{cp} = 0.23$ $\text{m}\cdot\text{s}^{-1}$ (white); simulation results without cross-flow from the model of chapter 4 (dashed line).

When considering the error bars, it seems that threshold amplitudes are not significantly different with or without cross-flow, for the conditions tested. As explained in 1.1, the cross-flow velocity used is low, thus the shear induced may not be sufficient to notably assist the stretching mode.

In the experiments with cross-flow, it seems that there is a slight increase in threshold amplitudes with increasing forcing frequency (white points). However, this is not expected

from the model. It relates the experimental difficulties to detect the threshold amplitude and stretching mode in the present configuration with cross-flow.

3. Conclusions

Drop detachment was studied with the combination of vibration and shear. For the cross-flow velocity tested, the shear induced was too low to observe an impact on the threshold amplitudes for the stretching mode. Results with and without cross-flow are comparable in these conditions.

The range of frequencies tested was limited with the current experimental setup. It could be interesting to perform trials for higher cross-flow velocities and higher frequencies, *e.g.* on an industrial membrane.

These results show the importance of choosing the suitable combination of cross-flow velocities and forcing parameters in transversally vibrating ME. The drop size obtained without vibration for the set cross-flow velocity must be larger than the drop size at resonance for the set forcing frequency (if the aim is to control drop size by resonance).

Appendix 5: Jets simultaneously submitted to vibration and cross-flow

1. Experimental observations: different transitions

The impact of vibration on jetting in cross-flow was investigated. Indeed, this can bring insight into transversally vibrating ME if the drops are initially generated in jetting mode. Different transitions were observed and are detailed below.

1.1. First transition: from jetting to dripping

The continuous and dispersed phase velocities were set at 0.23 m.s^{-1} and 0.62 m.s^{-1} , respectively. Without vibration, *i.e.*, $A = 0 \text{ mm}$, these conditions lead to the generation of a jet, according to the criterion described in chapter 5 ($L_n/D_d = 1.05$ and $1.03 > 1$ (fig. A5.1(a) and (b), resp.)). The jet is in the widening regime, at the limit between dripping and jetting.

For $f = 100 \text{ Hz}$, as the forcing amplitude increases, drop size decreases slightly, but not significantly. However, the ratio L_n/D_d falls well below 1 at $A_1 = 0.18 \text{ mm}$ (fig. A5.1(a)). This depicts a transition from jetting to dripping mode, according to our criteria. Thus, vibration (above a certain forcing amplitude) delays the dripping to jetting transition, as illustrated by other authors [62,74,75].

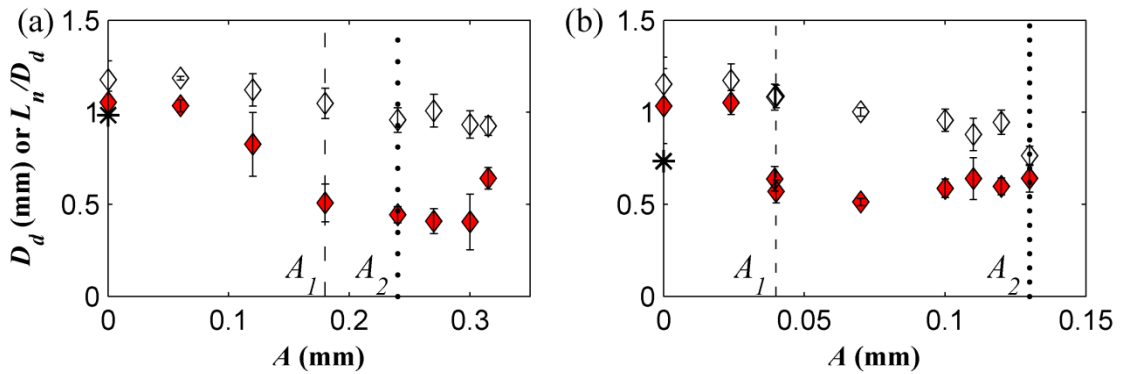


Figure A5.1: Drop diameter (white) and neck length to drop diameter ratio (red) as a function of the forcing amplitude, for the reference system, $D_p = 0.32 \text{ mm}$, $v_{dp} = 0.62 \text{ m.s}^{-1}$, $v_{cp} = 0.23 \text{ m.s}^{-1}$ for (a) $f = 100 \text{ Hz}$; (b) $f = 180 \text{ Hz}$. (*) theoretical drop size at resonance from the Bisch *et al.* law. Jetting to dripping transition (dashed line) at a threshold A_1 ; dripping to stretching transition (dotted line) at a threshold A_2 .

1.2. Second transition: from dripping to stretching

When performing the same experiment as above but for $f = 180 \text{ Hz}$, we find similar behaviour, with a transition from jetting to dripping once a sufficient forcing amplitude is reached (in this case, $A_1 = 0.04 \text{ mm}$) (fig. A5.1(b)).

However, at $A_2 = 0.13 \text{ mm}$, a second transition is observed with a marked decrease in drop size. This second transition corresponds to a transition from dripping to stretching mode, described in chapters 3 and 4 as well as in Appendix 3. Indeed, the resulting drop size is comparable to the theoretical drop size at resonance as given by Bisch *et al.* for $f = 180 \text{ Hz}$ (star) [117]. We note that the threshold amplitude previously observed for the stretching mode at this frequency was $A_{th} = 0.12 \text{ mm} \approx A_2$.

For the example of fig. A5.1(a), this second transition from dripping to stretching appears to be around $A_2 = 0.24$ mm, which would be in accordance with previous results. It is less clear than in the example of fig. A5.1(b) as initial drop size without vibration is only 16.4% higher than the theoretical drop size at resonance at $f = 100$ Hz (star).

2. Experimental results: observations

We performed the same amplitude sweeps as above for forcing frequencies ranging from 90 to 600 Hz for system 4 (high dispersed phase viscosity), then from 80 to 240 Hz for the reference system. A summary of the experimental data is exposed in the following sections.

2.1. System 4: high dispersed phase viscosity

We plot our experimental data for system 4 with a high dispersed phase viscosity depending on the drop generation regime (jetting, dripping or stretching, in blue, white and red, resp.) (fig. A5.2). This system is the first that we investigated. We set continuous and dispersed phase velocities at 0.23 m.s^{-1} and 0.69 m.s^{-1} , respectively. The dispersed phase velocity is about 11% higher than the jetting velocity without vibration.

The jetting to dripping transition (blue to white) is not well observed: for example, at $f = 200$ Hz, it seems the transition occurs at $A = 0.06$ mm but a jet is formed again at $A = 0.12$ mm. Thus, the transition may not have actually been reached. The jet may initially be too far into the jetting regime to see the transition to dripping (with the reachable forcing amplitudes).

The dripping to stretching transition is not observed. For $f = 100$ Hz, it seems the stretching mode appears at $A = 0.2$ mm however the stretching mode disappears at $A = 0.3$ mm and even returns to jetting mode at $A = 0.4$ mm.

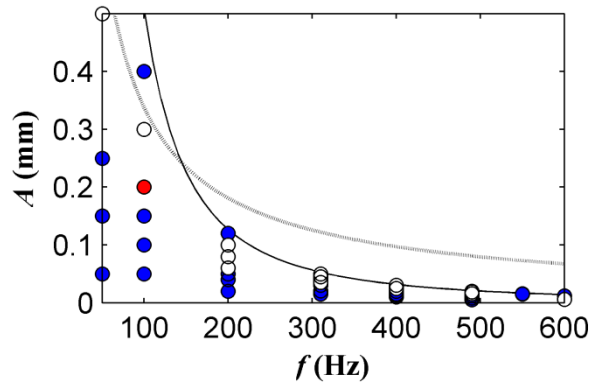


Figure A5.2: Drop detachment regime depending on the forcing frequency and amplitude, for system 4, $v_{dp} = 0.69 \text{ m.s}^{-1}$, $v_{cp} = 0.23 \text{ m.s}^{-1}$. Jetting (blue); dripping (white); stretching (red).

Simulation results without cross-flow from the model in chapter 4 (grey line). Maximum amplitude reachable with the present setup (solid line).

We note that we applied forcing amplitudes up to the limit of the vibrating exciter possibilities for the range of the frequencies tested (solid line, fig. A5.2). Therefore, this system is not appropriate to investigate the impact of vibration on jetting, with the current setup and

conditions. Indeed, the amplitudes induced do not enable us to observe either transition put to light in section 1.

2.2. Reference system

We thus studied the impact of vibration on jetting on the reference system (fig. A5.3). We set the continuous and dispersed phase velocities at 0.23 m.s^{-1} and 0.62 m.s^{-1} , respectively, which is at the jetting limit without vibration (as described for fig. A5.1). Again, we studied the impact of vibration up to the limit of the vibrating exciter possibilities (solid line, fig. A5.3), unless the stretching mode was observed before the limit.

The jetting to dripping transition (blue to white) occurs for low forcing amplitudes (in the order of a third of the jet diameter). It is logical that relatively low amplitudes are needed as the jet initially formed is already at the limit of the dripping mode. It seems that some frequencies are more favourable for the transition to dripping to occur ($f = 90, 140$ and 150 Hz). However, a larger number of experiments would be needed to validate this, especially considering that for these frequencies, the jetting regime was never actually observed (no blue points for these frequencies in fig. A5.3).

Concerning the dripping to stretching transition (white to red), for $f = 90$ and 100 Hz , drops seem to detach in stretching mode for lower amplitudes than for other frequencies. However, as mentioned before, the stretching mode is hard to detect as initial drop diameters are already close to the drop diameter for resonance.

These frequencies set aside, the dripping to stretching transition occurs for higher amplitudes than in previous experiments in dripping mode, without cross-flow (grey line) (which we saw gave similar results to the case with cross-flow in Appendix 4). It seems some frequencies are favourable to reach the stretching mode ($f = 90, 140$ and 180 Hz). These are the same frequencies that seemed to assist the first transition from jetting to dripping. Again, more experiments are needed for validation.

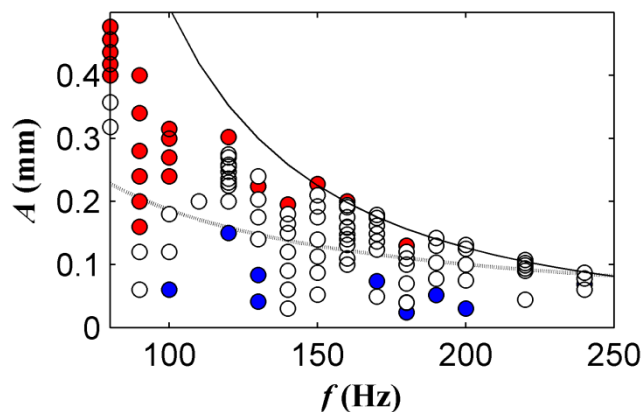


Figure A5.3: Drop detachment regime depending on the forcing frequency and amplitude, for the reference system, $v_{dp} = 0.62 \text{ m.s}^{-1}$, $v_{cp} = 0.23 \text{ m.s}^{-1}$. Jetting (blue); dripping (white); stretching (red). Simulation results without cross-flow from the model in chapter 4 (grey line). Maximum amplitude reachable with the present setup (solid line).

Although experiments should be repeated, it is reasonable to think that some frequencies may be favourable for the jetting to dripping or dripping to stretching transition. Indeed, the high dispersed phase velocities in these trials imply that drops being formed (before they reach a jet state) do not have time to reach steady-state oscillations. They typically undergo only one or two oscillations. The transient response will thus intervene in drop generation. The dynamics of the transient may change depending on the operating conditions (flow rates, vibration parameters), so drop generation will be impacted. This is similar to Wilkes and Basaran's work: for given conditions, varying only the initial rod position changed whether a drop was ejected or not, due to a different transient response [123].

3. Discussion

3.1. Different transitions

As in our experiments, other authors showed that vibration delays the dripping to jetting transition [62,74,75]. Drop size dispersion decreased with forcing in the trials of Cordero *et al.*, consistently with our data. Indeed, drop sizes by dripping have a narrower size distribution than by jetting [74].

For a set frequency, an increase in amplitude led to a larger delay in the dripping to jetting transition [75]. This is true for $f = 100$ Hz in fig. A5.1(a) as L_n/D_d decreases with the amplitude, but only until a limit ($A = 0.3$ mm). This is less clear at $f = 180$ Hz in fig. A5.1(b). We note that Zhu *et al.* considered a confined geometry (outer to inner diameter ratio of 3). Further experiments would be needed to verify this in our setup, equivalent to an unbounded case (ratio of ~ 19 , however we consider cross-flow rather than co-flow).

Previous authors also showed that the forcing frequency controlled drop size for certain amplitudes, with drop size reduction as the frequency increased [74,75]. This is the case during the transition we observed from jetting to stretching mode, where drop size was a function of $f^{-1/2}$, as seen in chapters 3 and 4 and in Appendix 3. Zhu *et al.* found a scaling for a transition from dripping to a regime where one drop was formed per forcing cycle of $f^{-1/3}$ (though we feel that this scaling is debatable), which they explained by mass conservation [75].

3.2. Drop size

Drop size is not significantly affected by vibration when remaining in the jetting regime: average relative differences between drop diameters in jetting without vibration and with vibration were of 3.7% on average and of 7.6% at most. We note that this was only investigated for a jet in the jet widening regime, with $v_{cp} = 0.23$ m.s⁻¹ and $v_{dp} = 0.62$ m.s⁻¹ (but for a wide range of frequencies). Further experiments would be necessary to generalise this conclusion.

3.3. Absolute and convective instabilities

In co-flowing liquids, Cordero *et al.* found that jets were convectively unstable, so frequencies applied were amplified, regardless of their amplitude. The forcing frequency affected the wavelength of jet perturbations [74]. Utada *et al.* studied a less confined geometry (inner to outer diameter ratio of 20 instead of 2 for Cordero *et al.*). They found that jet widening was an absolutely unstable regime. Consequently, external forcing should not impact jet behavior. Above a critical outer capillary number, jets became convectively unstable [142].

The configuration which most approaches ours is that of Utada *et al.* We also observed similar behavior to Utada *et al.*, for example in jet widening, neck oscillations grew in time before pinch off, with oscillations that seemed to remain nearly spatially stationary [142]. We therefore infer that in jet widening, an absolute instability occurs. In this case, the jet does not respond easily to external forcing [74]. Consequently, forcing should not impact strongly drop diameters, which was observed in section 3.2.

In jet narrowing, experiments were not performed. If the jets are convectively unstable (as expected from the work of Utada *et al.* [142]), then the forcing frequency should impact the perturbations and drop diameters may vary. In fact, for a convectively instability, jet oscillations become synchronized with the imposed frequency [74]. Thus, the wavelength of the Plateau-Rayleigh instabilities are controlled by the forcing frequency. Consequently, drop diameters are also controlled by the forcing frequency. This remains to be explored.

4. Conclusions

We found that vibration delays the dripping to jetting transition, as previously shown [62,74,75]. This can enable to remain in dripping mode (or even stretching mode) for higher dispersed phase flow rates. This is interesting as this induces a better control on drop size, even for higher dispersed phase throughput or in the case of local turbulences.

In jet widening, vibration did not significantly affect drop size when remaining in the jetting regime, for the parameters tested. Drops may undergo an absolute instability in this jetting regime, thus forcing does not impact jet behavior in the same manner as for convective instabilities (described above).

Further work remains to be performed: other systems, pore diameters and cross-flow velocities could be tested (by adapting the setup for the latter parameter). It would notably be interesting to observe the impact of vibration in jet narrowing, where the instabilities may be convective rather than absolute.

Overall, mechanisms and models are still lacking to describe the behavior of jets submitted to vibration: it could be interesting to pursue this work. Also, a linear stability analysis could be done adapted to this configuration, to precisely determine the absolute or convective regions.

Appendix 6: Understanding previous results in industrial transversally vibrating membrane emulsification

1. Results of C. Arnaud

Previously, we stated that C. Arnaud performed transversally vibrating ME and found a decrease in the peak of the volume-weighted drop size distribution (from 30 μm to 10 μm) between $f = 15$ and 20 kHz compared to without vibration (unknown forcing amplitude). The trials were carried out with a soy oil-water system with 0.5% Tween 20 [1]. This constituted the starting point of our work. The aim was thus to understand and model the mechanisms inducing drop detachment with vibration, which could explain the observed decrease in drop size.

1.1. Calculations

The continuous and dispersed phase flow velocities used in the process were not indicated in the patent of C. Arnaud. Thus drop sizes generated without vibration could not be estimated from the torque balance exposed in chapter 5.

With vibration, drop sizes of 10 μm were generated. This leads to a drop to pore diameter ratio of 12.5 (since $D_p = 0.8 \mu\text{m}$). As a result, the equation of Strani and Sabetta [141] better applies than the law of Bisch *et al.*, only validated until $D_d/D_p = 7$ [117]. For $D_d/D_p = 12.5$, we find a dimensionless drop eigenpulsation $\omega^* \approx 0.62$. We note that the eigenmodes (necessary to calculate ω^*) were calculated using $\rho_{dp} = 801 \text{ kg.m}^{-3}$ and $\rho_{cp} = 997 \text{ kg.m}^{-3}$. These are the densities for which we performed calculations closest to those of C. Arnaud ($\rho_{dp} = 920 \text{ kg.m}^{-3}$ and $\rho_{cp} = 997 \text{ kg.m}^{-3}$). From ω^* , we calculate the theoretical drop size $D_{d,th}(f)$ which should be produced at a forcing frequency f :

$$D_{d,th}(f) = \left[\left(\frac{\omega^*}{2\pi f} \right)^2 \frac{8\gamma}{\rho_{dp}} \right]^{1/3} \quad (\text{A6.1})$$

We estimate the interfacial tension at $\gamma \approx 7 \text{ mN.m}^{-1}$, as this is the equilibrium value reported by Schröder *et al.* (1998) for a vegetable oil-water system with 0.1% or 2% Tween 20 [27]. We finally approximate $D_{d,th}(15 \text{ kHz}) \approx 14 \mu\text{m}$ and $D_{d,th}(20 \text{ kHz}) \approx 11 \mu\text{m}$.

1.2. Drop generation mechanisms

With the forcing frequencies applied by C. Arnaud, we found theoretical drop sizes from eq. (A6.1) between 11 and 14 μm , compared to $D_d = 10 \mu\text{m}$ obtained experimentally on the industrial membrane. We consider that these values are in agreement. As a result, drop generation with vibration in the experiments of C. Arnaud can be explained by the stretching mode which we put to light in chapters 3 and 4. It could therefore be possible to predict drop diameters and threshold amplitude necessary for drop detachment from the model which we developed in chapter 4.

We suppose that without vibration, drops detach in dripping mode due to the shear induced by the continuous phase. However, extra data (phase velocities) is necessary to validate this.

2. Results of E. Lepercq-Bost

Previously, we reported that E. Lepercq-Bost applied forcing frequencies of 7740 Hz to 12710 Hz, with a forcing amplitude of 1.1 μm on the same membrane as C. Arnaud. A PDMS 770-water system was studied with 2 wt% SDS. The mean drop diameter shifted from 6.14 μm without vibration to 1.57 μm with vibration. A population of drops of 0.2 μm appeared with vibration, which is smaller than the pore size. With soy oil as the oil phase, no significant change in drop size was found for the same operating conditions [2].

The drop size distributions obtained with and without vibration on the first system are reported in fig. A6.1. Without vibration, we distinguish 3 peaks: one around 0.7 μm , one between 1 and 2 μm and one around 15 μm . With vibration, the same peaks appear with an extra peak at approximately 0.2 μm .

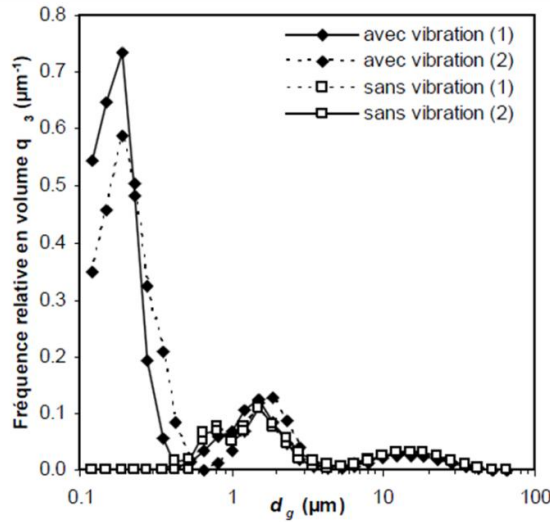


Figure A6.1: Drop size distribution obtained by E. Lepercq-Bost on a PDMS-2 wt% SDS-water emulsion without vibration (white) and with vibration (black).

1.1. Drop generation without vibration

1.1.1. Continuous phase velocity

According to E. Lepercq-Bost, the average continuous phase velocity v_{cp} in the membrane is calculated by:

$$v_{cp} = \left[\frac{\tau_w}{0.0275 \rho_{cp} \left(1 - \frac{D_r}{D_{mb}}\right)^{0.1} \left(\frac{\eta_{cp}}{v_{cp} D_h \rho_{cp}}\right)^{0.2}} \right]^{1/2} \quad (A6.2)$$

with τ_w the shear stress at the membrane surface, D_r the rod diameter (a rod is placed inside the membrane, in its centre, to increase the shear at the membrane surface), D_{mb} the membrane inner diameter and D_h the hydraulic diameter of the ring section (reported at 5, 7 and 2 mm, resp.). The shear rate was estimated at $\tau_w = 33$ Pa by E. Lepercq-Bost. Thus, we estimate

$v_{cp} \approx 2.8 \text{ m.s}^{-1}$ and the outer capillary number $\text{Ca}_{\text{out}} = \eta_{cp} v_{cp} / \gamma \approx 5.0 \times 10^{-1}$ (since $\eta_{cp} = 0.89 \text{ mPa.s}$ and we estimate $\gamma \approx 5 \text{ mN.m}^{-1}$, according to Schröder *et al.* for a vegetable oil-water system with 2% SDS [27]).

1.1.2. Dispersed phase velocity

A transmembrane pressure of 1 bar was reported. Considering the same membrane ($D_p = 0.8 \text{ }\mu\text{m}$), with $\tau_w = 33 \text{ Pa}$ but with a soy oil-2 wt% SDS-water system, E. Lepercq-Bost estimated the dispersed phase flux at $J_d = 36.6 \text{ L.h}^{-1}.\text{m}^{-2}$ during an increasing pressure phase (and $170.0 \text{ L.h}^{-1}.\text{m}^{-2}$ during a decreasing pressure phase).

The total number of pores n_{tot} on the membrane surface is:

$$n_{\text{tot}} = \frac{4S_m \varepsilon}{\pi D_p^2 \psi} \quad (\text{A6.3})$$

with $\varepsilon = 0.4$ the membrane porosity, $S_m = 48.4 \text{ cm}^2$ the membrane surface area and $\psi \approx 1$ the tortuosity (we consider straight cylindrical pores). We find $n_{\text{tot}} \approx 3.9 \times 10^9$ leading to $n_{\text{act}} \approx 3.9 \times 10^8$ and 1.6×10^9 active pores during an increasing and decreasing pressure phase, respectively (10% and 42% of active pores were estimated at 1 bar, resp., obtained from [2]).

We finally estimate the average dispersed phase flow rate v_{dp} through a pore by:

$$v_{dp} = \frac{4J_d S_m}{n_{\text{act}} \pi D_p^2} \quad (\text{A6.4})$$

We find $v_{dp} \approx 2.5 \times 10^{-4} \text{ m.s}^{-1}$ and $v_{dp} \approx 2.8 \times 10^{-4} \text{ m.s}^{-1}$ for an increasing and decreasing pressure phase, respectively. This leads to inner Weber numbers $\text{We}_{\text{in}} = \rho_{dp} D_p v_{dp}^2 / \gamma \approx 9.5 \times 10^{-9}$ and 1.2×10^{-8} , respectively (since $\rho_{dp} = 918 \text{ kg.m}^{-3}$, $D_p = 0.8 \text{ }\mu\text{m}$ and $\gamma \approx 5 \text{ mN.m}^{-1}$).

We note that the dispersed phase flux was obtained by considering a system with soy oil, which is more viscous than the PDMS used in the experiments reported in fig. A6.1. Thus, dispersed phase velocities (and inner Weber numbers) may be slightly underestimated.

1.1.3. Drop generation mechanisms

In cross-flow without vibration, from our estimations according to the data available, we found $\text{Ca}_{\text{out}} \approx 5.0 \times 10^{-1}$ and $\text{We}_{\text{in}} \approx 10^{-8}$. This is in the dripping region described by Meyer and Crocker [69]. However, it is not far from the dripping to jetting transition limit, which occurs at $\text{We}_{\text{in}} \approx 2.3 \times 10^{-7}$ for $\text{Ca}_{\text{out}} = 5.0 \times 10^{-1}$, with an inner Ohnesorge number $\text{Oh}_{dp} = \eta_{dp} / \sqrt{\rho_{dp} \gamma D_p} = 2.6$ (since $\rho_{dp} = 918 \text{ kg.m}^{-3}$, $\eta_{dp} = 5 \text{ mPa.s}$, $D_p = 0.8 \text{ }\mu\text{m}$ and $\gamma \approx 5 \text{ mN.m}^{-1}$).

If the drops are generated in dripping mode, we estimate a theoretical drop diameter from a torque balance (neglecting $v_{xd} \ll v_{cp}$): we find $D_{d,th} \approx 0.6 \text{ }\mu\text{m}$. This corresponds to one of the peaks in fig. A6.1, for drops generated without vibration.

We now consider that part of the drops may be generated in jetting mode, as we are close to the dripping to jetting transition limit (mentioned above). This may explain the peak between 1 and 2 μm observed in fig. A6.1. Drop sizes were not estimated in previous work in cross-flow

configurations [69,70]. Also, we cannot extrapolate our data for such low We_{in} and high Ca_{out} compared to our experiments exposed in chapter 5.

We thus hypothesize that drops could be formed by Plateau-Rayleigh instabilities in jetting mode. We consider the optimal wavelength for the Plateau-Rayleigh instabilities $\lambda_{PR}^* = \pi D_p \sqrt{2}$ and estimate a simple theoretical drop diameter $D_{d,th}$ by solving:

$$\lambda_{PR}^* \frac{\pi D_p^2}{4} = \frac{\pi}{6} D_{d,th}^3 \quad (A6.5)$$

We find $D_{d,th} \approx 1.5 \mu\text{m}$. This roughly corresponds to the peak between 1 and 2 μm in fig. A6.1 without vibration.

Therefore, without vibration, drops may be formed partly in dripping mode, with drop detachment induced by cross-flow shear (0.6 μm peak) and partly in jetting mode, with drop breakup by Plateau-Rayleigh instabilities (1.5 μm peak). The experimental conditions being close to the dripping to jetting transition may explain the varying drop generation mode. Additional explanations could be that there are velocity variations in the continuous phase flow (the flow is in fact reported as turbulent in the annular section).

We note that the small peak around 15 μm without vibration could be explained by the coalescence of drops, as it does not correspond to any mechanism of individual drop formation.

1.2. Drop generation with vibration

With vibration, we also observe the small peak around 15 μm , which we attribute to drop coalescence. This peak is not specific to the experiments with vibration.

Apart from this peak, drop sizes are below 1.5 μm , thus $D_d/D_p < 2$ (since $D_p = 0.8 \mu\text{m}$). We thus use the simple equation of Bisch *et al.* to estimate the theoretical drop diameter $D_{d,th}$ if drops detach in stretching mode, due to resonance. This is done with eq. (4.10) of chapter 4. We find $D_{d,th} \approx 10$ to 12 μm (since $\gamma \approx 5 \text{ mN}\cdot\text{m}^{-1}$, $\rho_{dp} = 918 \text{ kg}\cdot\text{m}^{-3}$, $D_p = 0.8 \mu\text{m}$ and $f = 7740$ to 12710 Hz). This peak does not appear in fig. A6.1 (the peak at 15 μm already existed without vibration and it is no larger than in the case without vibration). As described in Appendix 4, drop sizes formed due to shear are smaller than drop sizes theoretically generated in stretching mode. Therefore, growing drops do not have time to grow and resonate. They detach earlier, by shear, around 0.6 μm (peak present in one of the two experiments with vibration). Therefore, the mechanisms of stretching mode described in chapters 3 and 4 do not explain the results of E. Lepercq-Bost. Drops still seem to detach due to a combination of shear and Rayleigh-Plateau instabilities.

The question remains concerning the 0.2 μm peak which appears with vibration. For a jet in a co-flowing outer liquid with mechanical vibration applied, Zhu, Tang and Wang (2016) found that above a critical forcing amplitude, satellite drops appeared. These were due to fluid suction into the nozzle, which led to the appearance of a thin thread. This thread broke up leading to small satellite drops [75].

We assume that the peak at 0.2 μm corresponds to satellite drops. Abundant literature exists on satellite drop formation (a few examples in [143–148]). According to Tjahjadi, Stone and Ottino (1992), for an elongated drop in an outer fluid, the number of satellite drops generated increases with decreasing viscosity ratio ($\zeta = \eta_{dp}/\eta_{cp}$) [145]. This could explain why satellite drops would appear for the results of E. Lepercq-Bost ($\zeta \approx 6$) and not for those of C. Arnaud ($\zeta \approx 56$). Similarly, Ambravaneswaran, Wilkes and Basaran (2002) numerically simulated a pendant drop in air. For high Ohnesorge numbers, *i.e.*, high drop viscosities, above a critical Weber number, satellite drops were suppressed [148].

For $\zeta \approx 6$, as in the trials of E. Lepercq-Bost, the size of the main satellite drop was found to be 0.4 to 0.5 times that of the mother drop [145]. This would form slightly larger satellite drops than the experimental 0.2 μm obtained (0.2 to 0.8 μm are predicted). However, the presence of vibration may modify the breakup dynamics of the thread [145]. Thus it is reasonable to assimilate the peak at 0.2 μm to satellite drops, which only appear with vibration.

3. Conclusions

From our work, we were able to understand the resulting drop sizes in transversally vibrating membrane emulsification, which first motivated our research. Concerning C. Arnaud's experiments, without vibration, drops most likely detached in dripping mode due to cross-flow shear. With vibration, they detached in stretching mode due to resonance. For E. Lepercq-Bost's trials, without vibration, drops probably detached in both dripping and jetting modes. With vibration, drop detachment mechanisms did not change but the appearance of satellite drops with vibration probably explain the decrease in mean drop diameters, due to the appearance of a new peak at 0.2 μm .

These two examples typically show that to control drop size, drop generation mechanisms must be understood. Indeed, in the tests of E. Lepercq-Bost, the possible appearance of satellite drops with vibration results in uncontrolled drop sizes and lead to bimodal drop size distributions, which is not industrially optimal. If the parameters were well controlled (to suppress satellite drops and by setting an adequate forcing frequency given the other operating parameters), monodispersed drops of controlled size could be obtained from this vibrating process by forming drops only in stretching mode.

In order to pursue the work further, the investigation of satellite drop formation could be performed, in order to optimize the conditions where they are suppressed. The optimization of the continuous phase flow in the industrial membrane could also be looked into.

References

- [1] C. Arnaud, « Procédé et dispositif de fabrication d'une dispersion ou d'une émulsion », European patent EP 1 551 540 B1, 2006.
- [2] E. Lepercq-Bost, « Etude d'un procédé d'émulsification par membrane vibrante: compréhension des mécanismes, modélisation et optimisation », PhD Thesis, Ecole Centrale Paris, p. 224–233, 2008.
- [3] P. Brochette, « Emulsification – élaboration et études des émulsions », *Ed. Techniques Ingénieur*, J 2150, p. 1–22, 1999.
- [4] J.-P. Canselier and P. Martine, « Procédés d'émulsification – mécanismes de formation des émulsions », *Ed. Techniques Ingénieur*, J 2152, p. 1–12 2004.
- [5] P.-G. de Gennes, F. Brochard-Wyart and D. Quéré, *Gouttes, bulles, perles et ondes*, (Éditions Belin), p. 11–68 ; 99–126 ; 171–188, 2002.
- [6] D. Myers, *Surfaces, interfaces, and colloids: principles and applications* (Wiley-VCH, 2nd Ed.), p. 8–20 ; 97–124 ; 179–213 ; 253–292, 1999.
- [7] P. Pomerantz, W. Clinton and W. Zisman, « Spreading pressures and coefficients, interfacial tensions, and adhesion energies of the lower alkanes, alkenes, and alkyl benzenes on water », *J. Colloid Interface Sci.*, 24 (1), p. 16–28, 1967.
- [8] S. R. Deshiikan, D. Bush, E. Eschenazi and K. D. Papadopoulos, « SDS, Brij58 and CTAB at the dodecane-water interface », *Colloids Surf. Physicochem. Eng. Asp.*, 136 (1), p. 133–150, 1998.
- [9] M. J. Rosen and J. T. Kunjappu, *Surfactants and interfacial phenomena*, (Wiley, 4th Ed.), p. 39–200 ; 235–271 ; 272–307 ; 336–367, 2012.
- [10] C. Larpent, « Tensioactifs », *Ed. Techniques Ingénieur*, K342, p. 1–16, 1995.
- [11] S. Roustel, « Homogénéisation à haute pression des dispersions alimentaires liquides », *Ed. Techniques Ingénieur*, F2710, p. 1–13, 2010.
- [12] S. Schultz, G. Wagner, K. Urban and J. Ulrich, « High-Pressure Homogenization as a Process for Emulsion Formation », *Chem. Eng. Technol.*, 27 (4), p. 361–368, 2004.
- [13] J.-P. Canselier, H. Delmas, A. M. Wilhelm and B. Abismaïl, « Ultrasound Emulsification—An Overview », *J. Dispers. Sci. Technol.*, 23 (1–3), p. 333–349, 2002.
- [14] O. Behrend, K. Ax and H. Schubert, « Influence of continuous phase viscosity on emulsification by ultrasound », *Ultrason. Sonochem.*, 7 (2), p. 77–85, 2000.
- [15] Y.-F. Maa and C. Hsu, « Liquid-liquid emulsification by rotor/stator homogenization », *J. Controlled Release*, 38 (2–3), p. 219–228, 1996.
- [16] R. K. Thakur, C. Vial, K. D. P. Nigam, E. B. Nauman and G. Djelveh, « Static Mixers in the Process Industries—A Review », *Chem. Eng. Res. Des.*, 81 (7), p. 787–826, 2003.
- [17] T. Nakashima, M. Shimizu, and M. Kukizaki, « Membrane Emulsification by Microporous Glass », *Key Engineering Materials*, 61–62, p. 513–516, 1992.

- [18] T. Nakashima, M. Shimizu and M. Kukizaki, « Particle control of emulsion by membrane emulsification and its applications », *Adv. Drug Deliv. Rev.*, 45 (1), p. 47–56, 2000.
- [19] C. Charcosset, « Preparation of emulsions and particles by membrane emulsification for the food processing industry », *J. Food Eng.*, 92 (3), p. 241–249, 2009.
- [20] U. Lambrich and H. Schubert, « Emulsification using microporous systems », *J. Membr. Sci.*, 257 (1–2), p. 76–84, 2005.
- [21] A. Nazir, K. Schroën and R. Boom, « Premix emulsification: A review », *J. Membr. Sci.*, 362 (1–2), p. 1–11, 2010.
- [22] A. Laouini, H. Fessi and C. Charcosset, « Membrane emulsification: A promising alternative for vitamin E encapsulation within nano-emulsion », *J. Membr. Sci.*, 423–424, p. 85–96, 2012.
- [23] D. H. Oh, P. Balakrishnan, Y.-K. Oh, D.-D. Kim, C. S. Yong and H.-G. Choi, « Effect of process parameters on nanoemulsion droplet size and distribution in SPG membrane emulsification », *Int. J. Pharm.*, 404 (1–2), p. 191–197, 2011.
- [24] A. J. Abrahamse, R. Van Lierop, R. G. M. Van der Sman, A. Van der Padt and R. M. Boom, « Analysis of droplet formation and interactions during cross-flow membrane emulsification », *J. Membr. Sci.*, 204 (1), p. 125–137, 2002.
- [25] F. Spyropoulos, R. D. Hancock and I. T. Norton, « Food-grade emulsions prepared by membrane emulsification techniques », *Procedia Food Sci.*, 1, p. 920–926, 2011.
- [26] G. T. Vladisavljević and H. Schubert, « Influence of process parameters on droplet size distribution in SPG membrane emulsification and stability of prepared emulsion droplets », *J. Membr. Sci.*, 225 (1), p. 15–23, 2003.
- [27] V. Schröder, O. Behrend and H. Schubert, « Effect of Dynamic Interfacial Tension on the Emulsification Process Using Microporous, Ceramic Membranes », *J. Colloid Interface Sci.*, 202 (2), p. 334–340, 1998.
- [28] E. Lepercq-Bost, M.-L. Giorgi, A. Isambert and C. Arnaud, « Estimating the risk of coalescence in membrane emulsification », *J. Membr. Sci.*, 357 (1–2), p. 36–46, 2010.
- [29] R. D. Hancock, F. Spyropoulos and I. T. Norton, « Comparisons between membranes for use in cross flow membrane emulsification », *J. Food Eng.*, 116 (2), p. 382–389, 2013.
- [30] J. Zhu and D. Barrow, « Analysis of droplet size during crossflow membrane emulsification using stationary and vibrating micromachined silicon nitride membranes », *J. Membr. Sci.*, 261 (1–2), p. 136–144, 2005.
- [31] H. G. Gomma, J. Liu, R. Sabouni and J. Zhu, « Experimental and theoretical analysis of emulsification characteristics using a high porosity microscreen under oscillatory shear conditions », *Colloids Surf. Physicochem. Eng. Asp.*, 456, p. 160–168, 2014.
- [32] E. Lepercq-Bost, M.-L. Giorgi, A. Isambert and C. Arnaud, « Use of the capillary number for the prediction of droplet size in membrane emulsification », *J. Membr. Sci.*, 314 (1–2), p. 76–89, 2008.

- [33] S. J. Peng and R. A. Williams, « Controlled production of emulsions using a crossflow membrane: Part I: Droplet formation from a single pore », *Chem. Eng. Res. Des.*, 76 (8), p. 894–901, 1998.
- [34] M. Kukizaki, « Shirasu porous glass (SPG) membrane emulsification in the absence of shear flow at the membrane surface: Influence of surfactant type and concentration, viscosities of dispersed and continuous phases, and transmembrane pressure », *J. Membr. Sci.*, 327 (1–2), p. 234–243, 2009.
- [35] S. R. Kosvintsev, G. Gasparini and R. G. Holdich, « Membrane emulsification: droplet size and uniformity in the absence of surface shear », *J. Membr. Sci.*, 313 (1), p. 182–189, 2008.
- [36] A. Timgren, G. Trägårdh and C. Trägårdh, « Effects of pore spacing on drop size during cross-flow membrane emulsification - A numerical study », *J. Membr. Sci.*, 337 (1–2), p. 232–239, 2009.
- [37] Y. Mine, M. Shimizu and T. Nakashima, « Preparation and stabilization of simple and multiple emulsions using a microporous glass membrane », *Colloids Surf. B Biointerfaces*, 6 (4), p. 261–268, 1996.
- [38] R. Katoh, Y. Asano, A. Furuya, K. Sotoyama and M. Tomita, « Preparation of food emulsions using a membrane emulsification system », *J. Membr. Sci.*, 113 (1), p. 131–135, 1996.
- [39] N. Christov, D. Ganchev, N. Vassileva, N. Denkov, K. Danov and P. Kralchevsky, « Capillary mechanisms in membrane emulsification: oil-in-water emulsions stabilized by Tween 20 and milk proteins », *Colloids Surf. Physicochem. Eng. Asp.*, 209 (1), p. 83–104, 2002.
- [40] A. J. Abrahamse, A. van der Padt, R. M. Boom and W. B. C. de Heij, « Process fundamentals of membrane emulsification: Simulation with CFD », *AIChE J.*, 47 (6), p. 1285–1291, 2001.
- [41] S. M. Joscelyne and G. Trägårdh, « Membrane emulsification—a literature review », *J. Membr. Sci.*, 169 (1), p. 107–117, 2000.
- [42] H. G. Goma, J. Liu, R. Sabouni and J. Zhu, « Operational characteristics of oscillatory micro-screen emulsifier: Coupling effects and energy dissipation », *Chem. Eng. Sci.*, 117, p. 161–172, 2014.
- [43] A. Timgren, G. Trägårdh and C. Trägårdh, « Effects of cross-flow velocity, capillary pressure and oil viscosity on oil-in-water drop formation from a capillary », *Chem. Eng. Sci.*, 64 (6), p. 1111–1118, 2009.
- [44] J. D. H. Kelder, J. J. M. Janssen and R. M. Boom, « Membrane emulsification with vibrating membranes: A numerical study », *J. Membr. Sci.*, 304 (1–2), p. 50–59, 2007.
- [45] D. M. Lloyd, I. T. Norton and F. Spyropoulos, « Processing effects during rotating membrane emulsification », *J. Membr. Sci.*, 466, p. 8–17, 2014.
- [46] E. Guyon, J. P. Hulin and L. Petit, *Hydrodynamique physique* (Editions du CNRS, 3^e Ed.), p. 1–60 ; 563–608, 2012.

- [47] J. Eggers and E. Villermaux, « Physics of liquid jets », *Rep. Prog. Phys.*, 71 (3), 036601, 2008.
- [48] Savart, « Suite du memoire sur le choc d'une veine liquide lancée contre un plan circulaire », *Ann. Chim. Phys.*, 54, p.1133–145, 1833.
- [49] Plateau, *Experimental and theoretical statics of liquids subject to molecular forces only*, II (X), p. 309–334, 1873.
- [50] Rayleigh, « On the instability of jets », *Proceeding Lond. Math. Soc.*, 10, p. 4–13, 1878.
- [51] W. van Hoeve, S. Gekle, J. H. Snoeijer, M. Versluis, M. P. Brenner and D. Lohse, « Breakup of diminutive Rayleigh jets », *Phys. Fluids*, 22 (12), 122003, 2010.
- [52] C. Weber, « Zum Zerfall eines Flüssigkeitsstrahles », *Ztschr. f. Angew. Math. Mech.*, 11 (2), p. 136–154, 1931.
- [53] A. Lindner and C. Wagner, « Viscoelastic surface instabilities », *Comptes Rendus Phys.*, 10 (8), p. 712–727, 2009.
- [54] J. Hagedorn, N. Martyts and J. Douglas, « Breakup of a fluid thread in a confined geometry: droplet-plug transition, perturbation sensitivity, and kinetic stabilization with confinement », *Phys. Rev. E*, 69 (5), 056312, 2004.
- [55] V. Duclaux, C. Clanet and D. Quéré, « The effects of gravity on the capillary instability in tubes », *J. Fluid Mech.*, 556, p. 217–226, 2006.
- [56] A. J. Yule and Y. Al-Suleimani, « On droplet formation from capillary waves on a vibrating surface », *Proc. R. Soc. Lond. A*, 456, p. 1069–1085, 2000.
- [57] D. Terwagne and J. W. M. Bush, « Tibetan singing bowls », *Nonlinearity*, 24 (8), R51–R66, 2011.
- [58] S. A. Thorpe, « Turbulence in stably stratified fluids: A review of laboratory experiments », *Bound.-Layer Meteorol.*, 5 (1–2), p. 95–119, 1973.
- [59] C. Clanet and J. C. Lasheras, « Transition from dripping to jetting », *J. Fluid Mech.*, 383, p. 307–326, 1999.
- [60] A. S. Utada, A. Fernandez-Nieves, H. A. Stone and D. A. Weitz, « Dripping to Jetting Transitions in Coflowing Liquid Streams », *Phys. Rev. Lett.*, 99 (9), 094502, 2007.
- [61] B. Ambravaneswaran, H. J. Subramani, S. D. Phillips, and O. A. Basaran, « Dripping-Jetting Transitions in a Dripping Faucet », *Phys. Rev. Lett.*, 93 (3), 034501, 2004.
- [62] D. R. Webster and E. K. Longmire, « Jet pinch-off and drop formation in immiscible liquid-liquid systems », *Exp. Fluids*, 30 (1), p. 47–56, 2001.
- [63] G. F. Scheele and B. J. Meister, « Drop formation at low velocities in liquid-liquid systems: Part II. Prediction of jetting velocity », *AIChE J.*, 14 (1), p. 15–19, 1968.
- [64] J. R. Richards, A. N. Beris, and A. M. Lenhoff, « Drop formation in liquid–liquid systems before and after jetting », *Phys. Fluids*, 7 (11), p. 2617–2630, 1995.
- [65] E. Castro-Hernández, V. Gundabala, A. Fernández-Nieves and J. M. Gordillo, « Scaling the drop size in coflow experiments », *New J. Phys.*, 11 (7), 75021, 2009.
- [66] Y. Chen, L. Wu and C. Zhang, « Emulsion droplet formation in coflowing liquid streams », *Phys. Rev. E*, 87 (1), 013002, 2013.

- [67] C. Cramer, P. Fischer and E. J. Windhab, « Drop formation in a co-flowing ambient fluid », *Chem. Eng. Sci.*, 59 (15), p. 3045–3058, 2004.
- [68] P. Guillot, A. Colin, A. S. Utada and A. Ajdari, « Stability of a Jet in Confined Pressure-Driven Biphasic Flows at Low Reynolds Numbers », *Phys. Rev. Lett.*, 99 (10), 104502, 2007.
- [69] R. F. Meyer and J. C. Crocker, « Universal Dripping and Jetting in a Transverse Shear Flow », *Phys. Rev. Lett.*, 102 (19), 194501, 2009.
- [70] M. Pathak, « Numerical simulation of membrane emulsification: Effect of flow properties in the transition from dripping to jetting », *J. Membr. Sci.*, 382 (1–2), p. 166–176, 2011.
- [71] L. Crane, S. Birch and P. D. McCormack, « The effect of mechanical vibration on the break-up of a cylindrical water jet in air », *Br. J. Appl. Phys.*, 15 (6), p. 743–750, 1964.
- [72] J. G. Wissema and G. A. Davies, « The formation of uniformly sized drops by vibration-atomization », *Can. J. Chem. Eng.*, 47 (6), p. 530–535, 1969.
- [73] A. Sauret, C. Spandagos and H. C. Shum, « Fluctuation-induced dynamics of multiphase liquid jets with ultra-low interfacial tension », *Lab. Chip*, 12 (18), p. 3380–3386, 2012.
- [74] M. L. Cordero, F. Gallaire and C. N. Baroud, « Quantitative analysis of the dripping and jetting regimes in co-flowing capillary jets », *Phys. Fluids*, 23 (9), 94111, 2011.
- [75] P. Zhu, X. Tang and L. Wang, « Droplet generation in co-flow microfluidic channels with vibration », *Microfluid. Nanofluidics*, 20:47, 2016.
- [76] T. Tate, « On the magnitude of a drop of liquid formed under different circumstances », *Phil. Mag.*, 27, p. 176–180, 1864.
- [77] W. D. Harkins and F. E. Brown, « The determination of surface tension (free surface energy), and the weight of falling drops: the surface tension of water and benzene by the capillary height method », *J. Am. Chem. Soc.*, 41, p. 499–524, 1919.
- [78] Y. H. Mori, « Harkins-brown correction factor for drop formation », *AIChE J.*, 36 (8), p. 1272–1274, 1990.
- [79] G. F. Scheele and B. J. Meister, « Drop formation at low velocities in liquid-liquid systems: Part I. Prediction of drop volume », *AIChE J.*, 14 (1), p. 9–15, 1968.
- [80] X. Zhang and O. A. Basaran, « An experimental study of dynamics of drop formation », *Phys. Fluids*, 7 (6), p. 1184–1203, 1995.
- [81] D. M. Henderson, W. G. Pritchard and L. B. Smolka, « On the pinch-off of a pendant drop of viscous fluid », *Phys. Fluids*, 9 (11), p. 3188–3200, 1997.
- [82] G. I. Taylor, « The Formation of Emulsions in Definable Fields of Flow », *Proc. R. Soc. A*, 146 (858), p. 501–523, 1934.
- [83] H. P. Grace, « Dispersion phenomena in high viscosity immiscible fluid systems and application of static mixers as dispersion devices in such systems », *Chem. Eng. Commun.*, 14 (3–6), p. 225–277, 1982.
- [84] B. J. Bentley and L. G. Leal, « An experimental investigation of drop deformation and breakup in steady, two-dimensional linear flows », *J. Fluid Mech.*, 167 (1), p. 241–283, 1986.

- [85] H. A. Stone, B. J. Bentley and L. G. Leal, « An experimental study of transient effects in the breakup of viscous drops », *J. Fluid Mech.*, 173, p. 131–158, 1986.
- [86] H. A. Stone and L. G. Leal, « The effects of surfactants on drop deformation and breakup », *J. Fluid Mech.*, 220, p. 161–186, 1990.
- [87] R. M. S. M. Schulkes, « The contraction of liquid filaments », *J. Fluid Mech.*, 309 (1), p. 277–300, 1996.
- [88] P. K. Notz and O. A. Basaran, « Dynamics and breakup of a contracting liquid filament », *J. Fluid Mech.*, 512, p. 223–256, 2004.
- [89] A. A. Castrejón-Pita, J. R. Castrejón-Pita, and I. M. Hutchings, « Breakup of Liquid Filaments », *Phys. Rev. Lett.*, 108 (7), 074506, 2012.
- [90] G. De Luca, F. P. Di Maio, A. Di Renzo and E. Drioli, « Droplet detachment in cross-flow membrane emulsification: Comparison among torque- and force-based models », *Chem. Eng. Process. Process Intensif.*, 47 (7), p. 1150–1158, 2008.
- [91] J. Xu, G. Luo, G. Chen and J. Wang, « Experimental and theoretical approaches on droplet formation from a micrometer screen hole », *J. Membr. Sci.*, 266 (1–2), p. 121–131, 2005.
- [92] A. Timgren, G. Trägårdh and C. Trägårdh, « A model for drop size prediction during cross-flow emulsification », *Chem. Eng. Res. Des.*, 88 (2), p. 229–238, 2010.
- [93] M. Yasuno, M. Nakajima, S. Iwamoto, T. Maruyama, S. Sugiura, I. Kobayashi, A. Shono and K. Satoh, « Visualization and characterization of SPG membrane emulsification », *J. Membr. Sci.*, 210 (1), p. 29–37, 2002.
- [94] M. Rayner, G. Trägårdh, C. Trägårdh and P. Dejmeek, « Using the Surface Evolver to model droplet formation processes in membrane emulsification », *J. Colloid Interface Sci.*, 279 (1), p. 175–185, 2004.
- [95] E. van der Zwan, R. van der Sman, K. Schroën and R. Boom, « Lattice Boltzmann simulations of droplet formation during microchannel emulsification », *J. Colloid Interface Sci.*, 335 (1), p. 112–122, 2009.
- [96] Lord Rayleigh, « On the Capillary Phenomena of jets », *Proc. R. Soc. Lond.*, 29, p. 71–97, 1879.
- [97] M. Minnaert, « XVI. On musical air-bubbles and the sounds of running water », *Lond. Edinb. Dublin Philos. Mag. J. Sci.*, 16 (104), p. 235–248, 1933.
- [98] G. Brant Foote, « A numerical method for studying liquid drop behavior: Simple oscillation », *J. Comput. Phys.*, 11 (4), p. 507–530, 1973.
- [99] E. Trinh and T. G. Wang, « Large-amplitude free and driven drop-shape oscillations: experimental observations », *J. Fluid Mech.*, 122 (1), p. 315–338, 1982.
- [100] J. A. Tsamopoulos and R. A. Brown, « Nonlinear oscillations of inviscid drops and bubbles », *J. Fluid Mech.*, 127 (1), p. 519–537, 1983.
- [101] T. Patzek, R. Benner, O. Basaran and L. Scriven, « Nonlinear oscillations of inviscid free drops », *J. Comput. Phys.*, 97 (2), p. 489–515, 1991.
- [102] Prosperetti, « Normal-mode analysis for the oscillations of a viscous liquid drop in an immiscible liquid », *J. Mécanique*, 19 (1), p. 149–182, 1980.

- [103] M. Perez, L. Salvo, M. Suéry, Y. Bréchet and M. Papoular, « Contactless viscosity measurement by oscillations of gas-levitated drops », *Phys. Rev. E*, 61 (3), p. 2669–2675, 2000.
- [104] H. Lamb, *Hydrodynamics*, 6th Edition (Cambridge University Press, Cambridge, UK), p. 473–475, 1932.
- [105] R. S. Valentine, N. F. Sather and W. J. Heideger, « The motion of drops in viscous media », *Chem. Eng. Sci.*, 20 (8), p. 719–728, 1965.
- [106] C. A. Miller and L. E. Scriven, « The oscillations of a fluid droplet immersed in another fluid », *J. Fluid Mech.*, 32 (3), p. 417–435, 1968.
- [107] H.-L. Lu and R. E. Apfel, « Shape oscillations of drops in the presence of surfactants », *J. Fluid Mech.*, 222, p. 351–368, 1991.
- [108] O. A. Basaran, T. C. Scott and C. H. Byers, « Drop oscillations in liquid-liquid systems », *AIChE J.*, 35 (8), p. 1263–1270, 1989.
- [109] E. Trinh, A. Zwern and T. G. Wang, « An experimental study of small-amplitude drop oscillations in immiscible liquid systems », *J. Fluid Mech.*, 115 (1), p. 453–474, 1982.
- [110] E. H. Trinh, D. B. Thiessen and R. G. Holt, « Driven and freely decaying nonlinear shape oscillations of drops and bubbles immersed in a liquid: experimental results », *J. Fluid Mech.*, 364, p. 253–272, 1998.
- [111] N. A. Chebel, F. Risso and O. Masbernat, « Inertial modes of a periodically forced buoyant drop attached to a capillary », *Phys. Fluids*, 23 (10), 102104, 2011.
- [112] M. Strani and F. Sabetta, « Free vibrations of a drop in partial contact with a solid support », *J. Fluid Mech.*, 141, p. 233–247, 1984.
- [113] J. B. Bostwick and P. H. Steen, « Capillary oscillations of a constrained liquid drop », *Phys. Fluids*, 21 (3), 032108, 2009.
- [114] J. Vejrazka, L. Vobecka and J. Tihon, « Linear oscillations of a supported bubble or drop », *Phys. Fluids*, 25 (6), 062102, 2013.
- [115] J. Vejrazka, L. Vobecka, S. Orvalho, M. Zednikova and J. Tihon, « Shape oscillations of a bubble or drop attached to a capillary tip », *Chem. Eng. Sci.*, 116, p. 359–371, 2014.
- [116] H. Rodot, C. Bisch and A. Lasek, « Zero-gravity simulation of liquids in contact with a solid surface », *Acta Astronaut.*, 6 (9), p. 1083–1092, 1979.
- [117] Bisch, Lasek and Rodot, « Comportement hydrodynamique de volumes liquides sphériques semi-libres en apesanteur simulée », *Journal de mécanique théorique et appliquée*, 1 (1), p. 165–183, 1982.
- [118] Smithwick and Boulet, « Vibrations of Microscopic Mercury Droplets on Glass », *J. Colloid Interface Sci.*, 130 (2), p. 588–596, 1989.
- [119] M. Strani and F. Sabetta, « Viscous oscillations of a supported drop in an immiscible fluid », *J. Fluid Mech.*, 189, p. 397–421, 1988.
- [120] O. A. Basaran, « Nonlinear oscillations of viscous liquid drops », *J. Fluid Mech.*, 241 (1), p. 169–198, 1992.

- [121] E. D. Wilkes and O. A. Basaran, « Forced oscillations of pendant (sessile) drops », *Phys. Fluids*, 9 (6), p. 1512–1528, 1997.
- [122] E. D. Wilkes and O. A. Basaran, « Hysteretic response of supported drops during forced oscillations », *J. Fluid Mech.*, 393, p. 333–356, 1999.
- [123] E. D. Wilkes and O. A. Basaran, « Drop Ejection from an Oscillating Rod », *J. Colloid Interface Sci.*, 242 (1), p. 180–201, 2001.
- [124] O. A. Basaran and D. W. DePaoli, « Nonlinear oscillations of pendant drops », *Phys. Fluids*, 6 (9), p. 2923–2943, 1994.
- [125] X. Noblin, A. Buguin and F. Brochard-Wyart, « Vibrated sessile drops: Transition between pinned and mobile contact line oscillations », *Eur. Phys. J. E*, 14 (4), p. 395–404, 2004.
- [126] D. W. DePaoli, J. Q. Feng, O. A. Basaran and T. C. Scott, « Hysteresis in forced oscillations of pendant drops », *Phys. Fluids*, 7 (6), p. 1181–1183, 1995.
- [127] A. H. Nayfeh and D. T. Mook, *Nonlinear Oscillations*, (Wiley Classics), p. 161–257 1995.
- [128] H.-Y. Kim, « Drop fall-off from the vibrating ceiling », *Phys. Fluids*, 16 (2), p. 474–477, 2004.
- [129] B. Vukasinovic, M. K. Smith and A. Glezer, « Dynamics of a sessile drop in forced vibration », *J. Fluid Mech.*, 587, p. 395–423, 2007.
- [130] A. J. James, M. K. Smith and A. Glezer, « Vibration-induced drop atomization and the numerical simulation of low-frequency single-droplet ejection », *J. Fluid Mech.*, 476, p. 29–62, 2003.
- [131] J. Li, N. Mittal, S. Y. Mak, Y. Song and H. C. Shum, « Perturbation-induced droplets for manipulating droplet structure and configuration in microfluidics », *J. Micromechanics Microengineering*, 25 (8), 084009, 2015.
- [132] D. R. Lide, *CRC handbook of chemistry and physics: a ready-reference book of chemical and physical data*, (CRC Press, 84th Ed.), p. 6-5, 2003.
- [133] P. M. Kruglyakov, *Hydrophile-lipophile balance of surfactants and solid particles: physicochemical aspects and applications*, (Elsevier, 1st Ed.), p. 314–365, 2000.
- [134] G. Serrien and P. Joos, « Dynamic surface properties of aqueous sodium dioctyl sulfosuccinate solutions », *J. Colloid Interface Sci.*, 139 (1), p. 149–159, 1990.
- [135] A. Bonfillon, F. Sicoli and D. Langevin, « Dynamic Surface Tension of Ionic Surfactant Solutions », *J. Colloid Interface Sci.*, 168 (2), p. 497–504, 1994.
- [136] P. Chartier, « La surface du verre: bases scientifiques pour la recherche industrielle », *Verre*, 3 (3), p. 5–13, 1997.
- [137] W.S. Rasband, ImageJ, U. S. National Institutes of Health, Bethesda, Maryland, USA, <http://imagej.nih.gov/ij/>, 1997-2014.
- [138] K. Thirumalai, A. Singh and R. Ramesh, « A MATLABTM code to perform weighted linear regression with (correlated or uncorrelated) errors in bivariate data », *J. Geol. Soc. India*, 77 (4), p. 377–380, 2011.

- [139] D. York, N. M. Evensen, M. L. Martínez and J. De Basabe Delgado, « Unified equations for the slope, intercept, and standard errors of the best straight line », *Am. J. Phys.*, 72 (3), p. 367–375, 2004.
- [140] C. Perruchet and M. Priel, *Estimer l'incertitude: mesures - essais*. (AFNOR), p. 39–60, 2000.
- [141] M. Strani and F. Sabetta, « Free vibrations of a drop in partial contact with a solid support », *J. Fluid Mech.*, 141, p. 233–247, 1984.
- [142] A. S. Utada, A. Fernandez-Nieves, J. M. Gordillo and D. A. Weitz, « Absolute Instability of a Liquid Jet in a Coflowing Stream », *Phys. Rev. Lett.*, 100 (1), 014502, 2008.
- [143] D. F. Rutland and G. J. Jameson, « Theoretical prediction of the sizes of drops formed in the breakup of capillary jets », *Chem. Eng. Sci.*, 25 (11), p. 1689–1698, 1970.
- [144] N. N. Mansour and T. S. Lundgren, « Satellite formation in capillary jet breakup », *Phys. Fluids A*, 2 (7), p. 1141–1144, 1990.
- [145] M. Tjahjadi, H. A. Stone and J. M. Ottino, « Satellite and subsatellite formation in capillary breakup », *J. Fluid Mech.*, 243 (1), p. 297–317, 1992.
- [146] D. F. Zhang and H. A. Stone, « Drop formation in viscous flows at a vertical capillary tube », *Phys. Fluids*, 9 (8), p. 2234–2242, 1997.
- [147] P. K. Notz, A. U. Chen and O. A. Basaran, « Satellite drops: Unexpected dynamics and change of scaling during pinch-off », *Phys. Fluids*, 13 (3), p. 549–552, 2001.
- [148] B. Ambravaneswaran, E. D. Wilkes and O. A. Basaran, « Drop formation from a capillary tube: Comparison of one-dimensional and two-dimensional analyses and occurrence of satellite drops », *Phys. Fluids*, 14, (8), p. 2606–2621, 2002.

List of figures

Figure 1.1: Main types of emulsions: (a) oil-in-water (O/W); (b) water-in-oil (W/O); (c) water-in-oil-in-water (W/O/W); (d) oil-in-water-in-oil (O/W/O).	12
Figure 1.2: Contact angle θ of an oil drop in water on a solid substrate.	14
Figure 1.3: Emulsion destabilisation mechanisms: (a) Ostwald ripening; (b) coalescence; (c) flocculation; (d) creaming.	15
Figure 1.4: Schematic representation of a surfactant molecule.	17
Figure 1.5: Surfactant concentration impact on interfacial tension of an O/W emulsion.	18
Figure 1.6: Radial diffuser dispersion unit (from [11], modified).	19
Figure 1.7: Rotor-stator device (from [15]).	20
Figure 1.8: Static mixers: (a) open design with helices; (b) with blades; (c) corrugated plates; (d) multi-layer; (e) closed design with channels or holes (from [16], modified).	21
Figure 1.9: Direct membrane emulsification.	22
Figure 1.10: Premix membrane emulsification (from [20]).	22
Figure 1.11: Microchannel membrane emulsification (from [20]).	23
Figure 1.12: Drop diameter depending on the energy density for a colloid mill; rotor stator (UT); microfluidizer; high pressure homogeniser (HPH) with flat valve (solid line) and orifice valve (dashed line); ME (with dispersed phase fraction below) (from [24]).	24
Figure 1.13: Drop detachment regime depending on P_{tm} : (a) cross-flow shear; (b) transmembrane pressure; (c) Plateau-Rayleigh instability (from [29], modified).	26
Figure 1.14: Membrane coalescence depending on the contact angle (from [39], modified).	28
Figure 1.15: Plateau-Rayleigh instability for a 40 wt% glycerol solution in a 0.9 wt% saline solution and schematic representation, with scale bar representing 50 μm (from [52]).	36
Figure 1.16: Faraday waves for a 2 mm deep water tray vibrated at 300 Hz (from [57]).	38
Figure 1.17: Kelvin-Helmholtz instability for fresh water on top (flow from right to left) and brine below (flow from left to right), from instability to turbulence (from [59], modified).	39
Figure 1.18: Saffman-Taylor instability for an air-silicon oil system, from the interface to fingers (from [54], modified).	40
Figure 1.19: Flow modes from a 2.769 mm diameter nozzle: (a) dripping ($We = 0.063$); (b) intermediate chaotic regime ($We = 1.73$); (c) jetting ($We = 2.3$) (from [60]).	40
Figure 1.20: Dripping to jetting transition depending on the inner Weber number We_{in} and outer capillary number Ca_{out} , for various surface tensions and viscosity ratios.	

Black: dripping; white: jetting (from [61]).	42
Figure 1.21: Grace curve: force ratio (viscous to interfacial forces) for burst E_B depending on the viscosity ratio $p = \eta_{dp}/\eta_{cp}$ (from [84]).	46
Figure 1.22: Critical elongation ratio L/a (drop half length to the undeformed drop radius) for breakup as a function of the viscosity ratio $\lambda = \eta_{dp}/\eta_{cp}$ (from [86]).	47
Figure 1.23: Fluid thread final shapes depending on the initial aspect ratio L_0 (initial thread half length to the initial thread radius) and Oh (from [89]).	48
Figure 1.24: Forces exerted on a drop in ME for (a) torque balance; (b) force balance. Forces: Young-Laplace F_{YL} , buoyancy F_{BG} , dynamic lift F_{DL} , drag F_{DR} , capillary F_γ (from [91]).	49
Figure 1.25: Drop shapes from the Rayleigh theory for modes $n = 2$ to 5, depending on the axial ratio γ (horizontal to vertical axis length) (from [99]).	55
Figure 1.26: Summary of work on free, vibrated drops depending on the ratio of the interface deformation A to a length scale proportional to the drop radius L and the ratio of time scales: small-amplitude oscillations $A/L \rightarrow 0$; moderate-amplitude oscillations $A/L \ll 1$; large-amplitude oscillations $A/L \approx O(1)$ (from [102]).	56
Figure 1.27: Internal flow patterns: (a) oscillating drop in mode $n = 2$; (b) rotating-oscillating drop; (c) rotating drop after drive is stopped; (d) still drop (from [110], modified).	58
Figure 1.28: Experimental points for (a) eigenfrequency in mode k ; (b) damping rate, for different attachment angles θ_a on a tube compared to the models of Strani and Sabetta (1984) (solid lines) and Bostwick and Steen (2009) (dashed lines) (from [116], modified).	60
Figure 1.29: First four resonance modes for a partially bound drop. From left to right: mode 1 (1 Hz), mode 2 (2.5 Hz), mode 3 (4 Hz), mode 4 (5.9 Hz) (from [118], modified).	61
Figure 1.30: Drop shape for mode 1 resonance depending on the position of the circle of contact (points) (from [114], modified).	62
Figure 1.31: Hysteresis in drop response depending on the dimensionless amplitude A (rod oscillation amplitude divided by the rod radius R), for a dimensionless frequency (rod oscillation frequency multiplied by the capillary time $t_c = \sqrt{\rho_{dp}R^3/\gamma}$ of 3.4, for different $Re = \rho/\eta \sqrt{\gamma R/\rho} = 1/Oh$ (from [123]).	64
Figure 1.32: Drop ejection from an oscillating rod: dimensionless amplitude A (rod oscillation amplitude over the rod radius R) function of the dimensionless frequency Ω (rod oscillation frequency multiplied by the capillary time $t_c = \rho_{dp}R^3/\gamma$) for $1/Oh = 20$ (from [124]).	65
Figure 2.1: Photograph of the single drop formation setup: (a) continuous phase; (b) capillary tube; (c) screw; (d) syringe; (e) syringe pump; (f) vibrating exciter; (g) laser	

sensor; (h) anti-vibration table (i) light source; (j) macro lens mounted on high speed camera.	74
Figure 2.2: Vibration amplitude of the empty setup, depending on the signal generator tension, for different frequencies.	77
Figure 2.3: Vibration amplitude of the empty setup depending on the forcing frequency, for different tensions.	77
Figure 2.4: Vibration amplitude depending on the forcing frequency, for different setup configurations and tensions.	78
Figure 2.5: Representation of a dodecane molecule.	80
Figure 2.6: Representation of a glycerol molecule.	80
Figure 2.7: Representation of an SDS molecule.	80
Figure 2.8: Schematic representation of the dispersed phase feeding system: (a) fused silica capillary; (b) sleeve; (c) fitting for sleeve; (d) silicon; (e) part of the bottom of the PVC cell; (f) NanoTight Union; (g) fitting; (h) PEEK tube; (i) and (i') olives; (j) rubber seal; (k) Teflon.	85
Figure 2.9: Photograph of the experimental setup with continuous phase flow: (a) PVC cell; (b) PEEK tube for dispersed phase flow; (c) and (c') plastic tubing for continuous phase flow; (d) flowmeter; (e) vibrating exciter; (f) steel profile; (g) rubber support; (h) anti-vibration table; (i) cold light source; (j) high-speed camera mounted with macro lens.	86
Figure 2.10: Schematic representation of the feedback loop for vibration amplitude control.	88
Figure 2.11: Average velocity vectors in the setup cell channel for a flowrate of 45.3 L.h ⁻¹ . Flow velocity scale in m.s ⁻¹ . Capillary outline with a dashed pink line.	89
Figure 2.12: Continuous phase flow velocity in the channel as a function of the set flow rate.	90
Figure 2.13: Dynamic interfacial tension as a function of $1/\sqrt{t}$, for (a) the reference system; (b) system 1. I: plateau region; II: slight decrease region.	95
Figure 2.14: Optic microscopy images for the capillary tube pores at the surface for the first experimental setup: (a) $D_p = 0.11$ mm; (b) $D_p = 0.32$ mm; (c) $D_p = 0.35$ mm; (d) $D_p = 0.75$ mm. Circular pores circled with a dashed red line.	97
Figure 2.15: Optic microscopy image for the fused silica capillary tube pore at the surface for the second experimental setup. Pore circled with a dashed red line.	97
Figure 2.16: Average contact angle of a water drop on the glass slide immersed in 3 vol% Mucosal solution, for different times.	99
Figure 2.17: Steps for image analysis, with images from the first setup: (a) original image; (b) binary image; (c) border filling and analysis.	100
Figure 2.18: Light refraction for dodecane drops in water: (a) large drop (3 mm diameter); (b) small drop (1 mm diameter). Shadow zones (double arrows).	101

Figure 2.19: Dimensions to estimate the bound drop diameter from the Guldinus theorem. A half drop area, $x_{1/2}$ centre of mass of the half drop, r_d distance from the axis to $x_{1/2}$. 102

Figure 2.20: Drop before break off in jetting mode for the reference system (second setup), $v_{cp} = 0.73 \text{ m.s}^{-1}$, $v_{dp} = 0.24 \text{ m.s}^{-1}$. Characteristic lengths: elongated neck length L_n , pore diameter D_p . 103

Figure 2.21: Drop formation in time for the reference system for the first setup, $D_p = 0.32 \text{ mm}$, $q = 3.6 \text{ }\mu\text{L.s}^{-1}$, $f = 100 \text{ Hz}$, $A = 0.210 \text{ mm}$. Characteristic lengths: drop length L , maximum drop length L_{max} and drop diameter D_d . 103

Figure 3.1: Experimental setup: 1, high speed camera; 2, computer; 3 and 3', windows; 4, light source; 5, continuous phase; 6, dispersed phase; 7, glass capillary; 8, 8' and 8'', LED sensor, emerging rod and distance measured; 9, vibrating motion; 10, syringe; 11, syringe pump; 12, exciter; 13, flexible seal; 14, optical table. 111

Figure 3.2: (a) Drop diameter D_d depending on the peak-to-peak capillary amplitude A_{pp} for $f = 100 \text{ Hz}$, $D_p = 0.32 \text{ mm}$, $q = 4.3 \text{ }\mu\text{L.s}^{-1}$: (\diamond) measurements, measured amplitude threshold (dash-dotted line), (*) estimates from eq. (3.1), estimates from the balance $F_b = F_Y^{max}$ (dotted line), estimates from the balance $F_b + F_{exc}^{peak} = F_Y^{max}$ (dashed line), estimates from eq. (3.9) (solid line). (b) Drop image just before detachment in dripping mode (left, $A_{pp} = 0.095 \text{ mm}$), in stretching mode (centre and right, $A_{pp} = 0.419 \text{ mm}$). 112

Figure 3.3: Threshold amplitude depending on the forcing frequency: (\square) $D_p = 0.11 \text{ mm}$, $q = 2.2 \text{ }\mu\text{L.s}^{-1}$, (\diamond) $D_p = 0.32 \text{ mm}$, $q = 6.5 \text{ }\mu\text{L.s}^{-1}$, (o) $D_p = 0.35 \text{ mm}$, $q = 6.9 \text{ }\mu\text{L.s}^{-1}$, (x) $D_p = 0.75 \text{ mm}$, $q = 10.1 \text{ }\mu\text{L.s}^{-1}$. 113

Figure 3.4: Drop diameter depending on the forcing frequency: (\square) $D_p = 0.11 \text{ mm}$, $q = 2.2 \text{ }\mu\text{L.s}^{-1}$, (\diamond) $D_p = 0.32 \text{ mm}$, $q = 6.5 \text{ }\mu\text{L.s}^{-1}$, (o) $D_p = 0.35 \text{ mm}$, $q = 6.9 \text{ }\mu\text{L.s}^{-1}$, (x) $D_p = 0.75 \text{ mm}$, $q = 10.1 \text{ }\mu\text{L.s}^{-1}$. Estimates from eq. (3.9): $D_p = 0.11 \text{ mm}$ (dotted line), $D_p = 0.32 \text{ mm}$ (dash-dotted line), $D_p = 0.35 \text{ mm}$ (solid line), $D_p = 0.75 \text{ mm}$ (thick solid line). 113

Figure 3.5: (\diamond) Drop length L , capillary displacement x (solid line), approximate boundaries of the resonance zone RZ (dashed line), phase shift estimation guidelines (dotted line): $f = 50 \text{ Hz}$, $D_p = 0.32 \text{ mm}$, $A_{pp} = 0.56 \text{ mm} < A_{th} = 0.88 \text{ mm}$, $q = 4.3 \text{ }\mu\text{L.s}^{-1}$. 115

Figure 3.6: Calculated mode 1 resonance frequency [5] versus set experimental frequency: (\square) $D_p = 0.11 \text{ mm}$, $q = 2.2 \text{ }\mu\text{L.s}^{-1}$, (\diamond) $D_p = 0.32 \text{ mm}$, $q = 6.5 \text{ }\mu\text{L.s}^{-1}$, (o) $D_p = 0.35 \text{ mm}$, $q = 6.9 \text{ }\mu\text{L.s}^{-1}$, (x) $D_p = 0.75 \text{ mm}$, $q = 10.1 \text{ }\mu\text{L.s}^{-1}$. 116

Figure 3.7: Elongation ratio function of drop to pore diameter ratio ($f = 30 \text{ Hz} - 150 \text{ Hz}$): (\square) $D_p = 0.11 \text{ mm}$, (\diamond) $D_p = 0.32 \text{ mm}$, (o) $D_p = 0.35 \text{ mm}$, (x) $D_p = 0.75 \text{ mm}$. 119

Figure 4.1: Cross-section side view of the setup by CAD: 1, tank; 2, continuous phase; 3, glass capillary (nozzle); 4, dispersed phase drop; 5, flexible seal; 6, central element fixed on the vibrating exciter; 7, axial, vibrating motion; 8, windows; 9, dispersed phase supply system; 10, light source; 11, high-speed camera with macro lens. 129

Figure 4.2: Visual summary of the output data. Drop detaching in stretching mode in time t for the reference system, $D_p = 0.32$ mm, $q = 3.6$ $\mu\text{L}\cdot\text{s}^{-1}$, $f = 100$ Hz, $A = 0.209$ mm. 130

Figure 4.3: Transition from dripping to stretching mode: generated drop diameter as a function of the forcing amplitude for the reference system, $D_p = 0.32$ mm, $f = 100$ Hz, $q = 3.6$ $\mu\text{L}\cdot\text{s}^{-1}$. (\diamond) Experimental data; experimental threshold (dashed line); (\circ) theoretical drop size without vibration from Eq. (4.2); simulation results of section 2.6.3, Eq. (4.14) (dotted line); of section 2.6.4, Eq. (4.17) with $\alpha = -1.9$, $\mathcal{C} = 4.4$ (solid line). 131

Figure 4.4: Impact of pore size on (a) threshold amplitude A_{th} and (b) drop diameter at A_{th} , for the reference system. (\square) $D_p = 0.11$ mm, $q = 2.2$ $\mu\text{L}\cdot\text{s}^{-1}$; (\diamond) $D_p = 0.32$ mm, $q = 6.1$ $\mu\text{L}\cdot\text{s}^{-1}$. Simulations from Eq. (4.14) of section 2.6.3 (dashed line); Eq. (4.17) of section 2.6.4 (solid line): $D_p = 0.11$ mm (thick); $D_p = 0.32$ mm (thin). 134

Figure 4.5: Impact of interfacial tension on (a) threshold amplitude A_{th} and (b) drop diameter at A_{th} , for $D_p = 0.32$ mm, $q = 3.6$ $\mu\text{L}\cdot\text{s}^{-1}$. (\diamond) Reference system; (\blacklozenge) system 1; (\blacklozenge) system 2. 135

Figure 4.6: Impact of dispersed phase viscosity on (a) threshold amplitude A_{th} and (b) drop diameter at A_{th} , for $D_p = 0.32$ mm, $q = 6.1$ $\mu\text{L}\cdot\text{s}^{-1}$. (\diamond) Reference system; (\blacktriangleleft) system 3; (\blacktriangleright) system 4. 136

Figure 4.7: Dimensionless forcing pulsation depending on the drop to pore diameter. (a) For different interfacial tensions and pore diameters: reference system (white); system 1 (grey); system 2 (black). (\square) $D_p = 0.11$ mm; (\diamond) $D_p = 0.32$ mm. (b) For different dispersed phase viscosities, $D_p = 0.32$ mm: (\blacktriangleleft) system 3; (\blacktriangleright) system 4. Curve of the dimensionless eigenpulsation from: Eq. (4.3) of Bisch *et al.* [6] (dashed line); Eq. (4.12) of S&S [7] for the reference system (solid line), system 3 (dash-dotted line) and system 4 (dotted line). 137

Figure 4.8: Analogy between the present drop bound to a nozzle (left) and a drop in partial contact with a solid spherical cap (right) as defined by S&S [7,8]. 137

Figure 4.9: Drop elongation ratio function of the drop to pore diameter. Reference system (white); system 1 (grey); system 2 (black). (\square) $D_p = 0.11$ mm; (\diamond) $D_p = 0.32$ mm; (\blacktriangleleft) system 3, $D_p = 0.32$ mm; (\blacktriangleright) system 4, $D_p = 0.32$ mm. Curve from Eq. (4.13) (dashed and solid lines). 138

Figure 4.10: Simulation and experimental values for different forcing frequencies for (a) threshold amplitudes A_{th} and (b) drop diameters at A_{th} . Reference system (white);

system 1 (grey); system 2 (black). (\square) $D_p = 0.11$ mm; (\diamond) $D_p = 0.32$ mm; (\triangleleft) system 3, $D_p = 0.32$ mm; (\triangleright) system 4, $D_p = 0.32$ mm. 141

Figure 4.11: Sketch of an attached drop oscillating between prolate and oblate shapes. 143

Figure 4.A1: Dynamic interfacial tension as a function of $1/\sqrt{t}$, for system 1. 144

Figure 4.C1: Impact of dispersed phase flow rate on (a) threshold amplitude A_{th} and (b) drop diameter at A_{th} , for the reference system, $D_p = 0.32$ mm. (\square) $q = 2.4$ $\mu\text{L}\cdot\text{s}^{-1}$; (\diamond) $q = 3.6$ $\mu\text{L}\cdot\text{s}^{-1}$; (\circ) $q = 6.1$ $\mu\text{L}\cdot\text{s}^{-1}$; (\times) $q = 14.4$ $\mu\text{L}\cdot\text{s}^{-1}$. 147

Figure 4.D1: Impact of continuous phase viscosity on (a) threshold amplitude A_{th} and (b) drop diameter at A_{th} , for $D_p = 0.32$ mm, $q = 6.1$ $\mu\text{L}\cdot\text{s}^{-1}$. (\diamond) Reference system; (*) System 5. 147

Figure 4.D2: Dimensionless forcing pulsation depending on the drop to pore diameter, for $D_p = 0.32$ mm, (*) system 5. Curve of the dimensionless eigenpulsation from: Eq. (4.3) of Bisch *et al.* [117] (dashed line); Eq. (4.12) of S&S [112] for system 5 (solid line). 148

Figure 4.E1: Position of the drop centre of mass in time with respect to the capillary surface X_d for reference system, $D_p = 0.32$ mm, $f = 100$ Hz, $A = 0.150$ mm, $q = 6.1$ $\mu\text{L}\cdot\text{s}^{-1}$. (\circ) Experimental data; capillary motion (thin solid line); theoretical curve from Eq. (4.14) (dashed line); Eq. (4.17) with $\alpha = -1.9$, $\mathcal{C} = 4.4$ (thick solid line). 149

Figure 5.1: Cell cross-section by CAD (to scale). Cell (left): (a) continuous phase flow axis; (b) optical axis; (c) dispersed phase flow axis; (d) cell binding point; (e) frame for zoom. Zoom in the cell (right): 1, dispersed phase inlet (microfluidic system); 2, continuous phase flow; 3, growing drop; 4, nozzle; 5, formed drop carried away; 6, optical glass window; 7: window for user. 158

Figure 5.2: Drop diameter D_d function of the continuous phase velocity v_{cp} , $v_{dp} = 0.031$ $\text{m}\cdot\text{s}^{-1}$. See table 5.1 for symbols. 160

Figure 5.3: Drag coefficient C_D function of the particle Reynolds number Re_p . Experimental results from eq. (5.1), see table 5.1 for symbols. Feng and Michaelides predictions for $\zeta = 1.5$ (dashed line); our fit from eq. (5.3) with $C_0 = 0.14$ and $\delta_0 = 17.7$ (solid line). 162

Figure 5.4: Reference system snapshots ($\text{Oh}_{cp} = 7.0 \times 10^{-3}$): (a) jet widening, $\text{Ca}_{out} = 5.1 \times 10^{-3}$; (b) jet narrowing, $\text{Ca}_{out} = 1.3 \times 10^{-2}$. Continuous phase flow from right to left. 163

Figure 5.5: Characteristic values at the DJT, see table 5.1 for symbols: (a) We_{in} function of Ca_{out} . Widening to narrowing limit Ca^* for the reference system (dashed line); (b) Drop to pore diameter ratio D_d/D_p function of Ca_{out} . 164

Figure 5.6: Model configuration with the different variables involved. 165

Figure 5.7: Characteristic values at the DJT, see table 5.1 for symbols. (a) We_{in} function of Ca_{out} ; (b) Drop to pore diameter ratio D_d/D_p function of Ca_{out} . Simulation results for the reference system (grey); system 2 (black). Uniform nozzle-sized thread

limit of section 2.5.3.1 (solid line); maximal narrowing limit of section 2.5.3.2 (dashed line).	168
Figure 5.A1: Average velocity vector map in the centre of the cell channel at a flow rate of 45.3 L.h ⁻¹ . Velocity scale below in m.s ⁻¹ ; nozzle tip superimposed in grey.	171
Figure 5.A2: Velocity component along the x -axis function of the position above the capillary y , for the example of fig. 5.A1.	171
Figure 5.B1: Figure 5.B1: Illustration of thread surface oscillations in jet widening: snapshots for the reference system ($Oh_{cp} = 7.0 \times 10^{-3}$), $We_{in} = 2.04$, $Ca_{out} = 5.1 \times 10^{-3}$. t_0 is the initial point, taken just after the previous drop detachment, $t_n = t_{n-1} + 656 \mu s$ and finally, the current drop detaches between t_{11} and t_{12} .	172
Figure 5.B2: Drop neck diameter variations in time for: reference system, $We_{in} = 2.04$ and $Ca_{out} = 5.1 \times 10^{-3}$ (black); system 1, $We_{in} = 0.82$ and $Ca_{out} = 6.8 \times 10^{-3}$ (grey).	172
Figure 5.C1: We_{in} function of Ca_{out}/Oh_{cp} , see table 5.1 for symbols.	173
Figure 5.D1: We_{in} function of Ca_{out} at the DJT, see table 5.1 for symbols. Pathak's DJT criterion (dashed line); Meyer and Crocker's DJT criterion (solid line).	174
Figure 5.E1: Evolution of the dimensionless neck width (D_{neck}/D_p) in time: (o) reference system data, for $v_{cp} = 0.39$ m.s ⁻¹ and $v_{dp} = 0.031$ m.s ⁻¹ ; exponential fit with $\tau_n = 0.0019$ s (solid line).	174
Figure 5.E2: Necking growth rate function of $(8\gamma/D_p^3\rho_{dp})^{1/2}$, obtained on the reference system ($v_{cp} = 0.18$ to 0.44 m.s ⁻¹), system 1 ($v_{cp} = 0.11$ to 0.35 m.s ⁻¹) and system 2 ($v_{cp} = 0.10$ to 0.20 m.s ⁻¹), with $v_{dp} = 0.031$ m.s ⁻¹ . Fit passing through the origin (solid line).	175
Figure 5.A11: Drop diameter function of the continuous phase velocity for different dispersed phase velocities, for the reference system. (o) $v_{dp} = 0.016$ m.s ⁻¹ ; (\diamond) $v_{dp} = 0.031$ m.s ⁻¹ ; (x) $v_{dp} = 0.063$ m.s ⁻¹ ; (\star) $v_{dp} = 0.14$ m.s ⁻¹ ; (\square) $v_{dp} = 0.21$ m.s ⁻¹ .	175
Figure A1.1: Tween 20 (Polysorbate 20).	184
Figure A1.2: Tween 80 (Polysorbate 80).	184
Figure A1.3: Span 80 (Sorbitane monooleate).	184
Figure A1.4: Brij 58 (Polyethylene glycol hexadecyl ether).	185
Figure A1.5: CTAB (Cetyl trimethylammonium bromide).	185
Figure A1.6: SDS (Sodium dodecyl sulphate).	185
Figure A2.1: CAD designed by Joel Casalinho of the entire setup (to scale). (a) Tank; (b) capillary tube (nozzle); (c) window for image acquisition; (d) position of rubber seal between the upper and lower parts of the tank; (e) central element linking the capillary to the vibrating exciter; (f) vibrating exciter; (g) setup support; (h) bottom support placed on the anti-vibration table; (i) screw to support capillary and for amplitude displacement measurement; (j) dispersed phase influx element.	188
Figure A2.2: CAD designed by Joel Casalinho of the entire cell, fixed onto the	

vibrating exciter (to scale). Dispersed phase flow direction and vibration axis (blue arrow); continuous phase flow axis (green arrow); optical axis (red arrow). 189

Figure A2.3: CAD designed by Joel Casalinho of the cross-section of the inside of the cell (to scale). (a) cell; (b) screws to close the setup; (c) window for user observation; (d) drop in formation; (e) capillary tube (nozzle); (f) screw for microfluidic system (downstream); (g) sleeve; (h) connector; (i) screw for microfluidic system (upstream); (j) tube for dispersed phase influx; (k) screw to fix cell on vibrating exciter; (l) drop carried away by the continuous phase flow; (m) silicon; (n) window for image acquisition. 190

Figure A3.1: Impact of dispersed phase flow rate on (a) threshold amplitude A_{th} and (b) drop diameter at A_{th} , for the reference system. (\square) $D_p = 0.11$ mm, $q = 2.2$ $\mu\text{L}\cdot\text{s}^{-1}$ (blue), $q = 3.1$ $\mu\text{L}\cdot\text{s}^{-1}$ (red); (o) $D_p = 0.35$ mm, $q = 3.8$ $\mu\text{L}\cdot\text{s}^{-1}$ (blue), $q = 6.4$ $\mu\text{L}\cdot\text{s}^{-1}$ (red). Simulations from eq. (4.17) of chapter 4: $D_p = 0.11$ mm, $\alpha = -1.4$, $\mathcal{C} = 8.2$ (yellow); $D_p = 0.35$ mm, $\alpha = -1.9$, $\mathcal{C} = 4.4$ (black). Lowest flow rates (dotted line); highest flow rates (solid line). 192

Figure A3.2: Impact of dispersed phase flow rate on (a) threshold amplitude A_{th} and (b) drop diameter at A_{th} , for system 2, $D_p = 0.32$ mm. $q = 1.2$ $\mu\text{L}\cdot\text{s}^{-1}$ (red); $q = 2.4$ $\mu\text{L}\cdot\text{s}^{-1}$ (blue); $q = 3.6$ $\mu\text{L}\cdot\text{s}^{-1}$ (yellow); $q = 6.1$ $\mu\text{L}\cdot\text{s}^{-1}$ (black). 193

Figure A3.3: Impact of dispersed phase flow rate on (a) threshold amplitude A_{th} and (b) drop diameter at A_{th} , for system 2. (o) $D_p = 0.35$ mm, $q = 3.8$ $\mu\text{L}\cdot\text{s}^{-1}$ (blue); $q = 6.4$ $\mu\text{L}\cdot\text{s}^{-1}$ (red); (x) $D_p = 0.75$ mm, $q = 9.6$ $\mu\text{L}\cdot\text{s}^{-1}$ (blue), $q = 19.1$ $\mu\text{L}\cdot\text{s}^{-1}$ (red). 194

Figure A3.4: Impact of dispersed phase flow rate on (a) threshold amplitude A_{th} and (b) drop diameter at A_{th} . (\diamond) System 1: $q = 2.4$ $\mu\text{L}\cdot\text{s}^{-1}$ (blue), $q = 3.6$ $\mu\text{L}\cdot\text{s}^{-1}$ (red); (\triangleleft) System 3: $q = 2.5$ $\mu\text{L}\cdot\text{s}^{-1}$ (blue), $q = 4.3$ $\mu\text{L}\cdot\text{s}^{-1}$ (red); (\triangleright) System 4: $q = 2.5$ $\mu\text{L}\cdot\text{s}^{-1}$ (blue), $q = 4.3$ $\mu\text{L}\cdot\text{s}^{-1}$ (red); (*) System 5: $q = 2.5$ $\mu\text{L}\cdot\text{s}^{-1}$ (blue), $q = 4.3$ $\mu\text{L}\cdot\text{s}^{-1}$ (red). 194

Figure A3.5: Impact of pore diameter on (a) threshold amplitude A_{th} and (b) drop diameter at A_{th} , for system 2. (\square) $D_p = 0.11$ mm, $q = 1.1$ $\mu\text{L}\cdot\text{s}^{-1}$; (\diamond) $D_p = 0.32$ mm, $q = 3.6$ $\mu\text{L}\cdot\text{s}^{-1}$; (o) $D_p = 0.35$ mm, $q = 6.4$ $\mu\text{L}\cdot\text{s}^{-1}$; (x) $D_p = 0.75$ mm, $q = 9.6$ $\mu\text{L}\cdot\text{s}^{-1}$. 195

Figure A3.6: Impact of the continuous phase viscosity on (a) threshold amplitude A_{th} and (b) drop diameter at A_{th} , for $D_p = 0.32$ mm, $q = 3.6$ $\mu\text{L}\cdot\text{s}^{-1}$. (\diamond) System 2, $\eta_{cp} = 0.89$ mPa.s; (*) System 6, $\eta_{cp} = 4.18$ mPa.s. 196

Figure A3.7: Dimensionless forcing pulsation depending on the drop to pore diameter. System 2: (\square) $D_p = 0.11$ mm, $q = 1.1$ $\mu\text{L}\cdot\text{s}^{-1}$; (\diamond) $D_p = 0.32$ mm, $q = 3.6$ $\mu\text{L}\cdot\text{s}^{-1}$; (o) $D_p = 0.35$ mm, $q = 6.4$ $\mu\text{L}\cdot\text{s}^{-1}$; (x) $D_p = 0.75$ mm, $q = 9.6$ $\mu\text{L}\cdot\text{s}^{-1}$. (*) System 6, $D_p = 0.32$ mm, $\eta_{cp} = 4.18$ mPa.s, $q = 3.6$ $\mu\text{L}\cdot\text{s}^{-1}$. Curve of the dimensionless eigenpulsation from: eq. (4.3) in chapter 4 of Bisch *et al.* (dashed line); eq. (4.12) in chapter 4 of Strani and Sabetta (solid line). 197

Figure A3.8: Simulation and experimental values for different forcing frequencies for

(a) threshold amplitudes A_{th} and (b) drop diameters at A_{th} , for system 2. (\square) $D_p = 0.11$ mm, $q = 1.1 \mu\text{L}\cdot\text{s}^{-1}$; (\diamond) $D_p = 0.32$ mm, $q = 3.6 \mu\text{L}\cdot\text{s}^{-1}$; (o) $D_p = 0.35$ mm, $q = 6.4 \mu\text{L}\cdot\text{s}^{-1}$; (x) $D_p = 0.75$ mm, $q = 9.6 \mu\text{L}\cdot\text{s}^{-1}$. 198

Figure A4.1: Drop diameter as a function of the forcing amplitude, for the reference system with $D_p = 0.32$ mm, $f = 100$ Hz, $q = 2.5 \mu\text{L}\cdot\text{s}^{-1}$. $v_{cp} = 0.23 \text{ m}\cdot\text{s}^{-1}$ (white); $v_{cp} = 0.40 \text{ m}\cdot\text{s}^{-1}$ (red); (*) theoretical drop size at resonance for $f = 100$ Hz according to the Bisch *et al.* law. 200

Figure A4.2: Drop diameter as a function of the vibration amplitude, for the reference system with $D_p = 0.32$ mm, $f = 150$ Hz, $q = 2.5 \mu\text{L}\cdot\text{s}^{-1}$. $v_{cp} = 0.23 \text{ m}\cdot\text{s}^{-1}$. (*) Theoretical drop size at resonance for $f = 150$ Hz according to the Bisch *et al.* law. 201

Figure A4.3: Drop eigenfrequency at the threshold calculated by the law of Bisch *et al.* versus the forcing frequency: reference system, $D_p = 0.32$ mm, $q = 2.5 \mu\text{L}\cdot\text{s}^{-1}$, $v_{cp} = 0.23 \text{ m}\cdot\text{s}^{-1}$. 202

Figure A4.4: Threshold amplitudes as a function of the forcing frequency: reference system, $D_p = 0.32$ mm, $q = 2.5 \mu\text{L}\cdot\text{s}^{-1}$. Results from setup 1 without cross-flow (blue); from setup 2 with $v_{cp} = 0.23 \text{ m}\cdot\text{s}^{-1}$ (white); simulation results without cross-flow from the model of chapter 4 (dashed line). 202

Figure A5.1: Drop diameter (white) and neck length to drop diameter ratio (red) as a function of the forcing amplitude, for the reference system, $D_p = 0.32$ mm, $v_{dp} = 0.62 \text{ m}\cdot\text{s}^{-1}$, $v_{cp} = 0.23 \text{ m}\cdot\text{s}^{-1}$ for (a) $f = 100$ Hz; (b) $f = 180$ Hz. (*) theoretical drop size at resonance from the Bisch *et al.* law. Jetting to dripping transition (dashed line) at a threshold A_1 ; dripping to stretching transition (dotted line) at a threshold A_2 . 206

Figure A5.2: Drop detachment regime depending on the forcing frequency and amplitude, for system 4, $v_{dp} = 0.69 \text{ m}\cdot\text{s}^{-1}$, $v_{cp} = 0.23 \text{ m}\cdot\text{s}^{-1}$. Jetting (blue); dripping (white); stretching (red). Simulation results without cross-flow from the model in chapter 4 (grey line). Maximum amplitude reachable with the present setup (solid line). 207

Figure A5.3: Drop detachment regime depending on the forcing frequency and amplitude, for the reference system, $v_{dp} = 0.62 \text{ m}\cdot\text{s}^{-1}$, $v_{cp} = 0.23 \text{ m}\cdot\text{s}^{-1}$. Jetting (blue); dripping (white); stretching (red). Simulation results without cross-flow from the model in chapter 4 (grey line). Maximum amplitude reachable with the present setup (solid line). 208

Figure A6.1: Drop size distribution obtained by E. Lepercq-Bost on a PDMS-2 wt% SDS-water emulsion without vibration (white) and with vibration (black). 213

List of tables

Table 1.1: Effects of various parameters on ME.	33
Table 1.2: Criteria for the onset of liquid breakup.	53
Table 1.3: Effects of various parameters on drop vibration.	69
Table 2.1: Different systems investigated and their physicochemical properties.	81
Table 2.2: Summary of the parameters investigated for each system.	84
Table 2.3: Summary of the trials performed on the second setup.	94
Table 4.1: Properties of the different systems investigated.	128
Table 4.2: Identified values of coefficients α and C for β_{film} .	140
Table 5.1: Investigated system composition and properties.	157
Table 5.2: Operating conditions investigated.	159

French summary (résumé français)

Contexte

Une émulsion (simple) est un système liquide-liquide, dans lequel une des phases est dispersée sous forme de gouttes au sein de la phase extérieure immiscible, continue. Un exemple commun est la vinaigrette ou la mayonnaise. Les émulsions sont produites dans de nombreuses industries, telles que l'industrie agro-alimentaire mais aussi dans les industries cosmétique (crèmes, démaquillants), pharmaceutique (vaccins) ou chimique (bitume, fluides de forage). Afin de disperser la première phase dans la seconde et ainsi générer l'émulsion, plusieurs procédés d'émulsification ont été développés. Dans l'industrie, les procédés les plus courants sont les homogénéisateurs à haute pression et les appareils à rotor-stator. Ces procédés ont été abondamment étudiés afin de mieux contrôler la taille et la distribution de taille des gouttes générées. En effet, ces deux caractéristiques ont un impact sur les propriétés du produit fini : elles affectent sa texture, son apparence et surtout sa stabilité.

L'émulsification membrane (EM) est un procédé qui a été développé plus récemment au Japon, dans les années 90. La phase dispersée est forcée à travers une membrane inorganique poreuse et les gouttes sont formées de l'autre côté de la membrane, dans la phase continue qui s'écoule. Les gouttes se détachent suite au cisaillement exercé par cette phase continue circulante. Les deux phases s'écoulent perpendiculairement l'une vis-à-vis de l'autre. Cette configuration est nommée « cross-flow ». La phase continue est recyclée en entrée du module d'émulsification jusqu'à l'obtention de la fraction volumique en phase dispersée désirée dans l'émulsion. Pour le moment, les débits appliqués en EM sont trop faibles pour en permettre une industrialisation à grande échelle. Par contre, ce procédé reste intéressant à développer car il possède d'autres avantages par rapport aux procédés classiques mentionnés ci-dessus. En particulier, sa densité énergétique est plus faible pour produire une même taille de gouttes moyenne. Aussi, des températures et cisaillements moins élevés sont induits, permettant d'inclure des ingrédients sensibles dans le produit fini. De plus, des émulsions contrôlées de faible taille peuvent être obtenues, avec une distribution de taille étroite (monodispersité). Ceci est recherché notamment pour améliorer la stabilité des émulsions. L'impact de nombreux paramètres sur l'EM a déjà été étudié depuis la création de ce procédé dans les années 90. Ces paramètres sont regroupés en paramètres liés au procédé (pression transmembranaire, débit des phases, température), à la membrane (taille et espacement des pores, matériau) et à la formulation (type et concentration d'un émulsifiant, viscosité des phases).

Plus récemment, l'EM a été couplée avec des vibrations afin de mieux maîtriser la taille des gouttes produites et ainsi mieux contrôler le produit fini. Vu que les premières études avec vibration datent des années 2000, l'impact de ce paramètre a été moins étudié que ceux

mentionnés précédemment. Quelques travaux et modèles ont été proposés pour le procédé couplé avec des vibrations longitudinales (parallèles à la surface de la membrane). Par contre, le couplage avec des vibrations transversales (perpendiculaires à la surface de la membrane) a été beaucoup moins étudié. C'est ce cas de figure qui nous intéresse dans ce travail. C. Arnaud (2006) a déposé un brevet sur ce procédé couplé avec des vibrations transversales. Une diminution de la taille moyenne des gouttes de 30 à 10 μm a été observée en imposant une vibration de fréquence de forçage entre 15 et 20 kHz (comparé au cas sans vibration). Sur la même membrane, E. Lepercq-Bost (2008) a appliqué des fréquences de forçage de 7740 à 12710 Hz avec des amplitudes de vibration de la membrane de 1,1 μm . Lorsque la phase dispersée était constituée de polydiméthylsiloxane (PDMS 770), la taille de goutte moyenne a diminué de 6,14 μm sans vibration à 1,57 μm avec vibration. Cette diminution est expliquée surtout par l'apparition d'une population de gouttes de taille 0,2 μm avec vibration. On note que ceci est plus petit que le diamètre moyen des pores (0,8 μm). Lorsque la phase dispersée était constituée d'huile de soja (plus visqueuse), aucun impact sur la taille de goutte n'a été observé avec vibration. Ainsi, les vibrations transversales pourraient réduire la taille de gouttes significativement, mais seulement dans des conditions opératoires bien précises.

En résumé, les observations précédentes montrent que l'EM couplée avec des vibrations transversales permettait de significativement réduire la taille des gouttes dans certaines conditions opératoires par rapport à l'EM classique (sans vibration). Par contre, aucun mécanisme de décrochement des gouttes n'a été proposé dans cette configuration. Ainsi, il n'est pas possible de prédire si la diminution de taille des gouttes aura lieu, ni quelle sera la taille de gouttes générée en connaissant la formulation du système et les paramètres du procédé *a priori*. Afin de mieux contrôler les émulsions produites, il est donc nécessaire de comprendre les mécanismes et d'essayer de les modéliser. C'est l'objectif initial de ce travail.

Dans d'autres configurations que le procédé qui nous intéresse, la rupture de jets ou de gouttes a été abondamment étudiée et est aujourd'hui bien comprise. Plusieurs instabilités hydrodynamiques sont parfaitement connues. Par exemple, l'instabilité de Plateau-Rayleigh induit la rupture d'un jet en gouttes sous l'effet de la tension de surface (observé dans la vie courante lorsqu'un jet s'écoule d'un robinet et se fragmente en gouttes, par exemple). Dans les cas où les instabilités connues ne s'appliquent pas directement au cas de figure considéré, des études ont été réalisées afin de comprendre les mécanismes de rupture des fluides. Un cas détaillé par plusieurs auteurs est celui d'une goutte ou d'un fragment de fluide se rompant après avoir été soumis à un cisaillement simple, élongationnel ou rotationnel. Dans le cas spécifique de l'EM sans vibration, de nombreux modèles ont été proposés pour décrire le décrochement des gouttes de la surface interne de la membrane, en régime « dripping » (goutte à goutte). Des modèles microscopiques ont été développés, par exemple en CFD ou basés sur la minimisation de l'énergie libre de Gibbs du système. La plupart des modèles établis sont des modèles macroscopiques (bilan des forces ou des moments). En EM couplée avec des vibrations

longitudinales, un terme supplémentaire de cisaillement a été ajouté à ces bilans macroscopiques afin de mieux modéliser le décrochement des gouttes. Par contre, en EM couplée avec des vibrations transversales, aucun modèle n'a été établi, comme précisé auparavant, d'où l'intérêt de ce travail.

Concernant le comportement des gouttes soumises à une vibration, les travaux ont débuté avec les recherches de Lord Rayleigh en 1879. Lord Rayleigh a étudié le comportement d'une goutte libre dans le vide, soumise à des oscillations de faibles amplitudes (domaine linéaire). Ses travaux ont été poursuivis afin de prendre en compte plusieurs effets dont la gravité, la viscosité de la goutte, des amplitudes élevées (domaine non-linéaire) ou une phase externe liquide. Depuis les années 80, l'impact d'un support a également été étudié, avec les gouttes partiellement liées à ce support. Les travaux pionniers de Bisch, Rodot et Lasek ont démontré que la présence du support avait comme effet principal l'apparition d'un mode supplémentaire de résonance (le mode 1). Le mode 1 est un mode à plus basse fréquence que les modes pour la goutte libre (qui commencent au mode 2) et il se produit avec un déplacement du centre de masse de la goutte. La plupart des études sur les gouttes liées considère le comportement d'une goutte soumise à des oscillations linéaires. Lorsque les amplitudes de vibration sont élevées (domaine non-linéaire), les études se limitent souvent à des gouttes qui restent attachées au support, afin d'observer l'hystérèse (le fait que la goutte ne se comporte pas de la même façon dans les mêmes conditions à cause de son histoire) ou l'impact des vibrations sur les fréquences propres de la goutte. Dans les rares études où les vibrations sont poussées jusqu'au détachement de la goutte du support, il a été démontré que la résonance en mode 1 assistait le décrochement. Par contre, aucun modèle satisfaisant n'a été proposé pour décrire et/ou prédire le décrochement. Nous verrons que notre étude permet d'approfondir ce sujet des gouttes liées soumises à une vibration jusqu'au décrochement. En effet, nous assimilons les gouttes générées en EM avec vibration à des gouttes partiellement liées à un support vibrant.

Pour conclure, les différentes études sur la rupture de fluides ou de gouttes puis sur le comportement des gouttes soumises à une vibration donnent des premiers éléments pour la compréhension de notre sujet. Toutefois, aucune étude ne nous permet de comprendre et modéliser les mécanismes de décrochement des gouttes en EM avec vibrations transversales *a priori*. On note que les études qui se focalisent sur les gouttes fixées à des supports vibrants avec un décrochement sont celles qui se rapprochent le plus de notre configuration (EM). Par contre, ces études sont principalement numériques. De plus, elles concernent majoritairement des systèmes air-liquide plutôt que liquide-liquide, tels qu'en EM. Aussi, la taille de goutte est généralement fixée (pas de croissance, alors qu'en EM, la taille des gouttes croît avec le temps du fait de l'alimentation continue en phase dispersée). Enfin, les gouttes mouillent la plupart du temps le support dans ces études, alors qu'en EM, c'est la phase continue qui mouille la surface de la membrane. Ainsi, notre configuration de l'EM n'est pas couverte par ces études, d'où l'apport de notre travail.

Problèmes posés

L'objectif initial de ce travail est de comprendre puis modéliser les mécanismes de décrochement des gouttes en EM couplée avec des vibrations transversales. Cette problématique est issue d'expérimentations d'autres auteurs sur un procédé pilote. Ces derniers ont observé une diminution de la taille des gouttes produites avec ce procédé vibrant, sans que l'origine de la diminution n'ait été comprise. Cette compréhension est nécessaire, notamment pour mieux contrôler les émulsions produites par la suite.

Les problèmes qui se posent sont donc :

- Pourquoi de plus petites gouttes sont-elles produites dans certaines conditions opératoires ? Quels sont les mécanismes impliqués ?
- Comment les autres paramètres (de procédé, membrane ou formulation) affectent-ils les mécanismes mis en évidence ?
- Est-il possible de reproduire et/ou prédire les tailles de gouttes générées en connaissant les paramètres d'entrée ? Peut-on contrôler le procédé afin d'obtenir les émulsions avec les caractéristiques souhaitées ?

Méthodologie adoptée

Afin de comprendre l'impact de la vibration sur le décrochement des gouttes, deux configurations simplifiées ont été étudiées pour imiter l'EM couplée avec une vibration transversale. Pour chacune, un dispositif expérimental dédié a été développé.

Le premier dispositif permet d'observer la formation d'une goutte individuelle de phase dispersée dans une phase continue stationnaire, c'est-à-dire, sans écoulement. Cette goutte est formée à travers un capillaire unique, qui est amené à vibrer de façon axiale, à l'aide d'un pot vibrant. Cela permet d'observer expérimentalement l'impact d'une vibration (et uniquement d'une vibration) sur le décrochement de gouttes. La phase dispersée est forcée à travers le capillaire à l'aide d'un pousse-seringue. Ainsi, les gouttes croissent avec le temps. On note que le capillaire est nettoyé de façon à ce que les gouttes ne mouillent pas la surface du capillaire. Les gouttes produites émergent une par une dans la phase continue contenue dans une cuve. Le capillaire vibre de façon axiale à une fréquence de forçage fixée et les amplitudes de forçage induites varient de faibles à fortes amplitudes. Ce montage expérimental permet ainsi d'imiter les vibrations transversales du procédé d'EM vibrant qui nous intéresse. En effet, les amplitudes de forçage dans le procédé qui induisaient la diminution de la taille des gouttes étaient élevées, puisqu'elles pouvaient atteindre l'ordre de grandeur de la taille des gouttes. Ceci est reproduit ici. La formation des gouttes est enregistrée grâce à une caméra rapide et les images sont analysées par la suite afin d'obtenir différentes données, dont la taille des gouttes produites.

Sur ce dispositif, un système de référence (eau/dodécane, sans tensioactif) et un capillaire de référence (diamètre interne de 0,32 mm) ont d'abord été étudiés. Différents mécanismes pouvant intervenir ont été considérés puis un mécanisme a été maintenu. Ensuite, l'impact de la taille de pore, du débit de la phase dispersée, de la tension interfaciale et des viscosités des phases ont été étudiés. Cela a permis de conforter les mécanismes mis en évidence et de développer un modèle qui décrit le comportement des gouttes se détachant sous l'impulsion de vibrations axiales de forte amplitude. Le résumé des mécanismes et du modèle sont détaillés dans la partie résultats, plus bas.

Le second dispositif est similaire au premier : une phase dispersée est forcée à travers un capillaire unique dans une phase continue contenue dans une cellule. Par contre, la phase continue n'est pas stationnaire mais elle circule perpendiculairement à l'axe du capillaire (et donc à l'écoulement de la phase dispersée). On imite ainsi la configuration « cross-flow » du procédé membranaire. Encore une fois, le capillaire est fixé sur un pot vibrant, pouvant induire des vibrations axiales de fréquence connue, de faibles à fortes amplitudes. Cela permet d'observer l'impact d'une vibration en combinaison avec l'impact du cisaillement induit par la phase continue. Les conditions d'EM avec vibration transversale sont donc approchées dans ce deuxième montage expérimental, qui permet de coupler vibration et écoulement. De même que sur le dispositif précédent, les images de formation de gouttes sont acquises par caméra rapide et analysées ensuite.

Sur ce deuxième dispositif, l'impact de l'écoulement seul a d'abord été considéré, tel qu'en EM sans vibration. Puis le couplage avec la vibration a été réalisé, tel qu'en EM couplée avec vibrations transversales. L'étude a été poursuivie en considérant la transition entre les régimes « dripping » (goutte à goutte) et « jetting » (jet continu). En effet, peu d'études existent sur cette transition en écoulement transversal (« cross-flow ») en comparaison avec un co-écoulement. De plus, cette étude est intéressante car dans certaines conditions opératoires, des gouttes peuvent être générées en régime « jetting » en EM. Après l'étude de la transition de « dripping » à « jetting », une étude préliminaire a été effectuée sur l'impact de la vibration axiale sur le mode « jetting », afin de poursuivre l'idée de mieux comprendre l'EM couplée avec des vibrations transversales. Les résultats et interprétations obtenus sur ce deuxième montage sont également exposés dans la partie résultats, plus bas.

Même si ces deux dispositifs permettent de mieux comprendre le procédé d'EM couplée avec des vibrations transversales, on note qu'il reste quelques différences majeures entre nos deux configurations expérimentales et le procédé industriel. Les diamètres des pores des capillaires étudiés dans nos essais sont de l'ordre de la centaine de microns alors qu'industriellement, les pores sont plus petits, de l'ordre du micron ou de la dizaine de microns. Aussi, les fréquences de forçage sont de l'ordre de la dizaine ou centaine de hertz dans nos

essais, alors qu'industriellement, elles sont de l'ordre du kilohertz ou de la dizaine de kilohertz. Enfin, on étudie un pore unique, alors qu'industriellement, les gouttes sont formées à des pores adjacents. Dans ce cas, les gouttes peuvent interagir dans certaines conditions, ce qui modifiera leur comportement et par conséquent, leur taille (par exemple, mécanismes de « push-off » ou de coalescence, selon la tension de surface dynamique).

Malgré les différences soulevées et qui doivent être gardées à l'esprit, on peut tout de même améliorer les connaissances sur le procédé d'émulsification membranaire couplé avec des vibrations transversales grâce à nos expériences. De façon plus large, notre travail permet aussi de mieux comprendre le comportement des gouttes liées soumises à des vibrations suffisamment fortes pour induire un décrochement. En effet, on a vu précédemment que cela a été relativement peu étudié auparavant. De même, notre travail permet d'améliorer la connaissance sur la transition de « dripping » à « jetting », qui a été assez peu étudiée et surtout peu modélisée en situation d'écoulement transversal, ou « cross-flow ».

Résultats principaux sans écoulement de la phase continue

Pour une fréquence de forçage donnée, nous avons formé des gouttes en réalisant un balayage croissant en amplitude. Une diminution significative et brutale de la taille des gouttes produites a été observée au-delà d'une amplitude seuil de forçage. Nous essayons donc d'expliquer l'apparition de ce seuil et la taille de gouttes qui en résulte.

À partir d'une amplitude seuil, des petites gouttes sont formées par rapport à la taille de goutte initiale (générée sans vibration). Lors de sa formation au cours du temps, une goutte grossit car elle est alimentée en continu en phase dispersée. Elle résonne en mode 1 lorsque sa fréquence propre coïncide avec la fréquence de forçage expérimentale. Ceci est équivalent à dire que la goutte entre en résonance lorsqu'elle atteint une taille donnée pour la fréquence de forçage fixée. Le fait que la goutte résonne en mode 1 est confirmé par les formes caractéristiques qu'elle adopte, avec un déplacement du centre de masse qui se produit. La goutte liée qui résonne se détache du capillaire vers le pic de la résonance (mais seulement lorsque l'amplitude seuil est atteinte).

Dans nos calculs, les fréquences propres en mode 1 ont été calculées comme dans les travaux de Bisch, Lasek et Rodot en première approximation, puis avec les équations de Strani et Sabetta, pour une applicabilité plus vaste. On obtient bien la relation entre fréquence de forçage et taille de goutte expérimentale (détachée au seuil, lors de la résonance) en $f \sim D_d^{-1/2}$. Ceci est la relation attendue pour une goutte liée qui résonne (au lieu de $f \sim D_d^{-2/3}$ pour une goutte libre). L'accord entre la fréquence propre et la fréquence de forçage expérimentale a été vérifié pour les différents paramètres que nous avons fait varier (tension interfaciale, diamètre de pore, masse volumique des phases). Le système ayant une viscosité de phase continue élevée

est la seule exception à l'accord obtenu. Dans ce cas, les gouttes formées sont plus petites qu'attendu. En conclusion, on peut globalement contrôler la taille des gouttes produites en fixant la fréquence de vibration, tant que l'amplitude de forçage est suffisamment élevée.

Afin de modéliser le décrochement des gouttes induit par la résonance, on considère qu'une goutte (qui résonne en mode 1) se comporte comme un oscillateur harmonique linéaire forcé. En mesurant la variation de la longueur de la goutte durant sa croissance, on confirme que ce choix de modèle est pertinent par rapport aux variations des amplitudes d'oscillation de la goutte et aux déphasages entre les oscillations de la goutte et les oscillations du capillaire. On écrit l'équation différentielle correspondante pour obtenir le mouvement du centre de masse de la goutte, en prenant en compte les paramètres de forçage, la fréquence propre de la goutte (telle qu'établie par Strani et Sabetta) et la dissipation visqueuse (telle qu'exprimée par Bisch, Lasek et Rodot). On rajoute un terme de dissipation visqueuse pour prendre en compte la friction supplémentaire qui intervient dans le film de phase continue entre la goutte et la surface du capillaire. En effet, ce film de liquide est mis en mouvement (va-et-vient dans le coin entre la goutte et le capillaire) avec les oscillations de la goutte, puisque dans notre configuration, la goutte ne mouille pas le capillaire.

Le terme supplémentaire de dissipation visqueuse est fonction de deux paramètres à identifier, ce que nous avons réalisé sur le système de référence, pour deux diamètres de pores. En effet, nous avons démontré que les gouttes se comportaient de deux façons différentes selon le rapport du diamètre de la goutte sur le diamètre du pore. Pour de faibles rapports (en dessous de 3), les gouttes se déforment entièrement lors de la résonance. Au-delà de 3, la déformation est plutôt localisée dans le col. Les paramètres sont donc identifiés selon le rapport du diamètre de la goutte sur le diamètre du pore mais aussi selon le rapport de viscosité des phases. En effet, lorsque la viscosité de la phase dispersée est augmentée, la dissipation dans le coin augmente également.

On établit ensuite un critère de décrochement de la goutte : lorsque la force de rappel est supérieure à la force capillaire maximale qui retient la goutte au pore du capillaire, alors, la goutte se détache. Cela donne un critère sur l'amplitude de déplacement du centre de masse, obtenue précédemment par le modèle de l'oscillateur harmonique. Ce déplacement est directement lié à l'amplitude de vibration du capillaire (il dépend également de la fréquence propre de la goutte, de la fréquence de forçage et des paramètres physico-chimiques des phases). Ce critère explique pourquoi au-delà d'une amplitude seuil, les gouttes se décrochent pendant la résonance. En effet, dans ce cas, elles atteignent une élongation telle qu'elles peuvent se détacher. C'est pourquoi nous avons nommé ce mode de détachement le « stretching » mode.

Grâce à notre modèle basé sur l'oscillateur harmonique avec le terme de dissipation visqueuse supplémentaire, nous avons bien décrit les amplitudes seuils et les tailles de gouttes résultantes, pour la plupart des systèmes. Nous avons, de plus, raisonnablement prédit ces valeurs caractéristiques du mode « stretching » pour les systèmes avec tensioactif en utilisant les paramètres identifiés sur le système de référence pour les mêmes rapports de viscosité. Le seul système qui n'est pas correctement décrit par le modèle est le système avec une phase continue plus visqueuse. Pour améliorer l'accord entre le modèle et les expériences pour ce cas, il faudrait calculer la fréquence propre de la goutte en incluant la dissipation visqueuse qui se produit dans le film de phase continue entre la goutte et la surface du capillaire (dissipation visqueuse qui n'est pas prise en compte dans le calcul de Strani et Sabetta).

Si les gouttes n'atteignent pas une élongation suffisante pour se détacher à la résonance (c'est-à-dire, si l'amplitude est en dessous du seuil), alors elles continuent à grossir et se détachent à de plus grandes tailles. Le décrochement des gouttes est dans ce cas contrôlé principalement par la flottabilité. En effet, les gouttes ont alors des tailles comparables à celles des gouttes formées sans vibration, en « dripping ». Une diminution légère de taille de goutte est toutefois observée par rapport aux gouttes générées sans vibration. Cette diminution de taille est attribuée à la résonance d'un mode supérieur au deuxième mode qui assisterait le décrochement des gouttes. Cela n'est pas l'objet de l'étude puisque nous nous concentrons sur le « stretching » mode. Nous n'avons donc pas étudié la zone pour des amplitudes faibles (en dessous de l'amplitude seuil) plus dans le détail, mais cela pourrait être intéressant pour des travaux ultérieurs.

Résultats principaux avec écoulement de la phase continue

Lorsque les gouttes sont soumises à un écoulement de la phase continue (sans vibration), leur taille diminue avec une augmentation de la vitesse de l'écoulement. Ceci est attendu car une vitesse d'écoulement plus élevée induit un cisaillement plus fort. Les gouttes se détachent à une taille bien prédite par un bilan des moments, ce qui a été vérifié pour des systèmes avec des tensions de surface différentes et des viscosités de phase dispersée variables. Les forces intervenant dans le bilan des moments sont la force de traînée due au cisaillement de la phase continue et la force capillaire qui retient la goutte au capillaire. Dans une moindre mesure, la force de flottabilité intervient mais elle a été négligée afin d'obtenir une loi d'échelle simple. L'application d'un bilan des moments est en accord avec d'autres travaux et est cohérent avec les images acquises. En effet, les gouttes restent généralement sphériques et se détachent en rotation autour du capillaire.

Lorsque les gouttes sont soumises simultanément à un écoulement de la phase continue et à une vibration axiale, on s'attendrait à ce que les gouttes puissent toujours se détacher en mode « stretching » avec une taille de goutte équivalente au cas sans écoulement. Par contre, l'amplitude seuil nécessaire devrait être plus faible. En effet, si les gouttes se détachent par le

même mécanisme, leur taille ne varie pas (elle correspond à celle de la fréquence propre de la goutte pour la fréquence de forçage donnée). Par contre, il existerait une force de traînée supplémentaire (induite par l'écoulement de la phase continue) par rapport à la force de rappel simple pour assister le décrochement de la goutte. Cela permettrait d'abaisser l'amplitude de forçage nécessaire au décrochement. Cela n'a pas été observé avec le système et les conditions opératoires utilisés. Il faudrait réaliser des essais sur un autre montage, voire sur un pilote industriel. D'après nos essais, nous avons surtout pu constater l'importance de bien choisir les paramètres de forçage en fonction des débits d'écoulement de la phase continue pour pouvoir contrôler les gouttes produites par le mode « stretching ».

En EM sans vibration, les gouttes sont générées en « dripping ». Mais il est possible que dans certains cas, des gouttes soient formées en « jetting » (ce qui semble être le cas dans les essais de E. Lepercq-Bost), par exemple en présence de turbulences à proximité de la surface de la membrane. Nous avons donc étudié la transition entre les régimes « dripping » et « jetting ». En premier lieu, nous avons étudié cette transition sans vibration, simplement en présence d'écoulement de la phase continue (en « cross-flow »). La transition se produit selon un nombre de Weber interne (propre au jet) et un nombre capillaire externe (propre à la phase continue) mais aussi selon un nombre d'Ohnesorge externe (propre à la phase continue). Ceci est attendu car les gouttes se détachent principalement à cause du cisaillement, confirmé par le bilan des moments établi précédemment. Deux régimes de « jetting » ont été observés selon les vitesses relatives des deux phases. Pour des vitesses de jet faibles par rapport à la phase extérieure, un régime « widening » est observé, avec un jet long et large, subissant des oscillations de surface. Pour des vitesses de jet élevées par rapport à la phase extérieure, un régime « narrowing » est obtenu, avec un jet qui devient plus étroit en s'éloignant du capillaire.

Un modèle basé sur l'équation de mouvement de la goutte en formation, similaire à celui de Clanet et Lasheras, a été développé. Ce modèle se base sur les forces capillaires, de cisaillement et de moment, avec une goutte qui se forme petit à petit à l'extrémité d'un jet qui se rétracte. Encore une fois, la flottabilité est négligée. D'après l'équation de mouvement, on obtient le déplacement maximal de la goutte en recul. Ceci correspond à la distance entre le point du début du recul (quand la goutte précédente se détache) et le point où se commence le détachement de la goutte considérée. On compare cette distance à la distance de décrochement d'une goutte par « end-pinching », qui s'effectue dans le sens opposé au recul. Le « end-pinching » est le mécanisme de décrochement d'une goutte par le pincement de son col, sous l'action des forces capillaires. Lorsque la distance de décrochement par « end-pinching » est supérieure à la distance maximale du mouvement en recul, alors le point de détachement avance à chaque cycle et un jet est formé. On a donc cherché la vitesse de la phase dispersée telle que ces deux distances sont égales pour trouver la vitesse limite qui induit le « jetting ». Avec le modèle, on extrait également la taille de la goutte formée au niveau de la transition.

Pour résoudre le modèle, on a considéré deux cas limites en régime « narrowing ». Soit on néglige les effets d'amincissement du jet induits par l'écoulement externe. Dans ce cas, on considère que le diamètre du jet est environ égal au diamètre du pore et la vitesse du jet correspond à la vitesse d'injection de la phase dispersée. Soit on considère qu'il y a un amincissement maximal du jet en considérant qu'il y a une diffusion de moment effective dans le jet. Ainsi, la vitesse du jet correspond à la vitesse de la phase continue. Dans les deux cas limites étudiés, en régime « widening », on considère toujours un jet uniforme, de diamètre égal à celui du pore.

D'après le modèle et avec les approximations sur les diamètres de jets décrites ci-dessus, on reproduit bien les vitesses critiques expérimentales pour la transition de « dripping » à « jetting ». On décrit également bien la taille des gouttes produites. En effet, les résultats expérimentaux se situent entre les deux cas limites considérés pour le régime « narrowing ». Par contre, en régime « widening », les vitesses critiques et tailles de gouttes sont surestimées par le modèle. En effet, le profil du jet est complexe, avec des oscillations de surface qui apparaissent et un amincissement moyen du jet au niveau du col de la goutte. On pourrait affiner le modèle en établissant un profil de jet rigoureux dans les deux régimes de « jetting ». Toutefois, les résultats restent convaincants, d'autant plus que le modèle est plus adapté que les précédents exposés dans la littérature. En effet, notre modèle se base sur la physique de la transition et rend compte des différents comportements des jets selon le rapport des vitesses des phases ou selon la tension interfaciale.

Enfin, nous avons commencé à étudier la transition de « dripping » à « jetting » en présence de vibrations axiales. Il semblerait que les vibrations permettent de retarder la transition de « dripping » à « jetting », comme cela a été démontré par d'autres auteurs. Cela permettrait de continuer à former des gouttes en « dripping », voire en « stretching » selon les paramètres de forçage, en utilisant des débits supérieurs (rendement amélioré) mais en continuant à maîtriser le procédé. En effet, dans ces deux cas, les tailles de gouttes sont mieux contrôlées qu'en « jetting ». Ce sujet reste encore à approfondir car peu de données ont été recueillies et les mécanismes ou le modèle n'ont pas encore été établis.

Conclusions

L'objectif initial de ce travail était de comprendre les mécanismes de décrochement des gouttes en émulsification membranaire avec des vibrations transversales. En effet, C. Arnaud (2006) et E. Lepercq-Bost (2008) ont observé que, dans certaines conditions opératoires, la vibration permettait de réduire significativement la taille des gouttes produites comparé au cas sans vibration. Par contre, les mécanismes demeuraient inconnus, ce qui rend difficile la maîtrise du procédé.

Afin de comprendre les mécanismes et les modéliser par la suite, nous avons effectué une étude expérimentale, sur deux montages différents. Le premier consistait à étudier une goutte soumise à des vibrations axiales, sans écoulement de phase continue. Le deuxième montage, similaire, avait un écoulement de phase continue en plus.

Nous avons mis en évidence que, pour une fréquence de forçage donnée, au-delà d'une amplitude seuil, des gouttes significativement plus petites sont produites. Les gouttes qui grandissent résonnent en mode 1 (mode supplémentaire pour une goutte liée) lorsque leur fréquence propre coïncide avec la fréquence de forçage. Si elles atteignent une élongation critique lors de la résonance (ce qui se produit à partir d'une amplitude seuil), alors elles se détachent. Sinon, elles continuent à grossir et se détachent à des tailles plus grosses, phénomène essentiellement dû à la flottabilité. Les mécanismes ont été modélisés en considérant la goutte comme un oscillateur harmonique linéaire forcé. Un terme de dissipation supplémentaire a été ajouté par rapport au modèle classique afin de prendre en compte la dissipation visqueuse dans le film de phase continue entre la goutte et la surface du capillaire. Ce modèle rend bien compte de nos résultats et a même permis de prédire certains résultats sur des systèmes avec tensioactif.

Lorsque des gouttes sont soumises à un écoulement, elles se détachent à une taille bien prédite par un bilan des moments. Avec vibration, le mode « stretching » n'a pas été favorisé par l'écoulement à cause des limitations du montage expérimental. La transition des régimes « dripping » à « jetting » se réalise lorsque le nombre de Weber interne et le nombre capillaire externe atteignent des valeurs critiques, pour un système donné. Un modèle a été établi, basé sur l'équation du mouvement de la goutte qui se rétracte au bout du jet. La distance maximale du mouvement en recul est comparée à la distance de détachement par « end-pinching », pour déterminer le régime de formation de la goutte. Ce modèle rend bien compte des combinaisons de nombres adimensionnels à la transition et des diamètres de gouttes résultants. Enfin, en présence de vibrations, la transition de « dripping » à « jetting » est retardée. Cela permet de rester dans le mode « dripping » même pour des vitesses de phase dispersée plus élevées. Ceci est intéressant mais reste à approfondir.

D'après les mécanismes et modèles mis en évidence, nous avons réussi à expliquer les résultats initiaux de C. Arnaud et E. Lepercq-Bost. C'était l'objectif duquel découlait ce travail. Cela a aussi permis d'améliorer les connaissances sur la formation de gouttes en présence de vibrations axiales à forte amplitude et sur la transition de « dripping » à « jetting » en écoulement transversal (« cross-flow »).

Ce travail démontre aussi l'importance de comprendre les mécanismes de décrochement des gouttes afin de contrôler au mieux les tailles de gouttes générées dans les émulsions. Pour cela, il faut bien ajuster les différents paramètres opératoires en émulsification membranaire avec

vibrations transversales. Il faut bien évidemment être en mesure de maîtriser les paramètres fixés.

Perspectives

Plusieurs perspectives sont issues de ce travail, soit pour approfondir des éléments étudiés, soit pour poursuivre le travail sur d'autres pistes.

Tout d'abord, on pourrait calculer la fréquence propre d'une goutte en incluant la dissipation visqueuse dans le film de phase continue entre la goutte et la surface du capillaire. Cela permettrait de mieux comprendre les résultats obtenus avec une phase continue à viscosité plus élevée.

Afin de confirmer la validité de notre modèle et de se rendre compte des éléments qui restent à éclaircir, des essais pourraient être effectués sur une membrane industrielle, pour différents systèmes et paramètres de vibration. En effet, le point de départ de ce travail ne concernait que les résultats de deux essais de C. Arnaud et E. Lepercq-Bost. Sur le procédé industriel, il serait intéressant d'optimiser les écoulements afin d'éviter la production des gouttes en « dripping » et « jetting » (ce qui mène à une distribution de taille de gouttes bimodale).

En ce qui concerne la transition de « dripping » à « jetting », un modèle plus détaillé pourrait être élaboré à partir de notre modèle, en établissant les profils des jets réels, notamment en régime « narrowing ».

De plus, nous avons étudié en détail l'impact de la vibration sur le mode « dripping », mais notre étude de la vibration sur le mode « jetting » n'est qu'en phase préliminaire. Il serait intéressant de poursuivre cette étude, puisqu'on a pu voir que la vibration permettait de retarder la transition au « jetting ».

Enfin, l'étude de la formation des gouttes satellites en présence de vibration serait intéressante, puisque ces gouttes satellites ont une taille non contrôlée et induisent une distribution de taille de gouttes bimodales. Il faudrait déterminer les conditions où elles sont supprimées pour optimiser le procédé.

Titre : Compréhension des mécanismes de formation des gouttes en émulsification membranaire assistée par vibrations transversales.

Mots clés : émulsion, goutte, jet, vibration, résonance, hydrodynamique.

Résumé : Dans certaines conditions, une baisse significative de la taille des gouttes se produit en émulsification membranaire avec vibrations transversales. Pour comprendre les mécanismes impliqués, nous avons développé deux dispositifs expérimentaux, dans lesquels une goutte unique est formée à travers un capillaire dans une phase externe, qui est soit stationnaire, soit en écoulement. Le capillaire peut être mis en vibration parallèlement à son axe.

Lorsque la phase externe est stationnaire, au-delà d'une amplitude seuil de forçage, la taille des gouttes formées diminue significativement. La goutte entre en résonance quand sa fréquence propre coïncide avec la fréquence de forçage et elle se détache si elle atteint une élongation critique. La goutte est modélisée comme un oscillateur harmonique linéaire forcé. Un terme d'amortissement additionnel

décrit la dissipation visqueuse entre la goutte et la surface du capillaire. Ce modèle prédit bien les amplitudes seuils et les diamètres de gouttes. Lorsque la phase externe s'écoule, nous avons étudié deux régimes de formation de gouttes, en goutte à goutte (dripping) ou à partir d'un jet (jetting). Expérimentalement, la transition du dripping au jetting se produit à un nombre de Weber interne seuil, dont la valeur dépend des nombres capillaire et d'Ohnesorge externes. Le jet se rétrécit (narrowing) ou s'élargit (widening) selon le rapport de vitesses des phases choisi. En dripping, les diamètres de gouttes sont bien prédits par un bilan des moments. En jetting, un modèle basé sur l'équation du mouvement permet d'estimer la vitesse critique permettant la transition au jetting et les diamètres de gouttes résultants.

Title: Understanding drop generation mechanisms in transversally vibrating membrane emulsification.

Keywords: emulsion, drop, jet, vibration, resonance, hydrodynamics.

Abstract: In transversally vibrating membrane emulsification, significantly smaller drops are generated in certain conditions. We aim to explain the mechanisms involved. To do so, two experimental setups were developed. A single drop is formed from a nozzle into an outer phase, which is either stationary or cross-flowing. The nozzle can be submitted to axial vibrations.

For a drop formed into a stationary phase, a transition in drop generation occurs above a critical forcing amplitude. Below the threshold, a large drop forms by dripping. Above the threshold, a drop detaches when its first eigenfrequency and the forcing frequency coincide. The drop then resonates and detaches once a critical elongation ratio is reached. We

model a drop as a linearly forced harmonic oscillator and add an extra damping term to account for the viscous dissipation between the drop and nozzle surface. We well reproduce the threshold amplitudes and drop diameters.

We also study drops generated into cross-flow. In dripping mode, drop diameters are described by a torque balance. At a critical inner Weber number function of the outer capillary and Ohnesorge numbers, a transition to jetting occurs. Jet widening or narrowing takes place depending on the phase velocity ratio. We propose a model to account for the transition to jetting based on the drop equation of motion. Overall, we adequately account for the jetting velocity and drop diameters, with discrepancies which were explained.